

Proximity-Induced Magnetization in SrIrO₃ Thin Films

Zur Erlangung des akademischen Grades eines

DOKTORS DER NATURWISSENSCHAFTEN

(Dr. rer. nat.)

von der KIT-Fakultät für Physik des
Karlsruher Instituts für Technologie (KIT)
angenommene

DISSERTATION

von

M. Sc. Arun Kumar Jaiswal
Institute for Quantum Materials and Technologies
aus Siddharth Nagar, Uttar Pradesh, India



Karlsruher Institut für Technologie

Referent: Prof. Dr. Matthieu Le Tacon
Korreferent: Prof. Dr. Wulf Wulfhekel
Betreuer: Dr. Dirk Fuchs

Tag der mündlichen Prüfung – 28.06.2024

DECLARATION

By the Ph.D. Candidate

I hereby declare that this research thesis entitled “**Proximity-Induced Magnetization in SrIrO₃ Thin Films**”, which is being submitted to the Faculty of Physics **Karlsruhe Institute of Technology, Germany**, in partial fulfilment of the requirements for the award of the Degree of **Doctor of Philosophy in Physics** is a truly original report of the research work I carried out. I have not used sources other than those specified and cited in the bibliography. The contents of this thesis, in full or in parts, have not been submitted to any other Institution or University for the award of any degree or diploma.

Arun Kumar Jaiswal

Institute for Quantum Materials and Technologies
Karlsruhe Institute of Technology, Germany

Place:

Date:

Abstract

To reduce the increasing power consumption in information technology, energy-efficient devices are the need of the hour. In contrast to conventional electronic devices, which rely on charge transport, spintronic devices offer energy-saving alternatives and could pave the way for next-generation information processing. The magneto-electric coupling, essential for these devices, is usually provided by spin-orbit coupling (SOC). In $3d$ -transition metal oxides (TMOs), electron-electron correlation is strong; however, SOC, which evolves with increasing atomic numbers, is only small. On the other hand, in $5d$ -TMOs, which display strong SOC, the electron correlation is rather weak. Therefore, combining both $3d$ and $5d$ -TMOs in artificially grown heterostructures (HSs) provides a promising platform to search for new quantum materials showing exotic effects and potential for next-generation spintronic devices.

In this thesis, perovskite SrIrO_3 (SIO) HSs, in which $5d$ -TMO SIO is combined with magnetic $3d$ -TMO perovskite, are analyzed in detail with respect to proximity induced changes of the magnetization and electronic transport in the presence of a neighbored magnetic layer, *e.g.*, LaXO_3 or NdNiO_3 (LXO, NNO) with $X = \text{Mn, Fe and Co}$. To this purpose, high-quality LXO(NNO)/SIO HSs were produced by pulsed laser deposition (PLD). PLD is a commonly used thin film deposition technique to produce epitaxial TMO thin films and HSs with high epitaxial quality and thickness resolution of one unit cell.

In contrast to the SIO single layer, the LCO/SIO HSs, where LCO is a ferromagnetic (FM) insulator, display a strong intrinsic anomalous Hall effect (AHE) and anisotropic magnetoresistance indicating in-plane antiferromagnetic (AFM) ordering similar to that of layered Sr_2IrO_4 with effective moment (m_{eff}) along the pseudo-cubic (110) direction. Separating LCO and SIO by a 4 monolayer thick, insulating SrTiO_3 layer and increasing the SIO thickness in LCO/SIO HSs suppress the effects strongly and document proximity-induced AHE, magnetic moment and magnetocrystalline anisotropy in SIO.

Electrostatic doping by electric field effect in back gate geometry enhances AHE by a factor of 7 but leaves the magnetic moment of $m_{\text{eff}} \approx 0.02 \mu_{\text{B}}/\text{Ir}$ nearly unaffected. Therefore, the origin of the strong AHE is very likely caused by enhanced Berry curvature (BC) due to the topological band structure of SIO (also supported by recently published DFT results).

Substitution of the LCO layer by other magnetic $3d$ -TMO layers allows for more detailed analysis of the proximity effect, magnetic exchange, and coupling between SIO and the $3d$ -magnetic layer. With increasing $3d$ -electron number, interfacial charge transfer is observed from $5d$ -SIO to $3d$ -TMO which increases systematically from Mn to Co (Ni). However, the induced spin and orbital magnetic moment in SIO is very similar in all HSs. In contrast, the AHE shows significant enhancement when a FM layer (LCO, LMO) is interfaced with SIO, in comparison to SIO/AFM HSs; where the AHE is one order of magnitude smaller,

indicating the strong influence of the effective magnetic moment and effective local field associated with the magnetic layer at the interface on the BC and hence AHE.

The obtained results provide important information on the interfacial properties of $3d/5d$ HSs and demonstrate effective coupling between perovskite-related $3d$ -TMO and SIO. On the other side, proximity-induced SOC in the $3d$ -TMO layer is also very likely and could be useful for magnetization manipulation in $3d$ -TMOs by electric field via the Rashba effect. This issue will be addressed in future works.

Dedicated
to
my Grandparents
and
Parents

Contents

1	Motivation	1
2	Perovskite Related Transition Metal (<i>3d</i>, <i>5d</i>) Oxides	7
2.1	The <i>3d</i> transition metal oxides	8
2.1.1	Perovskite crystal structure	9
2.1.2	Octahedral crystal field and electronic correlation	11
2.1.3	<i>3d</i> TMO: LaCoO ₃ - crystal structure, electronic and magnetic properties	14
2.2	The <i>5d</i> transition metal oxides	16
2.2.1	SrIrO ₃ ($n = \infty$): crystal structure	18
2.2.2	SrIrO ₃ : electronic and magnetic properties	20
2.3	SrIrO ₃ thin film heterostructures and superlattices	22
3	Sample Preparation and Experimental Methods	29
3.1	Sample preparation	30
3.1.1	Target preparation using solid state synthesis	30
3.1.2	Substrate pre-treatment	31
3.1.3	Pulsed laser deposition	33
3.1.4	Device preparation	38
3.2	Experimental methods	40
3.2.1	Chemical analysis	40
3.2.2	Structural characterizations	41
3.2.3	Electronic transport measurement	46

3.2.4	Magnetization measurements	52
3.2.5	Spectroscopy measurements	54
4	Proximity Induced Magnetic State and Anomalous Hall Effect in 5d-TMO SrIrO₃	57
4.1	Structural properties of the LaCoO ₃ /SrIrO ₃ HSs	58
4.2	Electronic transport in LaCoO ₃ /SrIrO ₃ HSs	63
4.2.1	Longitudinal resistivity	63
4.2.2	Transversal (Hall) resistivity	67
4.2.3	Magnetoresistance	70
4.2.4	Interfacial charge transfer:	76
4.3	Magnetic properties of LaCoO ₃ /SrIrO ₃ HSs	79
4.3.1	Magnetization measurement	79
4.3.2	X-ray magnetic circular dichroism	80
4.4	Electric field control of the anomalous Hall effect in LaCoO ₃ /SrIrO ₃ HSs	81
4.4.1	Electric field effect in SIO/LCO HSs	82
4.4.2	Effect of electrostatic gating on magnetotransport	88
4.4.3	Effect of electrostatic gating on the magnetic anisotropy	90
4.4.4	Effect of electrostatic gating on Ir edge XMCD	91
4.5	Magnetism and band topology in SrIrO ₃	92
5	Charge Transfer and Magnetic Exchange in SrIrO₃ based 3d-5d Transition Metal Oxide Heterostructures	97
5.1	Structural Characterization of LXO(NNO)/SIO bilayer HSs	100
5.2	Electronic transport in LXO(NNO)/SIO bilayer HSs	104
5.2.1	Longitudinal resistivity	104
5.2.2	Transversal (Hall) resistivity	106
5.2.3	Magnetoresistance	107
5.3	Electron spectroscopy	109
5.4	Discussion	113

6 Conclusion & Future Directions	117
References	120
Appendix	139
Abbreviations	143
List of publications	147
Acknowledgements	149

CHAPTER 1

Motivation

The whole of science is nothing more than a refinement of everyday thinking.

Albert Einstein

The evolution of information technologies over the previous two decades that includes the processing, sensing, communication, and storage of data is ever-increasing. The increasing demand necessitates large number of microelectronic components embedded into a compact integrated circuit with sustainable power consumption [1]. Currently, the basic building block of such systems are the silicon-based complementary metal-oxide-semiconductor (Si-CMOS) devices, which however, now face two serious challenges-

i) Moore's law; which states that the number of microelectronic components (*e.g.* transistors) on a chip will be doubled every two years [2]. In other words, the critical dimension of transistors will be reduced by a factor of two every second year,

ii) Current state-of-the-art characteristic length scale of the devices are ~ 7 -10 nm, which is at the saturation level and possibly can't be further shrunk.

These two pose a serious concern as Moore's law will no longer be applicable, meaning one needs to consider beyond Moore's law technologies to fulfill the ever-increasing demands. Recently, it was estimated that the total energy consumption of microelectronic components in information and communication technology systems will grow to up to 20 % of the total energy by the year 2030 [1, 3]. We are again at a similar stage to when CMOS technology replaced bipolar transistors in 1990. Thus, we must explore new pathways to develop energy-efficient sub-nanometric electronic technologies.

In this direction, a surge in the exploration of "Quantum Materials" has emerged in the past decade. They have shown exotic physical phenomena such as ferromagnetism, ferroelectricity, superconductivity and multiferroic order behavior. The physics of these materials are governed by quantum mechanical effects. For example, transition metal based compounds represent a unique class of quantum materials with extremely rich and diverse physical properties originating from the electronic correlation of rather localized *d*-electrons in contrast to the delocalized *2p*-electrons in semiconductors [4].

Transition metal oxide (TMO) interfaces are analogous to semiconductor junctions. However, there are striking differences between the interfacial coupling in these two systems. Unlike conventional semiconductor devices where only charge degrees of freedom are exploited, TMOs offer spin, orbital, charge and lattice degrees of freedom. At the interface, they compete and/or couple with each other and their delicate interplay provides efficient control over various functionalities [5–8].

One unique characteristic of TMO based compounds is that they can accommodate many elements of the periodic table and thus offer countless design opportunities. This distinctive endeavor opens the large chemical variety to explore for possible application in electronic de-

vices [9]. In contrast, Si-CMOS devices are designed using only a few elements/compounds ($2p$ electron systems). Elements like Si, Ge and compounds such as GaAs, InSb, GaP and ZnO are few examples to name.

Technological advancements in growth techniques over the last 20 years have made it possible to grow oxide films with atomic-scale precision. This allows synthesis of artificial superlattices with sharp interfaces. Molecular beam epitaxy [10, 11], pulsed laser deposition [12, 13] and magnetron sputtering [13, 14] were employed to produce high-quality oxide heterostructures and interfaces.

The discovery of two-dimensional high-mobility electron system (2DES) at the base of two band insulators LaAlO_3 and SrTiO_3 (LAO/STO 2DES) has revolutionized the field of oxide electronics [15]. The discovery quickly caught the attention and led to a surge in the efforts to exploit the LAO/STO 2DES for device applications. A Nature Materials editorial article “The interface is still the device” highlights the discovery and characteristic features observed in LAO/STO 2DES [16]. The LAO/STO 2DES has shown numerous distinctive features such as electric field controllable low-temperature superconductivity [17, 18] and Rashba spin-orbit coupling (SOC) [19], ferromagnetism [20, 21], large spin-charge inter-conversion [22, 23] etc.

Spintronic devices that exploit the electron’s spin to carry information offer energy-saving alternatives and could pave the way for next-generation information processing. Datta-Das spin transistor and magneto-electric spin-orbit transistor (MESO) are few proposed prototype examples of spin-based transistors [24, 25]. Thus, the search for new spin-polarized 2DES is highly desirable as this will open the door to new oxide based spintronic devices [26]. Compared to CMOS devices, distinctive features include possible down scaling to sub-nanometric level, correlated phenomenon (*e.g.* magnetism) originating from localized d -electrons and SOC (or Rashba SOC). The efficient control of the spin-polarization, *i.e.*, magnetism is the key to information storage. Despite some experimental observations [20, 21], the intrinsic magnetism in LAO/STO 2DES is still in debate. Several experiments have suggested the interfacial defects or stoichiometric imbalance as the origin of magnetism in LAO/STO 2DESs [27–29]. The insertion of a few unit cell thin magnetic layers, *e.g.*, EuTiO_3 or LaMnO_3 have also shown the signature of magnetic ordering [30, 31]. However, the reported transition temperatures are limited to $< 10\text{-}20$ K which limits the use of these 2DESs in spin-based device application.

In this Ph.D. thesis, the focus is on the design of new 2D (or quasi-2D) spin-polarized electron systems (SPESs) on the base of TMO HS comprising correlated quantum materials.

The main interest here is not only the creation of highly spin-polarized electron systems, but also the possibility to manipulate the polarization, for example by strain or electric field.

Different routes towards the spin polarization of 2DES will be explored in detail, *e.g.*, proximity effect, interfacial doping or spatial confinement. The first one involves adding magnetic active layers to an already existing 2DES and to create spin-polarization by proximity effect. We will start with SrIrO₃/LaCoO₃ (SIO/LCO) heterostructures (HSs). The HSs comprise of semimetallic 5*d*-TMO SIO, which naturally displays large spin-orbit coupling and the strain-induced ferromagnetic insulator LCO. To establish 2D spin-polarized transport in SIO/LCO the main challenges are as follows: First, a quasi 2D electronic transport must be realized in SIO by reducing the layer thickness (the mean free electron path perpendicular to the film surface $\lambda_{\perp} \ll$ parallel to the the film surface λ_{\parallel}), maintaining high crystallinity and metallicity of SIO or by producing a confined potential via charge carrier depletion using the electric field effect. Second, magnetic order must be induced in SIO which is intended to be provided by LCO via proximity effect. The mutual competition of SOC and FM may also allow for new topological states [32] and the possibility to manipulate spin-polarization by the variation of SOC or magnetic anisotropy. For example, the strain-induced FM state of LCO gives the possibility for manipulation of the magnetization and magnetic anisotropy in LCO by epitaxy, which likely enables control of the 2D SPES in SIO as well. On the other side, SOC also provides the possibility to manipulate magnetization via the spin-Hall effect, resulting in a changed SP alike.

Compared to previously studied SrRuO₃/SrIrO₃ and La_{1-x}Sr_xMnO₃/SrIrO₃ HSs [33–35], where both constituent layers are conducting, the electronic transport strictly resides within the SIO layer in LCO/SIO HSs owing to the robust insulating nature of LCO [36] which allows for the unambiguous, selective characterization of SIO properties by means of transport experiments.

In addition, the heavy-metal/ferromagnet bilayer (HM/FM, *i.e.*, SIO/LCO) interfaces (conventional spintronic systems) offer the possibility to study the spin-charge interconversion originating from the spin Hall or Rashba-Edelstein effect. The spin-orbit torque generated at the interface can be used to switch the magnetization of the LCO layer. In comparison to commonly studied metallic spintronic systems consisting of 5*d*- heavy metals (W, Ta and Ir) and 3*d*- ferromagnetic metals (Mn, Fe and Co), the TMO HM/FM HSs have shown large interconversion efficiency, as exemplified by observation of large and gate tunable spin-charge conversion efficiency in LAO/STO 2DES [22, 23]. TMO perovskite related oxide interfaces offer the possibility for smooth and atomically sharp interfaces, the prerequisite

for large spin transparency [37]. A large spin Hall effect has been predicted and observed in SrIrO₃ based HM/FM HSs [38–41] which could be even enhanced in all oxide SrIrO₃ based HM/FM, *e.g.*, SrIrO₃/La_{1-x}Sr_xMnO₃ HSs [42–44]. Inversion symmetry breaking at the interface and the SOC of HM are expected to result in large DMI and can induce chiral magnetic texture in these systems alike.

The second route towards 2D-SPES is focused on the delta doping of existing 2DESs. For example, the delta doping by using a 1-2 unit cell thick EuTiO₃ layer between the LAO and STO results in the formation of 2D-SPES [30]. The main challenge here is the preparation of a well-defined atomically sharp interface. For example, disorder or ion-mixing at the interface may lead to strong fluctuations of the magnetic order parameter, preventing distinct spin-polarization. Furthermore, charge carrier freeze-out at interfacial defects reduces conductivity and should also be avoided.

CHAPTER 2

Perovskite Related Transition Metal (*3d*, *5d*) Oxides

If I have seen further, it is by standing on the shoulders of giants.

Isaac Newton

This chapter briefly introduces the physics of $3d$ and $5d$ transition metal oxides. As representative members, a brief introduction to the structural and physical properties of LaCoO_3 ($3d$) and SrIrO_3 ($5d$) are discussed. Finally, a survey of the existing work related to the SrIrO_3 -based thin films, heterostructures and superlattices is presented.

2.1 The $3d$ transition metal oxides

Transition metal oxides (TMOs) represent a class of functional materials that hold great promise for the technological replacement of semiconductor-based electronics. They provide a perfect playground to design exotic functionalities, *e.g.*, ferroelectricity, ferromagnetism, multiferroics, metal-to-insulator transition, high-temperature superconductivity etc [5–8]. In addition, the complex interplay of various degrees of freedom, *i.e.*, lattice, charge, orbital and spin provide additional knobs to control and manipulate the ground state.

The physics of TMOs, to a large extent, is governed by the d -electrons of the outermost shell of the transition metals and the hybridization between transition metals through oxygen ions [4]. The presence of strong electron correlations, crystal field splitting, spin-orbit coupling and their competition dictate the electronic and magnetic ground states in these compounds.

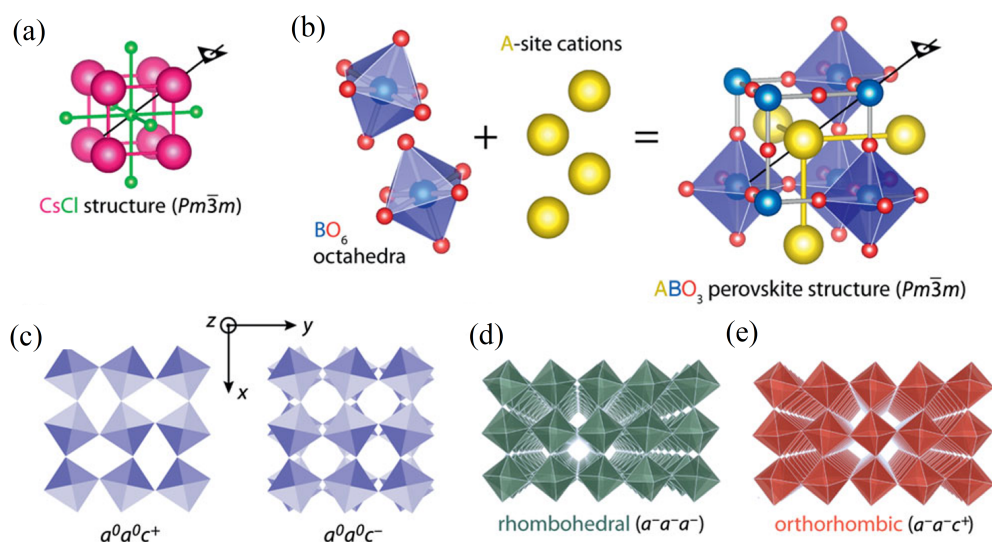


Figure 2.1: Perovskite crystal structure: (a) the cubic ($Pm\bar{3}m$) structure, (b) the BO_6 octahedra and A-site cations form the ideal cubic perovskite structure ABO_3 . The lower symmetric (c) tetragonal, (d) rhombohedral, (e) orthorhombic perovskite structures. The figure is adapted from Ref. [45].

2.1.1 Perovskite crystal structure

The basic building blocks of perovskite (ABO_3) are represented by the metal-oxygen octahedra (BO_6) and the A site cation. The ABO_3 structure can be visualized as the corner sharing BO_6 octahedra placed at the corner position (Cs) of the $CsCl$ ($Pm\bar{3}m$) cubic unit cell while A cations are placed at the Cl position, see Fig. [2.1a,b] [45]. Thus, the structure can be visualized as the 3-dimensional network of corner-sharing BO_6 octahedra where A cations are placed at the center of such 8 octahedra. The ideal cubic perovskite structure is centrosymmetric and thus provides a B-O-B (or M-O-M, M = transition metals) bond angle of 180° .

The unique feature of the ABO_3 TMO structure is its adaptability to accommodate most of the periodic table elements. However, depending on the size of different cations, only a few combinations exhibit ideal cubic lattice. Any mismatch from the ideal cubic structure, depending on the ionic radii of the A and B site cations, leads to the distortion of the cubic lattice and adaptation of a lower symmetric distorted perovskite structure. The perovskite lattice distortions can be described by the following two concepts:

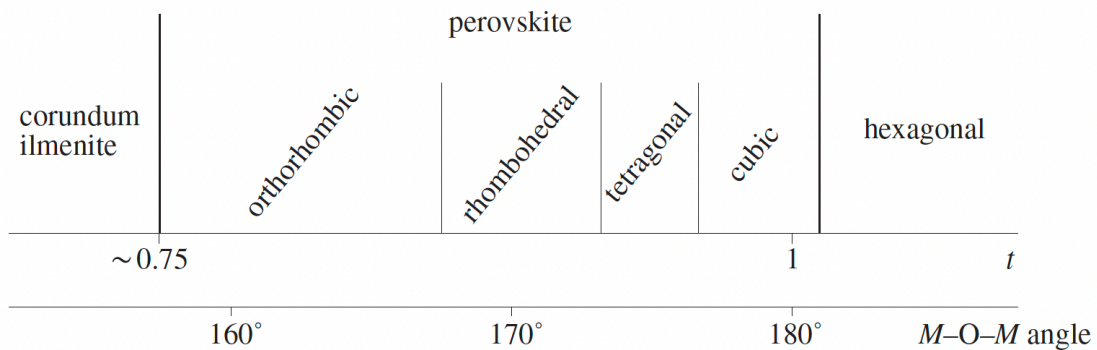


Figure 2.2: Tolerance factor for a perovskite structure: the reduced tolerance factor favors a lower symmetric structure following the octahedral distortions. The increased rotation reduces B-O-B hybridization and controls the physical properties of ABO_3 perovskite [4].

(i) The Goldschmidt tolerance factor:

The stability and classification of a perovskite lattice can be made on the basis of the atomic radii of its constituent ions. Let us consider the ionic radii R_i of ions ($i = A, B$ and O) of a perovskite lattice ABO_3 . For the simplest cubic case, we have the relation:

$$R_A + R_O = \sqrt{2}(R_B + R_O).$$

The above relation holds for the case of an ideal cubic perovskite. Based on the choice of smaller or larger ions at A or B site positions, the above relation will not be valid anymore. Any ionic radii mismatch leads to the distortion of an ideal cubic cell and consequently we need to invoke a factor accounting for the distortion:

$$R_A + R_O = t \times \sqrt{2}(R_B + R_O), \quad (2.1)$$

$$t = \frac{R_A + R_O}{\sqrt{2}(R_B + R_O)}. \quad (2.2)$$

The factor ‘ t ’ is known as Goldschmidt tolerance factor [46]. For $0.9 < t \leq 1.0$, the structure remains cubic, whereas $0.75 > t > 0.9$ drives to a lower symmetric tetragonal, orthorhombic or rhombohedral structure, depending on the cation radii R_A and R_B , see Fig. [2.2]. A large offset from $t = 1.0$ results in highly distorted, asymmetric non-perovskite structures, *e.g.*, ilmenite, *i.e.*, edge sharing octahedra ($t < 0.75$) and hexagonal, *i.e.*, face sharing octahedra ($t > 1.0$), respectively [4, 47].

(ii) The Glazer’s notation of octahedral rotation

In perovskite TMOs, B-O bond strength is stronger than A-O bonds resulting in the rather rigid BO_6 octahedra. Thus, perovskite distortions are usually accompanied by the rotations or tilts of the BO_6 octahedra along one or more crystal axis directions. The physical properties of perovskite oxides greatly depend on the detail of such distortions. The buckling of the BO_6 octahedra networks lead to the reduced B-O-B bond angles which modifies the hybridization between the $\text{Bnd-O}2p\text{-Bnd}$ orbitals and alters the physical properties. These octahedral rotations and tilts can be quantitatively defined using Glazer notations: $a^{(+/-/0)}b^{(+/-/0)}c^{(+/-/0)}$ [48, 49]. The a , b and c are the magnitude of rotations around x, y and z cubic (or pseudo-cubic in case of lower symmetric perovskites) axes, respectively and the superscripts +, - and 0 represent the in-phase, out-of-phase or no rotation of neighboring octahedra. Thus, for example, the Glazer notation of $a^-a^-c^+$, which represents the orthorhombic structure, corresponds to the out-of-phase BO_6 octahedra rotation around pseudo-cubic x, y (or a and b) axes with equal magnitude and in-phase BO_6 octahedra rotation around pseudo-cubic z (or c) axis with a larger magnitude than that of x and y axes, respectively. In Fig. [2.3], we show the different distorted perovskites in octahedral rotation

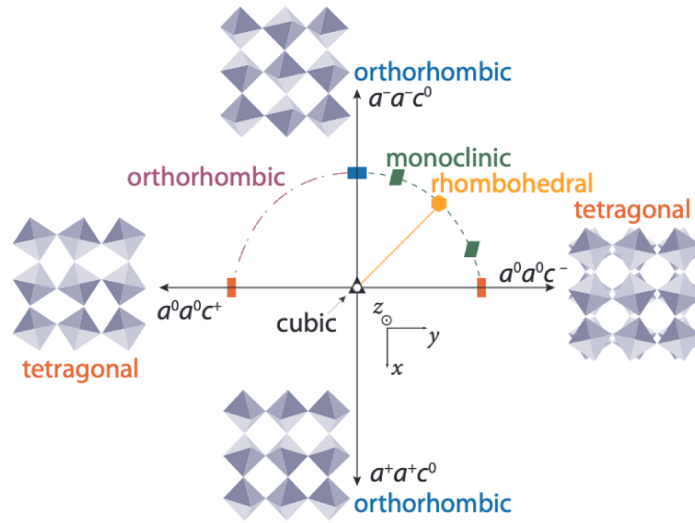


Figure 2.3: Octahedral rotation phase space: rotation of BO_6 octahedra around in-plane (a and b pseudocubic axes) and out-of-plane (c) axes leads to distortion of cubic perovskite and stabilization of lower symmetric tetragonal, orthorhombic, rhombohedral etc., structures. Based on the specific rotation pattern, total 23 tilt/rotation systems are possible [48]. The figure is taken from Ref. [50].

phase space [50].

Based on the limitation of octahedra rotations in 3-dimensions, a total 23 distinct tilt systems (14 three tilt systems, 6 two tilt systems, 2 one tilt system, 1 zero tilt systems) spanning 15 unique space groups are possible [48, 49]. The most commonly observed distorted perovskite systems are tetragonal ($a^0a^0a^{+/-}$), orthorhombic ($a^-a^-c^+$) and rhombohedral ($a^-a^-a^-$) structures.

Here, it is worth mentioning that external perturbations, such as a bi-axial or uni-axial pressure, substrate-induced strain in epitaxial films and ultrafast laser pulses can also cause lattice distortions and result in octahedral rotations. An off-stoichiometric composition as in ABO_x ($2.5 \leq x < 3$) also leads to the octahedra distortion and favors lower symmetric structures (*e.g.* brownmillerite phase).

The octahedral rotations/tilts result in doubling of the perovskite unit cells in real space. Thus, experimentally, the octahedra rotations can be probed by measuring the X-ray diffraction for specific set of half-integer reflections in reciprocal space [49].

2.1.2 Octahedral crystal field and electronic correlation

Crystal field splitting is a purely electrostatic phenomenon which originates from the incorporation of negatively charged anions (O^{2-}) in the surrounding of d -electrons of the transi-

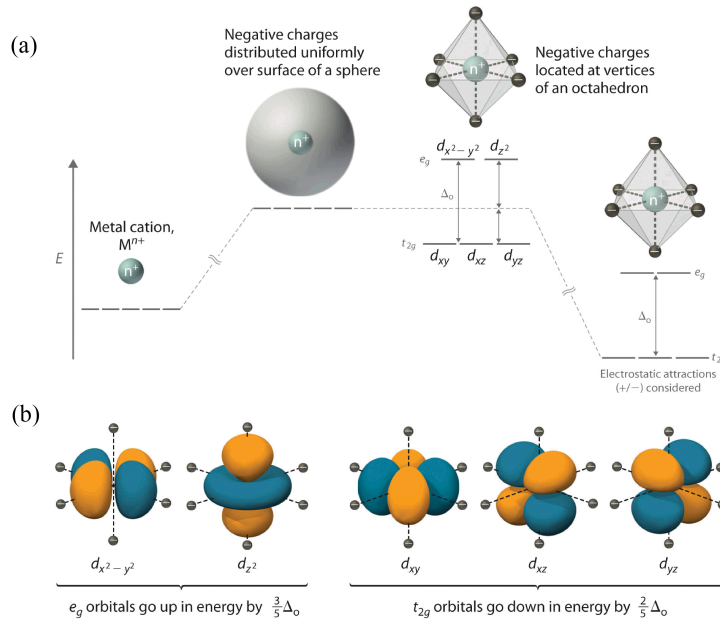


Figure 2.4: Crystal field splitting of 5-fold degenerate d -orbitals in octahedral environment: (a) distribution of O^{2-} ions at the octahedra sites rearranges the energy of d -orbitals depending on the electron density profile and leads to breaking of degeneracy and formation of t_{2g} (d_{xy} , d_{xz} , d_{yz}) and e_g ($d_{x^2-y^2}$, d_{z^2}) manifolds, (b) the electron density profile of the t_{2g} (d_{xy} , d_{xz} , d_{yz}) and e_g ($d_{x^2-y^2}$, d_{z^2}) orbitals [51].

tion metal ions (M^{n+} or B^{n+}) [4]. Depending on the spatial arrangement, the electric field produced by the O^{2-} ions leads to the increase or decrease of energy of the M^{n+} d -orbitals. If the 6 O^{2-} ions are distributed uniformly over a spherical surface, it only increases the energy of all five d -orbitals. However they remain degenerate [2.4a]. If the distribution is not symmetric, as in the case of octahedral symmetry, the fivefold degenerate d -orbitals split into two sets of non-degenerate orbitals: a lower lying triplet t_{2g} (d_{xy} , d_{xz} , d_{yz}) and a higher energy doublet e_g ($d_{x^2-y^2}$, d_{z^2}) depending on the orbital wavefunction distributions (*i.e.* electron density profiles), see Fig. [2.4a]. The e_g orbitals experience stronger Coulomb repulsion compared to t_{2g} orbitals, which raises the energy of e_g orbitals [4, 51]. The two set of orbitals are shown in Fig. [2.4b]. In a similar way, the tetrahedral symmetry, contraction or expansion of octahedra along specific directions will also break the degeneracy, depending on the Coulomb repulsion felt by the d -orbitals.

The crystal field plays very critical role in determining the electronic structure of TMOs. The network of BO_6 octahedra result in the lifting of d -orbital degeneracy and thus strongly influence the hybridization with the nearest neighbours via $O-2p$ orbitals.

The B-O hybridization generally allows for a distinct B-O-B exchange of electrons, which is often well described by the Hubbard model that includes the kinetic energy (H_{kin})

responsible for the hopping of an electron from one site to another and an onsite Coulomb repulsion ($H_{Coulomb}$) term describing interacting electrons [4, 52–54]. The relative strength of these two governs the metallic or insulating nature of the interacting electron system in the absence of other stronger energy interactions.

In 4d/5d TMOs, where shell radius and hence radial velocity of electrons are much larger compared to 3d, relativistic effects have to be taken into account. This generally results in spin-orbit interaction. In electron's rest frame of reference, it can be visualized as the interaction of the spin dipole of the electron with the magnetic field produced by the orbital motion of the nucleus. The coupling leads to a breaking of spin degeneracy of particular orbitals. Thus, in simplest form, the energy term representing spin-orbit coupling (SOC) can be given as- $H_{SOC} \propto \vec{\mu} \cdot \vec{B} = \lambda \vec{S} \cdot \vec{L}$, where μ, B, S, L are spin magnetic moment, orbital magnetic field, spin and orbital angular momentum respectively. The proportionality constant λ is known as the SOC constant. The 'atomic' λ becomes important for the heavier atoms as it evolves as $\lambda \propto Z^4$, where Z is the atomic number [4, 55].

Aside from the previously mentioned, a system may involve other energy interactions, such as the exchange interaction (H_{Exc}) responsible for magnetic ordering, Zeeman or Stark interactions relevant for lifting the degeneracy of orbitals under the influence of strong magnetic and electric fields, and the Jahn-Teller distortion commonly observed in manganites to avoid the degeneracy of ground state. To model a system with these energy interactions or others, it is important to consider all the relevant energy terms in the Hamiltonian (H) depending on their relative strength, *e.g.*,

$$H = H_{kin} + H_{Coulomb} + H_{SOC} + H_{CF} + H_{Exc}$$

Depending on the relative strength, a specific interaction can be ignored or treated as a perturbation to the system; however, if the interaction is strong enough to compete with others, it has to be taken into account in the Hamiltonian to describe the system accurately. For example, SOC can be ignored in the Hamiltonian of 3d-TMOs. However, in 4d and in particular 5d-TMOs, the strength of SOC is on a similar scale to that of the crystal field splitting and electron correlation, thus it has to be considered in the Hamiltonian separately to model the system.

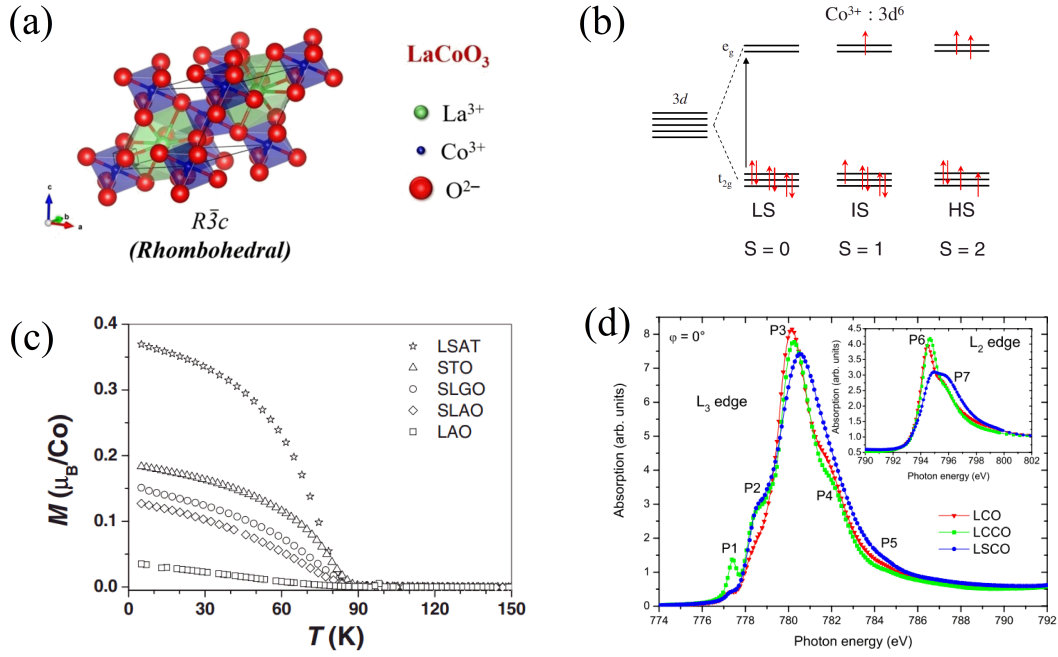


Figure 2.5: (a) Crystal structure of rhombohedrally distorted LaCoO₃, (b) different spin-state configuration of Co³⁺ (d^6) ion, (c) epitaxial strain induced ferromagnetic ordering in LaCoO₃ films, (d) X-ray absorption spectra of undoped, electron and hole doped LaCoO₃ films. The figures are taken from Ref. [56–59].

2.1.3 $3d$ TMO: LaCoO₃ - crystal structure, electronic and magnetic properties

Bulk LaCoO₃ (LCO) exhibits distorted rhombohedral perovskite structure ($R\bar{3}C$) and undergoes a rhombohedral to cubic transition at $T \sim 1610$ K [60]. The bulk lattice parameters are: $a = 5.44$ Å and $c = 13.10$ Å, which corresponds to a pseudo-cubic lattice constant $a_{pc} \approx 3.805$ Å [61, 62]. Depending on the competition between crystal field and Hund's exchange energy, Co³⁺ (d^6) can accommodate different spin state configurations, see Fig. [2.5b]. Bulk LCO shows non-magnetic and insulating ground state as all Co³⁺ are in a low spin state ($t_{2g}^6 e_g^0$, LS, $S = 0$) at $T = 0$ K. With increasing T , a cross-over to high spin state ($t_{2g}^4 e_g^2$, HS, $S = 2$) occurs at $T \sim 500$ K. However, such HS state of Co³⁺ can be promoted even at lower temperatures. The tensile strained LaCoO₃ films show a ferromagnetic transition with $T_c \sim 85$ K [62], where the magnetization increases with tensile strain imposed by the substrate, see Fig. [2.5c]. However, T_c saturates at the higher tensile strain ($\epsilon_{xx} \sim 1.6\%$) [58]. The crossover between different spin states depends on the competition between crystal field splitting and intra-atomic exchange interaction, *i.e.*, Hund's rule. This competition can be

tuned by, *e.g.*, electron or hole doping and chemical or external pressure. Increasing tensile strain results in an increase of unit-cell volume making the HS state with its large ionic radius energetically favorable compared to the LS state. A detailed XAS and multiplet calculation analysis resulted in the presence of 36 % Co^{3+} HS and 64 % LS state in the LaCoO_3 films grown on Nb-STO (001) substrate [59]. A superexchange between the Co^{3+} HS and LS state was argued as the responsible mechanism for the observed ferromagnetism [59].

In Fig. [2.5d], we show the X-ray absorption spectra of LaCoO_3 , $\text{La}_{0.7}\text{Sr}_{0.3}\text{CoO}_3$ (hole-doped) and $\text{La}_{0.7}\text{Ce}_{0.3}\text{CoO}_3$ (electron-doped) thin films [59]. The doping-induced changes of the Co valence state are clearly visible in the spectra. With respect to the manganite (*e.g.* LaMnO_3) physics, the striking difference in LaCoO_3 is the asymmetry of the phase diagram towards the electron and hole doping. An equivalent amount of electron or hole doping in manganites ($\text{Mn } t_{2g}^3 e_g^{1\pm x}$) leads to a very similar increase in magnetization, transition temperature and conductivity provided by the double exchange mechanism [63, 64]. Similar to manganite, a 30 % hole doping of LaCoO_3 ($\text{La}_{0.7}\text{Sr}_{0.3}\text{CoO}_3$) leads to an increased magnetization, transition temperature ~ 200 K (for $\text{LaCoO}_3 \sim 85$ K) and a metallic ground state. Such transition is induced by the double exchange mechanism mediated between the Co^{3+} HS state and the Co^{4+} HS state [59, 65, 66]. In stark contrast, 30 % electron doping of LaCoO_3 ($\text{La}_{0.7}\text{Ce}_{0.3}\text{CoO}_3$) suppresses the transition temperature strongly ~ 23 K, and the sample remains insulating. The 30 % Co^{2+} were found to be in HS state. A spin blockade phenomenon which prohibits the transfer of electrons from the Co^{2+} HS state to the Co^{3+} LS state, results in the electron localization and explains the reduced transition temperature and insulating state in electron-doped LaCoO_3 [59].

This asymmetry, however, could be very interesting for integrating LaCoO_3 in HSs and SLs. Undoped LaCoO_3 and electron doped LaCoO_3 (at least up to 30 % doping in $\text{La}_{0.7}\text{Ce}_{0.3}\text{CoO}_3$) does not lead to any measurable conductivity ≤ 100 K. Thus, in heterostructures where low (or negligible) electron transfer is expected from the contact layer to LaCoO_3 [67], the transport measurement will allow the unambiguous characterization of the contact layer. Even light hole-doping also does not result in an observable conductivity, see Fig. [4.6d]. This motivated us to combine SrIrO_3 with LaCoO_3 . The O-2p band alignment at the interface predicts interfacial electron transfer from SrIrO_3 to LaCoO_3 owing to the difference in the Fermi energy [68]. However, this electron transfer will not lead to any measurable conductivity in LaCoO_3 and will allow to measure the intrinsic transport related properties of SrIrO_3 originating from the interfacial coupling at the interface with ferromagnetic and insulating LaCoO_3 . One more point worth mentioning here is that LaCoO_3 shows small but

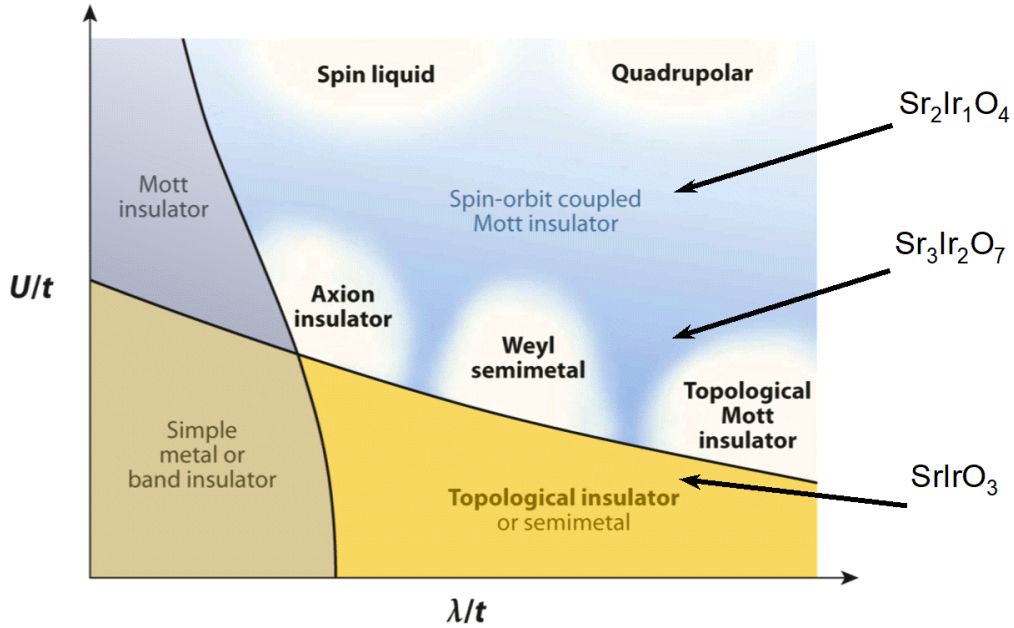


Figure 2.6: The phase diagram between the electron correlation U (represented by U/t) and spin-orbit coupling SOC (represented by λ/t), where t and λ are the hopping and SOC constant, respectively. In the limit of strong U and SOC, novel quantum states may emerge [32].

sizeable spin-orbit coupling which is vanishingly small in other $3d$ -TMO ferromagnets such as $\text{La}_{0.7}\text{Sr}_{0.3}\text{MnO}_3$. This, in addition, also provides advantages to $\text{SrIrO}_3/\text{LaCoO}_3$ interfaces over $\text{SrIrO}_3/\text{La}_{0.7}\text{Sr}_{0.3}\text{MnO}_3$ interfaces.

A brief introduction to the structural and physical properties of other $3d$ -TMOs used in this thesis work is given in Chapter 5.

2.2 The $5d$ transition metal oxides

Extensively studied $3d$ -TMOs have shown intriguing functionalities owing to the strong electron correlation (U) of the d -electrons. Observation of superconductivity, magnetism, and metal-insulator transitions are a few examples in the family of strongly correlated electron systems. SOC increases with Z ($\lambda \propto Z^4$) and its interplay with U opens a new world of exotic ground states in $4d/5d$ TMOs. For example, the schematic phase diagram in the U (represented by U/t) and SOC (represented by λ/t) space is shown in Fig. [2.6]. Here, t and λ are the hopping and SOC constant [32]. Clearly, one can explore the different regions of the phase diagram depending on the relative strength and competition between U and SOC.

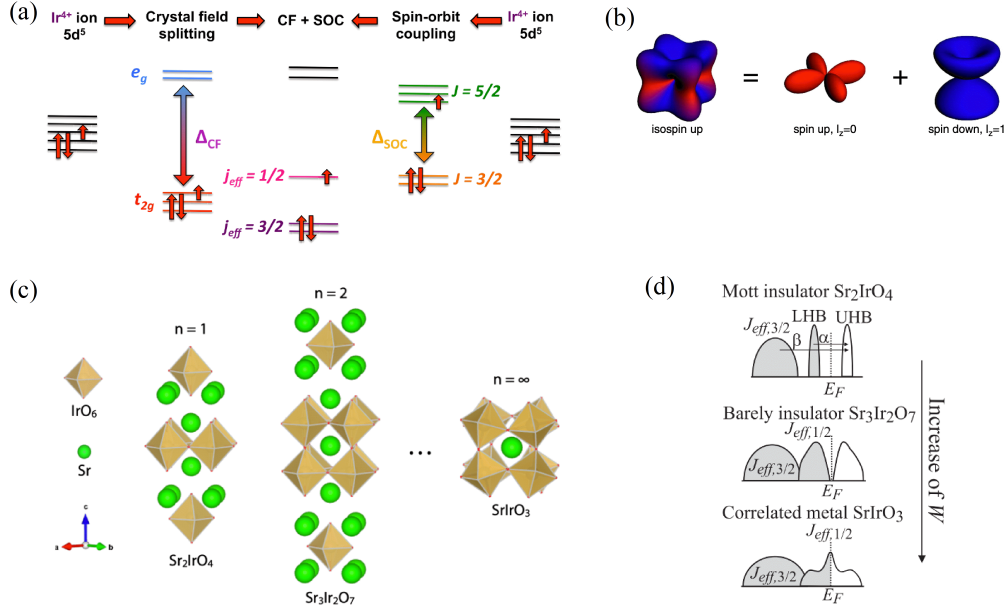


Figure 2.7: (a) The electronic ground state of Ir^{4+} ($5d^5$): Crystal field and SOC result in novel $J_{\text{eff}} = 1/2$ pseudospin state, (b) The electronic density profile of pseudospin-up state, (c) The crystal structure of Ruddlesden Popper series of 5d Iridates: $\text{Sr}_{2n+1}\text{Ir}_n\text{O}_{3n+1}$, $n = 1, 2$ and ∞ , (d) Increase of Ir-O-Ir hybridization, *i.e.*, electronic bandwidth as a function of increasing dimensionality (*i.e.* n) [69–72].

Ruddlesden-Popper series ($\text{A}_{n+1}\text{B}_n\text{O}_{3n+1}$)

Compared to 3d-TMOs, where orbital moment and SOC are quenched by non-spherical crystal field, a strong SOC is expected in 5d-TMOs. In the last decade, much attention has been focused on the Ruddlesden Popper (RP) series of 5d Iridates: $\text{Sr}_{n+1}\text{Ir}_n\text{O}_{3n+1}$, characterized by the pseudo-spin $J_{\text{eff}} = 1/2$ band. In an octahedral environment, the crystal field splits the fivefold degenerate $5d^5$ (Ir^{4+}) orbitals into t_{2g} and e_g levels. The threefold degenerate t_{2g} levels are described by angular momentum $l_z = 0, \pm 1$. The spin-orbit interaction, which can not be ignored here, again splits the t_{2g} manifold into the spin-orbital mixed $J_{\text{eff}} = 3/2$ and $1/2$ pseudospin states, see Fig. [2.7a]. Thus, the ground state Ir^{4+} is described by the $J_{\text{eff}} = 1/2$ pseudospin state. In Fig. [2.7b], the density profile of the iso(pseudo)-spin up state is shown which is the superposition of spin up density ($l_z = 0$) and spin down ($l_z = 1$) [70]. The crystal structure consists of n - SrIrO_3 perovskite layers intercalated between SrO layers, see Fig. [2.7c]. For $n = 1$, Sr_2IrO_4 shows a canted in-plane antiferromagnet structure with a Mott like insulating ground state [2.7d]. Even a moderate U splits the $J_{\text{eff}} = 1/2$ bands into upper and lower Hubbard bands (UHB and LHB) resulting in an insulating state. Very similar to Sr_2IrO_4 , $\text{Sr}_3\text{Ir}_2\text{O}_7$ ($n = 2$) also shows an antiferromagnetic insulating state,

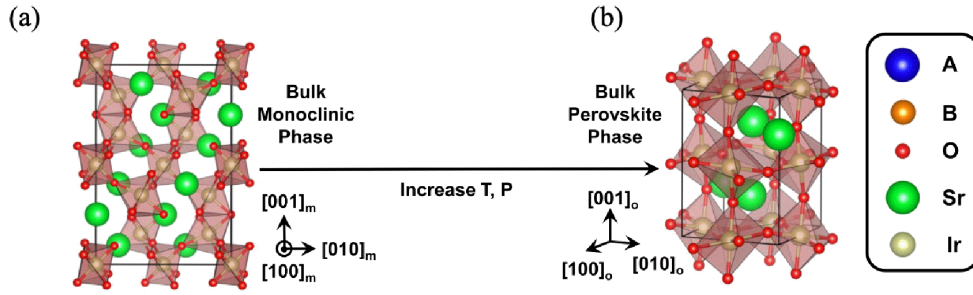


Figure 2.8: (a) The monoclinic SrIrO_3 (space group: $C2/c$), energetically favorable at room temperature and ambient pressure, transforms to (b) orthorhombic (space group: $Pbnm$) structure at high pressure and temperatures ($\geq 1000^\circ\text{C}$ and 40 kbar). The ions are shown with different colors [78].

however, the moments are collinearly aligned along the c -axis. For $n = \infty$, in SrIrO_3 , the bandwidth (W) increases ($W \gg U$) and hence a correlated semi-metallic and paramagnetic ground state evolves. Clearly, a bandwidth controlled metal-insulator and magnetic transition can be observed in RP- $\text{Sr}_{n+1}\text{Ir}_n\text{O}_{3n+1}$. This is also highlighted in the phase diagram, Fig. [2.6]. Therefore, SrIrO_3 is at the verge of a metal-insulator and magnetic transition, where the competition between different energy interactions can modify the ground state [73]. External perturbations, *e.g.*, strain, pressure, dimensionality confinement and proximity effects have shown great promise in realization of new ground states in SrIrO_3 or SrIrO_3 based interfaces or superlattices [74–76].

2.2.1 SrIrO_3 ($n = \infty$): crystal structure

Room temperature and atmospheric pressure synthesis of SrIrO_3 results into the formation of energetically favoured monoclinic structure (space group $C2/c$) [77]. The refined lattice parameters were extracted from the powder diffraction and are: $a = 5.604 \text{ \AA}$, $b = 9.618 \text{ \AA}$, $c = 14.17 \text{ \AA}$ and $\beta = 93.26^\circ$. The structure can be viewed as the distorted hexagonal BaTiO_3 (6H) structure [77]. At high temperature and pressure ($\geq 1000^\circ\text{C}$ and 40 kbar), the structure transforms to the orthorhombic structure ($a_o = 5.60 \text{ \AA}$, $b_o = 5.58 \text{ \AA}$, $c_o = 7.89 \text{ \AA}$, space group $Pbnm$) accompanied by a reduction of 3 % in volume. This corresponds to a pseudo-cubic unit cell with lattice constant of $a_{pc} \approx 3.96 \text{ \AA}$ ($a_{pc} = (a_o/\sqrt{2} + b_o/\sqrt{2} + c_o/2)/3$) [77, 78].

Despite the need of extreme conditions, there are few successful reports on the growth of single- and poly-crystalline orthorhombic SrIrO_3 crystals [77, 79–83]. A metastable phase can be stabilized by quenching the SrIrO_3 from high temperature and high pressure to ambi-

ent conditions [79, 80]. Synchrotron and neutron X-ray diffraction studies were performed to refine the crystal structure. From the refined atomic positions, two independent tilts of the IrO_6 octahedra were found: $\sim 11.5^\circ$ out of phase and $\sim 8.7^\circ$ in-phase along (110) and (001) axis, respectively at 300 K [80] which corresponds to the tilt pattern of ($a^-a^-c^+$) in Glazer notation [48, 49].

Even though it is possible, the metastable growth starting from the high-pressure phase poses technical challenges and makes it impractical for the study and application. This problem can be solved by thin film engineering. The substrate-induced in-plane epitaxial strain (ϵ_{xx}) can be used as a “effective pressure” to stabilize the perovskite SrIrO_3 phase at ambient conditions [84–90]. Moreover, it also offers great promise to integrate SrIrO_3 into HSs and SLs. The pseudocubic lattice constant $a_{pc} \approx 3.96 \text{ \AA}$, makes it compatible with large number of commercially available perovskite substrates and allows to grow with wide range of strain states. To accommodate the substrate induced strain; a distortion, tilt and/or rotation of the IrO_6 octahedra is expected, depending on the degree and sign of strain (compressive, $\epsilon_{xx} < 0$ or tensile, $\epsilon_{xx} > 0$) which can significantly modify the crystal structure. In perovskite oxides, electronic and magnetic properties are closely linked to structural properties and thus a significant change in the physical properties are expected as function of substrate strain [76, 87, 90].

The growth conditions and substrate choice can have strong influence on the film structure and so on physical properties. One needs to carefully optimize the growth parameters, see Chapter 3. The high volatility of IrO_3 does not allow to grow the films at very high temperatures. A high temperature growth ($> 700^\circ \text{C}$) can cause Ir deficiency favoring the insulating Sr_2IrO_4 phase instead of SrIrO_3 [71]. To protect the surface of ultrathin films, a thin insulating SrTiO_3 capping layer is usually recommended, which may avoid possible degradation. With increasing film thickness, rapid structure relaxation of the films is expected, which again limits the thickness (t) up to which high quality single crystalline films can be prepared. On lattice matched substrates, $t \sim 40\text{-}50 \text{ nm}$ can be achieved. Beside the impact of substrate strain, which will be discussed later in detail, the symmetry of substrate also plays very crucial role. Growth of SrIrO_3 on orthorhombic substrates (*e.g.* DyScO_3 , GdScO_3) generally results in the untwinned growth with c -axis of film in the film plane and parallel to that of the substrate. In contrast, a highly twinned growth was observed on cubic substrates (*e.g.* SrTiO_3 , $(\text{La}_{0.18}\text{Sr}_{0.82})(\text{Al}_{0.59}\text{Ta}_{0.41})\text{O}_3$) [90]. However, the twinned growth can be strongly suppressed using SrTiO_3 substrates with high miscut angle [91].

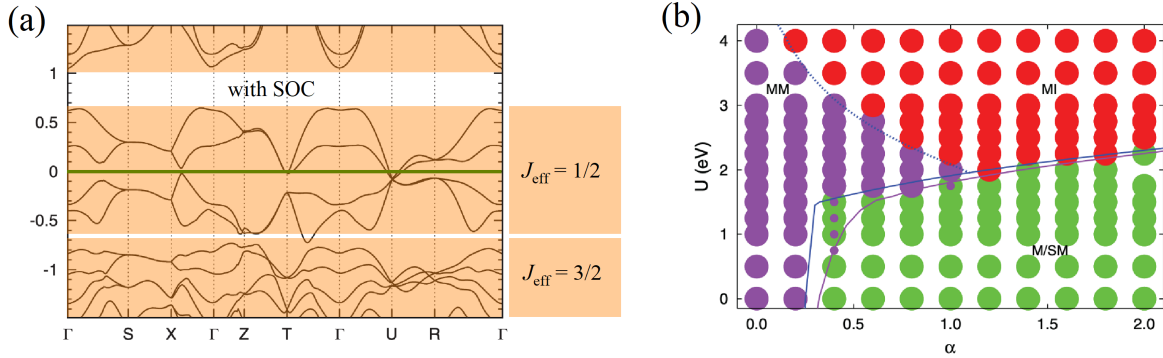


Figure 2.9: Electronic band structure of SIO: (a) DFT calculated band structure of bulk SIO ($Pbnm$) for $U = 2$ eV, $\alpha = 2$. The Fermi level and $J_{\text{eff}} = 1/2$, $3/2$ bands are shown, (b) the U -SOC phase diagram of SIO [73, 92]. Three different phases (MM = magnetic metal, M/SM = non-magnetic metal or semimetal, MI = magnetic insulator) are shown.

2.2.2 SrIrO_3 : electronic and magnetic properties

As mentioned briefly in last section, epitaxial films may have slightly (or largely) different structure compared to bulk perovskite SrIrO_3 which can strongly influence the electronic and magnetic ground state alike.

In Fig. [2.9], we show the electronic band structure of SrIrO_3 . The band structure was calculated for bulk SrIrO_3 using density functional theory incorporating Hubbard interaction (U) and SOC (represented by α , a unitless prefactor of the SOC term in Hamiltonian). A range of U and α were chosen carefully to observe the impact on electronic structure [92]. In Fig. [2.9b], the band structure is shown for $U = 2$ eV and $\alpha = 2$. The band structure near the Fermi level is made of $J_{\text{eff}} = 1/2$ band. Most importantly, a Dirac-like linear node point is found along the U -point, consistent with the semimetallic nature of SrIrO_3 . A qualitatively similar band structure and line node near the U -point was also observed in the band structure calculated by the tight-binding model which shows the robustness of the feature [92]. The interplay of U and α strongly modifies the band structure and thus the ground state of SrIrO_3 [73]. In Fig. [2.9b], the phase diagram as a function of U and α is shown. Clearly, one can observe a phase transition from nonmagnetic semimetal to magnetic metal or magnetic insulator depending on the competition between U and α . In a recent band structure calculation, even a richer phase diagram has been reported [93]. Experimentally, the electronic band structure of SrIrO_3 was measured using angle resolved photoemission spectroscopy on metastable SrIrO_3 films on LSAT (001) substrate. A semimetallic ground state with heavy

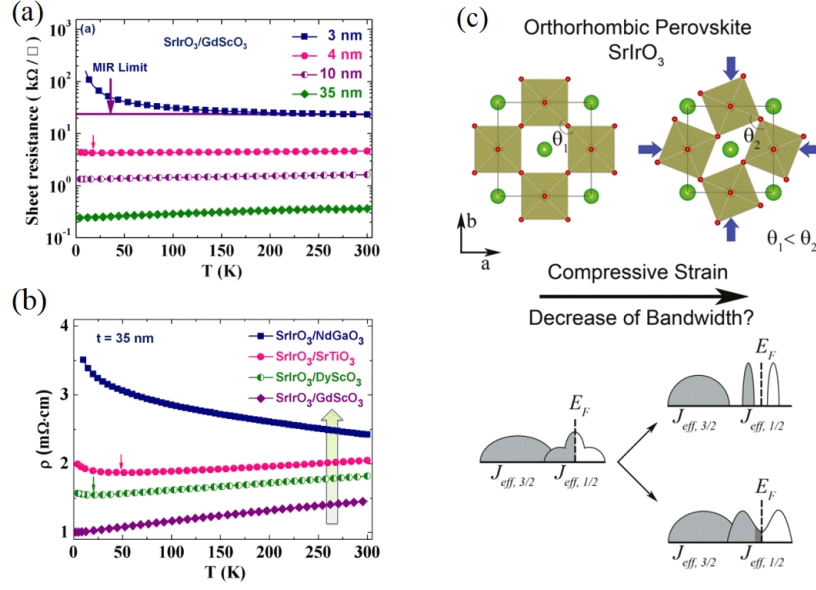


Figure 2.10: Electronic transport in SIO films: Resistivity vs temperature of SIO films as a function of (a) thickness and (b) substrate strain. MIT is observed for thin and compressively strained SIO films, (c) The compressive strain induced octahedral rotation and its consequence on the electronic structure of SIO. Figures are taken from [75, 85].

hole-like dispersion and light (nearly linear) electron-like bands were observed at the Fermi level [94]. The semi-metallic charge dynamics with different mobilities for electron and hole carriers in SIO films were further evidenced by the magnetotransport and Raman experiments [95, 96].

Owing to the presence of Dirac nodal line, SrIrO₃ is theoretically predicted as a toy model for the realization of topological phases [92]. Depending on the specific broken symmetry, SrIrO₃ can be grouped into various topological phases, *e.g.*, Dirac semimetal or topological insulator [97].

Electronic transport in bulk SrIrO₃ single crystals show metallic behavior down to 2 K. At high temperatures, the resistivity varies linearly with temperature, however at low temperatures, it follows a T^2 -dependence, characteristic of a Fermi liquid metal system [80]. In some samples, a resistive upturn at low temperature (≤ 30 K) originating from impurities were also discussed [79]. Magnetoresistance (MR) of bulk single crystals were found to follow a B^2 -magnetic field (B) dependence. In stark contrast, polycrystalline samples showed a very large linear MR $\sim 100\%$ at low temperatures [81]. A magnetic field-induced topological evolution of Dirac nodes was discussed as the origin of such large, unusual linear MR in polycrystalline SrIrO₃.

Resistivity behavior of thick (≥ 40 nm) SrIrO₃ films were found to be similar to that of

bulk. A metallic behaviour at higher temperatures accompanied with a resistivity upturn at low temperatures are commonly observed in SrIrO₃ films on different substrate. However, the upturn temperature is found to be inconsistent with strong dependence on the growth process and choice of substrate material.

Reducing the film thickness of SrIrO₃ to $t \leq 4$ monolayer (ML) can strongly influence the transport properties as well. Reducing film thickness usually results in an increased disorder, electronic correlation and structural distortion which significantly contribute to enhanced resistivity and insulating behavior. A disorder driven localization was reported as the origin of MIT as a function of thickness, see Fig. [2.10a], [75]. Similarly, a MIT and weak antilocalization to localization transition was observed in SrIrO₃ films below 4 ML thickness [98]. A simultaneous MIT and magnetic transition was observed in SrIrO₃ films below ≤ 3 ML, where suppression of octahedral rotation was found to open a charge gap at the Fermi level.

Beside dimensional confinement, MIT as a function of strain has also been reported in several studies [75, 85]. In Fig. [2.10b], the resistivity behavior of 35 nm film on different substrates is shown [75]. Compressive strain is found to support insulating transport in comparison to tensile strain, where metallic transport of SrIrO₃ was obtained. In SIO films, Ir-O-Ir bond angles are highly susceptible to lattice strain rather than the Ir-O bond length due to rigid IrO₆ octahedra [85]. An in-plane compressive strain results in a decreased Ir-O-Ir bond angle, see Fig. [2.10b], which consequently reduces the hopping between Ir *5d*-orbitals and hence the electronic bandwidth. Bandwidth reduction can put the system from a metallic to an insulating state either by the localization of states or even by opening a gap near the Fermi level [85]. An anisotropic electronic transport was also evident in untwinned SrIrO₃ films with lower resistivity along the *c*-axis direction [90, 91].

2.3 SrIrO₃ thin film heterostructures and superlattices

Since physical properties are closely related to the structure, the ground state of SrIrO₃, particularly of strained thin films, is shown to be highly tunable, for example, as a function of film thickness and substrate material. In this section, a survey on SrIrO₃-based HSs and SLs, comprising other *3d/4d* TMOs is given. The interfacial coupling between two dissimilar oxides can lead to the observation of new ground states that can be very different from either of the constituent layers.

The very first attempt to combine *3d-5d* TMO SLs was realized by Matsuno *et al.* [99],

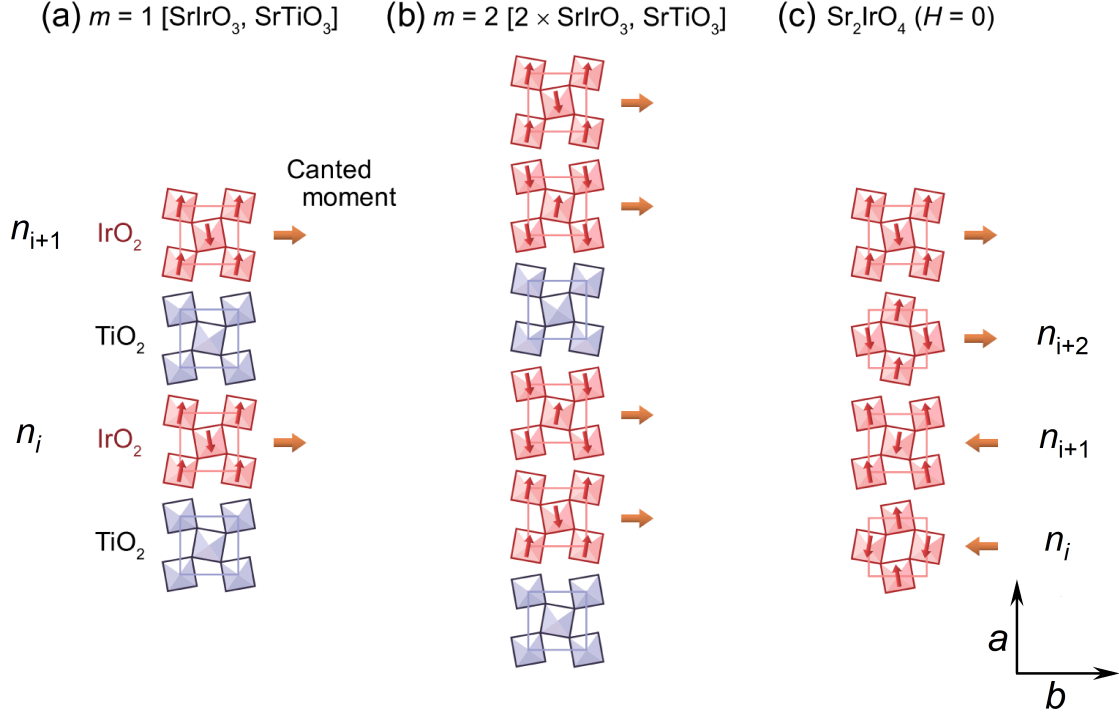


Figure 2.11: Magnetic ground state evolution in [(SrIrO₃)_m, (SrTiO₃)] superlattices: proposed magnetic structure for $m = 1$ (a), 2 (b) in comparison to Sr₂IrO₄ (c). The figure is adapted from Ref. [99].

where non-magnetic and insulating SrTiO₃ were combined with SrIrO₃ to study the effect of dimensional confinement and its interplay with SOC and U. Artificial [(SrIrO₃)_m, (SrTiO₃)] SLs with $m = 1, 2, 3, 4$ and ∞ , the number of unit cells, were grown with varying SIO stacking layers, *i.e.*, m . The SLs undergo simultaneous semimetal to insulator and ferromagnetic transition for $m \leq 3$. The concurrent transition suggests the strong coupling of charge gap and magnetic ordering in the SLs. The magnetic ground state can be expected to be very similar to that of Sr₂IrO₄. The different IrO₂ planes show weak effective in-plane magnetic moments resulting from the canting of the $J_{\text{eff}} = 1/2$ pseudo-spins. In Fig. [2.11], the proposed magnetic structure is shown. In contrast to the antiferromagnetic coupling of effective in-plane moments along c -axis in Sr₂IrO₄, the ferromagnetic ground state observed in [(SrIrO₃)_m, (SrTiO₃)] for $m = 1, 2$ can be explained by considering the ferromagnetic alignment of the effective in-plane moments of different IrO₂ planes along c -axis, see Fig. [2.11a,b].

For $m = 1$, an effective moment $m_{\text{eff}} \approx 0.02 \mu_{\text{B}}/\text{Ir}$ was reported which is about (1/4)th of the moments in Sr₂IrO₄ [100, 101]. As the net moment values strongly depend on the canting angle of the $J_{\text{eff}} = 1/2$ moments, a smaller rotation (8° instead of 11-12° in Sr₂IrO₄) of the

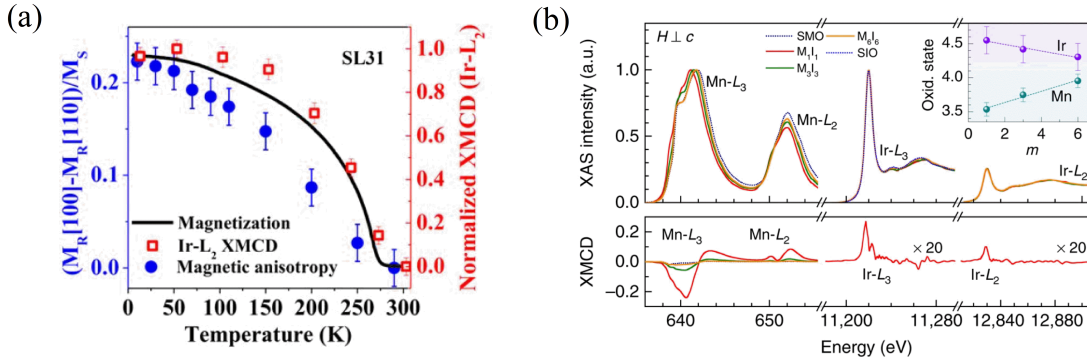


Figure 2.12: Magnetism evolution in SrIrO₃: (a) the magnetic anisotropy, Ir edge XMCD and magnetization measured with SQUID as a function of temperature for [(SrIrO₃)₁/(La_{2/3}Sr_{1/3}MnO₃)₃] SLs [34], (b) XAS and XMCD measured at Mn and Ir edge on a series of [(SrMnO₃)_m/(SrRuO₃)_n] SLs. The inset in (b) shows the relative interfacial charge transfer [35].

IrO₆ was argued to be the reason for smaller moments observed in [(SrIrO₃)_m/(SrTiO₃)₃].

In another pioneer work, Di Yi *et al.* prepared [(SrIrO₃)_m/(La_{2/3}Sr_{1/3}MnO₃)₃] SLs (labeled as $I_m M_3$, with $m = 1-10$, the number of SrIrO₃ unit cell) and studied the magnetic and transport properties [34]. A change of in-plane magnetic anisotropy in the $I_m M_3$ superlattices was observed as a function of SIO film thickness m . By controlling m , it is possible to tune the overall anisotropy energy systematically. Moreover, the change of magnetic anisotropy was also accompanied by the evolution of ferromagnetism in the SrIrO₃ see Fig. [2.12a]. The onset temperature ($T_c \approx 270$ K) and coercive field of ferromagnetism in SIO closely follow the ones in La_{2/3}Sr_{1/3}MnO₃, suggesting a strong correlation between the two. X-ray magnetic circular dichroism (XMCD) demonstrated anti-parallel alignment of Mn and Ir net moments with magnetic moment $m_l = 0.036 \mu_B/\text{Ir}$ and $m_{s,eff} = 0.002 \mu_B/\text{Ir}$. The large m_l/m_s ratio signifies the role of strong spin-orbit coupling in SrIrO₃. Note that the X-ray absorption spectroscopy did not report interfacial charge transfer in this system.

A large intrinsic anomalous Hall effect and proximity induced magnetism was also reported in SrIrO₃/La_{0.7}Sr_{0.3}MnO₃ HSs [102]. However, the metallic La_{0.7}Sr_{0.3}MnO₃ layer makes the characterization of the anomalous Hall or related topological transport phenomena in SIO complicated.

Another seminal work on manganite-iridate interfaces reported by J. Nichols *et al.* [35], investigated the magnetism and transport in the [(SrMnO₃)_m/(SrIrO₃)_n] $\times Z$ SLs, where m , n and Z are the numbers of SrMnO₃ and SrIrO₃ unit cells and the repetition, respectively. They combined the antiferromagnetic insulator SrMnO₃ with SrIrO₃. A strong interfacial

electron transfer from SrIrO₃ to SrMnO₃ for $m = n \leq 3$, reaching up to 0.5 electron/uc for $m = n = 1$ was determined from XAS experiments, Fig. [2.12b]. XMCD showed a clear magnetic response at Mn and Ir edges which becomes maximum for $m = n = 1$, see Fig. [2.12b]. In contrast to the negative XMCD at Mn L_3 edge, the XMCD at Ir L_3 is positive, which indicates anti-parallel alignment of the Mn and Ir net moments. Such anti-parallel alignment of the Mn and Ir moments was also observed for other manganite-iridate interfaces [34]. A sum rule analysis on Mn and Ir XMCD resulted in total moments of $m_{\text{Mn}} = 2.1 \mu_{\text{B}}/\text{Mn}$ ($m_l = 0.3 \mu_{\text{B}}/\text{Mn}$, $m_s = 0.9 \mu_{\text{B}}/\text{Mn}$) and $m_{\text{Ir}} = -0.08 \mu_{\text{B}}/\text{Ir}$ ($m_l = 0.057 \mu_{\text{B}}/\text{Ir}$, $m_s = 0.013 \mu_{\text{B}}/\text{Ir}$).

The induced ferromagnetism can greatly influence the transport below the transition temperature which is reflected, *e.g.*, in the magnetotransport. A negative hysteretic magnetoresistance (MR) is observed for $m = n \leq 4$ superlattices for $T \leq 75$ K. Concurrently, a hysteretic anomalous Hall resistance (AHR) has also been observed. It is important to mention here that the transport for superlattices $m = n \leq 2$ is dominated by the onset of conductivity in the SrMnO₃ layer.

Skoropata *et al.* [103] replaced the SrMnO₃ with LaMnO₃ and studied the interfacial properties of $[(\text{LaMnO}_3)_n/(\text{SrIrO}_3)_n] \times Z$ SLs. In contrast to an antiferromagnetic insulator ground state of bulk LaMnO₃, thin films show a ferromagnetic insulating state. In addition to the anomalous Hall, a topological Hall effect has been also discussed. However, as both SrIrO₃ and LaMnO₃ are conducting in the superlattices, the observation of topological like-Hall effect can be explained also by the superposition of two anomalous hall resistivity with opposite polarity. Note that an anomalous Hall effect has already been observed in single-layer (doped) LaMnO₃ thin films [63, 64].

Instead of 3d-TMO, there are also efforts to combine the 4d-TMO with SrIrO₃ to study the interfacial properties in 4d/5d HSs and SLs. Mainly, SrRuO₃, a ferromagnetic metal, was extensively used to realize such interfaces. In $[(\text{SrIrO}_3)_2, (\text{SrRuO}_3)_m]$ bilayers, with m being the number of SrRuO₃ unit cells, an AHE was observed for different m (4-7) [33]. A sign change of the AHE as a function of temperature was also reported, consistent with the earlier reports on SrRuO₃ [105]. In addition to an AHE, an additional hump-like feature (for $m = 4-6$) ascribed to topological Hall effect (THE) was observed over a range of temperatures and magnetic fields, see Fig. [2.13]. The large Dzyaloshinskii-Moriya interaction (DMI), resulting from the strong spin-orbit coupling in SrIrO₃ and inversion symmetry breaking at the SrRuO₃/SrIrO₃ interface, was discussed as the origin of the THE in the bilayers. The results advocate for the realization of Néel-type magnetic skyrmions at the SrRuO₃/SrIrO₃

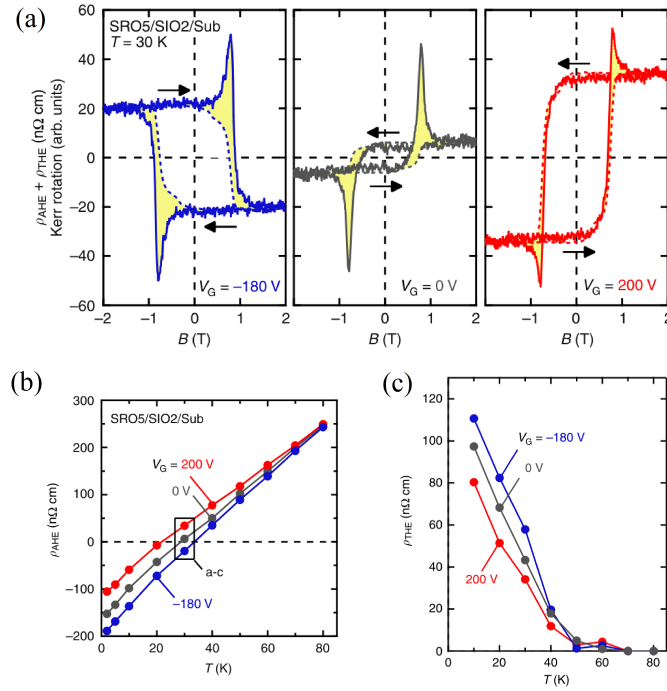


Figure 2.13: Electric field control of AHE and THE in SIO/SRO bilayers: (a) AHE+THE at 30 K as a function of gate voltage, (b) AHE and, (c) THE as a function of temperature at different gate voltages. The figure is adapted from [104].

interfaces.

Later, the same group also studied the electric field control of AHE and THE at the $\text{SrRuO}_3/\text{SrIrO}_3$ interfaces [104]. The AHE and THE both show strong gate voltage dependence and their temperature evolution as a function of gate voltage are shown in Fig. [2.13]. A change of spin-orbit coupling in SrIrO_3 with applied electric field was argued as the possible reason [104].

There are some further studies on $[(\text{SrIrO}_3)_n, (\text{SrRuO}_3)_m]$ HSs and SLs, where hump-like additional features were observed in total Hall that were ascribed to the THE resulting from the deviation of electrons in the transverse direction while crossing the magnetic skyrmions in real space. Some studies combined transport experiments with imaging methods like magnetic force microscopy (MFM) [106]. MFM images demonstrated the presence of magnetic features in these systems. However, the existence of skyrmions is still under debate [107]. A large discrepancy was found between the skyrmion number density obtained from the transport and MFM experiments.

Recently, similar AHE and hump-like additional features were observed in single-layer SrRuO_3 thin films. This strongly questions the origin of hump-like features at $\text{SrRuO}_3/\text{SrIrO}_3$

interfaces and strongly suggests the superposition of two AHEs with opposite polarity as the main reason for the observation of hump-like features [108, 109]. The magnetic properties of ultrathin SrRuO₃ films are strongly thickness dependent, with even a slight variation in thickness leading to magnetic inhomogeneity in the sample [110]. These inhomogeneous magnetic regions can result in AHE with opposite polarities (positive and negative), leading to the observation of hump-like features superimposed on the AHE in the Hall resistivity. The above hypothesis of “two-channel AHE” with opposite polarity in SrRuO₃ is reasonable as SrRuO₃ shows a sign change of the AHE as a function of temperature [105] and one can expect two AHEs with opposite polarities over a range of temperatures originating from different magnetic regions.

Thus, one should be very careful in choosing the magnetic layer with SrIrO₃. Ideally, a strong ferromagnetic insulator would be a good starting choice. Commonly used LaMnO₃ is an antiferromagnetic insulator in bulk. In contrast, strained LaMnO₃ thin films develop a ferromagnetic insulating ground state. However, as manganite physics is symmetric with respect to the electron-hole doping, hole or electron doping results in a metallic ground state in LaMnO₃ [63, 64, 111, 112]. Also, SrRuO₃ remains metallic down to 2-3 ML and contribute to the total conductivity of the HSs and SLs.

In this thesis work, we concentrate on the interfacial properties of SrIrO₃/LaCoO₃ interfaces by integrating them in HSs and SLs. Lightly doped LaCoO₃ remains insulating and allows electronic transport within the SIO layer only. At the end, we will provide a more general and comprehensive study on the *3d-5d* TMO based interfaces SrIrO₃/LaXO₃ (X = Mn, Fe, Co and Ni) and will discuss the interfacial electronic and magnetic exchange at such interfaces.

CHAPTER 3

Sample Preparation and Experimental Methods

An experiment is a question which science poses to Nature and a measurement is the recording of Nature's answer.

Max Planck

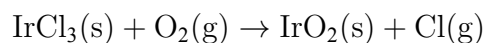
This chapter discusses the main experimental tools used throughout this thesis work. The first part reports on the sample growth and device preparation. In the second part, a brief introduction to the various experimental methods used to characterize the structural and physical properties of the samples is given.

3.1 Sample preparation

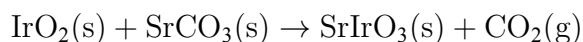
3.1.1 Target preparation using solid state synthesis

The first step towards the growth of a thin film consists of the preparation of the target material. In the course of this thesis work, home built targets were used for laser ablation. In the following, the details on the preparation of the SIO targets are provided. For this purpose, a solid-state synthesis methods were employed.

In a first step, IrCl_3 powder was annealed twice in flowing O_2 environment at $600\text{ }^\circ\text{C}$ for 15 hours. The heating and cooling rate was kept at $250\text{ }^\circ\text{C}/\text{hour}$. This results in the formation of homogeneous IrO_2 powder. In Fig. [3.1a], powder XRD of converted IrO_2 using a Mo K_α source is shown which confirms single phase IrO_2 with minor presence of pure Ir metal. The chemical reaction is given by-



Next, IrO_2 and SrCO_3 powders, taken in equal molar weight were mixed and ground together to form a homogeneous mixture. This mixture was calcined at $700\text{ }^\circ\text{C}$ for 10 hours which results in the formation of the SrIrO_3 monoclinic phase.



After the calcination, the powder was sintered at $1050\text{ }^\circ\text{C}$ for 40 hours. The sintered powder was then pressed into the pellets (diameter $\sim 15.2\text{ mm}$ and thickness $\sim 3\text{ mm}$) applying hydrostatic pressure of $\approx 0.27\text{ GPa}$. In a second sintering, pellets were sintered at $1150\text{ }^\circ\text{C}$ for 20 hours. In Fig. [3.1b], we show the XRD of the sintered powder and the pellet with black and blue lines, respectively. No changes were observed. Comparing the XRD of target with the reference data confirms the single phase monoclinic strontium iridate (space group: $C12/c1$ (15)) targets. The target density was estimated to 5.048 g/cm^3 which is about 59 % of the bulk density.

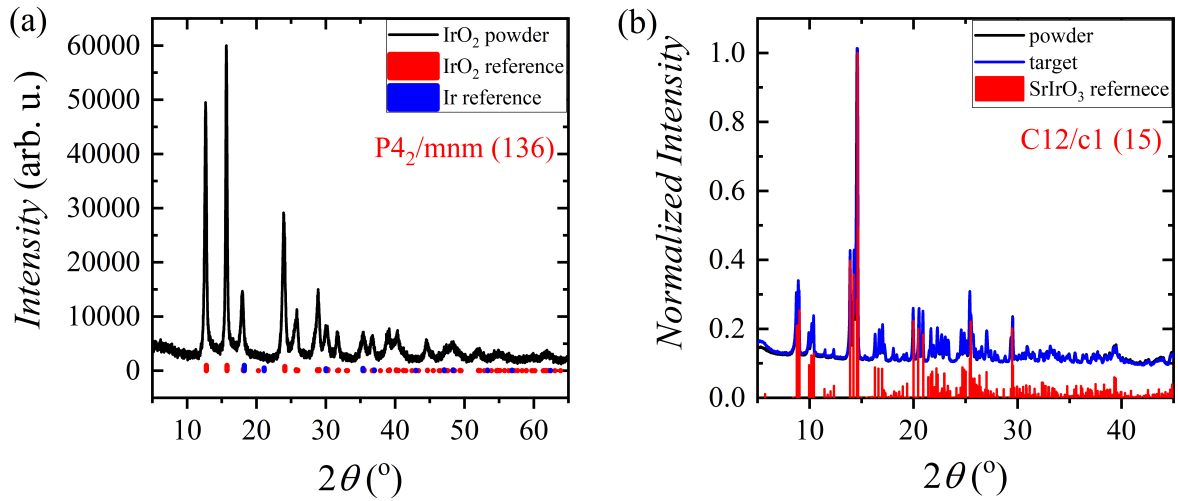


Figure 3.1: Structural characterization of SrIrO₃ target: (a) XRD of IrO₂ powder and (b) solid SrIrO₃ target. For the comparison reference data are provided.

3.1.2 Substrate pre-treatment

In order to grow high-quality epitaxial thin films, HSs and SLs with atomically sharp interfaces, the prerequisite step is to start with an atomically flat, well-defined surface terminated substrate. Prior to the film depositions, all the substrates used in this thesis were pre-treated to ensure well-defined atomic termination. This was done by combining chemical wet etching followed by annealing in a flowing oxygen environment.

(a) Surface termination:

For the termination of SrTiO₃ (STO) (001), substrates from CrysTec GmbH ($5 \times 5 \times 1 \text{ mm}^3$) were chemically etched and annealed to provide atomically flat, smooth surfaces [113–115]. The STO crystal structure can be visualized as a layered structure along the (001) crystallographic direction where the alternating SrO and TiO₂ planes (blue and orange blocks in Fig. [3.2a], respectively) are aligned parallel to each other. Freshly received STO substrates usually show a mixed terminated surface.

In a first step, STO substrates were kept in bi-distilled water for about 10 minutes. This leads to the formation of strontium hydroxide (Sr(OH)₂) on the surface. Strontium oxide reacts strongly to the water compared to the titanium oxide and this forbids the formation of titanium hydroxide (Ti(OH)₄) to a large extent. The (Sr(OH)₂) rich surface was then selectively etched by a buffered hydrogen fluoride solution for 30 seconds [116]. After the etching, a stopping bath in bi-distilled water for 10 seconds was carried out. In the last

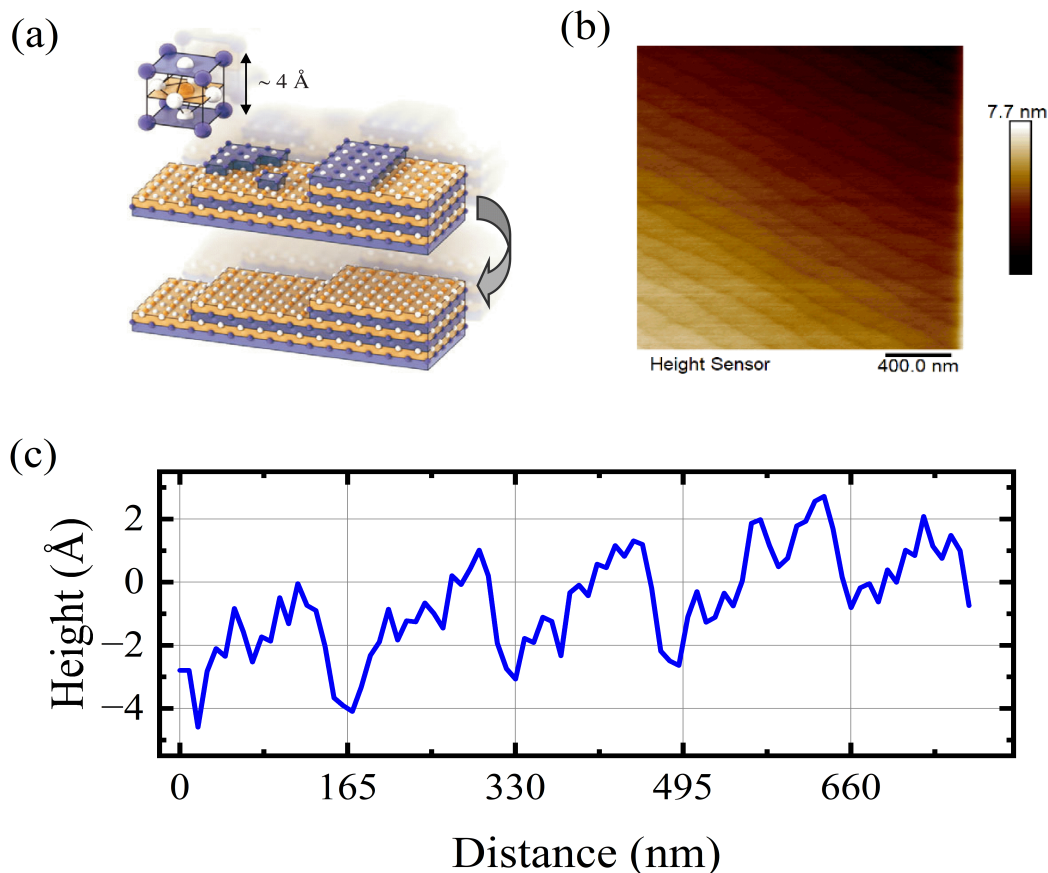


Figure 3.2: Substrate pre-treatment: (a) Surface termination of STO (001): freshly received surfaces are mixed terminated, which after the selective etching and annealing in O₂ transform to single termination [116], (b) Surface morphology of a TiO₂ terminated STO (001) substrate, (c) Height profile of the TiO₂- terminated STO (001) along the direction perpendicular to the terraces.

step, substrates were dried by the nitrogen blow. These chemically etched substrates were annealed at 950 °C for 5 hours in flowing oxygen environment. The whole process results in atomically sharp surfaces with step-terrace like surface structure where terrace height amounts to one perovskite unit cell (3.9-4.0 Å), see Fig. [3.2c].

(b) Atomic force microscopy:

The surface morphology of the single terminated STO (001) (and others also) substrates were characterized by atomic force microscopy (AFM). AFM is a powerful technique to image the surface topography with 3-dimensional precision. The main principle is to ‘feel’ or ‘touch’ the individual atoms of the surface utilizing an atomically sharp tip, attached to a flexible cantilever. The interaction between the tip and the surface atoms is used to create the 3-dimensional image of the surface down to the atomic scale. For our experiments, we used

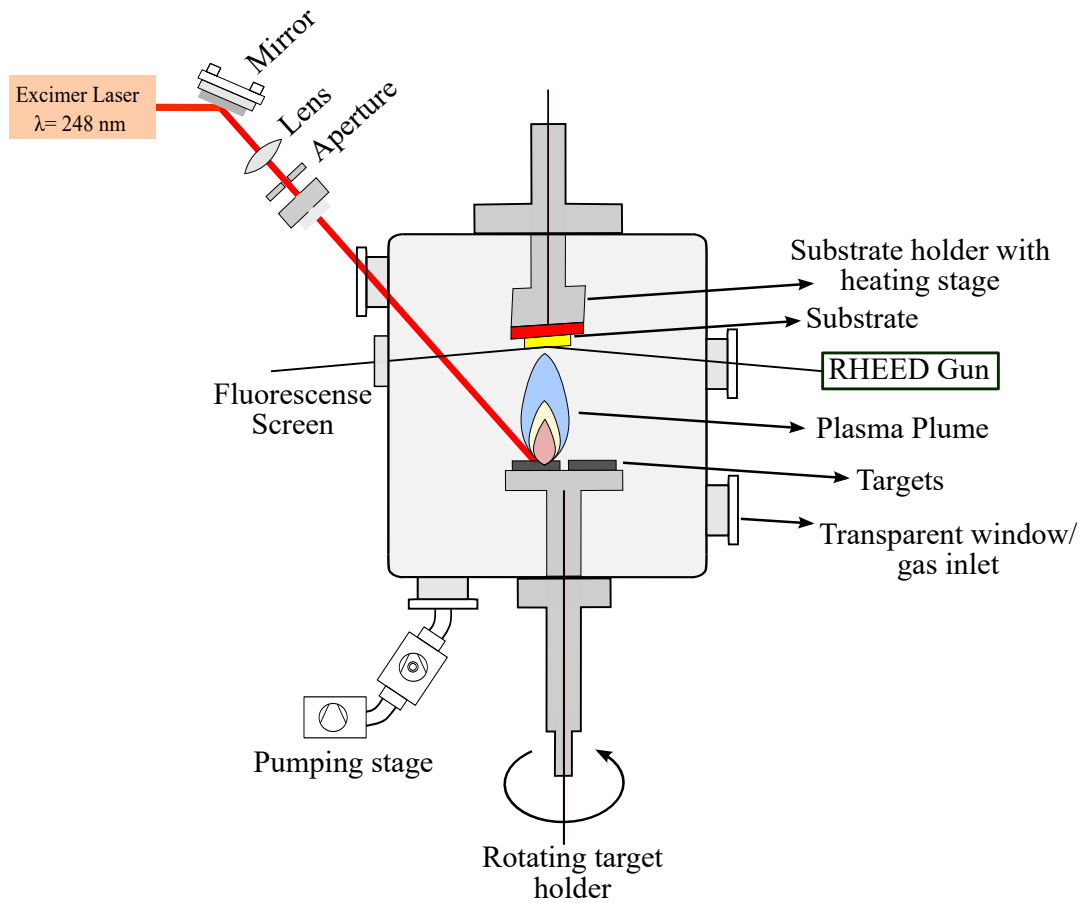


Figure 3.3: Cross-sectional view of the PLD system equipped with the RHEED for in-situ growth monitoring. A focused UV laser ablates the target material which later re-condensates on the heated substrate.

the contact mode where the tip directly touches the surface atoms. In Fig. [3.2b], we show the AFM surface topography of a TiO_2 -terminated STO (001) substrate showing step-terrace like surface structure. The height profile perpendicular to the terraces direction is also shown in Fig. [3.2c]. The terrace height amounts to one perovskite unit cell (3.9-4.0 Å).

The AFM experiments were performed at the Karlsruhe Nano Micro Facility at the Institute of Microstructure Technology (IMT), KIT, Germany.

3.1.3 Pulsed laser deposition

(a) Laser ablation:

During the course of this thesis, Pulsed Laser Deposition (PLD) was used for the growth of thin films, HSs and SLs unless stated otherwise. PLD is one of the most widely used deposition techniques for the growth of oxides. It allows the deposition in a wide range of

pressures- in ultrahigh vacuum or reactive gas environments such as oxygen, nitrogen, argon up to ambient conditions or even above [12, 13].

The basic principle of PLD lies in the ablation of a target material by a pulsed laser and its subsequent deposition on the substrate. An ultraviolet (UV) pulsed laser (KrF excimer laser, $\lambda = 248$ nm) is focused on the target surface and ablates the target material. The rather complex light-matter interaction, which involves the following sequential processes: UV light absorption, electron-phonon interaction, plasma (ions) formation and particle collision (*i.e.* thermalisation of high energetic particles), results in the formation of plasma plume directed perpendicular to the target surface. In the last step, deposition of the film takes place on the substrate surface, which strongly depends on the sticking coefficient, surface mobility of ad-atoms, and competition among different surface energies (*i.e.* surface wetting). The schematic of the PLD equipped with in-situ RHEED is shown in Fig. [3.3]. The target carousel can hold ten targets at a time, making it very suitable for the growth of superlattices comprising two or more individual layers. Note that the deposition of perfect stoichiometric films using PLD is challenging and often results in a slightly off-stoichiometric ratio.

(b) Growth modes:

The nucleation and subsequent film growth on the substrate surface is a very complex process and generally governs the structural and chemical properties of both substrate and film material. It depends on the sticking coefficient and surface mobility. The substrate temperature (T_S) and deposition rate (R) strongly influence the growth kinetics and nucleation process. Generally, higher T_S , *i.e.*, ad-atom surface mobility and lower R favor the fewer and larger nuclei, which is important for the smooth layered growth. In contrast, low surface mobility (*i.e.* T_S) and high supersaturation (*i.e.* R) favor 3D island growth. In addition, laser energy (E), background oxygen pressure (PO_2) and substrate induced epitaxial strain (ϵ_{xx}) also play an important roles. The growth modes can be categorized into following types:

(i) Island growth (3D growth): In this mode, film atoms tend to bound each other strongly compared to the substrate atoms and surface diffusion is rather slow. This results in the island (also known as Volmer-Weber) growth mode.

(ii) Layer plus island growth (3D mixed growth): This is more realistic and commonly observed in case of epitaxially grown films. In this mode, growth starts initially as layer-by-layer (2D) and transitions to the island growth (3D) after few layers. This is also known as

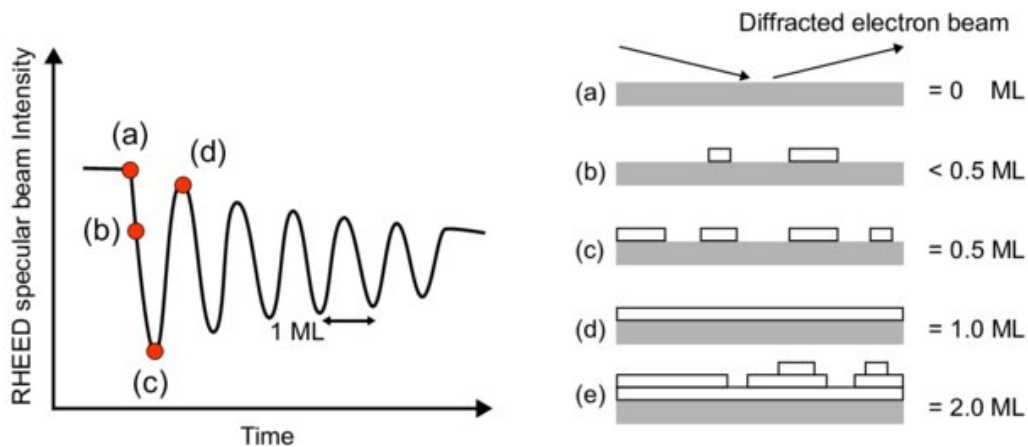


Figure 3.4: Working principle of RHEED: Thin film growth on the substrate (right side) and corresponding intensity change (oscillations) of specular spot as a function of time. This figure is adapted from [117].

Stranski-Krastanov mode.

(iii) Layer-by-layer growth (2D growth): In this mode, a layer-by-layer and smooth 2D growth takes place. Film atoms tend to bond strongly with substrate compared to each other and generally results in the highest crystalline quality films.

Layer by layer (also known as Frank-Van der Merve) growth mode results in the observation of well defined reflection high energy electron diffraction (RHEED) intensity oscillations, where one oscillation corresponds to the growth of one layer.

(iv) Step flow (2D growth): This is also a layer by layer 2D growth mode which usually takes place on the substrates with steps and terraces like surface structure. During the growth of a complete layer, the surface coverage remains constant and the intensity of diffracted spot does not change as a function of time, resulting in the steady RHEED intensity.

(c) Growth control:

Reflection high energy electron diffraction (RHEED) is a surface-sensitive technique commonly employed for thin film growth analysis and structural characterization. A high energy electron beam (~ 30 keV) is accelerated and focused on a substrate surface at grazing incidence ($1-5^\circ$) along a specific crystallographic direction, which makes it surface sensitive, see Fig. [3.3]. The e-beam interacts with the surface atoms and undergoes diffraction depending on the arrangement of the atoms at the surface. A fraction of diffracted electrons interfere constructively and hit and form a diffraction pattern at the detector screen. The

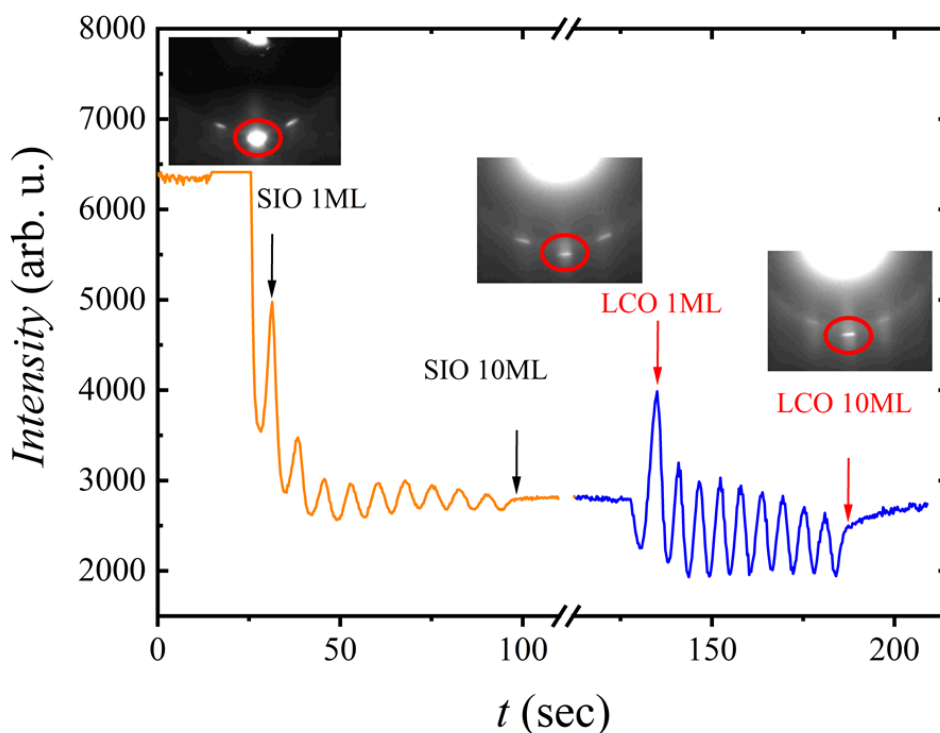


Figure 3.5: Intensity modulation of a specular diffraction spot (red ellipse) along the STO (100) surface as a function of time. The orange and blue lines represent the RHEED oscillation profile for SIO (10ML) and LCO (10ML), respectively

arrangement and intensity of these diffraction spots depend on the reflectivity of the sample surface. RHEED is a very powerful technique to in-situ monitor the film growth on the substrate and provides information on the layer thickness (number of unit cells), growth rate, surface roughness, epitaxial relation between the film and substrate and possible surface reconstruction during the growth.

As the deposition starts, the nucleation and growth of the film take place. As a consequence, the intensity of a particular diffraction spot changes, see Fig. [3.4a]. With increasing surface coverage on the substrate, intensity decreases and takes a minimum corresponding to the 50 percent coverage on the surface, Fig. [3.4b-c]. As the surface coverage further increases, intensity again starts increasing and then takes a maximum with the full coverage of the surface, Fig. [3.4d]. Thus, one complete oscillation corresponds to the growth of one atomic layer at the surface. Depending on the type of film growth, the RHEED oscillation profile can be very different in nature and thus provide very important information. Generally, intensity decreases with time (number of layers) due to imperfect layer growth, see Fig. [3.4e].

Film	T_s (°C)	PO_2 (mbar)	E (mJ) or (J/cm ²)
SrIrO ₃	600	0.1	40 (~ 1)
SrTiO ₃	700	0.1	40 (~ 1)
LaCoO ₃	650	0.3	80 (~ 2)
LaMnO ₃	700	0.3	80 (~ 2)
LaFeO ₃	700	0.3	80 (~ 2)
NdNiO ₃	700	0.1	40 (~ 1)

Table 3.1: Optimized set of growth parameters for the thin films used in the course of this thesis work. The substrate to target distance and laser frequency were kept fixed for all the films at 55 mm and 2 Hz, respectively.

The PLD chamber at IQMT, KIT is equipped with a electron source with 30 keV maximum energy from STAIB GmbH. Differential pumping is used to make RHEED compatible with the PLD that allows it to use even in higher background gas pressure. A software from k-space associates (kSA 400) analyses the changes in the intensity of a given spot and allows to monitor and control the growth in real time.

For example, we show the intensity modulation for a specular spot of RHEED pattern observed from the growth of a LCO(10ML)/SIO(10ML) bilayer in Fig. [3.5]. Clear thickness oscillations were observed for both layers, documenting the layer-by-layer growth mode. The film growth was stopped at the maxima of 10th oscillation which results in a growth of 10 ML LCO and SIO. The inset of Fig. [3.5] shows the images of RHEED diffraction patterns at different growth stages, documenting the layered growth of the films and smooth 2D like surface.

(d) Optimization of epitaxial growth:

As discussed in the last subsection, growth conditions and parameters have very strong influence on the epitaxy of deposited film. In this regard, laser parameters such as λ , E , frequency (f) and other parameters as T_s , PO_2 , target to substrate distance (l) are very important. To get a high quality single crystalline thin films, first, the growth parameters need to be optimized with respect to stoichiometry and crystallinity. In general, E and PO_2 play very critical role in the plasma expansion profile and strongly affect particle scattering and distribution of the ablated material. Hence, a careful optimization of the growth conditions is very important. This was done by varying a specific parameter, e.g., T_s (500 °-750 °C) or E (30-120 mJ) or

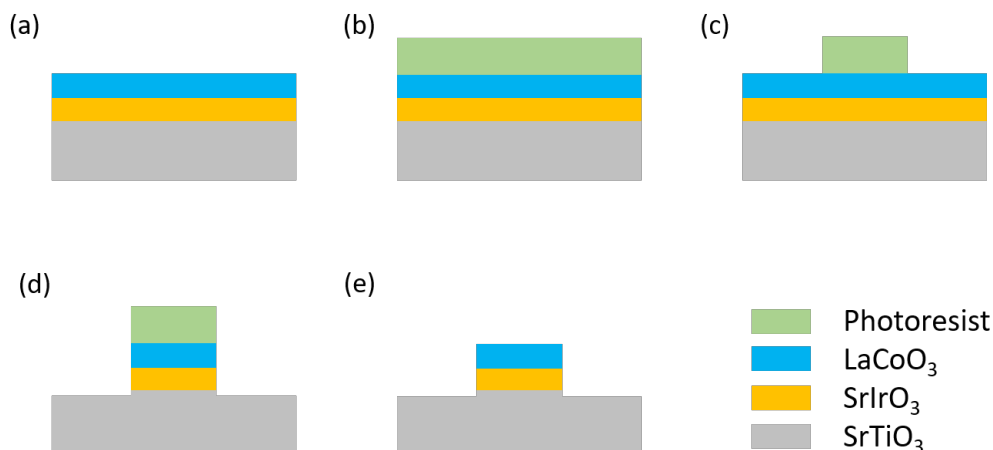


Figure 3.6: The sequential steps involved in the microstructuring of Hall bars using standard UV-photolithography and Ar-ion etching.

PO_2 (10^{-6} - 10^0 mbar) independently while keeping others constant. T_S strongly influences the epitaxy and crystallinity. Whereas E and PO_2 largely control the stoichiometry, defects (*e.g.* O₂ vacancy) and intermixing. The l and f were kept fixed to 55 mm and 2 H_z, respectively. The films were checked for structural properties (X-ray diffraction), stoichiometry (Rutherford Backscattering Spectrometry), electronic and magnetic properties.

Prior to each deposition, the targets were usually polished with a fine sand paper to achieve reproducible starting conditions of the target material. A pre-ablation with around 100 laser shots was also applied to provide clean surface for the ablation. To compensate for possible oxygen loss during the growth, all the films were post annealed in a 500 mbar O₂ atmosphere at 500 °C for around 30 minutes and then cooled down to room temperature.

In Table [3.1], we have summarized the optimized growth parameters for different films used in the study of this thesis work.

3.1.4 Device preparation

Electronic transport of the thin films, HSs and SLs were measured either in four point contact using Van der Pauw geometry on plane films or in six-point contact Hall bar geometry on microstructured samples. In this section, the details on the Hall bar device preparation that includes the Hall bar microstructuring of films using UV-photolithography, ion etching and subsequent solid back-gate device fabrication are briefly discussed.

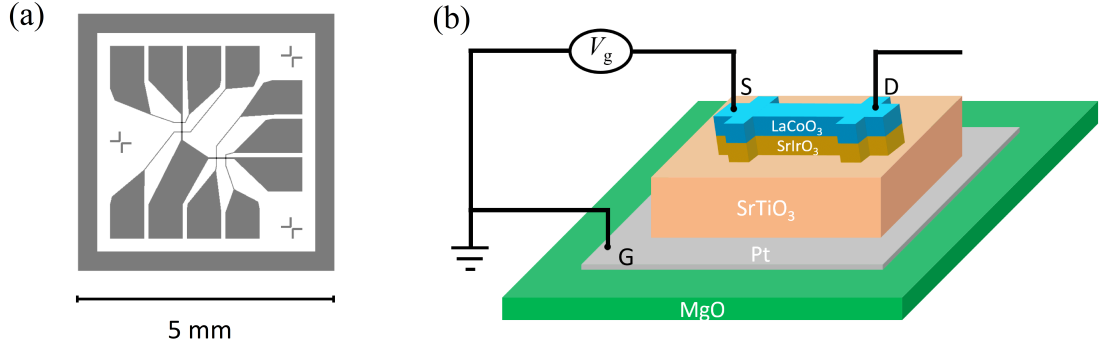


Figure 3.7: (a) The micrograph of the hard mask used for the Photolithography. Two perpendicular Hall bars parallel to the crystallographic directions are shown, (b) Layout of the 3-terminal global back gate device structure used in experiments. Contacts are provided by Al-wire bonding.

(a) Ultra violet photo lithography

Hall bars with surface dimension $40 \times 200 \mu\text{m}^2$ along two perpendicular crystallographic directions namely (100) and (010) (pseudo-cubic notations) were patterned using the combination of UV-photolithography and Ar-ion etching. The realization of Hall bars along two perpendicular directions allows to investigate the anisotropy (if any) in the electronic transport along these directions. The schematic of the sequential steps involved in the photolithography process are shown in the Fig. [3.6].

A positive photoresist (PR) (AZ MIR 701) was first deposited on the sample using spin-coating method with spinning speed of 4000 round per minute for 60 seconds. This results in the deposition of ~ 900 nm thick PR layer. After soft baking on a hot plate at 90°C for 60 seconds, the PR was exposed to UV-light using a mask aligner in hard contact (MA56/7.5s \times 18.4 mW/ cm^2 , Micro Chemicals) and developed using AZ 726 MiF (Micro Chemicals) for 45 seconds. The Cr mask used for the UV exposure is shown in Fig. [3.7a]. Next, the Ar-ions were bombarded in a sputtering chamber with $P(\text{Ar}) = 1.5 \times 10^{-5}$ to etch the desired surface area. The sputtering time was chosen carefully depending on the film thickness where etching rate amounts to $\sim 20 \text{ \AA}/\text{minute}$ under the given condition. In a next step, PR was lifted off using Technistrip P1316 in ultrasonic bath for around 20 seconds. As a last step, the samples were washed in bi-distilled H_2O for 10 seconds and finally dried using nitrogen blow.

Ar ion exposures for longer time may lead to creation of oxygen vacancies and consequently parasitic conductivity in STO. However, this can be avoided by annealing the samples in flowing O_2 atmosphere at 450°C for 5 hours after etching process.

(b) 3-terminal back gate device

Three terminal back-gate devices were fabricated employing STO substrate as dielectric material. Crystalline STO shows very good dielectric property which increases with decreasing temperatures. At low temperatures $T \leq 30$ K, the dielectric constant (ϵ) reaches the value of > 5000 which makes it efficient for gating devices. The schematic of the device is demonstrated in Fig. [3.7b]. The STO substrate was carefully thinned down to 0.1-0.2 mm from the backside to increase the electric field strength at given voltage. The gate terminal was provided by sputtering platinum (Pt) on the backside of the thinned STO substrate. In a final step, a Pt sputtered MgO was glued using silver paste on the backside of Pt- sputtered STO substrate.

3.2 Experimental methods

3.2.1 Chemical analysis

Rutherford backscattering spectrometry

In order to quantify the cationic ratio in the deposited film, we used Rutherford Backscattering Spectrometry (RBS). RBS is a non-destructive technique and allows the determination of elemental concentration in thin films. The basic principle of RBS is the classical scattering of high energy ions with the target (thin film) atoms which is governed by the Coulomb repulsion of the charge scatters (He^{++} ions). By measuring the energy and count of backscattered ions at a particular backscattering angle, one can identify the target atoms as the energy of the backscattered ions depend on the mass of target atoms [118].

In Fig. [3.8a], we show the schematic of a typical RBS spectra for a A_nB_m film on substrate S. The spectra consists of various regions related to the different element present in the sample. Considering the integrated peak areas A_A and A_B related to A and B elements respectively, the stoichiometry ratio can be given as [118]:

$$\frac{n}{m} = \frac{A_B \sigma_A}{A_A \sigma_B}, \quad (3.1)$$

where, σ_A (σ_B) is the scattering cross-section for A (B). In case of pure Coulombic scattering, the σ 's can be approximated as: $\sigma \approx Z^2$, where Z is the atomic number [118]. Therefore, we can write:

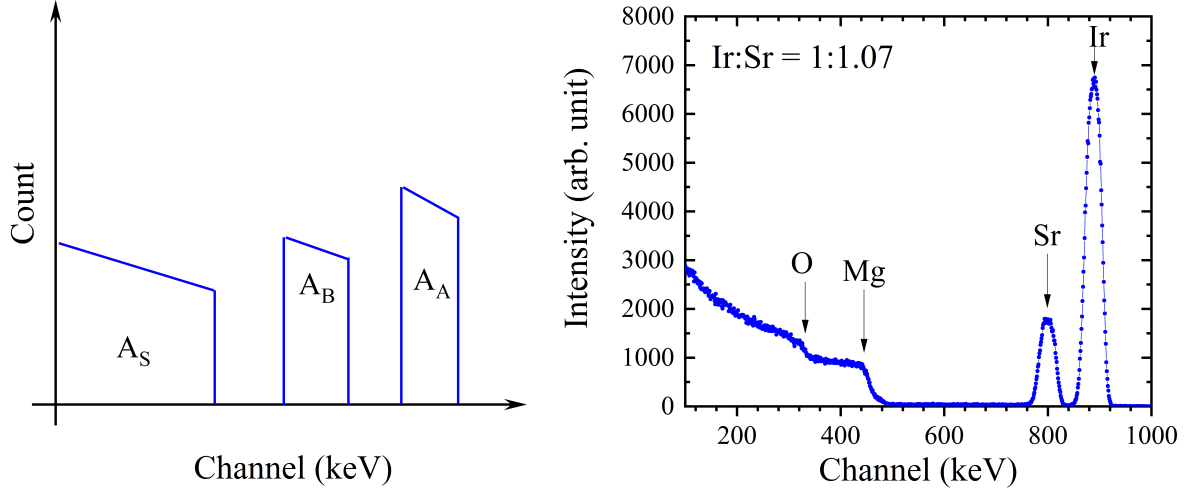


Figure 3.8: (a) Schematic of a typical RBS spectra of $A_n B_m$ film on S substrate. Integrated peak area corresponding to elements A, B and S are given as A_A , A_B and A_S , (b) RBS spectra of a SrIrO_3 films grown on MgO (001) substrate, presence of different elements are shown with arrows. The simulation resulted in a stoichiometry ratio $\text{Ir}:\text{Sr} = 1.00:1.07$.

$$\frac{n}{m} = \frac{A_B Z_A^2}{A_A Z_B^2}. \quad (3.2)$$

For the RBS measurement, thin films of thickness ~ 50 nm were deposited on MgO (001) substrates. RBS measurements were performed by Dr. J. Schubert at Forschungszentrum Jülich, Peter Grünberg Institute Jülich, Germany. In Fig. [3.8b], we show the RBS spectra for a SrIrO_3 film (~ 50 nm). The simulation of spectra resulted in the stoichiometry ratio $\text{Ir}:\text{Sr} = 1.00:1.07$. A slight Ir deficiency is often reported in SrIrO_3 films due to high volatile nature of IrO_3 .

3.2.2 Structural characterizations

Structural information are very important to understand the properties and functions of a material. Macroscopic structural properties were mainly investigated using X-ray based techniques. X-rays are widely used to probe structural information because their wavelength ($0.1 - 10 \text{ \AA}$) are in the same order of the atomic spacing. All the samples grown during the course of this thesis work were structurally investigated using a high resolution, four circle X-ray diffractometer D8 Discover from Bruker GmbH.

In the following, we discuss the different methods used to study the structural properties of epitaxial thin film samples.

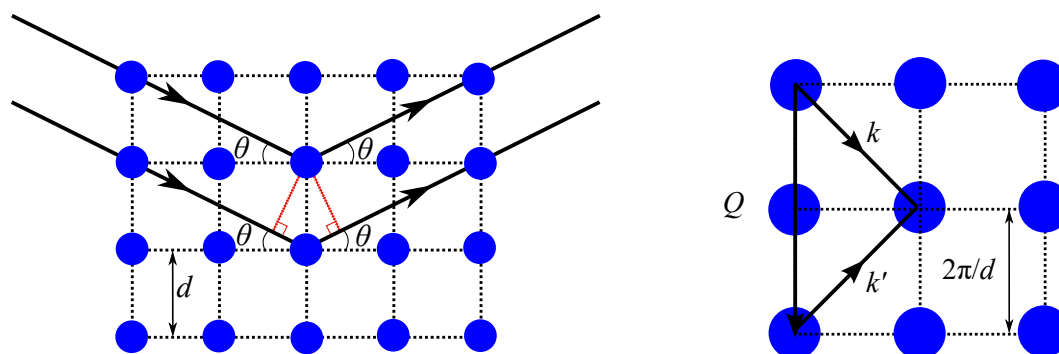


Figure 3.9: Illustration of the X-ray diffraction from the periodic arrangement of the atoms in a crystal. The condition of constructive interference is full-filled (a) in real space when the path difference is integral multiple of the X-ray wavelength $n\lambda$, (b) in reciprocal space when the wave-vector transfer $\Delta\vec{k}$ corresponds to some wave-vector \vec{Q}

(a) X-Ray reflectivity

X-ray reflectivity (XRR) was used to obtain the individual film thickness (t), electronic density (ρ) and the roughness (R) of the films. XRR is very sensitive to surface properties and is thus very suitable for the study of thin films, HSs and SLs. X-ray beam, in reflection mode, were used and the specularly reflected intensity was recorded as a function of incidence angle. Usually the incidence angle is very small, close to the critical angle (α_c), the angle below which the total reflection condition is satisfied. The reflected intensity profile shows two main characteristics. The one which decreases after α_c in accordance with the Fresnel reflectivity and the other comprise of Kiessig oscillations resulting from the constructive interference of X-rays reflected from the different diffractive layers and is directly related to the thickness of layers.

Experimentally measured XRR data were simulated using the LEPTOS v.7.05 software from Bruker AXS GmbH. The fitting parameters include film thickness, surface roughness while density was kept constant to bulk values unless stated otherwise.

(b) X-Ray diffraction

X-ray diffraction (XRD) is an elastic X-ray scattering process which is widely used to determine the structural properties of crystalline materials. The periodic arrangement of the atoms inside crystalline material act as a diffraction grating for the X-rays. Scattering of X-rays from these long-range atomic networks reinforce it to go under the constructive and destructive interference and as a consequence produce a diffraction pattern which is the fundamental signature of that crystalline material, see Fig. [3.9a]. The constructive interference

condition is given by the Bragg's equation

$$2.d_{hkl}(\theta_B) = n\lambda, \quad (3.3)$$

which states that the in-phase interference leads to the formation of diffraction peak in the pattern. Here d_{hkl} is the interplanar spacing between the planes with Miller indices (hkl) , θ_B is the Bragg angle satisfying the interference condition, λ is the X-ray wavelength used and n is the order of diffraction.

The intensity of a particular diffraction peak depends on the symmetry and geometrical form factor of the atoms inside the crystal.

(c) Reciprocal space maps

The reciprocal space (also known as momentum space/ K-space/ q-space) can be visualized as the Fourier transform of the direct real space. The reciprocal lattice corresponding to a real lattice can be constructed by arranging the each parallel set of Miller planes as a point normal to the plane direction at a distance equal to the reciprocal of inter-planar distance between the parallel planes. The 3-dimensional network of these points thus formed is called reciprocal lattice.

The condition of constructive interference defined by the Bragg's equation can also be understood by using the concept of reciprocal space. This condition is given by von Laue and is commonly known as Laue's equation.

If the wavevector of incident and diffracted wave are \vec{k} and \vec{k}' respectively then the wavevector transfer $\Delta\vec{k}$ during the scattering process will be $(\vec{k} - \vec{k}')$. According to the Laue's condition for the in-phase interference, the wavevector transfer $\Delta\vec{k}$ must correspond to some vector \vec{Q} in reciprocal space lattice, see Fig. [3.9b]:

$$(\vec{k} - \vec{k}') = \Delta\vec{k} = \vec{Q}. \quad (3.4)$$

In general, symmetric XRD measurements around a substrate peak provides information about the film lattice planes parallel to the substrate surface, *i.e.*, about out-of-plane lattice parameter. Hence, to extract the information about the in-plane lattice parameters, asymmetric XRD measurements are needed. This is done by recording the reciprocal space maps around specific allowed asymmetric lattice planes which allow to resolve the in-plane and out-of-plane parameters separately.

Reciprocal space mapping (RSM) is a high-resolution powerful technique to study the

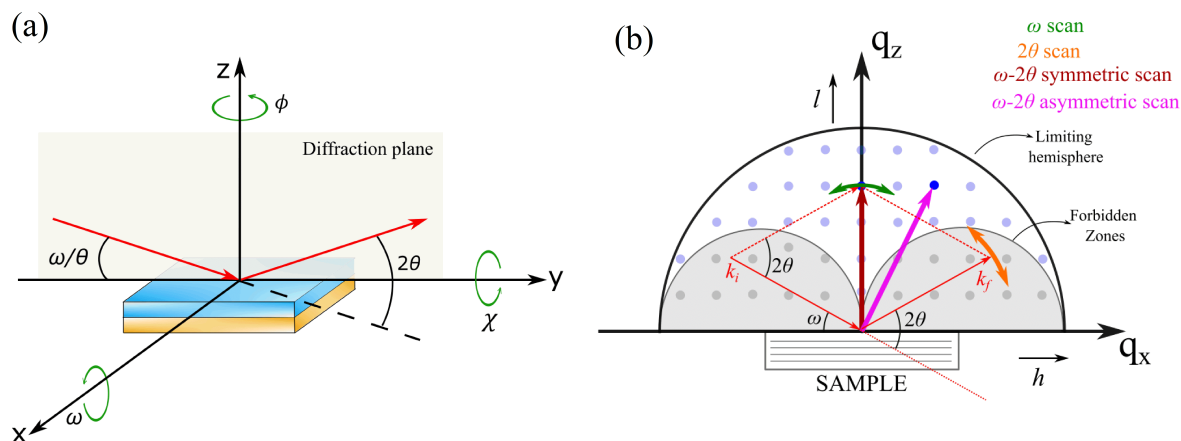


Figure 3.10: Schematic showing the different types of scans in (a) real space and (b) reciprocal space performed on the thin film heterostructures using a four circle diffractometer. The crystallographic and scattering directions are shown for the clear visualization.

epitaxial relationship between the constituent films and substrate, can be recorded by giving an offset $\Delta\omega$ to incident angle (ω) in the conventional coupled ($\omega - 2\theta$) scan around an asymmetric reflection, Fig. [3.10b]. By scanning an area in reciprocal space in the vicinity of an asymmetrical reflection, one can extract the out of plane and in plane information as well. It enables us to define the degree of relaxation, mosaicity, tilt, twist, strain, curvature present in the constituents films.

Due to constraints imposed by the source wavelength and the thickness of sample, only few reflection planes of k-space are allowed to be mapped. In reflection mode, these planes lie within the limiting semicircle (limiting hemisphere in 3-dimensional) of radius $\frac{\lambda}{2}$ and two forbidden zones (semicircles) centered at $\pm\frac{\lambda}{2}$ with radius $\frac{\lambda}{2}$, see Fig. [3.10b]. The forbidden zones are formed due to the thickness of sample, where absorption of incident or diffracted X-ray takes place when the incident angle or the scattered angle of the X-ray beam is less than zero.

Different types of scans, *i.e.*, rocking curve (ω scan), detector scan (2θ scan), azimuthal (ϕ scan) and coupled ($\omega-2\theta$ scan) in real and reciprocal space are demonstrated in Fig. [3.10a,b].

(d) Half integer reflection XRD

As pointed out in the Chapter 2, physical properties of the TMOs strongly depend on the arrangement of BO_6 octahedra, specially in SrIrO_3 , where strong pseudo-spin lattice coupling

is active. Thus, it is important to analyze the octahedra distortion (tilt or rotation pattern) of BO_6 octahedra in ABO_3 layer.

The oxygen octahedral distortions lead to a doubling of the pseudocubic unit cell along specific crystallographic axis in real space and thus allow to analyze the tilt or rotation pattern by measuring a set of specific pseudocubic half integer reflection (HIR-XRD). Considering the Glazer notation ($a^*b^*c^*$, $*$ = +/ - /0), see Section 2.1.1 and also [48], the in-phase (+) rotations a^+ , b^+ and c^+ produce hkl reflections: even(h)-odd(k)-odd(l) with $k \neq l$ (e.g. 013, 031), odd-even-odd with $h \neq l$ (e.g. 103, 301) or odd-odd-even with $h \neq k$ (e.g. 130, 310), respectively. While the out-of-phase (-) rotations a^- , b^- and c^- give hkl reflections: odd-odd-odd with $k \neq l$ (e.g. 131, 113), odd-odd-odd with $h \neq l$ (e.g. 113, 311) or odd-odd-odd with $h \neq k$ (e.g. 131, 311), respectively [49]. The intensity of these HIR depend on the strength of orthorhombic distortion and are often rather low. However, the high crystalline quality of the films sometime allow to probe such reflections using lab-based XRD systems.

(e) Scanning transmission electron microscopy

Transmission electron microscope (TEM) is a very powerful technique to image atoms/ surfaces/ interfaces of a sample with the resolution down to atomic scale. For example, an electron beam running at 100 kV offers a practical resolution of 0.5 nm and allows direct probing of individual atoms. The working principle is very similar to an optical microscope where the light source and optical lenses are replaced by the high energy electron source and electromagnetic lenses, respectively. The whole process takes place inside a high vacuum chamber which is decisive for the resolution and performance of the TEM [119].

A high energy, focused electron beam passes through an ultrathin sample and interacts with the atoms. The interaction involves several complex elastic and inelastic processes and results in backscattered, unscattered, secondary and Auger electrons and/or generation of X-rays. These emitted electrons and radiations can be used to deduce different information as elemental composition and topography of the sample specimen. In TEM, elastically scattered, transmitted electrons are collected by a detector and in a final step, used to create the magnified image of the sample.

The Scanning-TEM experiment were performed by D. Wang and V. Wollersen at the Institute of Nanotechnology, KIT. Investigations on HSs (total film thickness \sim 20-40 nm) were carried out using aberration corrected TEM in cross-section mode.

Furthermore, chemical analysis of the samples were also investigated performing electron energy loss spectroscopy (EELS). Integrating EELS within the TEM set-up provide

several advantages over the other chemical analysis techniques as energy-dispersive X-ray spectroscopy and allow imaging and chemical analysis parallelly with resolution down to atomic dimensions. A typical electron energy-loss spectrum consists of several key characteristics. The zero-loss peak, which corresponds to the unscattered and elastically scattered electrons during the interaction of the electron beam with the sample. The low loss region, also known as the valence region, provides information about the band structure and dielectric properties, including band gap, surface plasmon, etc. The last region at the higher energy loss side is known as the ionization edge or core energy loss region. The ionization edges, similar to the absorption edges in XAS (discussed later), provide information which includes the chemical analysis of the specimen sample.

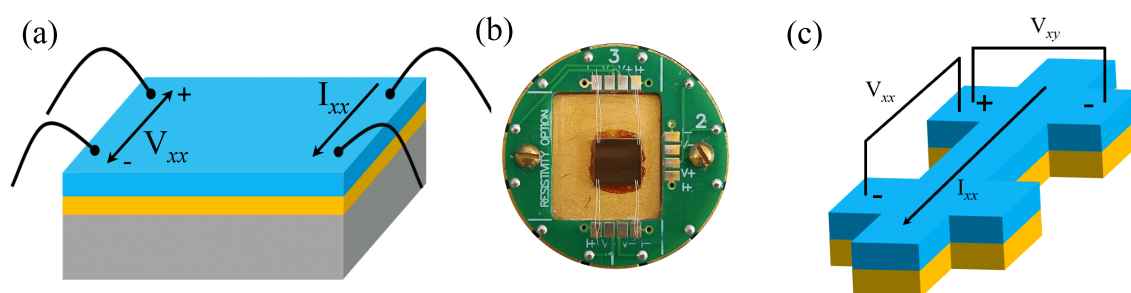


Figure 3.11: Electronic transport of the thin films and heterostructures: (a) Electrical connections for four-point contact measurement in Van der Pauw geometry and (b) the sample holder (puck) used for the experiments. (c) Electrical connections for six-point contact in Hall bar geometry. The connection between sample and puck was provided by Al-wire.

3.2.3 Electronic transport measurement

Electronic transport measurements are at the heart of the experimental techniques used in this thesis work. The transport measurements were performed with a Physical Property Measurement System (PPMS) from Quantum Design (model 6000) equipped with superconducting solenoid magnet with a maximum magnetic field of 14T. A Helium-4 cryostat equipped with nitrogen jacket allows the measurements in the range of temperatures between 350 K to 1.7 K. An AC current $I_{xx} = I_o \sin(\omega t)$ ($\omega = 2 \text{ Hz}$, $I_o = 1\text{-}100 \mu\text{A}$) was used for the measurements.

Measurements were performed either in Van der Pauw or in six-point contact geometry on microbridges, see Fig. [3.11]. The electrical connections between PPMS sample holder pads and the sample were realized using an ultrasonic wire bonder with a aluminium wire,

Fig. [3.11b]. In Van der Pauw geometry, the symmetric contacts were made at the corner of the square shaped sample. The longitudinal resistivity (ρ_{xx}) and transverse resistivity (ρ_{xy}) values were obtained using following expression,

$$\rho_{xx} = R_S \times t = \frac{\pi \times R_{xx}}{\ln 2} \times t, \quad R_{xx} = \frac{V_{xx}}{I_{xx}}, \quad (3.5)$$

$$\rho_{xy} = R_{xy} \times t, \quad R_{xy} = \frac{V_{xy}}{I_{xx}}, \quad (3.6)$$

with R_S , t , R_{xx} (V_{xx}) and R_{xy} (V_{xy}) are sheet resistance, film thickness, longitudinal and transverse resistance (voltage) respectively.

In six-point contact geometry on Hall bars, samples were microstructured using UV-lithography (see sample preparation section) into Hall bars and contacts were made on the pads of Hall bar structures. Resistivity values were calculated using following expression,

$$\rho_{xx} = \frac{R_{xx} \times A}{l}, \quad \rho_{xy} = R_{xy} \times t, \quad (3.7)$$

with R_{xx} , A , l and R_{xy} are longitudinal resistance, cross-sectional area of conduction channel, length of the bar and transverse resistance, respectively.

(a) Longitudinal resistivity and Magnetoresistance

The longitudinal resistivity as a function of temperature ($\rho_{xx}(T)$) was measured during cooling and warming of the sample between 300 K to 2 K. Any hysteretic effect related to structural or magnetic transition was carefully checked.

Magnetoresistance (MR) of a conductive sample is defined as its resistive response to internal magnetization or an applied magnetic field. It is defined as:

$$MR(\%) = \frac{\rho(B) - \rho(B=0)}{\rho(B=0)} \times 100, \quad (3.8)$$

The normal MR measurements were performed with an applied magnetic field perpendicular to the film surface. The classical or ordinary MR originates from the cyclotron motion of charge carriers under the influence of an applied field (B). In the limit of $\omega_c \tau > 1$, where $\omega_c (\propto B)$ and τ are the cyclotron frequency and mean scattering time respectively, it becomes dominant and follows quadratic field dependence.

In addition to classical MR, several distinct contribution to MR, depending on the choice of sample, are possible. For example, negative MR in ferromagnets [120], giant MR in metal-

lic multilayers and spin valves, colossal MR in manganites, tunneling MR in ferromagnet-insulator-superconductor multilayer etc [121]. In quantum transport limit, weak localization (WL) and weak anti-localization (WAL) can show dominant MR behavior at low fields [122].

(b) Transversal (Hall) resistivity

A conducting/semi-conducting material, when placed in a magnetic field, develops an additional transverse velocity perpendicular to the current and field direction as a consequence of Lorentz force acting on the charge carriers. This phenomenon was first reported by Edwin Hall in 1879 and commonly known as Hall effect [123, 124]. Since the Lorentz force acts and deflects positive (holes) and negative (electrons) charge carriers differently, Hall effect measurements are very useful to characterize the type and concentration of charge carriers. In single band transport, it shows a linear field dependence and is commonly known as ordinary (or linear) Hall effect.

For an ordinary Hall resistance R_{xy}^{OHE} , the Hall voltage V_{xy} generated due to Lorentz force acting on the charge carriers, transverse to the applied current I_{xx} and an external applied magnetic field B can be given as:

$$V_{xy} = V_H = \frac{R_H}{t} \times B \times I_{xx}, \quad (3.9)$$

$$\Rightarrow R_{xy} = \frac{V_H}{I_{xx}} = \frac{R_H}{t} \times B, \quad (3.10)$$

where $R_H (= \pm 1/ne)$ and t are Hall coefficient and the film thickness, respectively. In a single band model, one can calculate the charge carrier density n and mobility μ :

$$n = \frac{1}{e \times R_H}, \quad \mu = \frac{R_H}{\rho_{xx}} = \frac{1}{n \times e \times \rho_{xx}}. \quad (3.11)$$

Above relations are valid in case of single type charge carrier transport. If two different bands contribute to the electronic transport, the Hall resistance is given by:

$$R_{xy} = \frac{(n_h \mu_h^2 - n_e \mu_e^2) + \mu_h^2 \mu_e^2 (n_h - n_e) B^2}{(n_h \mu_h - n_e \mu_e)^2 + \mu_h^2 \mu_e^2 (n_h - n_e)^2 B^2}, \quad (3.12)$$

where n_h (n_e) and μ_h (μ_e) are the density and mobility of holes (electrons), respectively. Note that single SIO layers usually show a linear Hall effect with negative slope indicative of dominant electron type electronic transport. However, one can also simulate the linear behavior using a two band model considering the semi-metallic nature of SIO.

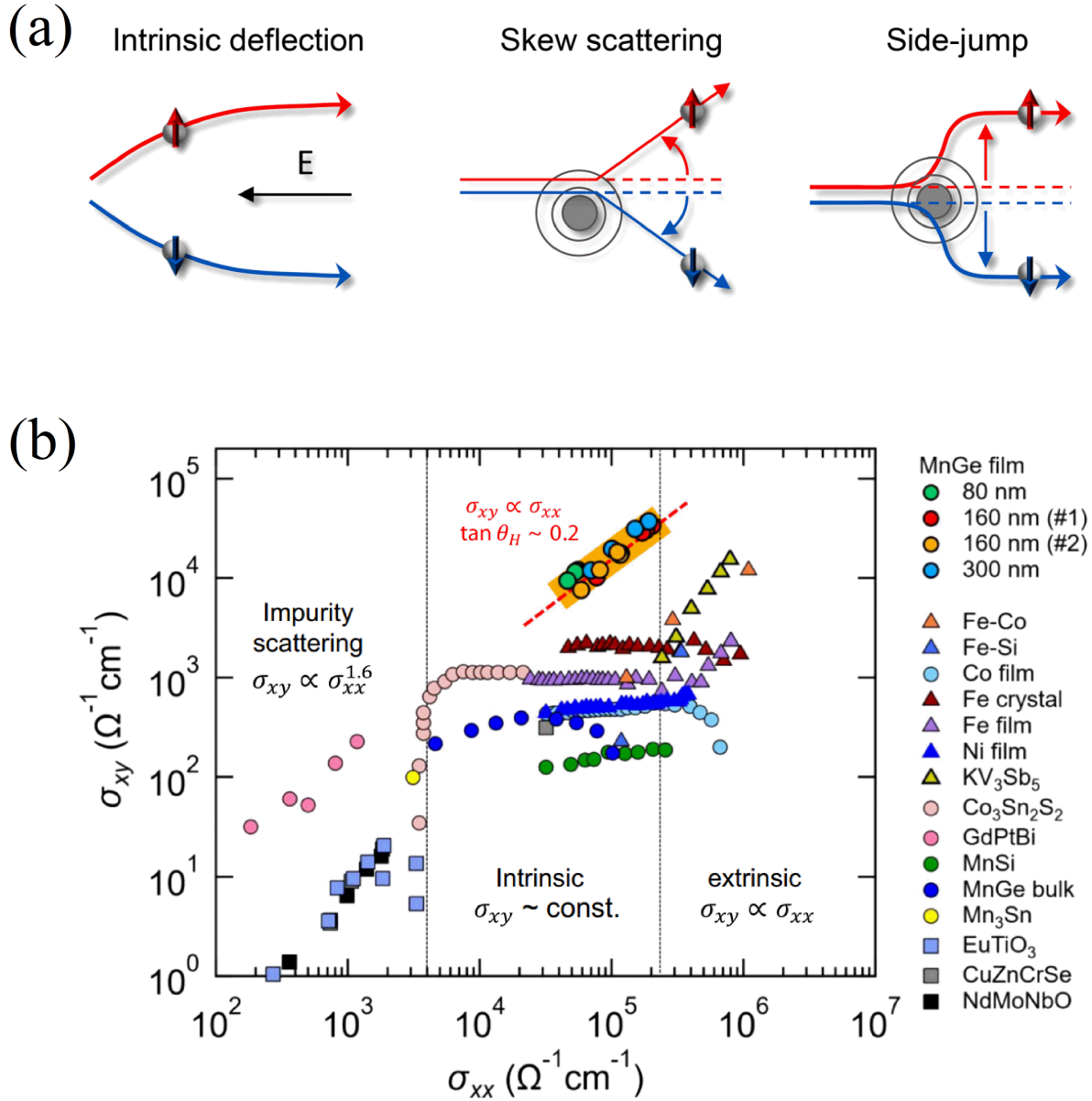


Figure 3.12: Origin of the anomalous Hall effect: (a) Intrinsic AHE related to the Berry curvature of the Bloch states at the Fermi level and extrinsic AHE including skew and side-jump scatterings, (b) Relation between σ_{xx} and $\sigma_{xy}^{AHE, s}$ in different conductivity regime. In dirty or moderate dirty limit, $\sigma_{xy}^{AHE, s}$ does not depend on σ_{xx} , *i.e.*, $\sigma_{xy}^{AHE, s} \neq f(\sigma_{xx})$ [125]. The figures are adapted from [126, 127].

In addition to R_{xy}^{OHE} , the total Hall resistance can be comprised of several other contributions related to different physical phenomena, *e.g.*, the anomalous Hall effect ρ_{xy}^{AHE} originating from the action of spin-orbit coupling in time-reversal symmetry broken systems [125]. It is also known as spontaneous Hall effect as it depends on the internal magnetization in ferromagnets and can be observed even in the absence of an external magnetic field. In early investigations on Fe, Ni and Co metals, the saturation value of AHE was found to be proportional to the magnetization, M [128]. Therefore, in a classical description, the total ρ_{xy} is given by the following empirical relation:

$$\rho_{xy} = \rho_{xy}^{OHE} + \rho_{xy}^{AHE} = R_o \times B + R_A \times M. \quad (3.13)$$

In 1954, the AHE was redefined as an additional “anomalous” contribution to the transverse velocity under the application of an external electric field [129]. In ferromagnets, the sum of this anomalous velocity over all the Bloch states at the Fermi level becomes non-zero and consequently results in the observation of an AHE. As this contribution is related to the band structure and does not depend on scattering, it is known as the intrinsic AHE. Later, the AHE was classified depending on the origin mechanism into intrinsic and extrinsic AHE. The intrinsic AHE results from SOC and topological band properties. It is related to the geometrical concept of Berry curvature and can be thought of originating from the effective magnetic field “Berry connection” in reciprocal space [130]. In presence of disorders, extrinsic mechanism can also contribute to the AHE, see Fig. [3.12a]. For example, skew scattering (SOC assisted electron scattering from impurities) or side-jump scattering (electron scattering from spin-orbit coupled impurities). A distinction among the different origins of the AHE can be made by scaling the longitudinal conductivity (σ_{xx}) and transverse anomalous conductivity ($\sigma_{xy}^{AHE, s}$), see Fig. [3.12b] [125], which can be deduced from the resistivities, ρ_{xx} and ρ_{xy}^{AHE} as follows:

$$\sigma_{xx} = \frac{\rho_{xx}^2}{\rho_{xx}^2 + \rho_{xy}^{AHE, s}{}^2}, \quad \text{and} \quad \sigma_{xy}^{AHE, s} = \frac{\rho_{xy}^2}{\rho_{xx}^2 + \rho_{xy}^{AHE, s}{}^2}. \quad (3.14)$$

First principal Berry curvature calculations have shown a large Berry curvature and hence intrinsic AHE around the band (anti-) crossings points near Fermi level. Thus, strong spin-orbit coupled materials with non-trivial crossing points in the band structure are expected to show a large intrinsic AHE [125].

Apart from the ordinary and anomalous Hall contributions, the transverse resistivity can be comprise of several other contributions, for example, topological, spin, inverse spin Hall

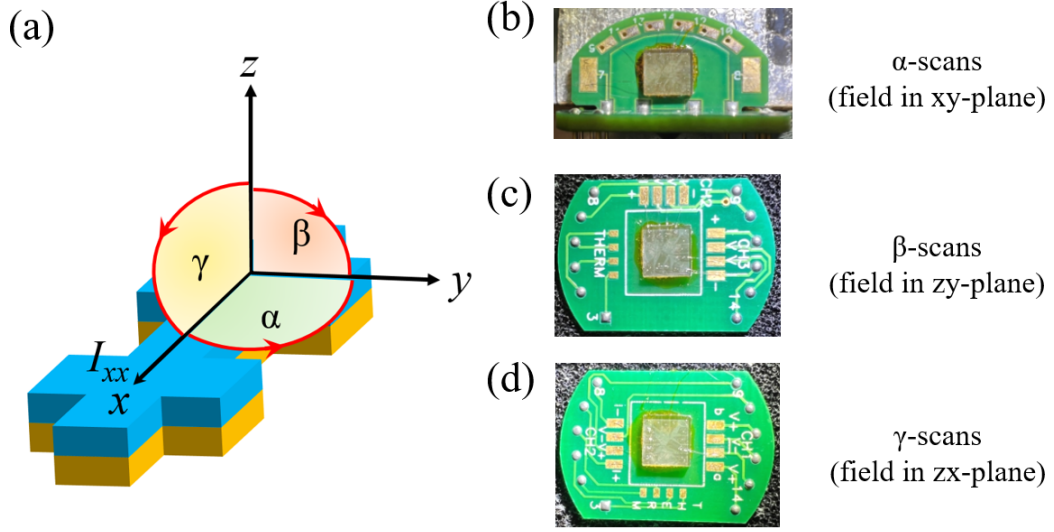


Figure 3.13: Definition of AMR(φ) ($\varphi = \alpha, \beta, \gamma$) scans: (a) Magnetic fields are swept in $xy(\alpha)$, $zy(\beta)$, and $xy(\gamma)$ planes. For the visualization, axes and different scans are shown. (b) Sample holders used with rotator for AMR measurements with magnetic field rotating in different planes.

effect etc.

Experimentally measured data (ρ_{xx} and ρ_{xy}) were corrected with respect to a linear drift and a residual offset. $\rho_{xx}(B)$ and $\rho_{xy}(B)$ were symmetrized and anti-symmetrized using $\frac{\rho_{xx}(B) - \rho_{xx}(B=0)}{2}$ and $\frac{\rho_{xy}(B) - \rho_{xy}(B=0)}{2}$, respectively.

(c) Angle dependent anisotropic magnetoresistance

Angle dependent anisotropic magnetoresistance AMR(φ) measurements were performed using a special sample holder and a sample rotator HR-133 from Quantum Design. Magnetic fields were swept in different crystallographic planes with current always along the x-axis. $\rho_{xx}/\rho_{xy}(\alpha)$, $\rho_{xx}/\rho_{xy}(\beta)$ and $\rho_{xx}/\rho_{xy}(\gamma)$ are defined as the longitudinal and transverse resistivities with magnetic field rotating in xy, zy and zx-plane, respectively, see Fig.[3.13]. Experimentally measured $\rho_{xx}/\rho_{xy}(\varphi)$, ($\varphi = \alpha, \beta, \gamma$) data were corrected with respect to sample wobbling due to any possible tilt of the sample glued to the sample holder and linear drift.

In magnetic materials, the conventional AMR is caused by spin-flip and exchange scattering between *s*- and *d*-electrons, *i.e.*, *s-d* scattering (sdS) and depends only on the relative direction between the current and the magnetization [131]. Thus, it is a powerful tool to probe magnetization in metallic samples. The *s-d* scattering in an isotropic magnetic material results in a two-fold symmetry of the AMR proportional to $\cos(2\varphi)$ ($\varphi = \alpha, \gamma$) where maxima appear at 0° and 180° for $\varphi = \alpha$, and 90° and 270° for $\varphi = \gamma$.

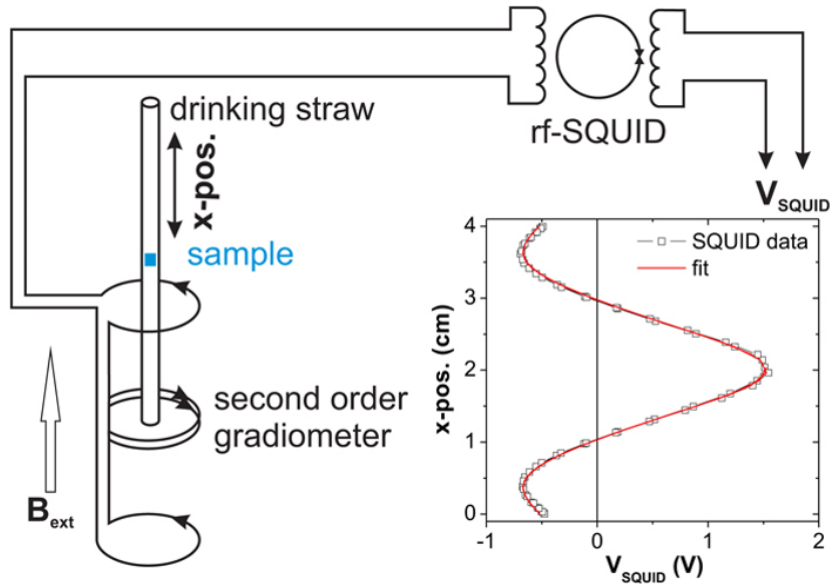


Figure 3.14: Working principle of a SQUID: A vertically moving magnetic sample scans the distance across the superconducting coil, which results in the change of the magnetic flux. This figure is taken from [134].

In heterostructures comprising magnetic insulating layers and metallic layers displaying strong SOC, as in LCO/SIO, the spin-Hall magnetoresistance (SMR) may be active as well [132]. Similar to the sdS -dominated conventional AMR, the SMR shows a two-fold symmetry alike for $\varphi = \alpha, \beta$ with maxima at 0° and 180° [133]. In addition, SMR ($\approx 10^{-4}$) is usually about one order of magnitude smaller than conventional AMR ($\approx 10^{-3}$).

3.2.4 Magnetization measurements

Magnetic properties of the samples were measured using a Superconducting QUantum Interference Device (SQUID) from Quantum Design (Magnetic Property Measurement System - MPMS). It allows the magnetization measurements in the temperature range 1.7 K-300 K with a magnetic field up to ± 7 Tesla. The measurements of the samples (films + substrate) were recorded either as a function of magnetic field $m(\mu_o H)$ or temperature $m(T)$. The samples were placed in a clean straw in different geometry in order to apply the magnetic field along the specific crystallographic directions, see Fig.[3.14]. This allows to characterize possible anisotropy of the magnetisation in the films.

Magnetic moment versus temperature ($m(T)$) measurements were performed to analyze the nature of magnetic ordering in the sample. Depending on the type of magnetic ordering, samples show different temperature dependence, see Fig.[3.15]. By analyzing the temperature dependence, we can identify the type of magnetic order in the sample. The magnetic

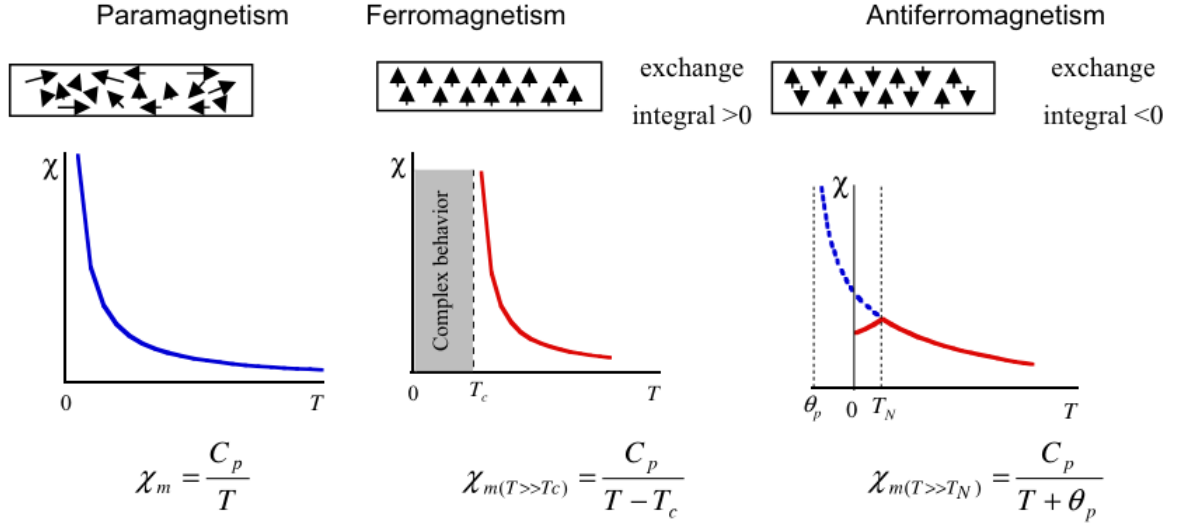


Figure 3.15: Temperature dependence of the magnetic susceptibility for different magnetic samples. The figure is taken from [135].

susceptibility of a magnetic material is defined as the ratio of magnetization and applied magnetic field ($\chi_m = \frac{\partial M}{\partial H} \approx \frac{\Delta M}{\Delta H}$). Paramagnets, ferromagnets and antiferromagnets show $\chi > 0$, but the magnitude and temperature dependence greatly depend on the type of magnetic ordering, see Fig.[3.15].

Magnetic moment versus field measurements ($m(\mu_o H)$) along a specific crystallographic direction provide information on the coercive field, easy and hard axis behavior of magnetization. It is very useful to characterize the magnetic anisotropy in the magnetic sample. As SQUID measures total m , it is important to subtract the substrate's contribution from the total signal. For a diamagnetic substrates like STO, this contribution is linear in magnetic field.

$m(T)$ and $m(\mu_o H)$ data were corrected to avoid any substrate (*e.g.* STO) induced diamagnetic contribution. As the diamagnetic contributions are temperature independent, we define $m^*(T)$ as $(m(T) - m(300K))$. This allows us to directly compare the $m^*(T)$ data from different samples. At higher fields, once the film magnetic moments are saturated, the total signal depends on the diamagnetic STO substrate only. Thus, we can define $m^*(\mu_o H)$ by subtracting the linear part at higher fields from the total ($m(\mu_o H)$). Magnetic impurities present in STO and other substrates show a strong increase in magnetic response at low temperatures ($T < 15$ K), which makes the data correction challenging in that T -range.

3.2.5 Spectroscopy measurements

(a) X-ray absorption spectroscopy

X-ray absorption spectroscopy (XAS) involves the irradiation and subsequent absorption of intense, monochromatic X-rays by a sample as a function of X-ray energy (0.1-100 keV). These experiments are performed at the synchrotron facilities which provide highly intense, monochromatic and energy tunable X-rays. The basic principle lies in the excitation of a core electron to above Fermi level by X-ray absorption. When the X-ray energy is sufficient enough to cross the threshold (absorption edge), absorption spectra shows a sharp jump in the absorption cross-section followed by a continuum. Since the each element has a set of specific absorption edge energies depending on the binding energies of its electrons, XAS is an element specific experiment and is independent of state of matter, *i.e.*, applicable to solids, liquids and gases as well. Thus, it is one of best technique to investigate the electronic structure of a sample. XAS measurements can be performed in different modes such as transmission, total electron yield (TEY) and fluorescence yield (FY) mode, depending on the detection methods. In transmission mode, the intensity of transmitted electrons are recorded while in TEY, the number of emitted Auger electrons are measured. Not all the generated Auger electrons have sufficient energy to escape the materials, only electrons from the surface region participate in the process, making TEY surface-sensitive technique. On the other hand, FY yield involves the measurement of fluorescence X-rays resulting from the de-excitation of an high energy electrons to the core levels. TEY is dominant process in case of soft X-ray XAS while FY is more likely in hard X-ray XAS.

A normal XAS spectra shows several regions including the pre-edge, edge, near edge and whiteline regions. The whole spectra can be divided in two regimes namely X-ray absorption near edge structure (XANES) around a edge jump involving low energy photoelectrons and extended X-ray absorption fine structure (EXAFS) far above (50-1000 eV) the edge jump involving high energy photoelectrons. XANES is used for the study of electronic structure, unoccupied density of states and oxidation state. The local environment generally results in the XANES fine structures, which allows to study the local electronic structure. While EXAFS is useful to extract information about the neighbouring atoms including type of atoms, distance between them, coordination number. It also provides information about the disorders. Depending on the energy of X-rays, one can study the different excitation, for example, *K*-edge (transition from $1s$ to empty nd level), *L*-edge (transition from $2s$ or $2p$ to empty nd level), *M*-edge (transition from $3s$ or $3p$ or $3d$ to empty nd level) etc.

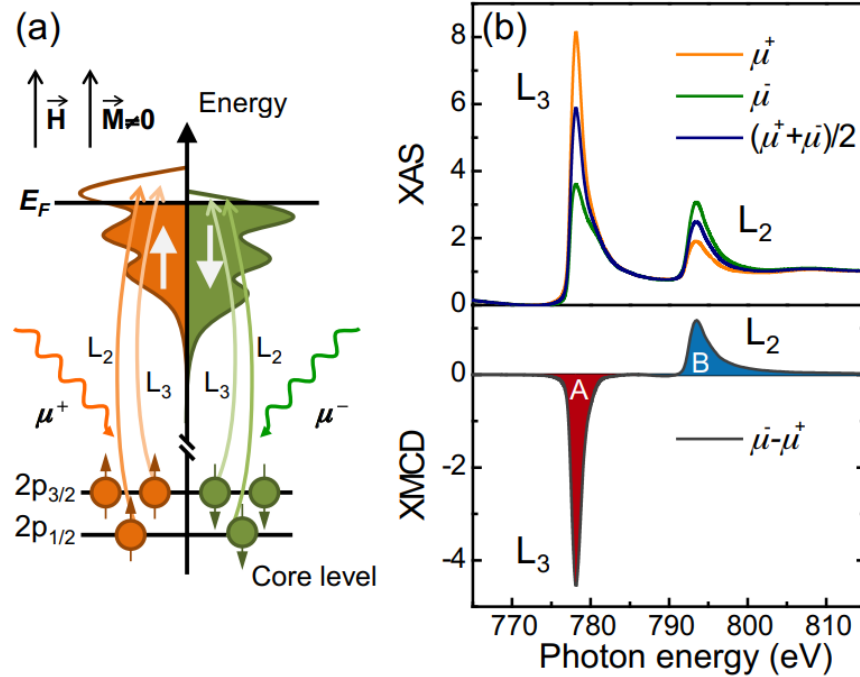


Figure 3.16: XAS and XMCD spectroscopy: (a) the principle of spin-dependent X-ray absorption in magnetic materials, (b) the XAS recorded with right and left circularly polarized X-rays and the average (difference) of two represents the XAS (XMCD) [136].

(b) X-ray circular magnetic dichroism

Dichroism, in general, is defined as the polarization selective absorption of light in a material. In X-ray magnetic circular dichroism (XMCD), two XAS spectra are recorded using left and right circularly polarized X-rays in an applied magnetic field (or zero field) and the difference between the two XAS spectra provides information on the magnetic properties of the sample. Left and right circularly polarized X-rays behave differently to the spin-up and spin-down electrons and account for the spin-dependent absorption of X-rays by the electrons. Thus, the difference between the two XAS, *i.e.*, XMCD directly correlates with the differential population of spin-up and spin-down electrons in the magnetic sample, see Fig. [3.16]. XMCD is element specific tool for the characterization of magnetization. It allows to calculate the spin and orbital moments separately using magneto-optical sum rule [137].

In this thesis work, Ir valence state, branching ratio and magnetism was investigated recording hard X-ray XAS and XMCD spectra at Ir L_3 and L_2 edge at the ID12 beamline of European Synchrotron Radiation Facility (ESRF), Grenoble. The spectra were collected in grazing incident (15° to the film surface) and fluorescence mode geometry with an applied in-plane magnetic field of $\pm 6\text{T}$ ($\pm 7\text{T}$ for LMO/SIO SL) using right and left circularly

polarized light. The XAS data were first normalized between 0 and 1 before and after the edge jump, respectively and then corrected with respect to the edge jump using an arc tangent step-function as described in Ref. [137]. The integrated L_3 and L_2 white-line sum area was used to estimate the hole density in Ir.

The L_2 edge corresponds to the X-ray absorption from $2p_{1/2}$ to $5d_{3/2}$ state while the L_3 is related to the transition from $2p_{3/2}$ to $5d_{3/2}$ and $5d_{5/2}$ states. The relative occupation of $5d$ states is represented by the branching ratio (BR) which is given as:

$$BR = \frac{I_{L_3}^{XAS}}{I_{L_3}^{XAS} + I_{L_2}^{XAS}} = \frac{2}{3} - \frac{\sum_i l_i \cdot s_i}{3 \langle n_h \rangle}, \quad (3.15)$$

where $\langle n_h \rangle$ is the total number of holes, $\sum_i l_i \cdot s_i$ is the expectation value of $l_i \cdot s_i$ operator summed over all electrons [137].

The total magnetic moment is the sum of orbital ($m_{orbital}$) and effective spin (m_{spin}) moments, *i.e.*,

$$m_{total} = m_{orbital} + m_{spin,eff} = -(\langle L_z \rangle + 2 \langle S_{eff} \rangle) \mu_B, \quad (3.16)$$

where $\langle L_z \rangle$ and $\langle S_{eff} \rangle$ are the expectation value of orbital and effective spin angular momentum, respectively which can be calculated using sum rule analysis on XMCD spectra as follows:

$$\langle L_z \rangle = \frac{2 \langle n_h \rangle}{3} \times \frac{I_{L_3}^{XMCD} + I_{L_2}^{XMCD}}{I_{L_3}^{XAS} + I_{L_2}^{XAS}}, \quad (3.17)$$

and

$$\langle S_{eff} \rangle = \langle S_z \rangle + \frac{7}{2} \langle T_z \rangle = \frac{\langle n_h \rangle}{2} \times \frac{I_{L_3}^{XMCD} - 2 \times I_{L_2}^{XMCD}}{I_{L_3}^{XAS} + I_{L_2}^{XAS}}. \quad (3.18)$$

where $\langle n_h \rangle$ is the number of holes in the d -orbital, $I_{L_3}^{XAS}$ ($I_{L_2}^{XAS}$) and $I_{L_3}^{XMCD}$ ($I_{L_2}^{XMCD}$) are the XAS and XMCD peak area of L_3 (L_2), respectively. $\langle T_z \rangle$ is magnetic dipole contribution [137].

CHAPTER 4

Proximity Induced Magnetic State and Anomalous Hall Effect in $5d$ -TMO SrIrO_3

If you can't explain it simply, you don't understand it well enough.

Albert Einstein

4.1 Structural properties of the $\text{LaCoO}_3/\text{SrIrO}_3$ HSs

The details on the growth optimization of single layer thin films are already discussed in the last Chapter 3. In this section, the focus is placed on the study of structural properties of the $\text{SrIrO}_3(\text{SIO})/\text{LaCoO}_3$ (LCO) HSs. For a systematic study, we prepared following samples; single layer films LCO(x ML), SIO(y ML), bilayers [LCO(x ML)/SIO(y ML)] and trilayers [LCO(x ML)/STO(z ML)/SIO(y ML)], where x , y and z are the thicknesses of LCO, SIO and STO layers respectively in units of monolayers (ML). In bilayers, LCO and SIO are in direct contact to each other whereas in trilayers they are separated by an ultrathin, insulating STO layer. Single layer SIO films were capped with a thin STO (3-4ML) layers to protect the surface from possible degradation. All the HSs and SLs were deposited on the TiO_2 -terminated STO (001) substrates. The growth was monitored in-situ by RHEED which allowed to control the film thicknesses precisely and to stop the deposition at a particular thickness.

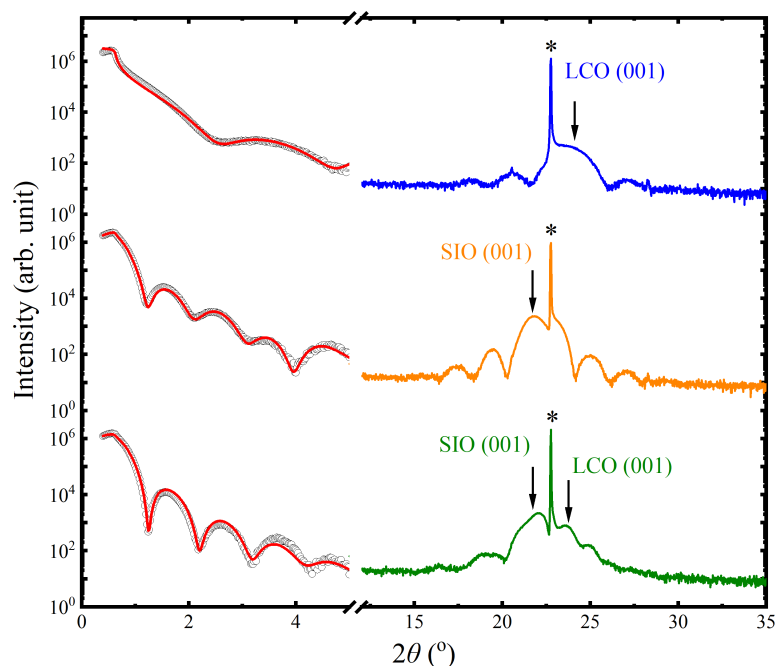


Figure 4.1: X-ray reflectivity (left) and X-ray diffraction (right) for the LCO, SIO and LCO/SIO samples grown on STO (001) substrates. Experimentally measured XRR are shown with the black symbols while fitting to the data are shown with the solid red lines. The substrate and film peaks are indicated by star (*) and arrows (↓), respectively. Note, SIO single layer film is capped with a STO protecting layer.

The XRR for SIO(10ML), LCO(10ML) and LCO(10ML)/SIO(10ML) samples are shown in the left side of Fig. [4.1]. All the measured XRRs show well-defined Kiessig fringes above the critical angle, which generally correlates with the inverse thickness of individual layers documenting the layer-by-layer growth of the constituent films. Measured data are shown with the open circles, whereas fits to the data are shown with the solid red lines. The thickness and roughness (thickness \pm roughness) values extracted from the simulation of data confirmed the same thickness as monitored by RHEED.

Next, symmetric XRD measurements were performed in the vicinity of the pseudocubic (00 l) peak family of STO. The right side of Fig. [4.1] shows the XRD close to the STO (001) peak. Substrate and film peaks are denoted by star (*) and arrows (\downarrow), respectively. Clear observation of Laue (thickness) oscillations on both sides of the main film peak indicates the high quality epitaxial growth of the films. The pseudocubic (cubic) lattice constant of STO (3.905 Å) results in a compressive and tensile strain for SIO (3.96 Å) and LCO (3.80 Å), respectively. This is clearly visible in the XRD as SIO (LCO) film peaks appear at a lower (higher) 2θ angle compared to the STO. The out-of-plane lattice parameters (d_{00l} or c) are calculated using Bragg's equation ($2d_{00l}\sin\theta = \lambda$) and are 4.05 Å and 3.78 Å for SIO and LCO, respectively.

In Fig. [4.2], we show the RSM in q_x - q_z space measured in the vicinity of the (204)+ peak of the STO substrate for SIO(10ML), LCO(10ML) and LCO(10ML)/SIO(10ML) HSs. Note that for SIO and LCO, pseudocubic (204) corresponds to equivalent orthorhombic (444, 206, 602) and rhombohedral (244) reflections, respectively. The q_x and q_z are the reciprocal space vectors along x (parallel to the (100) in-plane direction of STO) and z (perpendicular to the STO surface, *i.e.*, along the (001) out-of-plane direction), respectively. Hence, RSMs contain information on both the in-plane (a or b) and out-of-plane (c) lattice constants. The color profiles represent the intensity distribution of the peaks (where blue corresponds to the minimum and red to the maximum intensity). The rather low thicknesses (\sim 10ML) of the films result in a broadening of the peaks along the q_z direction. The q_x value of both single layer films and HS are the same as of the STO, *i.e.*, both films share the same in-plane lattice parameters as of STO (*i.e.* $a = 3.9$ Å) and are coherently strained to STO. The q_z values of SIO and LCO in single films and also in the HS, are at different values compared to STO. For SIO, it is at a lower q_z value (larger c) compared to STO, which means SIO is tetragonally distorted and compressively strained to STO. For LCO, q_z appears at a larger value compared to STO (*i.e.* shorter c), which corroborates the tensile strained growth of LCO on STO. This is in full agreement with the results obtained on the symmetric XRD. We also measured the

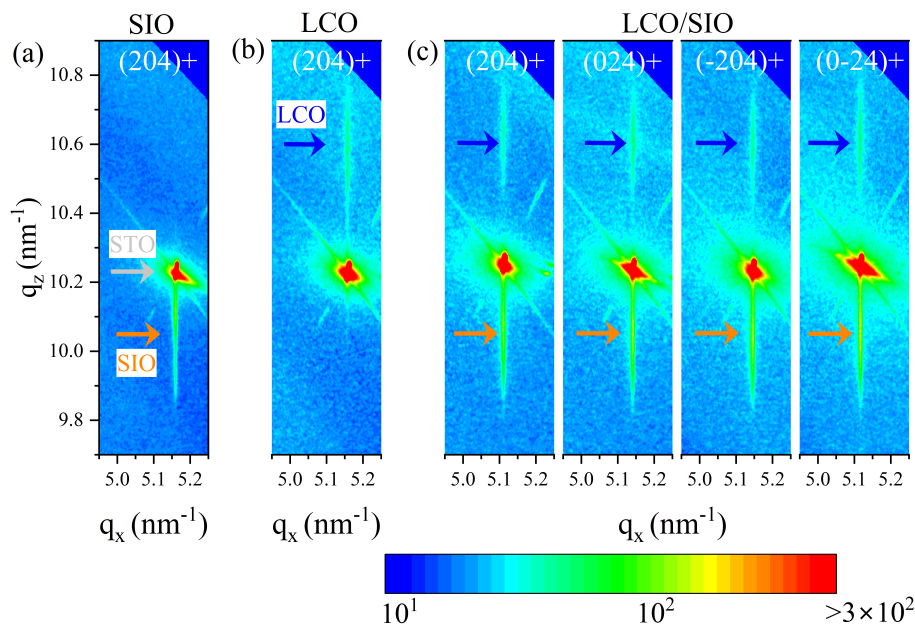


Figure 4.2: Reciprocal space maps around the asymmetric $(204)_+$ peak of STO (001) substrate for (a) SIO(10ML) film, (b) LCO(10ML) film and (c) LCO(10ML)/SIO(10ML) HS. For LCO/SIO, four maps were recorded around the (204) peak family. The film and substrate peaks are indicated by the arrows. The intensity is plotted on logarithmic scale and the profile is shown by the color scale at the bottom where blue and red correspond to minimum and maximum intensity respectively.

RSMs around symmetry equivalent peaks of $(204)_+$ family, shown in the Fig.[4.2c]. For this, RSM was measured 4 times while rotating the STO substrate in steps of $\varphi = 90^\circ$. The q_x values for all 4 maps appear at the same position as for STO which confirms that the films are coherently strained to the STO substrate. Despite the line broadening, distinct variations of the q_z values are not visible. They can be assumed to be the same in all four maps, which within the experimental resolution, rules out the presence of an orthorhombic distortion in the films. Thus, both SIO and LCO films in the HS possess pseudo-tetragonal symmetry with $a \approx b$, locked to the STO substrate (3.9 \AA) and c are higher (4.05 \AA) and lower (3.78 \AA) for SIO and LCO, respectively.

As pointed out in the Chapter 3, physical properties of the TMOs strongly depend on the arrangement of BO_6 octahedra, specially in SIO, where strong pseudo-spin lattice coupling is active. Thus, it is important to analyze the octahedral tilt or rotation pattern of IrO_6 and CoO_6 octahedra in SIO and LCO layers. To probe the octahedral rotations, we investigated a set of pseudo-cubic HIRs corresponding to different rotations, see Table [4.1]. In Fig. [4.3a], we show specific HIR-XRD for LCO/SIO bilayer, SIO and LCO single layers. In LCO/SIO bilayer, we did not observe any HIR corresponding to the in-phase rotations in SIO. The out-

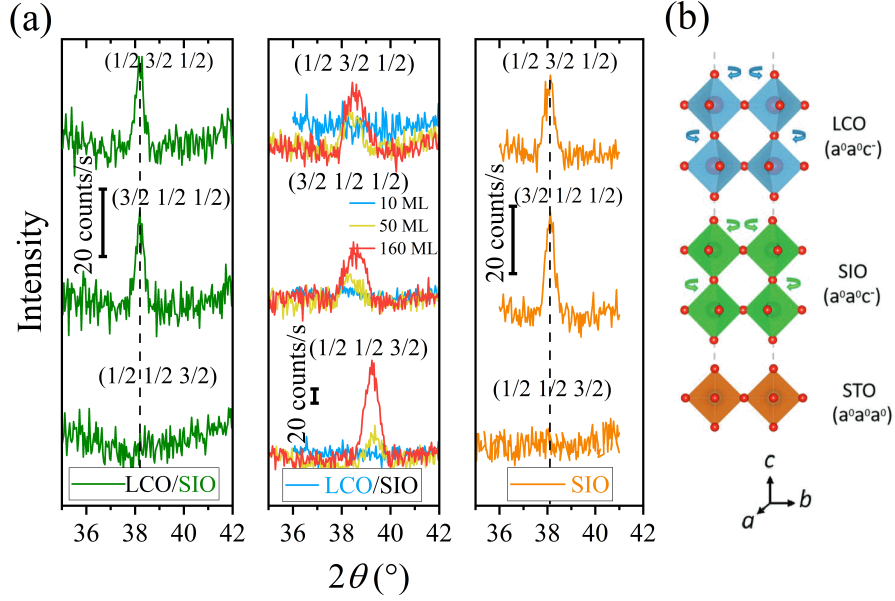


Figure 4.3: Octahedral rotation pattern of SIO and LCO: (a) XRD for specific set of HIRs in SIO (10ML) in LCO/SIO bilayer (left panel) and SIO (10ML) single layer (right panel) grown on STO corresponding to $a^0a^0c^-$ rotation pattern of IrO_6 octahedra. For LCO (10ML), the intensity was too low to be detectable with the lab XRD, however, with increasing thickness, $a^-a^-c^-$ rotation pattern evolves (see middle panel). (b) The sketch of the $a^0a^0c^-$ rotation pattern for IrO_6 and CoO_6 octahedra in LCO(10ML)/SIO(10ML) bilayer on STO substrate.

of-phase $(1/2, 3/2, 1/2)$ and $(3/2, 1/2, 1/2)$ reflections of SIO were observed which correspond to a c^- rotation of SIO, see left panel of Fig. [4.3a]. However, we did not observe intensity from the $(1/2, 1/2, 3/2)$ reflection corresponding to a a^- or b^- rotations. Thus, SIO in LCO/SIO bilayer has the $a^0a^0c^-$ rotation pattern, consistent with the pseudo-tetragonal symmetry of SIO. We also measured the single layer SIO film and found the same rotation pattern of $a^0a^0c^-$, right panel of Fig. [4.3a]. The HIR-XRD intensities and peak positions do not show any distinct differences, thus definitely ruling out any structural difference in SIO layers in the two samples such as additional strain from top LCO layer in LCO/SIO bilayer. The bulk SIO with orthorhombic symmetry shows the $a^-a^-c^+$ rotation pattern. The highly strained growth of few monolayer SIO on cubic STO ($a^0a^0a^0$) often results in the suppression of rotations around in-plane directions, *i.e.*, SIO not only adapts the in-plane lattice parameters albeit octahedral patterns of STO as well [76, 138].

For LCO in LCO/SIO bilayer, we could not observe any HIR-XRD, see middle panel of Fig. [4.3a], very likely due to the weak intensity expected from the lower X-ray scattering from Co compared to Ir. For this purpose, we investigated the evolution of octahedra pattern in LCO single layers as a function of thickness. With increasing thickness, the HIR

Rotations Clockwise (+) Anti-clockwise (-)	Investigated HIR <i>hkl</i>	Observed HIR SIO	Observed HIR LCO
a^+	213	No	No
a^+	231	No	No
b^+	123	No	No
b^+	321	No	No
c^+	132	No	No
c^+	312	No	No
a^-	131	Yes	Yes
a^-	113	No	No
b^-	113	No	No
b^-	311	Yes	Yes
c^-	131	Yes	Yes
c^-	311	Yes	Yes
		$a^0a^0c^-$	$a^0a^0c^-$

Table 4.1: Set of pseudo-cubic half integer reflections investigated to probe the octahedral rotation pattern of IrO₆ and CoO₆ octahedra in SIO and LCO, respectively. A $a^0a^0c^-$ rotation pattern was observed for both SIO and LCO in LCO/SIO bilayer HS.

corresponding to ($a^- a^- c^-$) starts appearing, in line with the rhombohedral symmetry of bulk LCO. The intensity of ($1/2 \ 1/2 \ 3/2$) peak which corresponds to a a^- or b^- rotation, increases much stronger compared to ($1/2 \ 3/2 \ 1/2$) and ($3/2 \ 1/2 \ 1/2$) reflection from c^- rotation. As the intensity directly correlates with the strength of octahedral rotations, we can assume the suppression of CoO₆ octahedra rotation around in-plane axes in LCO(10ML) as well. Thus, the 10 ML thick LCO and SIO both in LCO/SIO bilayer have the $a^0a^0c^-$ rotation pattern. In Fig. [4.3b], we sketch the octahedral rotation pattern for SIO and LCO in the LCO/SIO bilayer.

In Fig. [4.4a], we show the cross sectional TEM micrographs collected near the STO/SIO and SIO/LCO interfaces in a LCO/SIO bilayer grown on STO (001) substrate. Generally, the intensity is proportional to Z^2t , where Z is the atomic number and t is the thickness of the investigated lamella. Thus for a fixed t , the intensity directly depends on Z^2 . The cations are indicated with different colors, see legend Fig. [4.4a]. The TEM shows atomically sharp

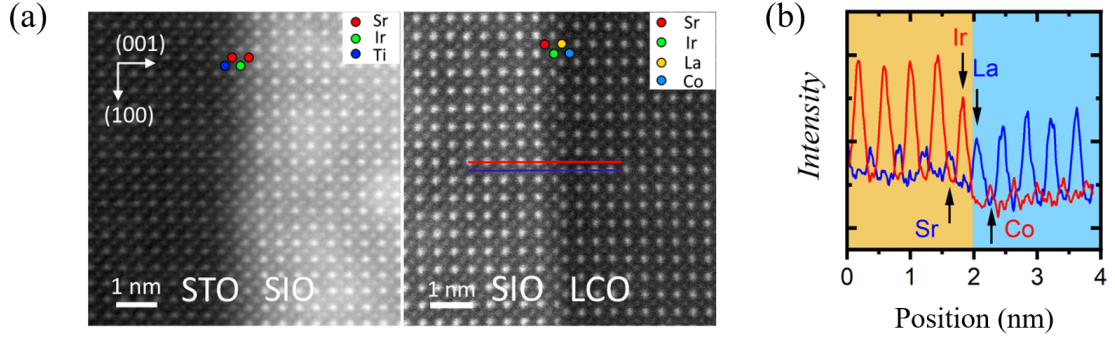


Figure 4.4: (a) Cross-sectional TEM micrographs showing the STO/SIO (left) and SIO/LCO (right) interfacial region in a LCO/SIO bilayer. Elements are indicated by color, see legend; (b) The elemental STEM line scans (indicated by red and blue lines in (a)) across the LCO/SIO interface. The intensity peaks corresponding to cations are indicated with the arrows.

and distinct STO/SIO and SIO/LCO interfaces with interdiffusion exceeding not more than one ML. The sample shows nearly stoichiometric composition without presence of any visible structural defects. The elemental line scans across the SIO/LCO interface measured with scanning-TEM (STEM) is also shown in Fig. [4.4b]. The atomic intensity peaks from different cations (Sr, Ir, La and Co) are shown and again verify the sharp LCO/SIO interface.

4.2 Electronic transport in $\text{LaCoO}_3/\text{SrIrO}_3$ HSs

In this section, we discuss the electronic transport in the SIO, LCO and LCO/SIO samples in detail. The samples were micro-patterned using photolithography and Ar-ion etching as discussed in Chapter 3. The electrical connections between the sample holder pads and HSs were realized by ultrasonic wire bonder using aluminium wire (diameter $20 \mu\text{m}$). Samples were kept at low temperatures ($< 10 \text{ K}$) for at least 12 hours to stabilize and avoid any photo-induced phenomenon. An alternating current ($I_{AC} \approx 1 - 100 \mu\text{A}$, 2 Hz) was used for the measurements. From now onward, thicknesses of the individual layers will be given in brackets and in units of monolayers ($1 \text{ ML} \approx 3.9\text{-}4.0 \text{ \AA}$).

4.2.1 Longitudinal resistivity

The temperature dependence of the longitudinal resistivity (ρ_{xx} vs T) of a single SIO(10) and LCO(10) as well as for a LCO(10)/SIO(10) HS is shown in Fig. [4.5a]. Beside these, we also measured LCO(10)/STO(4)/SIO(10) trilayer HS where a 4-ML thin insulating STO insertion layer was used intentionally to suppress any interfacial exchange between LCO and SIO.

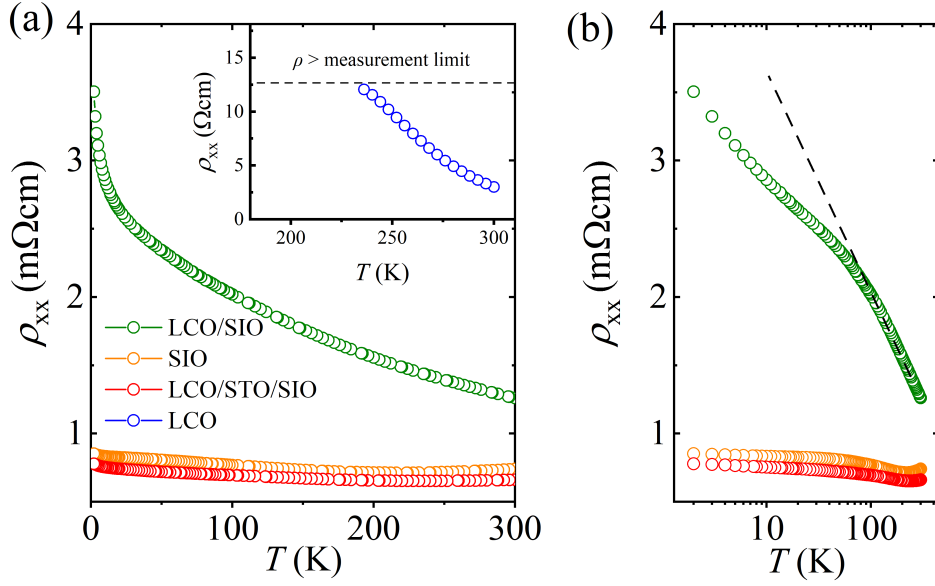


Figure 4.5: (a) Resistivity vs temperature, $\rho_{xx}(T)$ of SIO(10) single layer, LCO(10)/SIO(10) bilayer and LCO(10)/STO(4)/SIO(10) trilayer. In inset, the $\rho_{xx}(T)$ of LCO(10) is shown, (b) The $\rho_{xx}(T)$ of LCO(10)/SIO(10) bilayer on log- T scale, the dash line is the extrapolation of linear log- T behavior of $\rho_{xx}(T) \geq 100$ K.

LCO(10) single layer shows highly resistive behavior and $\rho_{xx}(T)$ was too high to be measured below 230 K, see inset of Fig. [4.5a]. The SIO(10) single and LCO(10)/STO(4)/SIO(10) trilayer HSs show nearly comparable semi-metallic behavior where $\rho_{xx}(T)$ first decreases with decreasing temperature, takes a minima around 200 K and then increases with decreasing temperature. This is well consistent with the previous reports on SIO single layers [75,90,91] and also documents that the electronic transport property of the trilayer is determined by the SIO and is not affected by the LCO.

In stark contrast to the SIO and LCO/STO/SIO, the LCO(10)/SIO(10) bilayer shows very different $\rho_{xx}(T)$ behaviour. The $\rho_{xx}(T)$ is increased (2-4 times larger compared to SIO and LCO/STO/SIO) and appears close to the metal-insulator transition (MIT). For single layer SIO (≤ 4 ML) films, a MIT has been previously reported [76] where gap opening at the Fermi level due to the tetragonal distortion was discussed as the main reason. However, in our case, as the thickness of SIO layer is same in SIO, LCO/SIO and LCO/STO/SIO HSs, the MIT behavior in LCO/SIO must be related to the interfacial exchange between the LCO and SIO layers and can be attributed to an the interfacial electron transfer (ICT) from SIO to LCO. This will be discussed later in detail when we provide experimental evidences for the ICT scenario.

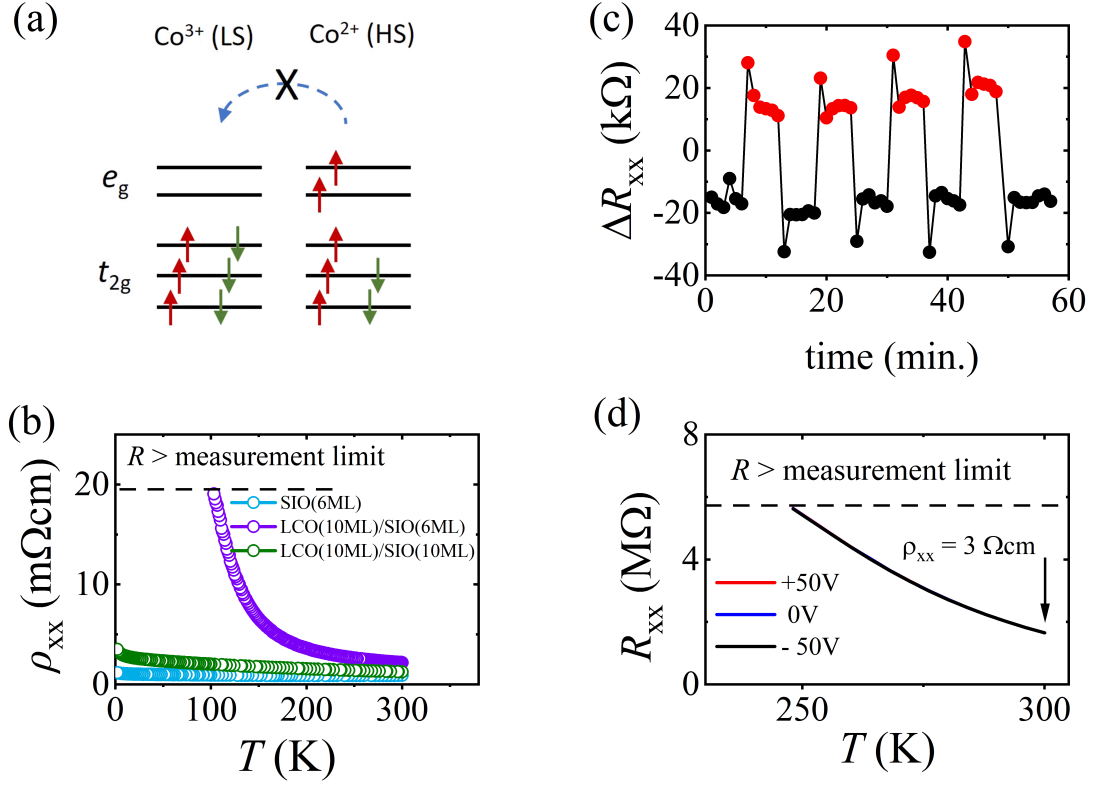


Figure 4.6: (a) Spin blockade phenomenon between Co^{3+} LS and Co^{2+} HS, (b) $\rho_{xx}(T)$ for SIO(6) and LCO(10)/SIO(6) HSs in comparison to LCO(10)/SIO(10) HS, (c) Electrostatic gating of LCO(10), switching behavior of R_{xx} as a function of time, (d) R_{xx} vs T of LCO(10) at different gate voltage V_g .

In Fig. [4.5b], we show the logarithmic temperature dependence of resistivity (ρ_{xx} vs $\ln(T)$) for LCO/SIO bilayer. The $\rho_{xx}(T)$ displays nearly linear $\ln(T)$ -dependence for $T > 100$ K. Below 100 K, $\rho_{xx}(T)$ is strongly reduced and hints towards a change of scattering rate in SIO. This could be related to reduced spin-flip scattering due to, *e.g.*, proximity induced spin-polarization in SIO by the neighboring LCO layer (strained LCO displays FM insulator behavior below $T \approx 85$ K).

Now, the question arises whether the electron transfer to LCO could induce measurable conductivity in LCO or not. LCO is a non-magnetic insulator in bulk form; however, it shows ferromagnetism with $T_c \approx 85$ K when grown as a tensile strained thin film. Ferromagnetism arises from the spin-state transition, where the tensile strain stabilizes the Co^{3+} HS state. The related exchange mechanism can be explained as super exchange between the Co^{3+} LS and Co^{3+} HS states. The hole-doping of LCO (*e.g.* $\text{La}_{0.7}\text{Sr}_{0.3}\text{CoO}_3$) results in the formation of Co^{4+} HS. This, in turn, favors the double exchange between Co^{4+} HS and Co^{3+} HS and a ferromagnetic metallic ground state with increased $T_c \approx 195$ K [59]. On the other

hand, the electron doping (*e.g.* La_{0.7}Ce_{0.3}CoO₃) promotes the Co²⁺ HS state. However, this results in the insulating state with strongly reduced ferromagnetic $T_c \approx 23$ K. Spin-blockade phenomenon, (see Fig. [4.6a]) commonly observed in other cobaltites, leads to the localization of the t_{2g} and e_g electrons and explains the insulating nature of La_{0.7}Ce_{0.3}CoO₃ [59]. In the following, we provide further experimental observations to exclude the contribution of LCO in the electronic transport of LCO/SIO HSs.

(i) In the Fig. [4.6b], we compare the ρ_{xx} of a SIO(6) film and a LCO(10)/SIO(6) bilayer in comparison to LCO(10)/SIO(10) bilayer. As expected from the proximity of SIO to a MIT (SIO usually becomes insulating for thicknesses of 4ML or less [76]), the ρ_{xx} of SIO(6) is increased with respect to that of the SIO(10), Fig. [4.5]. Therefore, it can be expected that a further depletion of the electron carriers in SIO by LCO (as in LCO/SIO bilayers) will shift the MIT to higher SIO thickness. In comparison to LCO(10)/SIO(10), the ρ_{xx} of LCO(10)/SIO(6) shows increased resistivity and becomes completely insulating below 100 K. If the electron transfer would yield any conductivity in the insulating LCO layer, the LCO(10)/SIO(6) bilayer would at least remain conductive, as the electron transfer to LCO can be assumed to be the same in both samples. Thus, the electron transfer from SIO to LCO reduces the conductivity of SIO but does not induce measurable conductivity in LCO.

(ii) We investigated the doping induced changes of the resistivity of LCO(10) single layer by electrostatic gating experiments exploiting STO as dielectric media and LCO as one of the conducting plate in parallel plate capacitor geometry. In Fig. [3.7b], device layout is shown. The external gate voltage V_g was applied between gate electrode (G) and source (S) and R_{xx} , R_{xy} was measured simultaneously at different V_g . In Fig. [4.6c], we show the relative change of R_{xx} , *i.e.*, $\Delta R/R$ as a function of V_g at $T = 300$ K. $\Delta R/R$ shows positive V_g field dependence, *i.e.*, R_{xx} increases with increasing V_g (> 0 V). This hints towards the hole dominated electronic transport behavior. Next, we show the R_{xx} versus T at different V_g , see Fig. [4.6d]. R_{xx} increases strongly with decreasing T and reaches the limit of measurement below 250 K for different V_g . Thus, for light hole or electron doping expected from the electrostatic gating, we could not observe any induced conductivity in LCO below 250 K. We also measured the Hall Resistance R_{xy} of LCO at 300 K for different V_g . R_{xy} does not show any V_g -dependence. However, the positive field dependence again supports the hole dominant transport as observed earlier.

Therefore, we can rule out the possibility of LCO being conducting below 100 K after light electron doping expected from the electron transfer from SIO to LCO in LCO/SIO

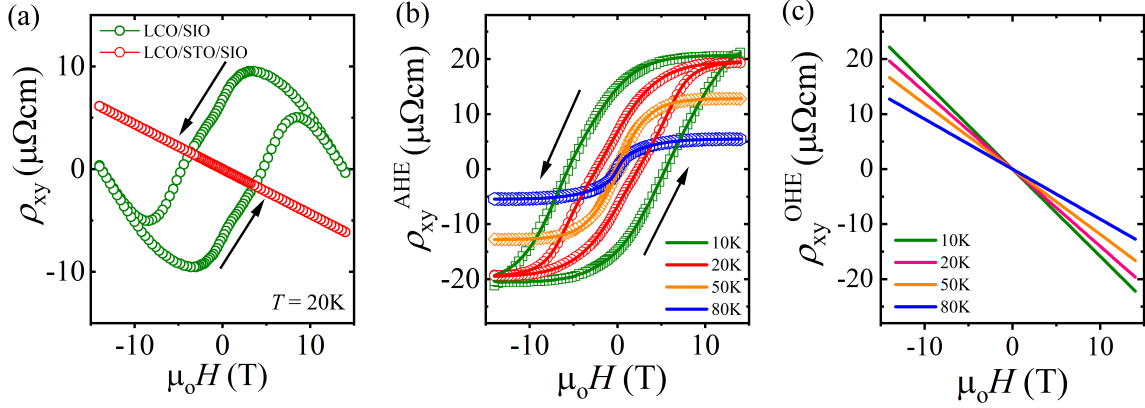


Figure 4.7: Anomalous Hall effect in LCO(10)/SIO(10) bilayer: (a) Hall resistivity $\rho_{xy}(\mu_oH)$ of LCO(10)/SIO(10) and LCO(10)/STO(4)/SIO(10) at $T = 20$ K, (b) anomalous Hall resistivity $\rho_{xy}^{AHE}(\mu_oH)$ and (c) ordinary Hall resistivity $\rho_{xy}^{OHE}(\mu_oH)$ of LCO(10)/SIO(10) as a function of T . The field sweep directions are indicated with the arrows.

bilayer and electronic transport in LCO/SIO bilayer strictly belongs to SIO only.

4.2.2 Transversal (Hall) resistivity

As shown in the last section, the SIO single- and LCO/STO/SIO trilayer HSs show nearly similar $\rho_{xx}(T)$ behavior, in stark contrast to the LCO/SIO bilayer; from now onward, we will focus on the bilayer and trilayer HSs only, where LCO and SIO are in direct contact with each other or not.

In Fig. [4.7a], we show the transverse resistivity $\rho_{xy}(\mu_oH)$ of the LCO(10)/SIO(10) bilayer and LCO(10)/STO(4)/SIO(10) trilayer HSs, measured in six-point contact geometry on Hall bars at $T = 20$ K. The trilayer LCO/STO/SIO HS shows linear field dependence within the applied field range. The behavior is well consistent with the single-carrier type ordinary Hall effect ($\rho_{xy}^{OHE} = R^o \times \mu_oH$, R^o is the Hall constant). The negative slope of the $\rho_{xy}(\mu_oH)$ documents the electrons as dominant charge carriers, well consistent with earlier reports on SIO thin films [90]. The Fermi surface of semi-metallic SIO consists of multiple light electron and heavy hole bands [94]. The quasi-particle mass of the electrons are 2-6 times lighter than the holes and explains the dominant electron-like behavior commonly observed in electronic transport [94]. In contrast, $\rho_{xy}(\mu_oH)$ of bilayer HS is dominated by an additional contribution that shows hysteretic field dependence. This additional contribution, known as anomalous Hall resistivity ($\rho_{xy}^{AHE}(\mu_oH)$), is commonly observed in ferromagnetic, metallic systems with SOC. Usually, ρ_{xy}^{AHE} is indicative of the ferromagnetic ordering and can be expressed as: $\rho_{xy}^{AHE} = R^A \times M_z$, where R^A is material specific parameter depending on

the longitudinal conductivity (σ_{xx}) and M_z is the perpendicular component of magnetization. As already shown, the strained LCO films display FMI behavior and do not contribute to conductivity, the observed ρ_{xy}^{AHE} must be related to the interfacial SIO layers.

The origin of ρ_{xy}^{AHE} can be very different in nature. Classically, AHE was explained to originate from the internal magnetization ($\rho_{xy}^{AHE} \propto M_z$). However, later it was redefined as a pure quantum mechanical phenomenon and was discussed in terms of the Berry curvature and Berry connection (equivalent magnetic field in reciprocal space) [125]. The strong SOC and time-reversal symmetry breaking are two important parameters deciding the strength of Berry curvature. As magnetism breaks the time reversal symmetry, ferromagnetic metals with strong SOC often show AHE alike.

At higher fields, ρ_{xy}^{AHE} displays saturation and ρ_{xy} shows linear field dependence. Thus, one can obtain the ρ_{xy}^{AHE} by subtracting the linear part (ρ_{xy}^{OHE}) at higher fields from ρ_{xy} :

$$\begin{aligned} \rho_{xy} &= \rho_{xy}^{OHE} + \rho_{xy}^{AHE}, \\ \Rightarrow \rho_{xy}^{AHE} &= \rho_{xy} - R^o \times \mu_o H. \end{aligned} \quad (4.1)$$

In Fig. [4.7b,c], we show the $\rho_{xy}^{AHE}(\mu_o H)$ and $\rho_{xy}^{OHE}(\mu_o H)$ of the LCO(10)/SIO(10) bilayer at different T . The field sweep directions are indicated with the arrows. The ρ_{xy}^{AHE} show clear hysteretic field dependence, which resembles the magnetization of typical ferromagnets. Both the saturation resistivity $\rho_{xy}^{AHE,s}$ (ρ_{xy}^{AHE} at 14 T) and coercive field H_c of ρ_{xy}^{AHE} show strong T -dependence and decrease with increasing T . ρ_{xy}^{AHE} is positive throughout the measured T -range.

Similar to the hysteretic magnetization behavior of a ferromagnet, we can fit the ρ_{xy}^{AHE} using a step-function as:

$$\rho_{xy}^{AHE} = R^A \times \tanh(\omega(H - H_c)), \quad (4.2)$$

where R^A , H_c and ω are saturation value, coercive field and slope of the hysteresis at H_c respectively. Fits to the data are shown in the Fig. [4.7b] with the solid lines (fitting parameter are give in Table [6.1]). A nearly perfect fit to the data were obtained using the above model which covers all important features observed in the measurements. Note that H_c becomes too large for $T < 20$ K and even 14 T magnetic field was not sufficient to saturate the ρ_{xy}^{AHE} .

Depending on the scattering mechanism, the AHE can be further subdivided into two categories: (i) intrinsic, and (ii) extrinsic AHE. Intrinsic AHE originates from the topological

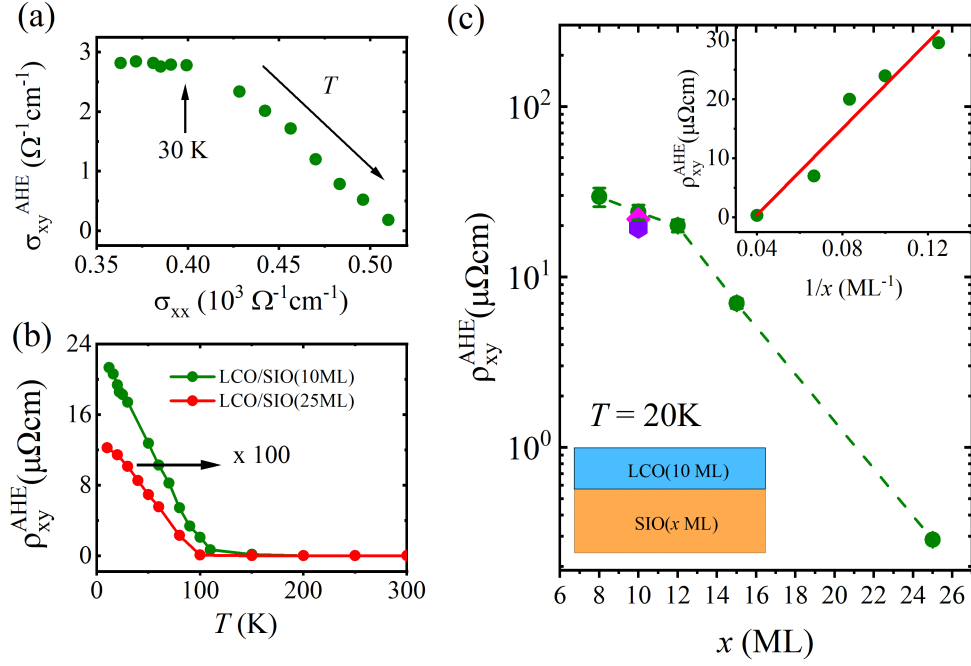


Figure 4.8: (a) Intrinsic AHE in LCO(10)/SIO(10): scaling of $\sigma_{xy}^{AHE,s}$ on σ_{xx} , nearly independent $\sigma_{xy}^{AHE,s}$ behavior for ≤ 30 K suggests intrinsic AHE in SIO, (b) The $\rho_{xy}^{AHE,s}$ vs T for LCO(10)/SIO(10) and LCO(10)/SIO(25) bilayers, (c) The $\rho_{xy}^{AHE,s}$ for a set of LCO(10)/SIO(x) bilayers. In inset, $\rho_{xy}^{AHE,s}$ is shown on $1/x$ scale demonstrating a nearly linear inverse thickness dependence.

band properties of the electronic band structure whereas the extrinsic AHE originates from the skew- or side jump scatterings [125]. A distinction among the different origins can be made by scaling the longitudinal conductivity (σ_{xx}) and transverse anomalous conductivity ($\sigma_{xy}^{AHE,s}$), which can be deduced from the resistivities, ρ_{xx} and ρ_{xy}^{AHE} as follows:

$$\sigma_{xx} = \frac{\rho_{xx}^2}{\rho_{xx}^2 + \rho_{xy}^{AHE,s}{}^2} \quad \text{and} \quad \sigma_{xy}^{AHE,s} = \frac{\rho_{xy}^{AHE,s}{}^2}{\rho_{xx}^2 + \rho_{xy}^{AHE,s}{}^2}. \quad (4.3)$$

In our LCO/SIO bilayer, SIO belongs to the moderately dirty metal group owing to the rather low $\sigma_{xx} \approx 500 \Omega^{-1} \text{cm}^{-1}$ (at $T = 80$ K). In this limit, the AHE does not depend on the transport lifetime and the scattering mechanism of the charge carriers, *i.e.*, $\sigma_{xy}^{AHE,s} \neq f(\sigma_{xx}^o)$. This is shown in Fig. [4.8a]. For $T \leq 30$ K, $\sigma_{xy}^{AHE,s}$ is independent on σ_{xx} ($\sigma_{xy}^{AHE,s} \propto \sigma_{xx}^o$) and results in a dissipation-less anomalous transverse current in the SIO [125]. The anomalous Hall angle ($\theta^{AHE} = \sigma_{xy}^{AHE,s} / \sigma_{xx}$) refers to the deflection of spin-up and spin-down electrons from the current direction. In LCO(10)/SIO(10) bilayer, the maximum of θ^{AHE} amounts to

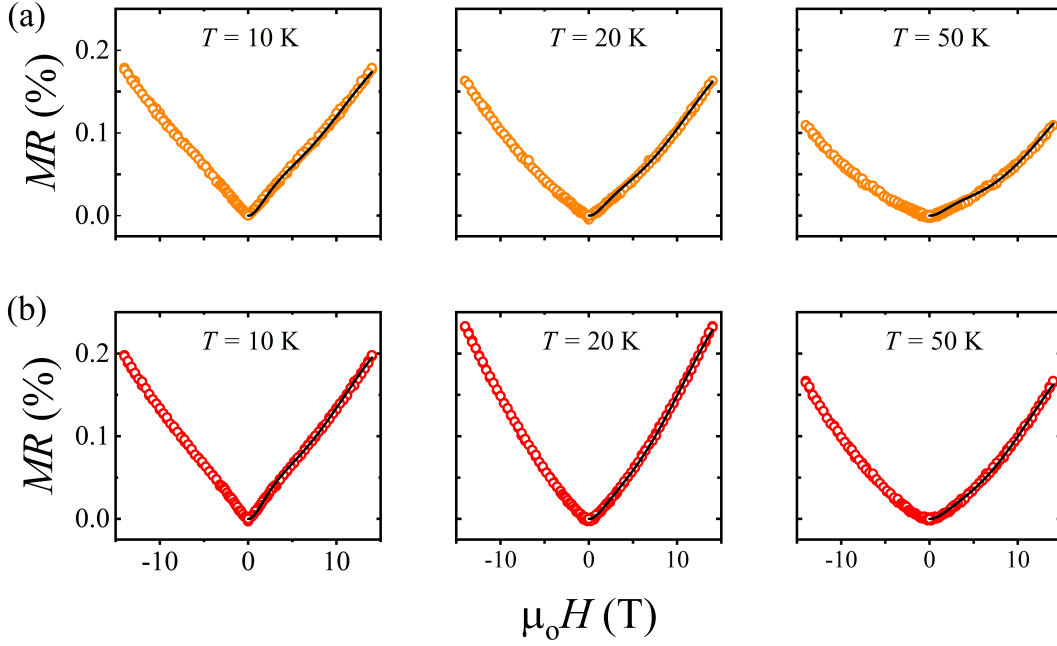


Figure 4.9: Magnetoresistance (MR) of (a) SIO(10) single layer and (b) LCO(10)/STO(4)/SIO(10) trilayer HSs at different T . Open symbols are the measured data and black solid lines are fits to the data including Kohler and Maekawa-Fukuyama terms accounting for the classical Lorentz and weak-antilocalization contribution respectively.

0.8 % (in some samples up to 1.2 %) and is comparable to that of other iridates and heavy metals with strong SOC and an order of magnitude larger than that of $3d$ metal oxides, *e.g.*, Co_xTi_{1-x}O_{2-δ} [139], La_{1-x}Sr_xMnO₃ [102].

In Fig. [4.8b], we show the $\rho_{xy}^{AHE, s}(T)$ for the two LCO/SIO bilayers with SIO thickness 10 ML and 25 ML. For LCO(10)/SIO(10), $\rho_{xy}^{AHE, s}$ decreases strongly with increasing T and is completely suppressed for $T \geq 100$ K, close to the ferromagnetic transition of the tensile strained LCO on STO ($T_c \approx 85$ K). Furthermore, the LCO(10)/SIO(25ML) shows a much weaker $\rho_{xy}^{AHE, s}$, albeit the same T -dependence. The nearly linear correlation of $\rho_{xy}^{AHE, s}$ versus the inverse SIO thickness (x) clearly demonstrates an interfacial, *i.e.*, proximity effects in SIO, see Fig. [4.8c]. The figure shows $\rho_{xy}^{AHE, s}$ for a set of LCO(10)/SIO(x) HSs with different SIO thickness (x) at 20 K. In inset, we show the $\rho_{xy}^{AHE, s}$ versus $1/x$, where a nearly linear dependence was observed.

4.2.3 Magnetoresistance

In the following, we discuss the normal magnetoresistance (MR) (defined as: $\text{MR} (\%) = [(\rho_{xx}(\mu_0 H) - \rho_{xx}(0))/\rho_{xx}(0)] \times 100 (\%)$) properties of the HSs with magnetic field ($\mu_0 H$)

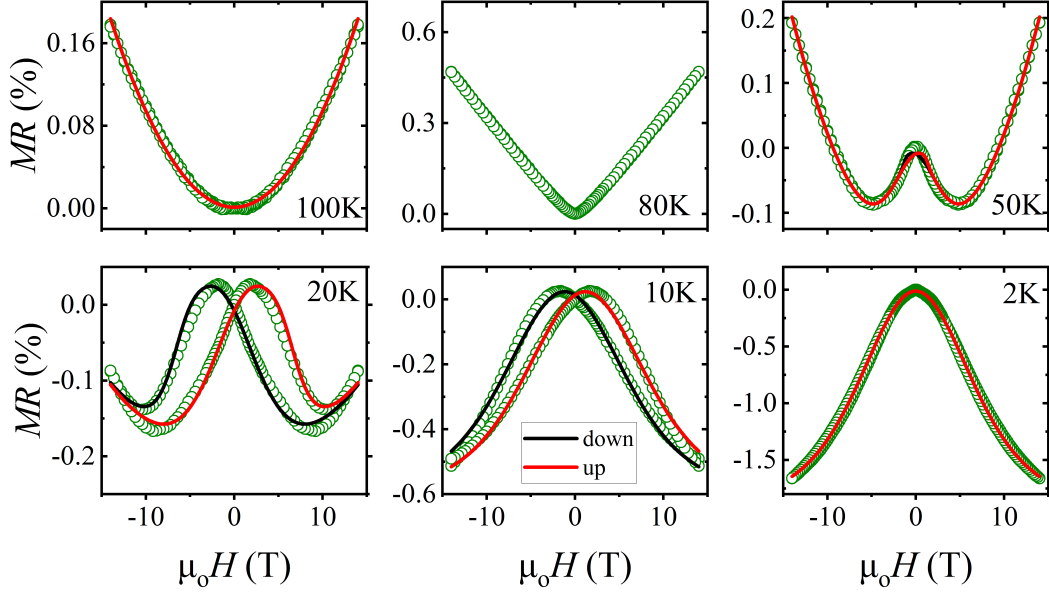


Figure 4.10: Magnetoresistance (MR) of LCO(10)/SIO(10) bilayer at different T . Open symbols are the measured data and black/red solid lines are fits to the data including the positive, classical Lorentz and negative contribution. Field sweep directions (down and up) are shown with black and red lines respectively.

applied normal to the film surface. First, we start with the discussion of MR for SIO(10ML) single layer and LCO(10ML)/STO(4ML)/SIO(10ML) trilayer. Similar to ρ_{xx} vs T , the two HSs display qualitatively similar and positive MR behavior, see Fig. [4.9]. At 50 K, MR displays quadratic field dependence that can be well described by the classical Lorentz scattering (LS) [140]. However for $T \leq 20$ K, an additional cusp like contribution to MR is visible. This additional contribution is dominant at lower fields and can be well described by weak-antilocalization (WAL). This has been already reported in the SIO thin films [98, 141]. Hence, the MR can be fitted using the two contributions, *i.e.*, Kohler term ($\propto H^2$) for LS [140] and the Maekawa-Fukuyama term accounting for WAL including the SOC and Zeeman terms [122].

Next, we discuss the MR properties of the LCO(10ML)/SIO(10ML) bilayer where LCO and SIO are in direct contact to each other, see Fig. [4.10]. For $T \geq 100$ K, MR display pure positive and quadratic field dependence behavior which again can be understood by the LS ($\propto H^2$). With decreasing temperatures, an additional negative contribution to MR (NMR) evolve and show complete crossover from a monotonic positive MR for $T \geq 100$ K to a dominant NMR for $T \leq 20$ K. At $T = 80$ K, in the crossover regime, MR displays enhanced quasi positive linear MR [142] which might be related to the electronic disorder

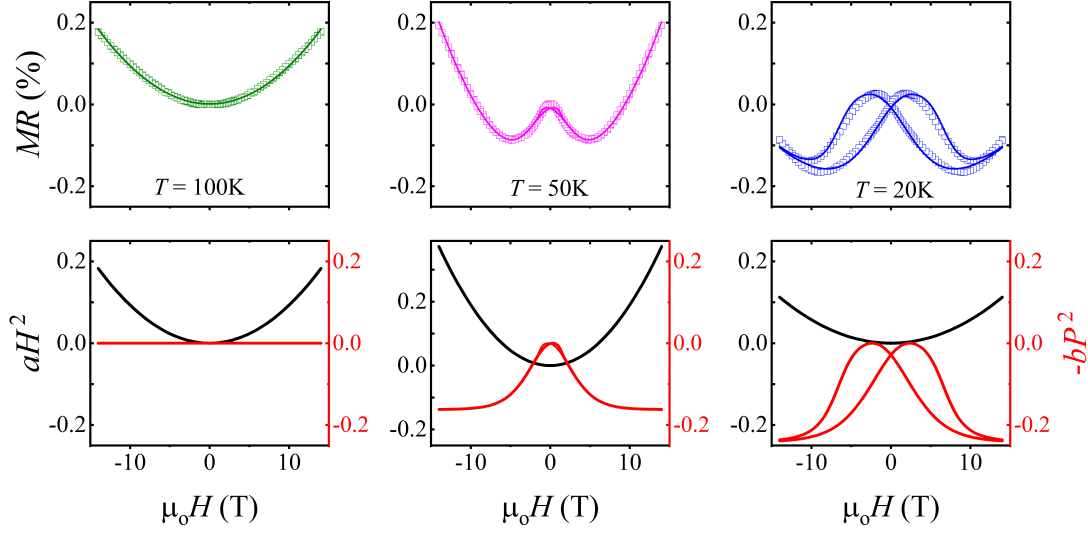


Figure 4.11: MR (upper panel) and positive & negative contributions to MR *i.e.* $PMR \propto H^2$ and $NMR \propto P^2$ (lower panel) for LCO(10)/SIO(10) bilayer are shown at $T = 100, 50$ and 20 K. The measured data points and fits to the data are shown with open symbols and solid lines respectively. The black (red) solid line represents the positive (negative) MR contributions respectively.

originating from the spin-fluctuations when approaching magnetic order or spin-polarized state [143]. For $T < 50$ K, the NMR becomes hysteretic. The field dependence and coercive field of NMR is very similar to that of ρ_{xy}^{AHE} . Similar to ρ_{xy}^{AHE} , the coercive field of the NMR is very large for $T \leq 10$ K so that even the maximum available field 14 T is not sufficient to saturate the hysteresis. The coupled behavior of NMR, ρ_{xy}^{AHE} and the suppression of ρ_{xx} for $T < 100$ K strongly suggest proximity-induced spin-polarized state in SIO. The magnetic order effectively suppresses the spin-flip scattering (SFS) and results in the appearance of NMR below the order temperature [144]. Similar to ρ_{xy}^{AHE} , a step-function can be used to model NMR as: $NMR = bP^2$ with $P = \tanh(\omega(H - H_c))$.

Thus, the total MR is well described by considering contributions from LS and SFS as: $MR = (aH^2 - bP^2)$, where a and b are proportionality constants, see Table [6.2] for fitting parameters. We can not rule out the presence of other minor contributions to MR, but as the classical LS and NMR are dominant here, this will not affect the main conclusion. In Fig. [4.11], we show the fits to the MR and the positive and negative contributions to MR separately. The positive contribution, which is quadratic in H , is shown with the solid black line while the NMR is shown with the solid red lines. At $T = 100$ K, the NMR is positive and the negative term is absent. With decreasing T , the NMR term increases and becomes dominant for $T \leq 30$ K.

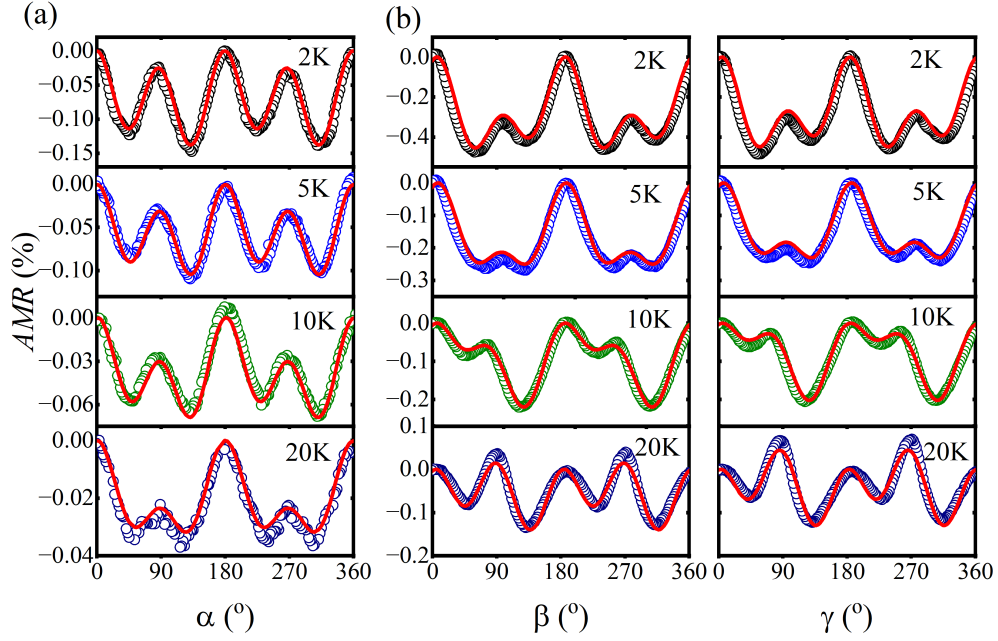


Figure 4.12: Anisotropic magnetoresistance $AMR(\varphi)$ for (a) $\varphi = \alpha$, (b) $\varphi = \beta$, and γ of LCO/SIO bilayer at different T (symbols). Data are well described by $AMR(\varphi) = c_0 + c_2 \times \cos 2(\varphi + \omega_2) + c_4 \times \cos 4(\varphi + \omega_4)$, see fits to the data (solid lines).

As shown above, SIO in the single and trilayer HSs do not show NMR. Even in bilayer HSs, the effects strongly get suppressed with increasing SIO thickness. Thus, the NMR of SIO in LCO/SIO bilayers are related to the proximity induced interfacial effects.

Recently, a proximity induced interfacial magnetism and AHE was observed in manganite/SIO HSs and SLs [35, 102]. The effects were explained as a consequence of charge transfer from SIO to manganite layer which provides the interfacial coupling via the formation of molecular orbitals at the interface [145]. A similar mechanism can also explain the observed interfacial magnetism in SIO in LCO/SIO HSs. An interfacial charge transfer (ICT) at LCO/SIO interface is expected where the $Co3d-O2p-Ir5d$ band alignment at the interface drives the electron from SIO to LCO [68]. We indeed observed ICT from SIO to LCO in LCO/SIO HSs (shown later). The ICT may provide a interfacial coupling between LCO and SIO. In addition, hole doping of SIO may also favor long range magnetic ordering as proposed by the Nagaoka physics [146, 147].

Beside normal MR, anisotropic MR (*i.e.* AMR) also gives useful insights on the magnetic properties of thin films. A detailed analysis of AMR in LCO/SIO bilayer was obtained by angle-dependent measurements: $AMR(\varphi) = [(\rho_{xx}(\varphi) - \rho_{xx}(0))/\rho_{xx}(0)]$, where φ ($\varphi = \alpha, \beta$, and γ) is the angle between magnetic field- and current-direction, see Fig. [3.13].

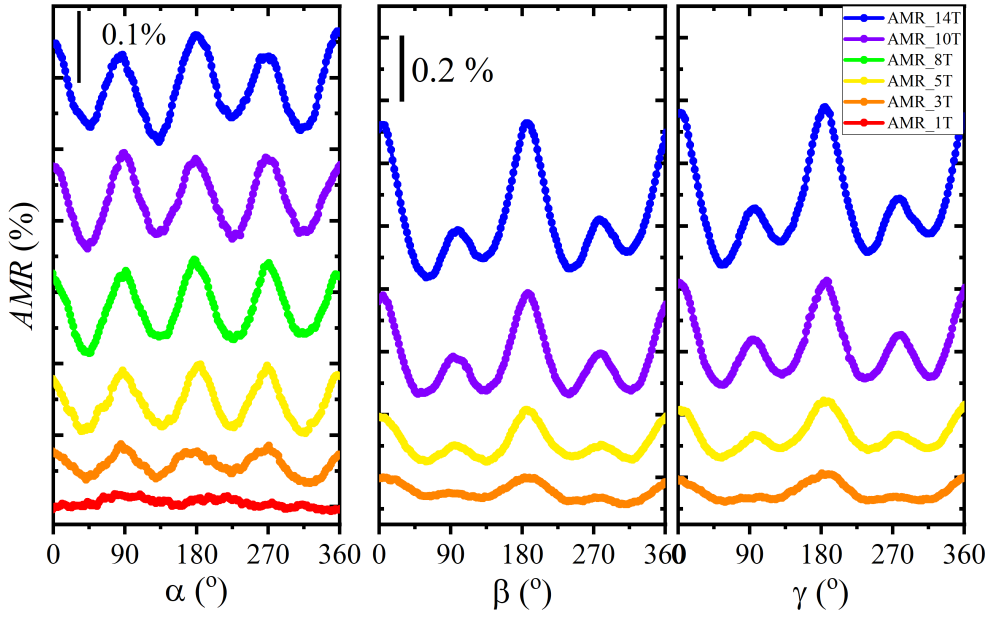


Figure 4.13: Anisotropic magnetoresistance $AMR(\varphi)$ for $\varphi = \alpha$, $\varphi = \beta$, and γ of LCO/SIO bilayer at $T = 2$ K for various field strength $\mu_o H$. Data are vertically shifted for clear visualization.

Generally, $AMR(\varphi)$ is very weak (nearly zero) for $T \geq 90$ K.

In magnetic materials, AMR is usually caused by spin-flip and exchange scattering between s - and d -electrons, *i.e.*, s - d scattering (sdS) [131] and depends only on the relative angle between the direction of the current and the magnetization and therefore provides a powerful tool to probe magnetization in metallic samples. The sdS in an isotropic magnetic material results in a two-fold symmetry of the AMR proportional to $\cos(2\varphi)$ ($\varphi = \alpha$ and γ), where maxima appears at 0° , 180° for $\varphi = \alpha$, and at 90° , 270° for $\varphi = \gamma$. In heterostructures comprising magnetic insulating layers and metallic layers displaying strong SOC, as in LCO/SIO, the spin-Hall magnetoresistance (SMR) may be active as well [132]. Similar to the sdS-dominated conventional AMR, the SMR shows a two-fold symmetry alike for $\varphi = \alpha$, β with maxima at 0° and 180° [133]. In addition, SMR ($\approx 10^{-4}$) is usually about one order of magnitude smaller than conventional AMR ($\approx 10^{-3}$).

In Fig. [4.12a], $AMR(\alpha)$ is shown for $2 \text{ K} \leq T \leq 20 \text{ K}$. Generally, $AMR(\alpha)$ increases with increasing field, see Fig. [4.13], so we concentrate in the following on measurements at $\mu_o H = 14 \text{ T}$. The $AMR(\alpha)$ displays a two-fold and a four-fold symmetric contribution. Data are well described by $AMR(\alpha) = c_0 + c_2 \times \cos 2(\alpha + \omega_2) + c_4 \times \cos 4(\alpha + \omega_4)$. The offset angles ω_2 and ω_4 amount to about few degrees and are likely caused by backlash error of the sample rotator or magnetic coercivity of the sample. At 2 K, $AMR(\alpha)$ is dominated by

the four-fold symmetric contribution indicating strong magnetocrystalline anisotropy and does not depend on the current direction parallel or perpendicular to field. The four-fold symmetric contribution, *i.e.*, c_4 decreases with increasing T and vanishes above 90 K. The two-fold contribution shows maxima for $\alpha = 0^\circ$ and 180° . The amplitude, c_2 , decreases with increasing T with a saddle point about at 40 K and disappears above 90 K as well.

AMR(β) and AMR(γ) are shown for $2 \text{ K} \leq T \leq 20 \text{ K}$ in Fig. [4.12b]. The β - and γ -dependence of the AMR is nearly the same and qualitatively similar to that of AMR(α). The two-fold symmetric contribution shows maxima at $\beta = \gamma = 0^\circ$ and 180° . The four-fold symmetric contribution is also present for AMR(β) and AMR(γ). In Fig. [4.13], AMR(φ) ($\varphi = \alpha, \beta, \text{ and } \gamma$) is shown as a function of field strength ($\mu_o H$) at $T = 2 \text{ K}$. AMR(φ) (*i.e.* the amplitudes c_2 and c_4) increases with increasing field.

Since AMR(φ) shows maxima at same α, β , and γ angle, dominant sdS and SMR can be ruled out. Electron scattering by magnetic domain walls (dwS) seems to be more plausible. When a magnetic field is applied along easy-axis direction, the dwS is effectively suppressed [148] resulting in minima of the AMR. In that context, the minima of the four-fold symmetric contribution at $\alpha = n \times 45^\circ$ ($n = 1 - 4$) indicate in-plane magnetic easy-axis along the (110) direction. Furthermore, as in the present case, $\text{AMR}(\beta) \approx \text{AMR}(\gamma) > \text{AMR}(\alpha)$ also indicates a magnetic proximity effect AMR which is different from the commonly observed normal AMR ($\text{AMR}(\alpha) \approx \text{AMR}(\gamma) > \text{AMR}(\beta)$) or SMR ($\text{AMR}(\alpha) \approx \text{AMR}(\beta) > \text{AMR}(\gamma)$) [132, 149].

Next, we compare the MR of LCO(10)/SIO(10) bilayer for out-of-plane and in-plane magnetic field. In Fig. [4.14a,b], we show the MR at 10 K with a magnetic field parallel ($H // n$) and perpendicular ($H \perp n$) to the surface normal (n). As shown before, for $H // n$, the MR is negative and shows large hysteretic behavior (also see Fig. [4.10]). In contrast, for $H \perp n$ the hysteresis is completely suppressed. The magnitude of the NMR (*i.e.* $|\text{NMR}|$) is nearly the same for $H // n$ and $H \perp n$, but the absence of hysteresis for in-plane field strongly suggests the easy axis of magnetization in the film-plane (ab -plane). A more careful experiment was done by changing the angle between H and current direction ($\alpha = 0/45/90^\circ$), [4.14b]. For $\alpha = 45^\circ$, a slightly larger $|\text{NMR}|$ was observed compared to $\alpha = 0^\circ$ or 90° . As the NMR is related to the magnetization in SIO, this demonstrates an in-plane (110) easy-axis. In Fig. [4.14c], we show again the AMR(α) and the extracted 2- and 4-fold components (c_2 & c_4) at 5 K and 14T. The c_4 component, which represents the magnetocrystalline anisotropy, shows minima for $\alpha = n \times 45^\circ$ ($n = 1 - 4$) and confirms a (110) easy-axis of magnetization.

Based on the ($a^0 a^0 c^-$) rotation pattern of IrO₆ octahedra and the observation of magnetic easy axis along (110) pseudocubic direction, we propose a magnetic structure of the induced

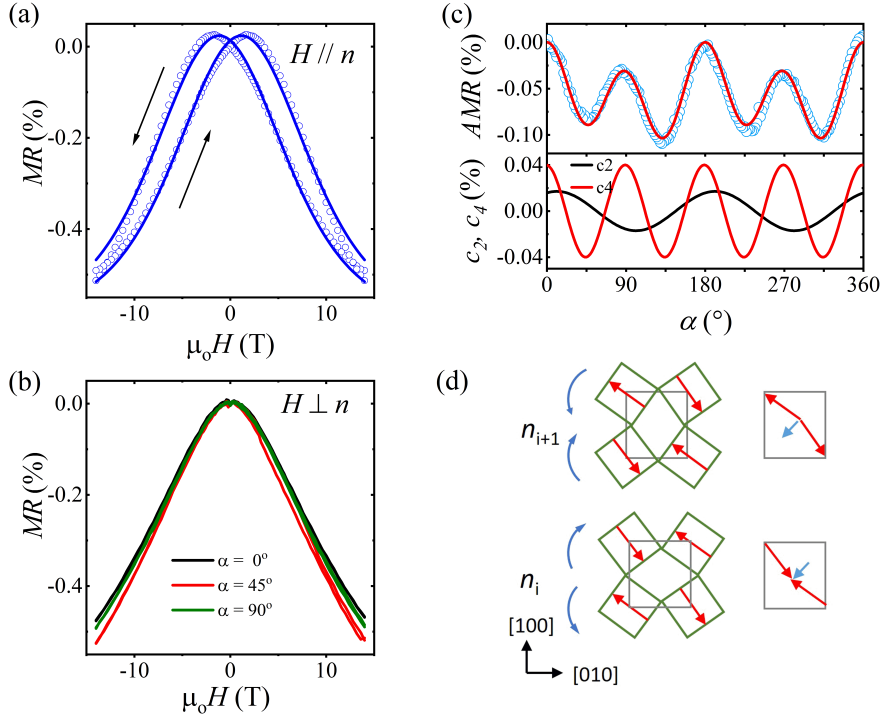


Figure 4.14: Magnetic anisotropy and structure in SIO: magnetoresistance (MR) with (a) $H // n$, (b) $H \perp n$ at 10 K and, (c) AMR at 5 K of LCO(10)/SIO(10) bilayer. (d) proposed magnetic structure in SIO considering the $a^0 a^0 c^-$ octahedral rotation pattern and (110) easy axis

magnetism in SIO, see Fig. [4.14d]. In Sr_2IrO_4 , a similar octahedral rotation pattern results in the canting of $J_{\text{eff}} = 1/2$ moments owing to the strong pseudospin-lattice coupling and consequently it shows weak ferromagnetism within the IrO_2 (*i.e.* ab) planes below $T_N = 240$ K. The net moments of different planes couple antiferromagnetically along the c -axis [150]. Similar to Sr_2IrO_4 , the Ir-pseudospins in SIO can be expected to be locked in the ab -plane of the octahedra. The out-of-phase rotation of neighbouring IrO_6 octahedra around (001)-direction favors a net moment within the ab -planes aligned along (110)-direction and parallel for neighbored layers n_i and n_{i+1} , *i.e.*, a ferromagnetic coupling along the c -axis. The strong pseudospin-lattice coupling in the ab -planes explains the large coercivity observed in the AHR and NMR, where magnetic field is applied perpendicular to the ab -plane.

4.2.4 Interfacial charge transfer:

(i) As SIO is a semi-metal and possess low charge carrier density (n) compared to normal metals, even small changes in n (*i.e.* Δn) can be easily visualized by the Hall effect measurements. Here, we calculated the n of SIO in two different samples, LCO/SIO bilayer and LCO/STO/SIO trilayer at $T = 150$ K, well above the critical temperature. Here again,

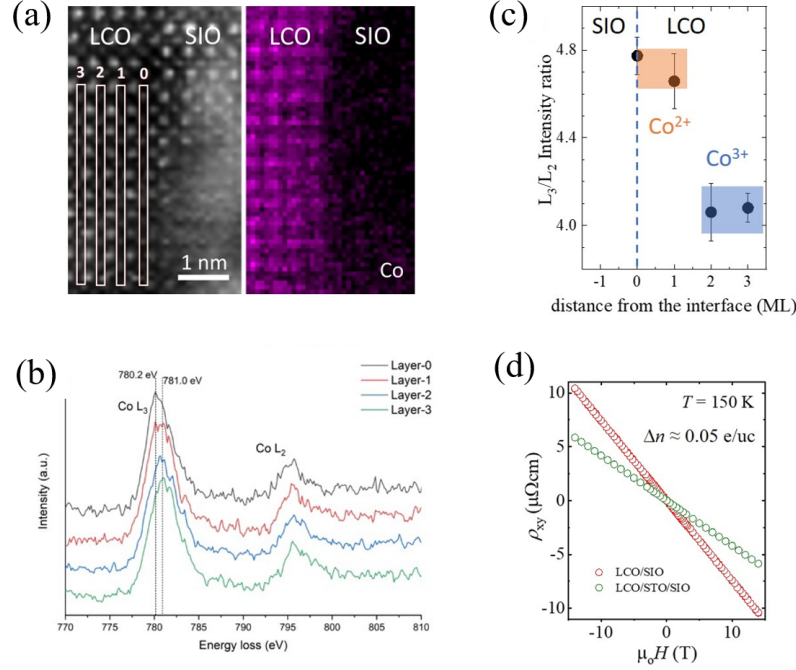


Figure 4.15: Interfacial charge transfer at LCO/SIO interface: (a) HAADF STEM image and Co map constructed from the integrated EELS L_3 , L_2 intensities near LCO/SIO interface region, (b) EELS spectra and (c) L_3/L_2 ratio for the four consecutive Co-layers at the interface labelled as 0, 1, 2 & 3, (d) ordinary Hall resistivity of the LCO(10)/SIO(10) bilayer at $T = 150$ K, well above the T_c .

we would like to recall that the LCO layer does not show any conductivity and the electric transport is exclusively related to SIO only. In Fig. [4.15d], we have shown ρ_{xy} versus $\mu_0 H$ for the two HSs. The linear field dependence with negative slope document the electron dominant transport behavior which is consistent with the earlier reports. However, the slope of the ρ_{xy} versus $\mu_0 H$ for the LCO/SIO bilayer is nearly half of that for the trilayer hinting towards the lower n in the bilayer. Calculations using a single band model result in $n \approx 1 \times 10^{21}$ and $\approx 1.9 \times 10^{21} / \text{cm}^3$ for the bi- and trilayer respectively. The difference Δn amounts to be around 9×10^{20} which is equivalent to 0.05 e/unit cell if we assume a uniform distribution throughout the 10 ML. The lower n of SIO clearly demonstrates the ICT from SIO to LCO in the bilayer. Considering, ICT is only restricted to the first SIO layer, a nominal valence state $\text{Ir}^{4.5}$ can be assumed for the SIO layer directly at the interface.

(ii) To verify the ICT at the LCO/SIO interface, the valence state of the Co, close to the interface was investigated by electron energy loss spectroscopy (EELS). In Fig. [4.15a], we show a high-angle annular dark-field (HAADF) STEM image (left) and the Co map constructed from the integration of L_3 and L_2 intensities (right) across the LCO/SIO interface.

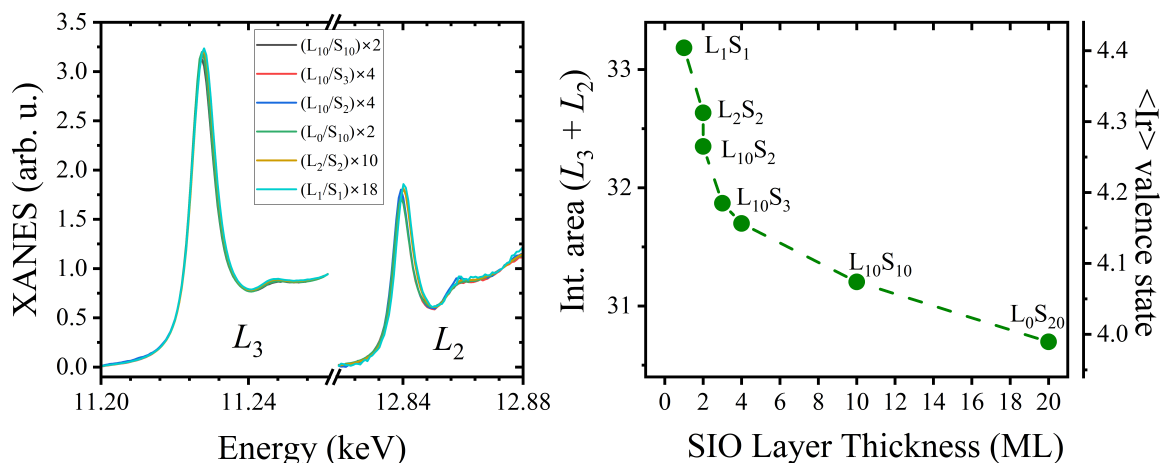


Figure 4.16: Interfacial charge transfer in LCO/SrIrO₃: (a) Ir L₃ and L₂ XAS spectra for a set of [LCO_m/SIO_n] x Z SLs at T = 20 K, (b) relative hole density (*i.e.* Ir-valence state) in [LCO_m/SIO_n] superlattices as a function of SIO layer thickness (*n*).

The Co map shows distinct Co atomic layers with sharp LCO/SrIrO₃ interface. The EELS spectra from these Co columns were integrated (see the area labeled as layer 0, 1, 2 & 3 in Fig. [4.15a]) and plotted as a function of Co layers, *i.e.*, distance from the LCO/SrIrO₃ interface, see Fig. [4.15b]. This allows the direct comparison of Co valence state locally in the interfacial region. The L₃- peak position shifts to higher energies as we go from interface (0) to deeper (1-3) Co- layers. For Co layer-0, the L₃ peak position is at 780.2 eV which shifts to 781.0 eV for Co layer-3. In general, a peak position shift to a higher(lower) energy side manifest a higher(lower) valence state of Co ion. Thus, the lower energy position shift by around 0.8 eV for L₃ peak for 0th layer indicates a lower valence state for the Co compared to deeper layers. A L₃ peak shift by 1.5 eV in Co₃O₄ compared to CoO has been previously reported [151]. The L₃/L₂ intensity ratio of different Co layers, which reflects the 3d occupancy of Co, is shown in Fig. [4.15c]. Clearly, for the layers directly at the interface, *i.e.*, 0th and 1st layers, the ratio is considerably high compared to the deeper 2nd and 3rd layers. The L₃/L₂ value for the first two layers adjacent to the interface compares well to the reported values for Co²⁺ state [151, 152]. Since changes of the valence state are restricted to the interfacial region, it is very likely caused by an electron transfer from the SIO layer. Oxygen vacancies may also lead to the formation of Co²⁺, which however, is expected to be homogeneous in such thin films.

Complementary EELS investigation of Ir valence state was not possible as the Ir L₃ or L₂ absorption edges are at much higher energies (11-12 keV) and are not accessible within the STEM-EELS setup.

For that reason, we studied the valence state of Ir in series of $[\text{LCO}_m/\text{SIO}_n] \times Z$ SLs by X-ray absorption spectroscopy (XAS) at 20 K. Here, m and n are the thickness of LCO and SIO layers in units of ML and Z is the repetition number in the SLs. The measurements were performed at the hard X-ray XAS XMCD beamline ID 12 of European Synchrotron Radiation Facility (ESRF) in Grenoble, France. In Fig. [4.16a], we show the Ir L_3 and L_2 edge XAS spectra. A clear shift in the L_2 , L_3 peak position and an increase of integrated peak area was observed with decreasing n . In the Fig. [4.16b], we show the integrated peak area of L_3 and L_2 (left axis) for different SLs as a function of n . The integrated peak area under L_3 and L_2 are generally proportional to the hole density. This obviously hints towards an increased valence state of Ir in SIO with decreasing n . If we assume a 4+ valence state of Ir (Ir^{4+}) in $[\text{LCO}_0/\text{SIO}_{10}] \times 2$ (or $\text{SIO}(20)$) SL, the relative change in the valence state can be estimated, see [4.16b] (right axis). For $[\text{LCO}_1/\text{SIO}_1] \times 18$ SL, a Ir valence state of ~ 4.45 was observed which corresponds to the 0.45 electron transfer from SIO to LCO and is well consistent with the Hall experiments discussed before.

The experimental findings, including transport and spectroscopy, confirm the accumulation and depletion of n in the LCO and SIO layer, respectively and establish the ICT in the LCO/SIO HSs and SLs. As already mentioned, ICT plays a very crucial role in the observation of proximity induced-magnetism in SIO and seems to provide the essential electronic coupling between LCO and SIO.

4.3 Magnetic properties of $\text{LaCoO}_3/\text{SrIrO}_3$ HSs

4.3.1 Magnetization measurement

In Fig. [4.17a], we show the field cooled magnetization measurement, *i.e.*, magnetic moment $m^*(= m(T) - m(300\text{K}))$ vs. T for the STO substrate, LCO(10), SIO(10) single layers and LCO(10)/SIO(10) bilayer. Measurements were recorded with an applied in-plane magnetic field of 100 Oe along the (100) direction of the STO substrate. STO does not show any T -dependent magnetization as expected from diamagnetic behavior. The strong increase of m^* below 15 K, which is present in all samples, is related to magnetic impurities in the STO substrate. The SIO layer shows paramagnetic behavior without any signature of a magnetic transition, whereas the LCO layer displays a ferromagnetic transition with $T_c \approx 75$ K. This is consistent with earlier reports where tensile strain induced ferromagnetism resulting from the stabilization of Co^{3+} HS in LCO have been commonly observed [58, 62].

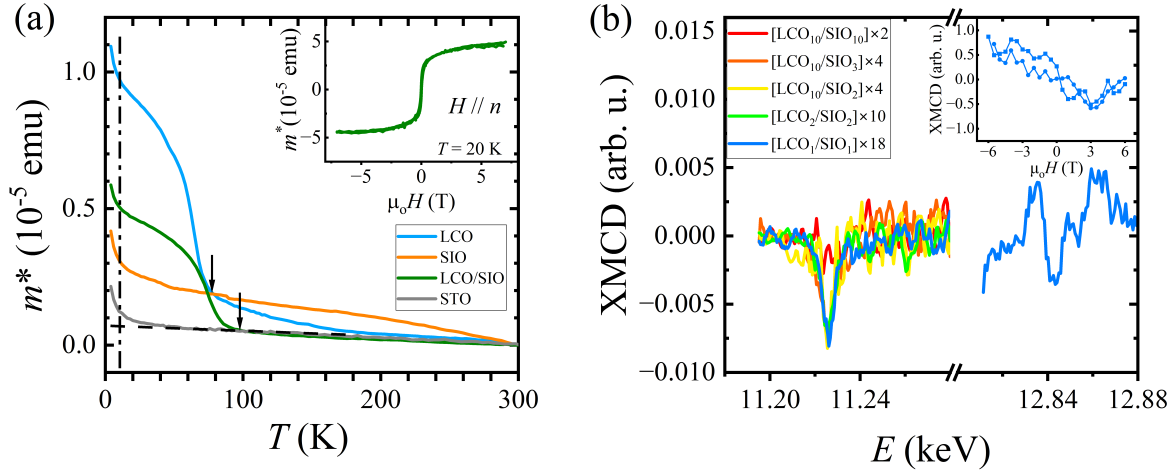


Figure 4.17: Proximity-induced magnetism in SIO in LCO/SIO SLs: (a) Field cooled SQUID measurements for LCO(10), SIO(10), LCO(10)/SIO(10) and STO substrate. A 100 Oe magnetic field was applied parallel to (100) pseudocubic direction, (b) The Ir L_3 and L_2 XMCD for $[\text{LCO}_m/\text{SIO}_n] \times Z$, SLs measured in grazing angle incident and ± 6 T magnetic field at 20 K. In inset, we show the field dependence of XMCD for $[\text{LCO}_1/\text{SIO}_1] \times 18$.

In contrast to LCO, the LCO/SIO bilayer displays a reduced m^* . A distinct quantitative analysis of SIO magnetic moments in LCO/SIO bilayer are not possible as the total magnetic signal is dominated by the ferromagnetic LCO and STO substrate. However, the reduced LCO moments can be attributed to the presence of Co^{2+} states resulting from the ICT to LCO. In the inset of Fig. [4.17a], we show the $m^*(\mu_0 H)$ at $T = 20$ K for LCO/SIO HS with a magnetic field applied along the in-plane (100) pseudo-cubic direction.

4.3.2 X-ray magnetic circular dichroism

In the following, we provide element specific X-ray magnetic circular dichroism (XMCD) on the Ir L edge which provide information on the induced magnetism in SIO. The measurements were performed at the hard x-ray XAS XMCD beamline ID 12 of European Synchrotron Radiation Facility (ESRF), see Chapter 3. The XMCD spectra were recorded at the Ir L_3 and L_2 edge in grazing incidence (15°) with an in-plane magnetic field of ± 6 T on a set of $[\text{LCO}_m/\text{SIO}_n] \times Z$ SLs. Here, m and n are the thickness of LCO and SIO layers in unit of ML and Z is the repetition number, *i.e.*, Z reflects the total number of LCO/SIO interfaces in the SLs.

In Fig. [4.17b], we show the L_3 and L_2 XMCD measured at 20 K for different SLs. The single SIO layer does not show any significant XMCD response. For $[\text{LCO}_{10}/\text{SIO}_{10}] \times 2$

SL, we could not observe any meaningful XMCD response. This is very likely due to the small volume fraction of magnetic SIO in the rather thick SIO (10ML). However, as we decrease the SIO thickness n and/or increase the number of interfaces Z , as in $[LXO_m/SIO_n] \times Z$ SLs, the Ir L_3 XMCD signal evolves and shows a weak but clear magnetic response which becomes strongest for $[LCO_1/SIO_1] \times 18$. The negative XMCD indicates a parallel alignment of the SIO moments with magnetic field direction, *i.e.*, the SIO moments are aligned parallel to that of the LCO layer documenting a ferromagnetic coupling at the SIO/LCO interface. Furthermore, the L_2 XMCD signal is even smaller compared to that of L_3 edge for all the samples. Generally the L_2 signals are weaker in iridates and a L_2/L_3 XMCD intensity ratio of about 5% was observed in Sr₂IrO₄ [153]. For $[LCO_1/SIO_1] \times 18$, the Ir spin moment m_s , orbital moment m_l and total moment m_t was calculated using the sum rule and are 0.011, 0.008 and 0.019 μ_B/Ir , respectively. This agrees well with observed total moments of SIO in other $3d/5d$ HSs, *e.g.*, La_{1-x}Sr_xMnO₃/SIO ($m_s, m_l, m_t = 0.003, 0.018, 0.021 \mu_B/\text{Ir}$) [102]. The striking difference here is the alignment of SIO net moments with respect to the LCO moments. In contrast to the anti-parallel alignment of SIO and LSMO moments in LSMO/SIO [34, 35, 102], the SIO net moments are aligned parallel to the LCO. This definitely calls for a deeper understanding of the interfacial coupling between the SIO and magnetic (LCO or LSMO) layer in these HSs, see Chapter 5. In the inset of Fig. [4.17b], we also show the XMCD for $[LCO_1/SIO_1] \times 18$ at 20 K as a function of magnetic field. This was done by recording the XMCD signal at its maximum for the L_3 edge while sweeping the field. Within the experimental resolution and due to small signal, no clear indication of hysteretic behavior has been observed.

4.4 Electric field control of the anomalous Hall effect in LaCoO₃/SrIrO₃ HSs

In the following, we focus on the systematic control of the proximity induced anomalous Hall effect in the SIO by electrostatic gating. Since the ICT seems to play a very important role, further doping of the SIO channel by electric field gating is a prominent direction. Doping can modify the available density of states at the Fermi level, which in turn can change the integral of the Berry curvature responsible for the occurrence of intrinsic AHE in SIO. To avoid complications arising from the chemical doping or liquid ion gating which may modify the structure, we adapt solid state back gating to dope the SIO by applying electric field effect [154]. STO is widely used as dielectric material and shows very high dielectric

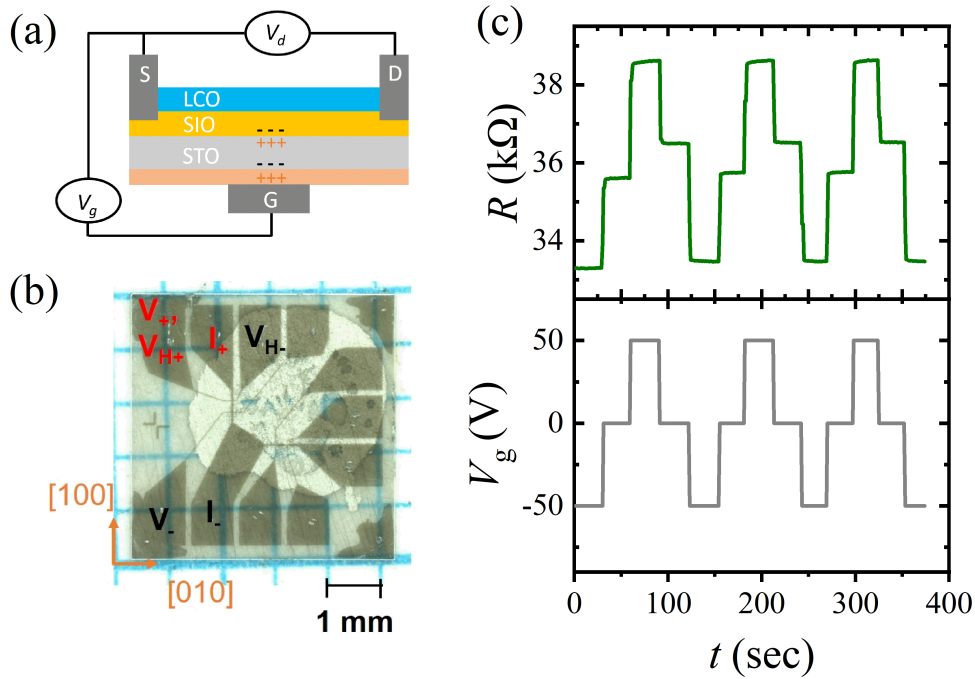


Figure 4.18: Three terminal gating device and switching behavior: (a) The device layout used for the electric field gating experiment of LCO(10)/SIO(10) HS, (b) the micrograph of the real device used in the study, connections for the magnetotransport are shown, (c) switching behavior of the SIO channel at $T = 2$ K as a function of applied gate voltage. Note, the R_{0V} adopts different values while sweeping the voltage from plus to minus and minus to plus.

constant with decreasing temperature which can reach $> 10^5$ below 30 K. The details on the device preparation are discussed in the Chapter 3.

4.4.1 Electric field effect in SIO/LCO HSs

In Fig. [4.18a & b], we show the cross-sectional layout and micrograph of the device used for the electric field gating experiments. The electric field was applied between the gate (G) and source (S) terminals of the Hall bar channel, see Fig. [4.18a]. For the magnetotransport experiments, electrical connections were made as indicated in the micrograph.

First, we show the gate voltage (V_g) switching behavior of the LCO(10)/SIO(10) HS at $T = 2$ K, see Fig. [4.18c]. V_g was swept from -50V to +50V repeatedly and the longitudinal resistance (R) was measured simultaneously. R shows a cyclic and reversible V_g -dependence. Note that $R(0)$ adapts different values while switching the V_g from -50V to +50V and vice versa.

Generally, a positive (negative) V_g results in an accumulation (depletion) of electrons

in the SIO channel. However, here, the application of positive V_g leads to an increase of R similar to what is expected for a hole-type transport. This is in contrast to the commonly observed electron dominant transport inferred from the ordinary Hall effect, see Fig. [4.15d]. This contrasting behavior has been previously observed in SIO films and is discussed as the balanced electron-hole transport as SIO is a semimetal with several electron and hole pockets with different mobilities at the Fermi level [95, 96].

The charge carrier modulation can be estimated by considering a parallel-plate capacitor configuration:

$$\Delta n = \frac{\varepsilon_0 \varepsilon_g E_g}{e d_{ch}}. \quad (4.4)$$

where ε_0 and ε_g are the permittivity of vacuum and STO, respectively, E_g is the applied gate electric field, e is the electron charge and d_{ch} is the conduction channel thickness. Considering $\varepsilon_g \approx 5000$ for $T \leq 40$ K [155], application of +50 V (*i.e.* $E_g = 5$ kV/cm) leads to an electron accumulation of $\Delta n_e \approx 3.5 \times 10^{18} \text{ cm}^{-3}$ in SIO.

Next, we address the effective screening length of the electric field (λ_{sc}), *i.e.*, the penetration depth of the electrostatic modulation.

In metals, the electric fields are screened at the surface and decay exponentially inside the metal. Similar can also be assumed for the SIO channel and we can describe the effective modulation length as:

$$E(z) = E(0) \exp(-z/\lambda_{TF}). \quad (4.5)$$

Here, λ_{TF} is known as the Thomas-Fermi screening length which is the distance ($z = \lambda_{TF}$) from the SIO surface (*i.e.* STO/SIO interface) at which the effective field $E(z)$ decays to 1/e of its original value $E(0)$ (at $z = 0$) [156]. λ_{TF} can be estimated using Lindhard theory for the free electron which gives,

$$\lambda_{TF} \approx \left(\frac{\varepsilon_0 \varepsilon_k}{N(E_F)} \right)^{1/2}, \quad (4.6)$$

with ε_0 , ε_k and $N(E_F)$ are the dielectric permittivity of the vacuum, channel material and density of states at the Fermi level E_F . In case of a 3-dimensional electron gas, this formula simplifies to

$$\lambda_{TF} \approx \left(\frac{\varepsilon_0 \varepsilon_k \hbar \pi^2}{m e^2} \right)^{1/2} \times \left(\frac{\pi}{3n} \right)^{1/6}. \quad (4.7)$$

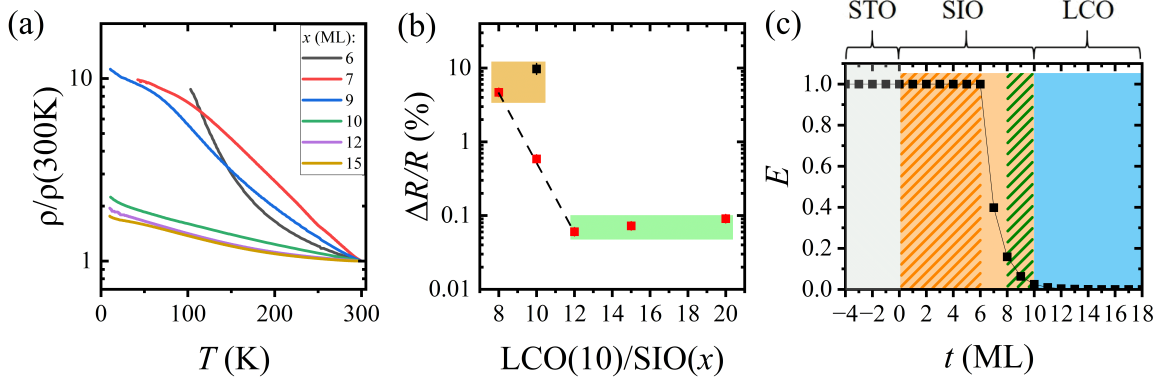


Figure 4.19: Electric field effect as a function of the SIO channel thickness: (a) normalized resistivity, $\rho/\rho(300K)$ vs T , (b) the $\Delta R/R$ for LCO(10)/SIO(x) bilayers, $x = 6-20$ ML. Note, for the red data points, devices with STO thickness 0.17 mm were used, whereas the black data point represents the LCO(10)/SIO(10) device with STO thickness of 0.10 mm and shows strong gating effects. The same device was used for the study of gating effect in LCO(10)/SIO(10) bilayer. (c) electric field screening in LCO(10)/SIO(10) bilayer. The different regions are indicated. A distinct electric field induced effects are expected in the magnetically active SIO, *i.e.*, the 9th and 10th SIO layer at the LCO/SIO interface.

where m and n are the charge carrier mass and density, respectively. As $\lambda_{TF} \propto (1/n)^{1/6}$, good metals show a very small $\lambda_{TF} \leq 1$ Å. However, this could be significantly larger in semiconductors or semimetallic oxides which show smaller n .

Usually, semimetals show a large ε_k [157]. For Sr₂IrO₄ and other Iridates $\varepsilon_k \approx 30$ [158] or even colossal values of ε_k (≥ 600) have been reported [159]. Assuming $\varepsilon_k = 10$ for SIO, λ_{TF} amounts to ~ 6 Å, which is larger compared to that of good metals, however still smaller than the SIO channel thickness ($d_{ch} = 40$ Å). Note that ε_k needs to be increased by two order of magnitude to get λ_{TF} increased by one order of magnitude, *i.e.*, in the range of 40 Å. One thing worth noticing here is that the classical Lindhard theory assumes uniform non-interacting free electrons, which is not the case here. As shown earlier, weak electron localization is expected in LCO/SIO HS which likely results in a larger electric field screening length λ_{TF} . For example, single layer SIO films show MIT with decreasing film thickness. An insulating state was observed below ≤ 3 ML [76,98]. In LCO/SIO bilayers, additional electron transfer from SIO to LCO results in the depletion of electrons in SIO and increased critical thickness of 6 ML for the MIT transition. Consequently, LCO(10)/SIO(6) bilayer shows insulating behaviour, see Fig. [4.6f]. Considering this, we can assume that the first 6 ML of SIO in the LCO(10)/SIO(10) bilayer are insulating and therefore, the electric field screening starts from the 7th layer onwards. To get more clarity on that, we studied the thickness dependence of gating effects in a set of bilayers LCO(10)/SIO(x) with different SIO film thicknesses (x

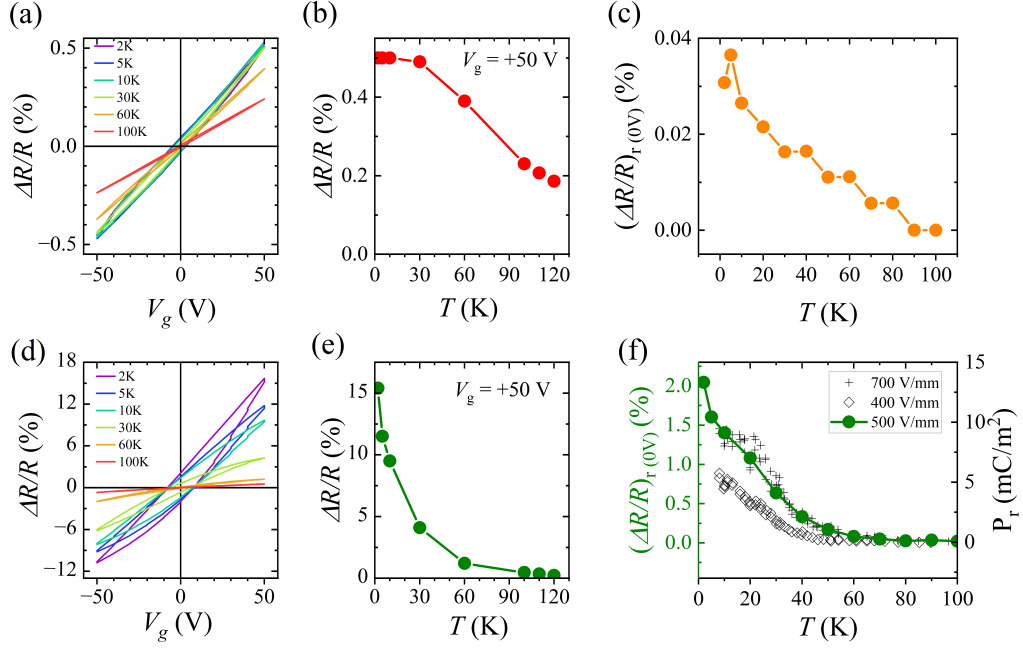


Figure 4.20: Electrostatic field induced switching behavior in LCO/STO/SIO and LCO/SIO: (a), (d) V_g induced relative changes in the resistance, *i.e.*, $\Delta R/R$ at different T ; (b), (e) $\Delta R/R$ versus T and (c), (f) remnant of $\Delta R/R$ at $V_g = 0\text{V}$, *i.e.*, $\Delta R/R_{r(0V)}$ versus T for LCO/STO/SIO (a,b,c) and LCO/SIO (d,e,f), respectively. In Fig. (f) right axis, we also show the temperature dependence of the electric field induced-remnant polarisation in STO at different electric fields. The data is taken from the Ref. [160]. The applied field here (500 V/mm) is strong enough to induced such ferroelectric like transition.

= 6-20 ML). In Fig. [4.19a], we show the normalized resistivity ($\rho_N = \rho(T)/\rho(300\text{K})$) versus T for different x . ρ_N strongly increases with decreasing T for $x < 10$ ML and becomes insulating below 100 K for $x \leq 6$ ML. In Fig. [4.19b], we show the strength of gating effect, *i.e.*, $\Delta R/R = [R(V_g) - R(0)]/R(0)$ for different x ($7 \leq x \leq 20$) at 20 K. $\Delta R/R$ decreases exponentially with x ($7 \leq x \leq 10$) and becomes vanishingly small for $x \geq 10$ which is in agreement with the expected classical electric field screening. Assuming $E \propto \Delta n/n \propto \Delta R/R$, we can estimate the λ_{TF} from the fitting of $\Delta R/R$ versus x ($7 \leq x \leq 10$) which amounts to be $\lambda_{TF} \sim 0.92$ ML. This is comparable to the calculated value of 6 Å for SIO considering $\epsilon_k = 10$. Thus, assuming the first 6 ML are insulating, a distinct gating effect is expected at the 9th & 10th SIO layer, *i.e.*, at the magnetically active side of SIO at the LCO/SIO interface. The electric field screening profile in the LCO(10)/SIO(10) bilayer is sketched in Fig. [4.19c] as a function of the layer number, *i.e.*, distance from the STO surface.

In Fig. [4.20], we show the relative change of longitudinal resistance R , *i.e.*, $\Delta R/R$ for LCO(10ML)/STO(4ML)/SIO(10ML) and LCO(10ML)/SIO(10ML) HSs as a function of V_g . From the back-gate capacitor model, $\Delta n_e \approx 3.5 \times 10^{18} \text{ cm}^{-3}$ (for $V_g = +50$ V) is

expected to be same in both samples which corresponds to $\Delta n_e/n_e = 0.18\%$ and 0.35% for LCO/STO/SIO ($n_e = 1.9 \times 10^{21} \text{ cm}^{-3}$) and LCO/SIO ($n_e = 1.0 \times 10^{21} \text{ cm}^{-3}$), respectively.

The $\Delta R/R$ for LCO/STO/SIO amounts to $+0.5(-0.5)\%$ for $V_g = +50(-50)$ V and $T \leq 30$ K. $\Delta R/R$ shows hysteretic behavior which is most likely related to the electric field induced ferroelectric behavior of the STO substrate, see below. In Fig [4.20b], the T -dependence of $\Delta R/R$ at $+50$ V is shown which increases with decreasing temperature and saturates below 30 K. As expected, this behavior is reminiscent of permittivity $\varepsilon(T)$ of STO where the $\varepsilon(T)$ increases with decreasing T and saturates below 30 K for $E_g > 1.5 \text{ kV/cm}$. Interestingly as mentioned before, $\Delta R/R$ increases for $V_g > 0$ despite the electron accumulation (*i.e.* $\Delta n_e/n_e > 0$ for $V_g > 0$). This hints towards a decreased electron mobility in SIO which can be understood considering $R \propto (n_e \mu_e)^{-1}$ in case of dominant electron type transport:

$$\Delta R/R = -(\Delta n_e/n_e + \Delta \mu_e/\mu_e). \quad (4.8)$$

For LCO/STO/SIO, $\Delta n_e/n_e = 0.18\%$ and $\Delta R/R = 0.5\%$. The relative decrease of mobility $\Delta \mu_e/\mu_e$ is thus $\approx -0.68\%$. This is well consistent with the reports on SIO and other oxide HSs where an decrease of μ is reported for an increase of n ($-\Delta \mu/\mu \approx 3 \times \Delta n/n$) for a charge carrier concentration in the range of $\sim 10^{20} - 10^{21} \text{ cm}^{-3}$ [95]. Thus, the gating behavior in SIO (*i.e.* LCO/STO/SIO trilayer) can be well explained considering simple electrostatics and the semimetallic behavior of SIO.

For the LCO/SIO bilayer, $\Delta R/R$ is significantly large and amounts to about $\approx 15\%$ at 2 K, which is about 30 times larger than that of LCO/STO/SIO. Assuming the same electron accumulation $\Delta n_e/n_e = 0.35\%$ (for $V_g = +50$ V) with respect to $\Delta R/R$, results in $\Delta \mu_e/\mu_e \approx -15.35\%$, hinting to a weak charge carrier localization in SIO. This is well consistent with the increased resistivity behavior of SIO in LCO/SIO bilayer compared to the SIO single layer and LCO/STO/SIO trilayer HSs, see Fig. [4.5]. Also, $\Delta R/R$ versus T , see Fig. [4.20e], shows different temperature dependence that can't be simply explained by the $\varepsilon(T)$ of STO alone, *i.e.*, the strong increase of $\Delta R/R$ down to 2 K.

In Fig. [4.20e], we show the remnant part of $\Delta R/R$ at $V_g = 0$ V, *i.e.*, $\Delta R/R_{r(0V)}$ as a function of T for LCO/SIO (also for LCO/STO/SIO in Fig [4.20c]). $\Delta R/R_{r(0V)}$ decreases with increasing T and strongly suppresses around 60 K. The T -dependence and onset temperature qualitatively show similar behavior where STO goes to a field induced ferroelectric like state below 60 K. In the right axis, we show the field induced remnant polarization of STO (P_r) for different electric field strength as a function of T [160]. The field induced ferroelectric state of STO explains the observed hysteresis behavior of $\Delta R/R$ versus V_g and enables the

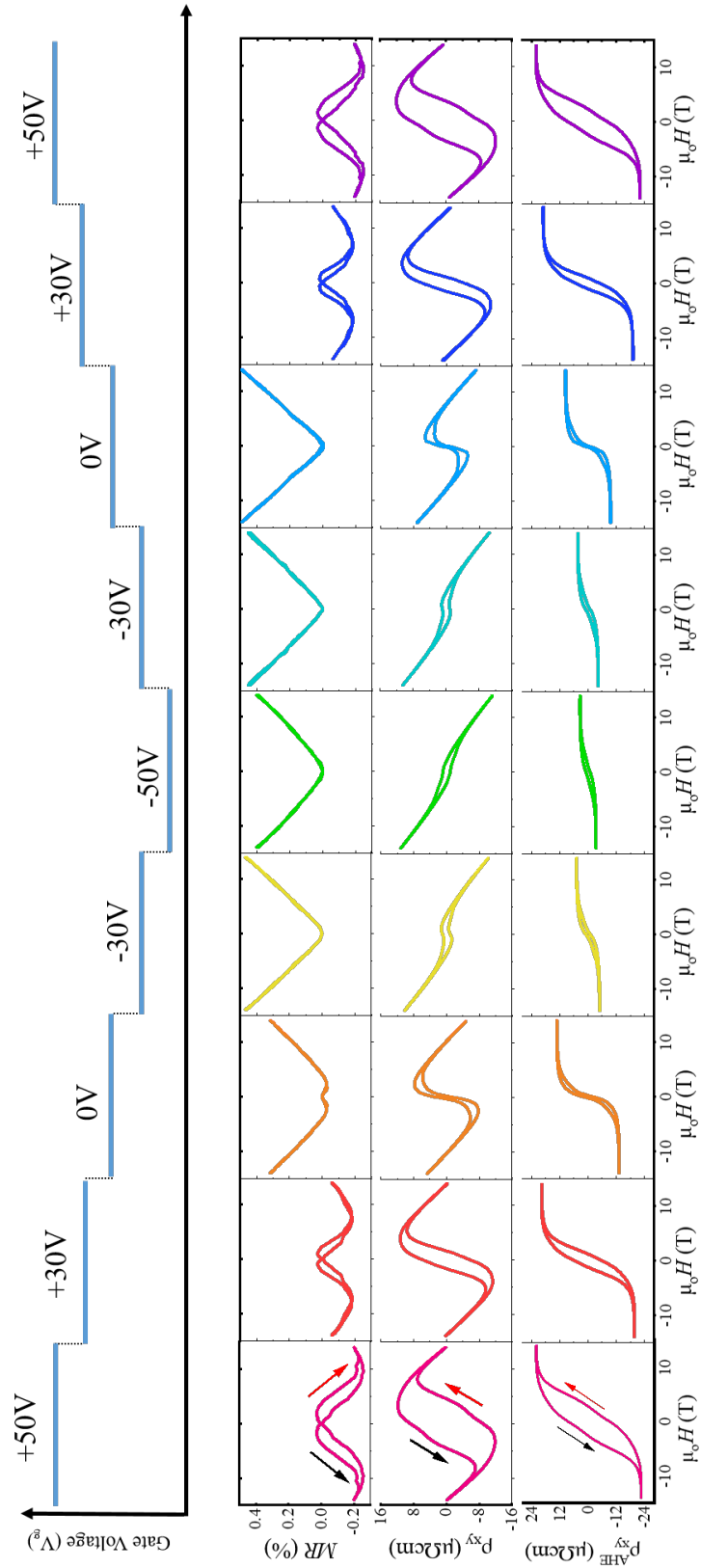


Figure 4.21: Effect of electrostatic gating on magnetotransport: MR (%), ρ_{xy} and ρ_{xy}^{AHE} at different V_g starting from +50 to -50 and then again to +50 V at 20 K. ρ_{xx} and ρ_{xy} were measured simultaneously while sweeping the V_g cyclically. Field sweep directions are indicated with the arrows.

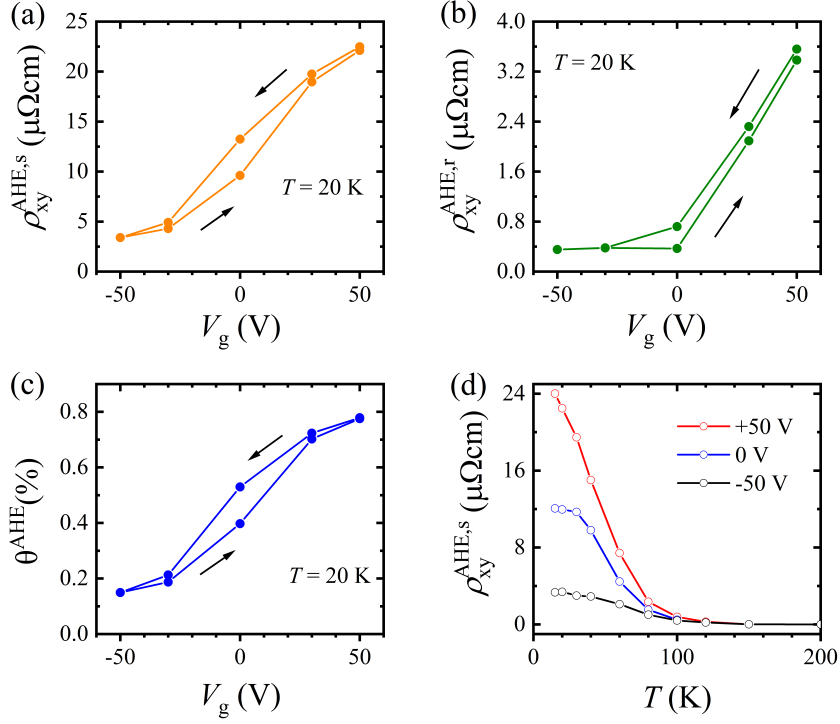


Figure 4.22: Effect of electrostatic gating on ρ_{xy}^{AHE} : (a) saturation $\rho_{xy}^{AHE,s}$ ($= \rho_{xy}^{AHE}$ (14T)), (b) remnant $\rho_{xy}^{AHE,r}$ ($= \rho_{xy}^{AHE}$ (0T)) and (c) Hall angle θ^{AHE} (%) as a function of V_g at $T = 20$ K. V_g sweep directions are shown with the arrows, and (d) T -dependence of $\rho_{xy}^{AHE,s}$ for different V_g .

non-volatile switching of $\Delta R/R$ in LCO/SIO bilayer.

4.4.2 Effect of electrostatic gating on magnetotransport

Now, after showing that the electric field and hence V_g enables modulation of the carrier density at the LCO/SIO interface, we concentrate on the study of magnetotransport as a function of V_g . We performed the experiments at $T \geq 20$ K where the full saturation of the AHE was observed. In Fig. [4.21], we show MR (%), ρ_{xy} and ρ_{xy}^{AHE} at 20 K as a function of V_g for a complete cycle of V_g -sweeps starting from +50 V to -50 V to again +50 V. As shown in the last section, MR and ρ_{xy}^{AHE} show similar hysteretic behavior that arises from the induced spin-polarization in SIO. With decreasing V_g (from +50 V to -50 V), the negative contribution to MR (*i.e.* NMR) and the strength of ρ_{xy}^{AHE} decreases. A complete crossover from a pure negative MR to positive MR is observed. At the same time, a strong decrease in the $\rho_{xy}^{AHE,s}$ (14 T) is observed. The process is reversible and MR , ρ_{xy}^{AHE} recovers back to the original values as the V_g was again swept from -50 V to +50 V. Again, MR and ρ_{xy}^{AHE} data can be fitted by using the same step function, see section 4.2, documenting consistency of

the magnetotransport.

To discuss the observations more quantitatively, we extracted the saturation value of ρ_{xy}^{AHE} at 14 T, *i.e.*, $\rho_{xy}^{AHE,s}$ and remnant of ρ_{xy}^{AHE} at 0 T, *i.e.*, $\rho_{xy}^{AHE,r}$, see Fig. [4.22a,b]. A strong increase of $\rho_{xy}^{AHE,s}$ by a factor of 7 is observed which increases from $\sim 3 \mu\Omega cm$ at -50 V to $\sim 23 \mu\Omega cm$ at +50 V, respectively. An even stronger, asymmetric increase of about one order of magnitude in $\rho_{xy}^{AHE,r}$ is observed, showing unipolar gating behavior. Despite the relatively small doping of about 0.35 %, the observed changes in ρ_{xy}^{AHE} are much stronger. The anomalous Hall angle (θ^{AHE}) is shown in Fig. [4.22c]. Similar to ρ_{xy}^{AHE} , a 6 fold increase of θ^{AHE} is observed, documenting the intrinsic nature of ρ_{xy}^{AHE} , *i.e.*, σ_{xy}^{AHE} is independent on σ_{xx} as discussed previously.

The temperature evaluation of $\rho_{xy}^{AHE,s}$ at different V_g is shown in Fig. [4.22d]. Measurements are consistent with the earlier observations and a strong increase of the $\rho_{xy}^{AHE,s}$ was observed when ramping V_g from -50 V to +50 V. However, the onset temperature is very robust and did not change as a function of V_g .

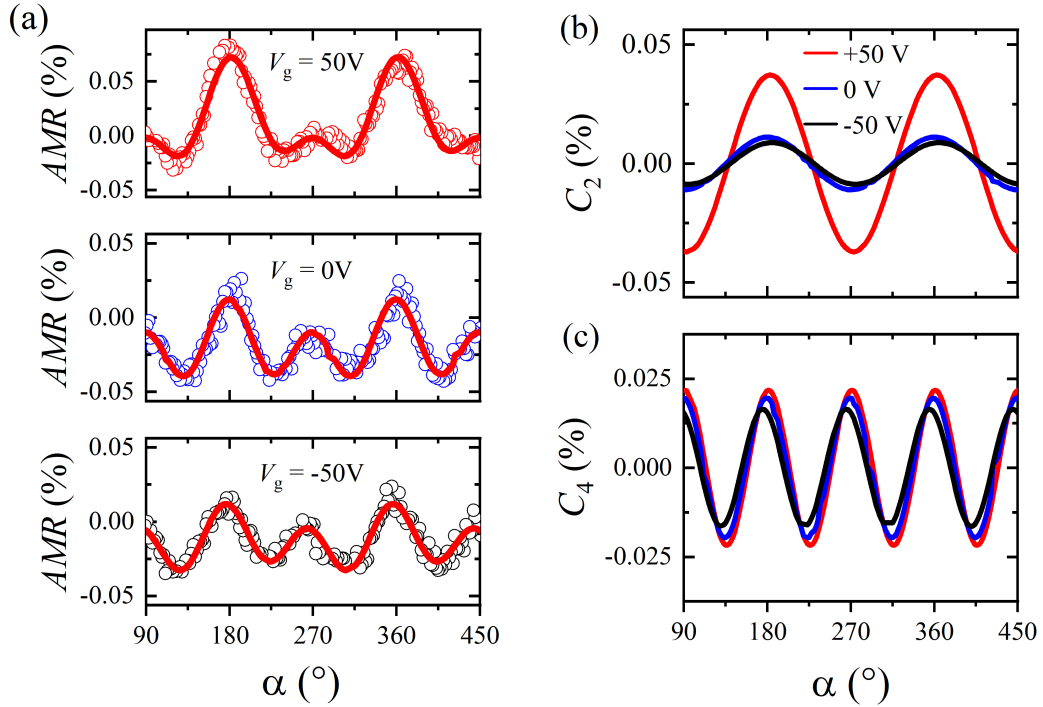


Figure 4.23: Effect of electrostatic gating on magnetic anisotropy: (a) AMR(α) at 20 K for different $V_g = +50$ V, 0 V and -50 V, respectively. Symbols are the measured data points and red solid lines are the fits to the data considering two- and four-fold symmetric terms, (b) The two- and (c) four-fold components extracted from the fitting of data at different V_g .

4.4.3 Effect of electrostatic gating on the magnetic anisotropy

As V_g not only changes the MR and ρ_{xy}^{AHE} , but also H_c ; influence on the magnetic anisotropy as a function of V_g might be alike. To this end, we studied the V_g -dependence of the AMR(α) (see Chapter 3 for the definition). In Fig. [4.23a], we show AMR(α) for different V_g at $T = 20$ K.

AMR(α) can still be described using the same phenomenological model which includes two-fold symmetric conventional AMR and four-fold symmetric magnetocrystalline anisotropy, see Table [6.4]. The $C_2(\alpha)$ and $C_4(\alpha)$ components extracted from the fitting of AMR(α) are shown in Fig. [4.23b,c], respectively. $C_2(\alpha)$ shows maxima for $\alpha = 0$ & 180° . A strong increase (4-5 times) of $C_2(\alpha)$ for $V_g = +50$ V and 0 V is observed compared to $V_g = -50$ V. However, the angular dependence does not show any distinct differences as function of V_g .

In contrast, $C_4(\alpha)$, which represents the magnetocrystalline anisotropy, is affected only slightly by V_g . By sweeping V_g from -50 V to +50 V, $C_4(\alpha)$ increases only by a factor of 1.3 which indicates only small changes of the magnetocrystalline anisotropy by V_g .

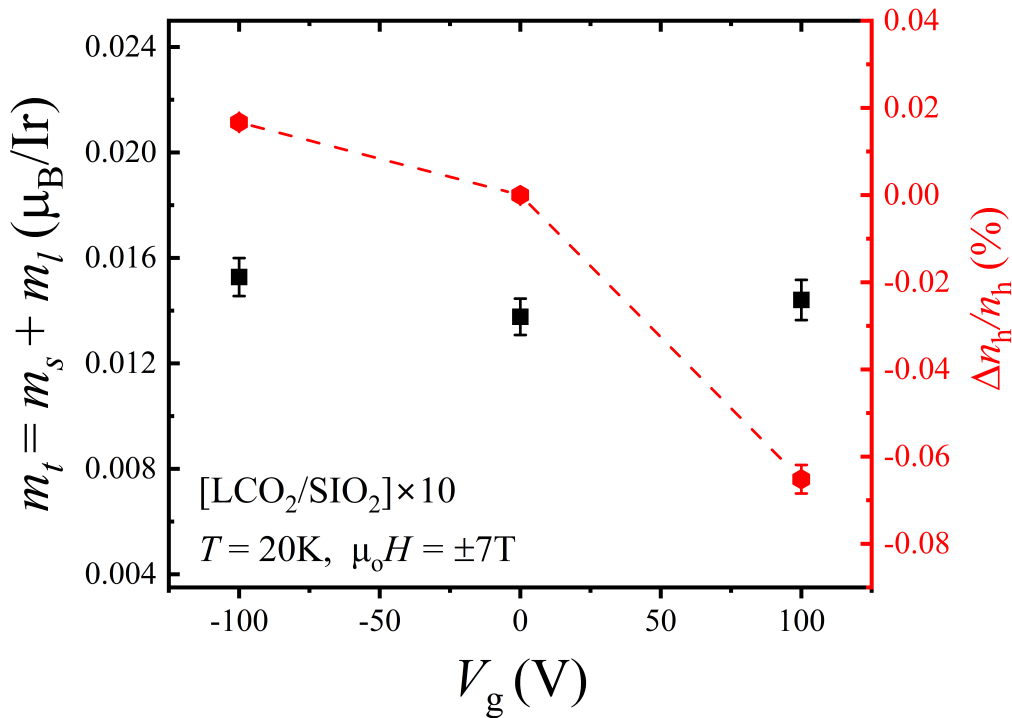


Figure 4.24: SIO magnetism as a function of gate voltage: (a) total magnetic moment ($m_t = m_s + m_l$) deduced from the Ir L_3, L_2 XMCD signal (left scale) and relative change of the hole-concentration $\Delta n_h/n_h$ at the Ir site (right scale) extracted from the Ir L_3, L_2 XANES peak area as a function of the gating voltage V_g .

4.4.4 Effect of electrostatic gating on Ir edge XMCD

To elucidate the origin of the strong electric field dependence of the AHE, we investigated SIO magnetism as a function of V_g measuring the XAS and XMCD at the Ir $L_{3,2}$ edge. The experiment was performed on a $[\text{SIO}_2/\text{LCO}_2] \times 10$ device (see Fig. [4.18] for the device) at $T = 20$ K with an in-plane applied magnetic field of ± 7 T. The doping effect was clearly visible as the Ir $L_{3,2}$ XAS whiteline (WL) peaks and area changes as a function of V_g . The magnetic moment was simultaneously monitored by the XMCD. The Ir L_3 XMCD signal is rather weak (0.9 %) and shows parallel alignment with respect to the magnetic field and did not show significant changes as a function of V_g . The L_2 XMCD signal is nearly zero consistent with our earlier studies on other $[\text{SIO}_n/\text{LCO}_n] \times Z$ SLs. From the sum of the Ir $L_{3,2}$ XAS WL-peak area and the integrated Ir $L_{3,2}$ XMCD area, the relative change of the Ir $5d$ hole density $\Delta n_h/n_h$ and magnetic moments (m_l , $m_{s,eff}$ and m_t) were calculated. The m_l , $m_{s,eff}$, and m_t values as a function of V_g are given in Table [4.2]. In Fig. [4.24], we have shown $\Delta n_h/n_h$ and m_t versus V_g . Note, for calculating $\Delta n_h/n_h$, we assumed $n_h = 5$ for $V_g = 0$ V, which is obviously not the case here. There is already an additional ICT at the LCO/SIO interface, which reduces n_h slightly. As expected, with increasing V_g (*i.e.* electron accumulation), $\Delta n_h/n_h$ (*i.e.* the number of holes, n_h) at the Ir site slightly decreases. However, for $m_t \approx 0.015 \mu_B/\text{Ir}$, there is no change within the experimental resolution is visible. The m_l , $m_{s,eff}$, and m_t values as a function of V_g are given in the Table [4.2]. From these results, we can conclude that the magnetization in SIO does not change during the variation of V_g .

Gate Voltage V_g (V)	Total Moment m_t (μ_B/Ir)	Orbital Moment m_l (μ_B/Ir)	Spin Moment $m_{s,eff}$ (μ_B/Ir)
-100	0.0152	0.0061	0.0091
0	0.0137	0.0055	0.0082
100	0.0144	0.0057	0.0086

Table 4.2: SIO magnetism as a function of gate voltage in $[\text{SIO}_2/\text{LCO}_2] \times 10$ SL: the m_l , $m_{s,eff}$, and m_t values as a function of V_g , estimated using magneto-optical sum rule [137]. Within the experimental error bars, a distinct difference is not visible.

4.5 Magnetism and band topology in SrIrO₃

Bulk polycrystalline perovskite SIO displays a paramagnetic ground state [79]. However, SIO is at the verge of magnetic order, so a magnetic state (FM or AFM) can be achieved by depending on the competition between SOC and U [73]. Therefore, the structural stabilization of crystalline SIO, *e.g.*, by thin film epitaxy, which usually results in a strained, and hence structurally modified state of the first few MLs of SIO, may lead to magnetic properties of thin SIO films. For example, ultrathin SIO films on cubic STO (001) have shown simultaneous MIT and magnetic transition for $x \leq 4$ ML accompanied with the suppression of in-plane octahedral rotations [76]. The electronic band structure of these films in 2D limit were found to be very similar to Sr₂IrO₄ [76]. The octahedral rotation pattern which was found to be responsible for the gap opening at the Fermi level, is similar to that of AFM insulator Sr₂IrO₄ [150]. A distinct canted AFM state with weak FM order was also recently reported in SIO/STO and CaIrO₃/STO SLs [142, 161].

In Sr₂IrO₄ (tetragonal, I4/mmm space group), the IrO₆ follow the (*a^oa^oc⁻*) rotation pattern and are rotated about the c-axis by $\sim 11.8^\circ$ [150]. Following the strong spin-octahedra locking [162], Ir moments (the spins and coupled orbital moments, *i.e.*, pseudospins) are also rotated in a similar fashion and result in a canted AFM structure in the *ab*-plane below $T_N = 240$ K. The net moment = $0.08 \mu_B/\text{Ir}$ within the in-plane layers were found to align along the (110) direction and an AFM ordering was observed along the *c*-axis [100]. Thus, the pseudospin-lattice coupling which is commonly observed in iridates [162, 163], is very important and the magnetic structure strongly depends on the arrangement of the octahedral network.

In our case, SIO in LCO(10)/SIO(10) bilayer also shows *a^oa^oc⁻* octahedral rotation pattern, thus a similar magnetic structure of the Ir⁴⁺ pseudospins ($J_{\text{eff}} = 1/2$) can be assumed in SIO. However, as already shown, SIO(10) single layers do not show magnetism and an AHE. Thus, structural modification together with proximity effect, *i.e.*, interfacial coupling to LCO are essential for the magnetic ground state of SIO in LCO/SIO HSs and SLs. This is documented by the absence of an AHE in LCO/STO/SIO trilayer alike. The proximity of structurally modified SIO to a ferromagnet, *e.g.*, LCO can trigger a ferromagnetic coupling of the Ir net moments within the *ab*-planes and along the *c*-axis direction. The proposed magnetic structure is shown in Fig. [4.14d]. The Ir-edge XMCD in LCO/SIO SLs showed a clear albeit weak XMCD signal with $m_t = 0.019 \mu_B/\text{Ir}$, $m_s = 0.011 \mu_B/\text{Ir}$ and $m_l = 0.008 \mu_B/\text{Ir}$ aligned parallel to the moments of LCO. The m_l/m_s ratio (≈ 0.67) is rather low and typical of

spin dominated magnetization instead of orbital dominated expected from the strong SOC in SIO. The total moments are consistent with other $3d/5d$ HSs, *e.g.*, La_{1-x}Sr_xMnO₃/SIO ($m_s = -0.003$, $m_l = -0.018$, $m_t = -0.021 \mu_B/\text{Ir}$) [102]. The striking difference here is the alignment of SIO net moments with respect to the LCO moments. In contrast to the anti-parallel alignment of SIO and LSMO moments in LSMO/SIO [34, 35, 102], the SIO net moments are aligned parallel to the LCO. Also, the m_l/m_s ratio in LSMO/SIO amounts to around 6, characteristic of orbital dominated moment. The discrepancy observed in the magnetic coupling at the $3d/5d$ interfaces in the two systems, *i.e.*, LCO/SIO and LSMO/SIO calls for the further experimental and theoretical investigation to understand the interfacial coupling in these systems, see Chapter 5.

Next, we discuss the giant tunability of AHE as a function of external electric field E (or gate voltage V_g). Beside the rather small charge carrier doping (0.35 %), which may control magnetism in iridates only to some extent, the electric-field dependence of the Rashba effect at the SIO interface might be important as well. The inversion symmetry breaking at the SIO interfaces result in a distinct Rashba interaction due to the presence of the strong SOC in SIO. The Rashba effect is commonly described by the Hamiltonian $H_R = \alpha_R(k\sigma) \cdot z$, where k is the electron momentum, σ its spin, and z the direction along the surface normal. The Rashba coefficient $\alpha_R \propto E$ for free electrons which provides control of the Rashba effect by an applied E . The Rashba effect introduces a momentum dependent magnetic field and therefore affects the AHE, leading to a quadratic, *i.e.*, symmetric dependence of σ^{AHE} on E or V_g ($\sigma^{AHE} \propto E^2$) [164]. However, in our SIO/LCO HSs, σ^{AHE} or ρ^{AHE} is found to be not symmetric with respect to E . In addition, significant changes of σ^{AHE} due to the E -dependence of α_R are expected only for $E > 10$ MV/cm, which is well beyond the field strength that has been applied here. Therefore, the field dependence of the Rashba effect can be ruled out as the main source for the tunability of the AHE.

Despite the weak magnetic moment in SIO, the large intrinsic σ^{AHE} and Hall angle hint towards the topological band properties in SIO. The bulk orthorhombic SIO ($Pbnm$) is predicted to host Dirac-like linear nodal point related to $J_{\text{eff}} = 1/2$ bands below Fermi level [92]. Depending on the specific symmetry breaking, SIO can comprise various topological phases, *e.g.*, a Dirac semimetal or a topological insulator [97].

Very recently, first principle calculations were employed to study the ICT, magnetism and topological properties of LCO/SIO SLs [165]. A [LCO_{*m*}/SIO_{*n*}] SL geometry, fully strained to the STO substrate, was considered for the calculations. The ferromagnetic Co-Co exchange in LCO was found to induce Ir-Ir ferromagnetic exchange and consequently SIO

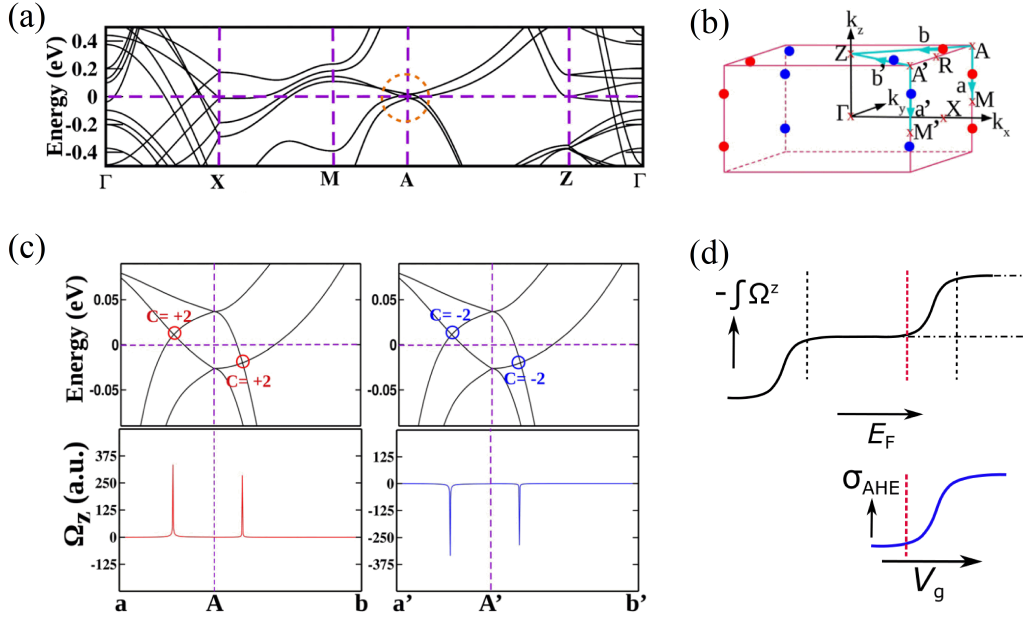


Figure 4.25: Electronic structure of tetragonally distorted ferromagnetic SIO: (a) Band structure along the high-symmetry reciprocal directions, see the (b) Brillouin Zone for the symmetry points, (c) Chern number and calculated Berry curvature associated with the Weyl points above and below E_F along a-A-b and a'-A'-b' respectively, (d) Electric field induced increase of Berry curvature (top) and anomalous Hall conductivity (bottom) respectively. The figures are adapted from [165, 166].

shows ferromagnetic order [165]. The interfacial magnetic coupling across the LCO/SIO interface was provided by the Co-Ir ferromagnetic exchange. Thus, the calculation explains the ferromagnetic alignment of the net SIO and LCO moments. The moments were found to be in in-plane similar to observed in our experiments.

For the study of topological band properties, the electronic band structure of tetragonally distorted, ferromagnetic SIO was calculated [165] and is shown in Fig. [4.25a]. In addition to two Dirac crossings points at high symmetry A (A') point, two linear band crossings (10 meV above and 20 meV below E_F) were observed along a-A-b direction, see Fig. [4.25c]. These crossing points were characterized as double Weyl points with topological charge $C = \pm 2$. The double Weyl points act as source of Berry curvature, see Fig. [4.25c]. The intrinsic σ^{AHE} calculated using the Berry curvature amounts to $7.5 \Omega^{-1} cm^{-1}$ and is of the same order of magnitude observed experimentally ($\sim 3 - 5 \Omega^{-1} cm^{-1}$). Thus, first principle calculations verify the experimental observations and strongly indicate topological band structure and Berry curvature as reason for the observed large AHE in the LCO/SIO HSs and SLs.

The electric field gating induced giant-tunability of AHE (σ^{AHE} vs V_g) can be also dis-

cussed considering the topological band properties of the ferromagnetic, tetragonal SIO. As shown above, the two Weyl points (20 meV below and 10 meV above E_F), act as large source of Berry curvature, *i.e.*, σ^{AHE} [165]. Considering the low density of states near the Fermi level, a 0.35 % doping expected from the electrostatic gating, shifts E_F close to the second Weyl point situated 10 meV above E_F . Once E_F reaches the second Weyl point, large increase in σ^{AHE} is expected following the large Berry curvature associated with the second Weyl point. The rather low magnetization $m_t \approx 0.02 \mu_B/\text{Ir}$ and insensitivity of ordering temperature T_c and magnetic anisotropy on V_g also advocate such scenario, *i.e.*, gating induced changes of topological properties of SIO (*i.e.* the “effective magnetism” related to the Berry connection).

CHAPTER 5

Charge Transfer and Magnetic Exchange in SrIrO₃ based 3*d*-5*d* Transition Metal Oxide Heterostructures

All life is an experiment. The more experiments you make the better.

Ralph Waldo Emerson

In this chapter, a detailed study on the SIO-based 3d/5d interfaces is presented. We systematically replaced the central 3d transition metal ion (X) in LaXO₃ layer and studied the interfacial properties in LaXO₃/SrIrO₃ (X = Mn, Fe, Co and Ni) HSs and SLs. LaMnO₃ (3d⁴), LaFeO₃ (3d⁵), LaCoO₃ (3d⁶) and LaNiO₃ (3d⁷) have different d-orbital occupancy and allow for different 3dⁿ/5d electron configurations. With increasing 3d electron number *n*, the energy difference between the X 3d and O 2p states decreases, see Fig. [5.1a] [167, 168]. In LaXO₃/SrIrO₃, this results in a Fermi energy mismatch ($\Delta\varepsilon_p$) at the interface and consequently electronic reconfiguration by, e.g., charge transfer as a function of X, see Fig. [5.1b,c] [68]. In the following, we start with the brief introduction of LaXO₃ (X = Mn, Fe, Co and Ni) TMOs and associated electronic and magnetic properties.

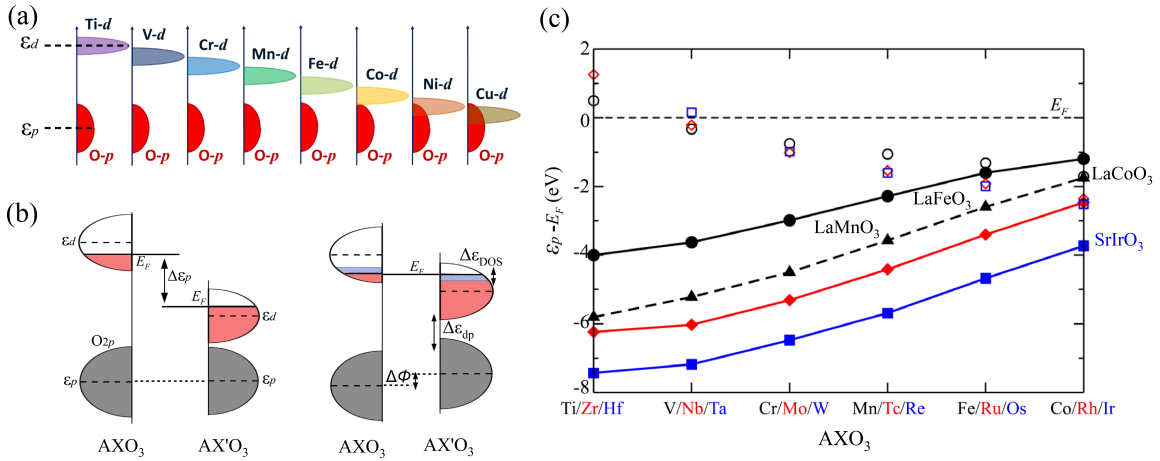


Figure 5.1: Interfacial charge transfer at AXO₃/AX'O₃ interfaces: (a) Shift of X-3d level with respect to O-2p in TMOs LaXO₃, (X = Ti-Cu) [167], (b) O-2p states alignment at the interface result in the Fermi energy mismatch ($\Delta\varepsilon_p$) which drives a charge transfer across the interface to achieve the equilibrium (right figure in (b)), (c) prediction of charge transfer between dissimilar AXO₃/AX'O₃ TMOs HS having XO₂-AO-X'O₂ interfaces. The data for 3d (black), 4d (red) and 5d (blue) X-site in SrXO₃ TMOs are shown with solid lines, whereas the LaXO₃ (X = 3d) are shown with the black dashed line [68].

(1) LaMnO₃ (3d⁴): LaMnO₃ in bulk form has orthorhombic (space group: *Pbnm*) crystal structure, and is an A-type antiferromagnetic, Mott insulator. However a ferromagnetic, insulating ground state can be achieved in strained thin films [169–171]. Oxygen vacancies and/or electronic reconstruction and/or self doping result in the formation of Mn²⁺ (or Mn⁴⁺) which together with Mn³⁺ establishes ferromagnetic double exchange. A hole or electron doping ($\sim 18\%$ or larger) in LaMnO₃ results in the metallic ground state with increased magnetization (*m*^{*}) and *T_c* owing to the double exchange provided by the different valence

state of Mn ions (*e.g.* Mn^{2+} , Mn^{3+} and Mn^{4+}) [63, 64, 111, 112].

(2) LaFeO_3 ($3d^5$): LaFeO_3 belongs to the family of orthoferrites and displays orthorhombically distorted perovskite structure (space group: $Pbnm$). The superexchange between the Fe^{3+} (high spin state, $S = 5/2$) nearest neighbors results in the G-type antiferromagnetic, wide-gap insulating ground state with the highest Néel temperature in the orthoferrite family, $T_N \sim 740$ K [172, 173]. However, a weak ferromagnetism has been observed due to spin canting [172, 174]. With respect to the doping, hole doping (*e.g.* by Sr substitution up to 40 %) and electron doping (*e.g.* by Mo substitution up to 20 %) does not lead to the change of the insulating AFM ground state [175–177] and suggests a robust AFM insulating state in LaFeO_3 . Thus, in case of light electron or hole doping, a conducting state is ruled out in LaFeO_3 . As thin film, it shows AFM or weak-FM insulating behavior [174, 178–181].

(3) LaCoO_3 ($3d^6$): Bulk LaCoO_3 with rhombohedral crystal structure (space group: $R\bar{3}C$) shows a non-magnetic, insulating ground state at low temperatures ($T < 100$ K) as all the Co^{3+} are in LS state and goes to a HS state transition at ~ 500 K. In contrast, tensile strained grown LaCoO_3 films show a ferromagnetic transition $T_c \sim 85$ K [58, 62]. A superexchange between the Co^{3+} HS and LS state was argued as the responsible mechanism for the observed insulating FM state [59].

With respect to the manganite (*e.g.* LaMnO_3) physics, the striking difference in LaCoO_3 is the asymmetry of the phase diagram towards the electron and hole doping. In manganites, an equivalent amount of electron or hole doping ($\text{Mn } t_{2g}^3 e_g^{1\pm x}$) leads to the qualitatively similar increase of m^* , T_c and conductivity [63, 64]. Similar to manganite, a 30 % hole doping of LaCoO_3 ($\text{La}_{0.7}\text{Sr}_{0.3}\text{CoO}_3$) leads to the increased m^* , T_c (~ 200 K) and a metallic ground state. Such transition is induced by double exchange mediated between the Co^{3+} HS and Co^{4+} HS [59, 65, 66]. On the other hand, in stark contrast, 30 % electron doping of LaCoO_3 ($\text{La}_{0.7}\text{Ce}_{0.3}\text{CoO}_3$) suppresses the T_c strongly (~ 23 K) and the sample remains insulating. The reduction in T_c and insulating state in electron doped LaCoO_3 is possibly explained by a spin blockade phenomenon, where the hopping of electrons from Co^{2+} HS to Co^{3+} HS is energetically forbidden [59].

(4) LaNiO_3 ($3d^7$): LaNiO_3 , the first member of the rare earth nickelates (RNiO_3 , R = rare earth, La, Pr,...Lu), possesses rhombohedrally distorted perovskite structure [182]. Unlike commonly observed AFM ordering and metal to insulator transition (MIT) in other RNiO_3 (*e.g.* R = Pr, Nd, Sm), LaNiO_3 shows a paramagnetic and metallic ground state [182]. Resistivity shows linear- T dependence for $T > 50$ K followed by T^2 -dependence for $T < 50$ K, typical of a Fermi liquid. As thin films, LaNiO_3 shows a paramagnetic metallic behavior,

however, an insulating state evolves with decreasing film thickness in ultrathin limits [183–185]. In some studies, the insulating state is accompanied by magnetic fluctuations [185]. Electron doping in LaNiO₃ (by Ce substitution [186] or ICT [187–190]) generally leads to an increased resistivity and also MIT may appear. Similarly, hole doping (Sr substitution at La-site, up to 40 %) increases the resistivity, however, it retains the metallic character with an upturn at lower temperatures [191]. Thus, both electron as well as hole doping increases resistivity in LNO.

Among all the above-mentioned 3d-TMOs, LaNiO₃ is the only metallic system. Therefore, the heterostructures consisting LNO and SIO will not allow the unambiguous selective characterization of the interfacial SIO properties by electronic transport, as the total transport will also comprise contributions from the metallic LNO. Thus, for transport measurements, we decided to use NdNiO₃ (NNO) with SIO instead of metallic LNO, *i.e.*, NNO/SIO interfaces. NNO displays an orthorhombic crystal structure and a paramagnetic metallic ground state at room temperature but undergoes a MIT and AFM ordering at low temperatures ($T_{MIT} \approx T_N \sim 200$ K). Below 100 K, the resistivity is about 4 orders of magnitude higher than SIO. Hole and electron doping suppress T_{MIT} depending on the doping concentration and a metallic state may emerge [192–196].

The LXO, NNO, SIO single layers, LXO(NNO)/SIO (X = Mn, Fe and Co) HSs and SLs were synthesized on TiO₂-terminated STO (001) substrates using pulsed laser deposition technique. The deposition always started with SIO on STO followed by a LXO (or NNO) layer. The details on the film preparation and optimized growth parameters are discussed in Chapter 3. The electronic transport and magnetization was studied on a set of LXO(NNO)(10)/SIO(10) bilayer HS in four point contact Van der Pauw geometry whereas spectroscopy (XAS and XMCD) was done on [LXO_m/SIO_m] \times Z ($m \times Z = 20$) SLs.

5.1 Structural Characterization of LXO(NNO)/SIO bilayer HSs

In this section, structural properties of the LXO(10)/SIO(10) and NNO(15)/SIO(10) bilayer HSs are discussed. For the comparison, data for SIO(10), LXO(10) and NNO(15) single layers are also given. Single layer SIO films are capped with a thin STO (3-4ML) layers to protect from possible degradation. The film growth was monitored in-situ by RHEED which allowed us to control the film thicknesses precisely and stop the deposition at a particular thickness. The individual layer thicknesses were again verified by measuring XRR (not

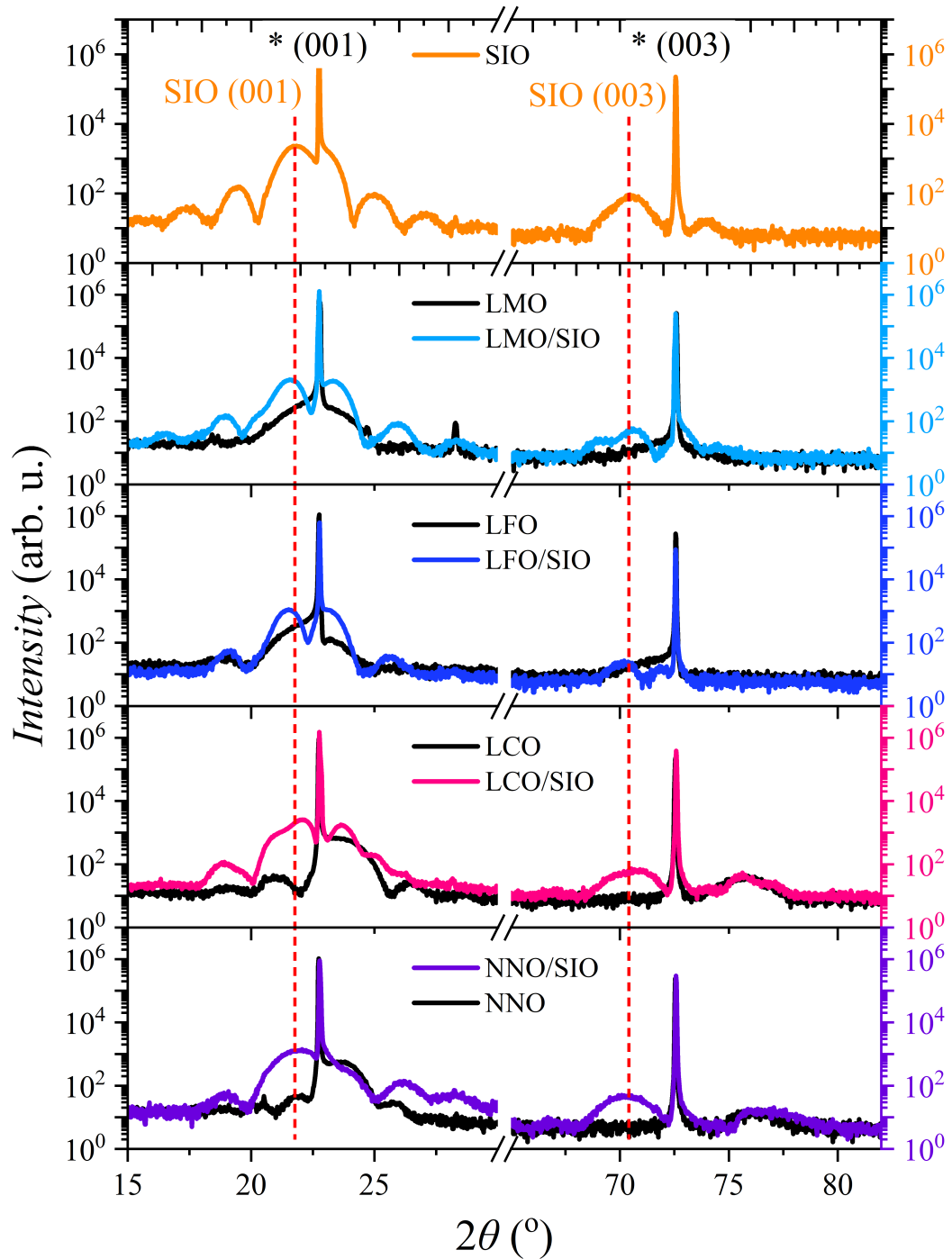


Figure 5.2: X-ray diffraction in the vicinity of symmetric (001) and (003) peak of STO (001) substrate for LNO(NNO)/SIO HSs with ($X = \text{Mn, Fe and Co}$). For the comparison, SIO and LXO (NNO) single layer are also shown. The STO substrate and SIO single layer film peaks are indicated by star (*) and red dashed line respectively. Note, SIO single layer film is capped with a STO protecting layer.

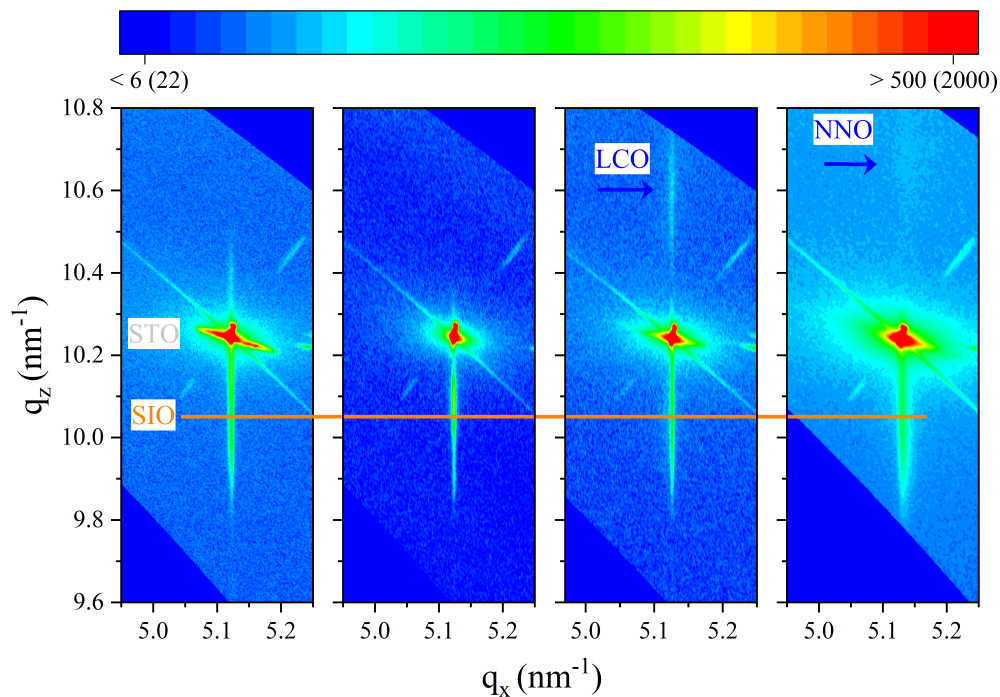


Figure 5.3: Reciprocal space maps around the asymmetric (204)+ peak of STO (001) substrate for LNO(NNO)/SIO HSs with (X = Mn, Fe and Co). The film and substrate peaks are indicated. The intensity is plotted on logarithmic scale and the profile is shown by the color scale at the top where blue and red correspond to the intensity count < 6 (22) and > 500 (2000) for LXO/SIO (NNO/SIO), respectively.

shown).

Symmetric XRD measurements were performed in the vicinity of pseudocubic (001) peak family of STO. In Fig. [5.2], we show the XRD close to the STO (001) and (003) peak, respectively. Clear observation of Laue (thickness) oscillations on both sides of the film peaks indicate the finite film thickness and homogeneity of the epitaxially grown films. First, we focus on the structural properties of LXO (NNO) single layers. The bulk pseudo-cubic lattice constant for SIO, LMO, LFO, LCO and NNO are 3.96, 3.93, 3.93, 3.80 and 3.81 Å, respectively which result in an in-plane lattice mismatch $((a_{substrate} - a_{bulk})/a_{bulk})$ of -1.51, -0.76, -0.76, 2.63, 2.36 % between the LXO (NNO) and STO substrate (3.90 Å). Here, + and - correspond to the compressive and tensile strain, respectively. For LMO and LFO, the film peaks appear very close (slightly left) to the STO (001)-reflections indicating a larger out-of-plane lattice parameter c . On the other hand, the LCO and NNO peaks appear at higher angle documenting smaller c . The out-of-plane c -lattice parameter are calculated using Bragg's law and are: 3.94 ± 0.01 , 3.98 ± 0.01 , 3.77 ± 0.01 and 3.74 ± 0.01 Å for LMO, LFO, LCO and NNO, respectively.

Sample	$a_{pc} = b_{pc}$ (Å) From RSM	c_{pc} (Å)	
		From RSM	From XRD
SIO(10)	3.90	3.99 ± 0.01	4.00 ± 0.01
LMO(10)/SIO(10)	3.90		3.99 ± 0.01
LFO(10)/SIO(10)	3.90	3.99 ± 0.01	4.000 ± 0.005
LCO(10)/SIO(10)	3.90	3.99 ± 0.01	3.994 ± 0.005
NNO(15)/SIO(10)	3.90	3.99 ± 0.01	4.00 ± 0.01

Table 5.1: SIO pseudo-tetragonal lattice constants for LXO(NNO)/SIO HSs: in-plane ($a_{pc} = b_{pc}$) and out-of-plane (c_{pc}) lattice constants estimated from the symmetric (00 l) and asymmetric (204) reflection. Rather low thickness of films and line broadening results in the large error bars.

Next, we focus on the structural properties of SIO in the bilayer HSs. The rather low intensity and broadening of the film peaks make quantitative analysis challenging. At low angles (*e.g.* around (001) STO), there is strong overlap of film peaks from LMO and SIO or LFO and SIO, where both LMO or LFO and SIO peaks appear at the same side of STO. Therefore, we calculated the out-of-plane c -lattice parameters using the (003) and (004) diffraction peak position, where the constituent film peaks in the HSs are well separated and the thickness oscillations are strongly suppressed. The extracted lattice parameters for SIO are shown in Table [5.1].

In Fig. [5.3], we show the RSM in q_x - q_z space measured in the vicinity of the (204)+ peak of the STO substrate for LXO(10)/SIO(10) and NNO(15)/SIO(10ML) HSs. The color profile represents the intensity distribution of the peaks, where blue and red correspond to the intensity count < 6 (22) and > 500 (2000) for LXO/SIO (NNO/SIO), respectively. The rather low thicknesses of the films result in the line broadening of the film peaks along the q_z direction. The q_x value for all constituent films are the same as for the STO peak, *i.e.*, films share the same in-plane lattice parameters of STO (*i.e.* $a = 3.9$ Å) and are coherently strained to STO.

Similar to symmetric XRD, the LMO and LFO peaks are very close to the STO peak, therefore a quantitative estimation of q_z are not possible for LMO and LFO. For LCO and NNO, the q_z value of (204)+ appears at larger value than that of STO, in agreement with symmetric XRD on (00 l) reflections. For SIO, the q_z appears at lower value compared to STO owing to a larger out-of-plane lattice parameter compared to STO. Despite the line broadening due to confinement, a distinct variation of the q_z values are not visible and can be assumed at the same value in all four HSs, which within the experimental resolution, rule

out the presence of structural difference in the SIO films in the HSs. The in-plane ($a_{pc} = b_{pc}$) and out of plane (c_{pc}) lattice parameters extracted from the (003), (004) symmetric XRD and (204) RSM are shown in the Table 5.1. Considering the line broadening induced large errors, a distinct difference in the SIO lattice parameters are not visible. However, slight differences in the micro-structural properties resulting from the top LXO (NNO) layer are possible, specifically in case of compressively strained LMO and LFO, where the Mn-O-Mn ($\sim 159.6^\circ$) and Fe-O-Fe ($\sim 155^\circ$) bond angles are distinct different to that of Ir-O-Ir (156.5°) in SIO.

5.2 Electronic transport in LXO(NNO)/SIO bilayer HSs

5.2.1 Longitudinal resistivity

In Fig. [5.4], we show the longitudinal resistance as a function of temperature $R_{xx}(T)$ (see Equ. [3.5] for definition) for LXO(NNO)/SIO bilayers in comparison to LXO(NNO) single layers. LMO, LCO and LFO show a highly insulating behavior which exceeds the measurement limit below $T \leq 270$ K. In comparison, NNO single layer shows a metallic behavior at high temperatures and undergoes a MIT at $T_{MIT} \sim 150$ K. At low temperatures ($T \leq 50$ K), $R_{xx}(T) > 10^5 \Omega$ which is about 4 order of magnitude larger compared to SIO. Generally, NNO films show a MIT with cooling and warming hysteresis, however, with increasing tensile strain and/or decreasing film thickness, the films become more insulating with suppressed hysteresis effect [197–200]. For example, NNO(15) films grown under identical conditions on NGO (110) substrate show strongly decreased resistivity above T_{MIT} compared to the films on STO, see Fig. [6.3]. NNO films on STO are often reported to show oxygen vacancies owing to the large tensile strain imposed by STO and consequently increased resistivity [200].

In Fig. [5.4e], we compare the $R_{xx}(T)$ of different bilayer HSs. All the bilayers (except NNO/SIO) show increased resistance behavior in comparison to SIO (or LCO/STO/SIO). This, to some extent, can be attributed to the ICT from SIO to LXO layer. Specially, in case of LFO/SIO and LCO/SIO bilayers where transport channel is limited to SIO only. In contrast, NNO/SIO bilayer shows very different T -dependence and lower resistance compared to both NNO and SIO single layers. The lower resistance is expected when both layers contribute parallelly to the conductivity as in NNO/SIO [201]. However, the total $R_{xx}(T)$ behavior is reminiscent of MIT in NNO films and thus can be assumed to be dominated by NNO, consistent with the earlier investigation on electron doped NNO films where a suppressed

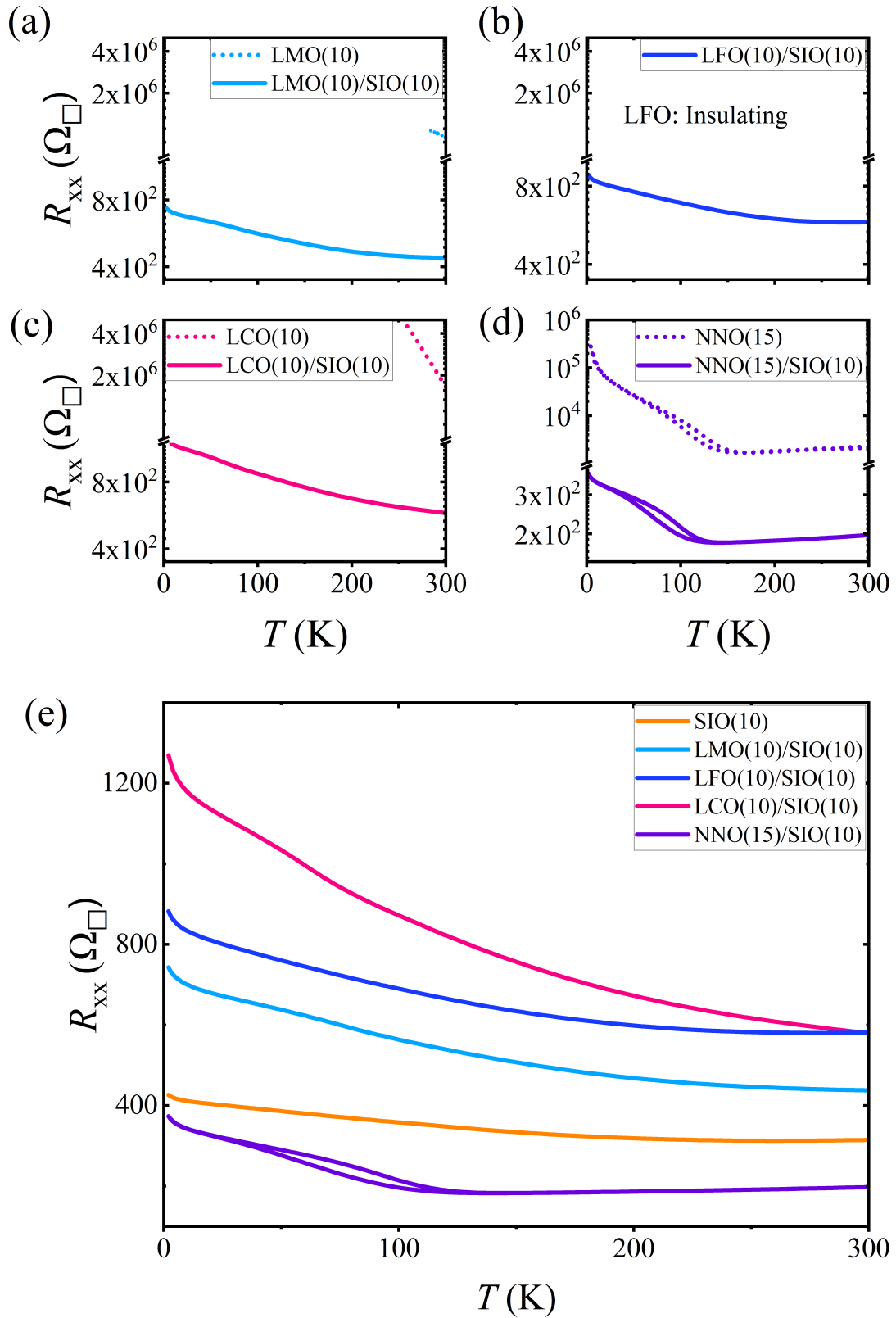


Figure 5.4: Resistance vs temperature $R_{xx}(T)$ in LXO, NNO and LNO(NNO)/SIO HSs with ($X = \text{Mn, Fe and Co}$): (a)-(d) $R_{xx}(T)$ for different bilayers. For the comparison, the data for LXO (NNO) layers is also shown. Note, LFO(10) layer was highly insulating that we couldn't measure at all. (e) $R_{xx}(T)$ for different bilayers and SIO single layer.

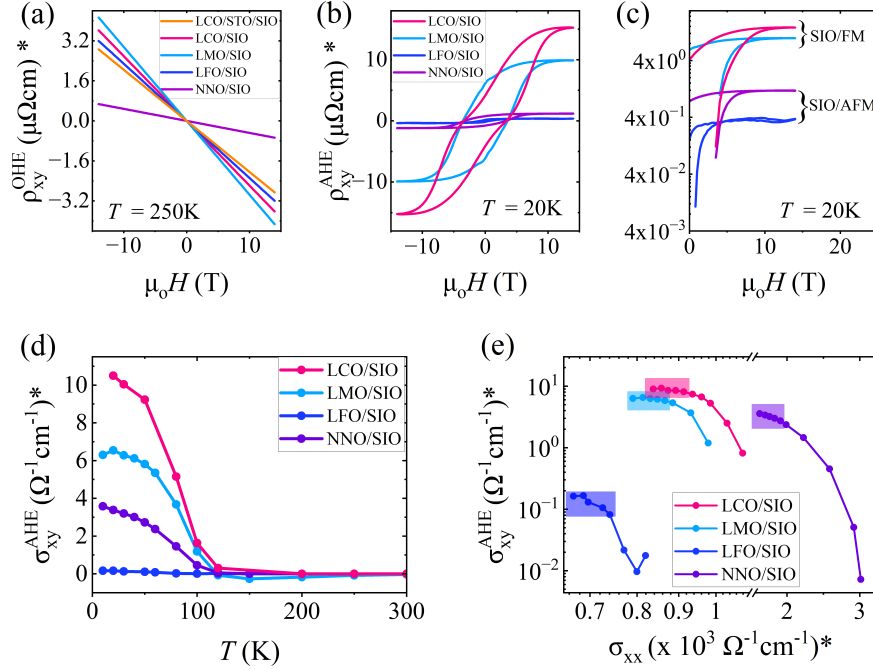


Figure 5.5: Anomalous Hall effect in LXO(NNO)/SIO ($X = \text{Mn, Fe and Co}$) HSs: (a) ordinary Hall resistivity (ρ_{xy}^{OHE}) vs μ_0H at 250 K, (b) & (c) anomalous Hall resistivity (ρ_{xy}^{AHE}) vs magnetic field (μ_0H) at $T = 20\text{K}$, (d) anomalous Hall conductivity ($\sigma_{xy}^{AHE,s}$) as a function of T , (e) the transverse $\sigma_{xy}^{AHE,s}$ versus longitudinal σ_{xx} . The shaded regions represent the data point for $10\text{K} \leq T \leq 50\text{K}$.

T_{MIT} has been observed as a function of electron doping [195, 196].

5.2.2 Transversal (Hall) resistivity

In Fig. [5.5], we show the ordinary (ρ_{xy}^{OHE}) and anomalous (ρ_{xy}^{AHE}) part of the Hall resistivity (ρ_{xy}) for different bilayers at 20 K as a function of magnetic field and temperature. Note that for the resistivity (ρ_{xx}, ρ_{xy}) and conductivity (σ_{xx}, σ_{xy}) calculations, only SIO thickness was considered. This is well justified for LCO/SIO and LFO/SIO bilayers, since light electron doping in LCO and LFO from ICT do not contribute to conductivity. However, a conductivity contribution from LMO in LMO/SIO and in particular from NNO in NNO/SIO bilayers is obvious as discussed previously. ρ_{xy} shows linear field dependence for $T > 150\text{K}$ with negative slope documenting dominant electron like transport in all the bilayers. From ρ_{xy}^{OHE} , the slope was extracted to calculate electron density (n_e). The rather low $n_e = 1.0 \times 10^{21}\text{cm}^{-3}$ of semi-metallic SIO makes ρ_{xy}^{OHE} very sensitive with respect to even small changes in n_e . To this end, we estimated the n_e in different bilayers at $T = 250\text{K}$, well above the magnetic transition temperature where the total Hall is given by: $\rho_{xy} = \rho_{xy}^{OHE}$. In Fig. [5.5a], ρ_{xy}^{OHE} is shown for different bilayers in comparison to LCO/STO/SIO trilayer. A distinct change

in the linear Hall slope is visible which document the different n_e in the bilayers. Here, a reliable estimation for charge transfer can be made only for LFO/SIO and LCO/SIO, as the transport is exclusively related to SIO only. The calculated n_e at 250 K shows the following sequence: n_e (LCO/STO/SIO) $>$ n_e (LFO/SIO) $>$ n_e (LCO/SIO). The lower n_e in LFO/SIO and LCO/SIO is likely attributed to the ICT from SIO to 3d TMO being stronger in LCO/SIO, consistent with the expectation from the electronic band-mismatch ($\Delta\varepsilon_p$), see Fig. [5.1c]. In case of LMO/SIO and NNO/SIO, a similar charge transfer estimation is not possible as both layers are conducting and Hall slope does not belong to SIO only.

With decreasing temperature, an additional contribution from the anomalous Hall resistivity (ρ_{xy}^{AHE}) appears. In Fig. [5.5b], we show ρ_{xy}^{AHE} ($= \rho_{xy} - \rho_{xy}^{OHE}$) for different bilayers at $T = 20$ K. ρ_{xy}^{AHE} has been extracted from the ρ_{xy} in the same way as described in Chapter 4. ρ_{xy}^{AHE} show hysteric field dependence with large coercive field (H_c) which is nearly similar for all the bilayers. However, a strong difference is observed in the strength of ρ_{xy}^{AHE} . In Fig. [5.5c], we show the ρ_{xy}^{AHE} on log scale. Clearly for LMO/SIO and LCO/SIO bilayers (*i.e.* FM/SIO), the ρ_{xy}^{AHE} (14T) (*i.e.* $\rho_{xy}^{AHE,s}$) is more than one order of magnitude larger compared to LFO/SIO and NNO/SIO bilayers (*i.e.* AFM/SIO).

The temperature dependence of $\sigma_{xy}^{AHE,s}$ is shown in Fig. [5.5d]. The $\sigma_{xy}^{AHE,s}$ are positive ($T \leq 100$ K) and decrease rapidly with increasing temperatures. A distinct difference in the onset temperature for positive AHE (T^*) is not visible here.

For LMO/SIO and LCO/SIO, $\sigma_{xy}^{AHE,s}$ amounts to $\sim 8-10 \Omega^{-1}cm^{-1}$ whereas for LFO/SIO (NNO/SIO), it is ~ 0.5 (4) $\Omega^{-1}cm^{-1}$ at 20 K. As NNO conduction dominates in NNO/SIO bilayer, $\sigma_{xy}^{AHE,s}$ calculation for NNO/SIO bilayer is not accurate, as different contributions in ρ_{xx} and ρ_{xy} related to SIO and NNO needs to be separated. The scaling between $\sigma_{xy}^{AHE,s}$ and σ_{xx} for different bilayers is shown in Fig. [5.5e]. For all LXO/SIO bilayers, $\sigma_{xy}^{AHE,s}$ is nearly independent on σ_{xx} (*i.e.* $\sigma_{xy}^{AHE,s} \propto \sigma_{xx}^0$) for $T \leq 50$ K, documenting the intrinsic AHE as the dominant contribution [125].

5.2.3 Magnetoresistance

In Fig. [5.6], we show the MR at $T = 20$ K for different bilayers. The field sweep directions are indicated by arrows. At higher temperatures, MR shows quadratic field dependence and is related to the classical Lorentz scattering, see Fig. [4.10]. With decreasing T , an additional negative contribution starts to appear. Qualitatively, MR in LFO/SIO and LCO/SIO bilayer can be explained by the sum of the two terms: classical Lorentz contribution (LS) and negative contributions (NMR) by spin-flip scattering (SFS) as discussed in Chapter 4. Similar

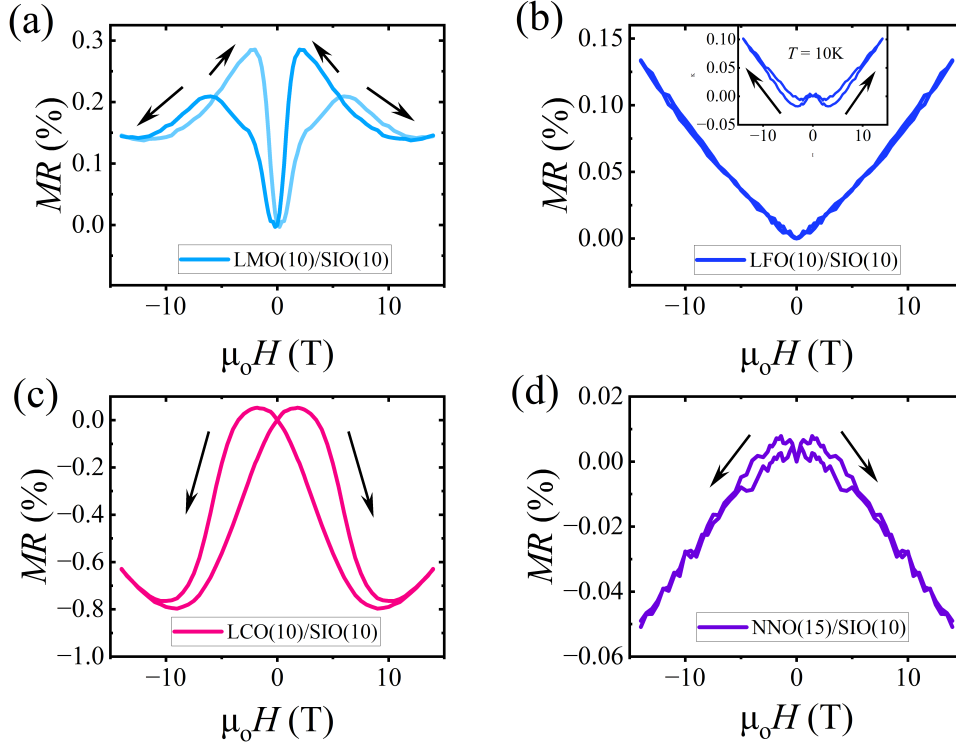


Figure 5.6: Magnetoresistance (MR) in LXO(NNO)/SIO, (X = Mn, Fe and Co) HSs: (a) LMO(10)/SIO(10), (b) LFO(10)/SIO(10), (c) LCO(10)/SIO(10) and (d) NNO(15)/SIO(10) bilayers respectively at $T = 20$ K. Field sweep directions are shown with the arrows. In inset of (b), the MR of LFO(10)/SIO(10) at 10 K is shown.

to the magnitude of AHE, a larger NMR is observed in LCO/SIO compared to LFO/SIO. In addition, the large H_c of NMR is very similar to that of ρ_{xy}^{AHE} documenting the consistency of magnetotransport. The coupled hysteretic behavior of ρ_{xy}^{AHE} and MR is also consistent with the recently proposed magnetotransport scenario induced by Berry curvature related AHE [202].

In NNO/SIO bilayer, MR can still be explained considering the LS and SFS contributions. In addition, NNO films also show small negative MR which may contribute alike [199]. However, for LMO/SIO bilayer, the MR is more complicated. In addition to above mentioned contributions, several other contributions related to electron doped LMO may contribute to the total MR. For example, electron doped LMO films show negative magnetoresistance below magnetic transition temperature [64]. However, still the H_c of hysteretic MR is similar to that of ρ_{xy}^{AHE} corroborating the close link between the two.

5.3 Electron spectroscopy

X-ray absorption spectroscopy (XAS) and X-ray magnetic circular dichroism (XMCD) were performed on a set of $[\text{LXO}_m/\text{SIO}_m] \times Z$, ($X = \text{Mn, Fe and Co}$) SLs at the Ir $L_{2/3}$ edge, see also Chapter 3.

In Fig. [5.7a], we show the normalized X-ray absorption near edge spectra (XANES) at 20 K for $[\text{LMO}_4/\text{SIO}_4] \times 5$, $[\text{LFO}_4/\text{SIO}_4] \times 5$, $[\text{LCO}_4/\text{SIO}_4] \times 5$ in comparison to $\text{SIO}(20)$ single layer (*i.e.* $[\text{LXO}_0/\text{SIO}_4] \times 5$ SL). For LMO/SIO SL, the XANES spectra is similar to that of $\text{SIO}(20)$ and only a slight shift of the $L_{2/3}$ peak position towards higher energy was observed. This means the Ir valence state is nearly identical in both samples (Ir^{4+}) and an ICT is very small and negligible. In contrast, a clear shift of the Ir L_3 and L_2 peak position towards higher energy side, as well as an increase of the integrated peak area were observed for LFO/SIO and LCO/SIO SLs. The integrated white-line (WL) sum area represents the hole density of Ir. Thus, the increased sum area manifest the increased hole density in LFO/SIO and LCO/SIO SLs, see Table [5.2]. This again confirms the electron transfer scenario at LXO/SIO interfaces. The WL sum area is larger for LCO/SIO compared to LFO/SIO showing a larger electron transfer from SIO to LCO in comparison to LFO. Assuming the number of holes $n_h = 5$ in SIO, a relative change in n_h can be estimated, which is shown in Fig. [5.7b].

Sample	Sum Area $\text{SA} = (I_{L_3}^{\text{XAS}} + I_{L_2}^{\text{XAS}})$	Branching Ratio $\text{BR} = I_{L_3}^{\text{XAS}} / (I_{L_3}^{\text{XAS}} + I_{L_2}^{\text{XAS}})$ or $I_{L_3}^{\text{XAS}} / I_{L_2}^{\text{XAS}}$
$[\text{SIO}_4] \times 5$	30.697	0.843 (5.37)
$[\text{LMO}_4/\text{SIO}_4] \times 5$	30.860	0.841 (5.23)
$[\text{LFO}_4/\text{SIO}_4] \times 5$	31.698	0.844 (5.42)
$[\text{LCO}_4/\text{SIO}_4] \times 5$	32.841	0.842 (5.31)

Table 5.2: Integrated white-line sum area (SA) and branching ratio (BR) estimated from the $L_{2/3}$ XANES measured at $T = 20$ K for different superlattices $[\text{LXO}_4/\text{SIO}_4] \times 5$, $X = \text{Mn, Fe and Co}$.

The amount and direction of ICT as shown in [5.7c] is in full agreement with the charge transfer estimated from the ordinary Hall resistivity (see Fig. [5.5f]). In Table [5.2], we summarize the branching ratio (BR) estimated from the integrated Ir $L_{2/3}$ WL sum area for $[\text{LXO}_4/\text{SIO}_4] \times 5$ ($X = \text{Mn, Fe and Co}$) SLs. BR represents the relative strength of Ir $L_{2/3}$

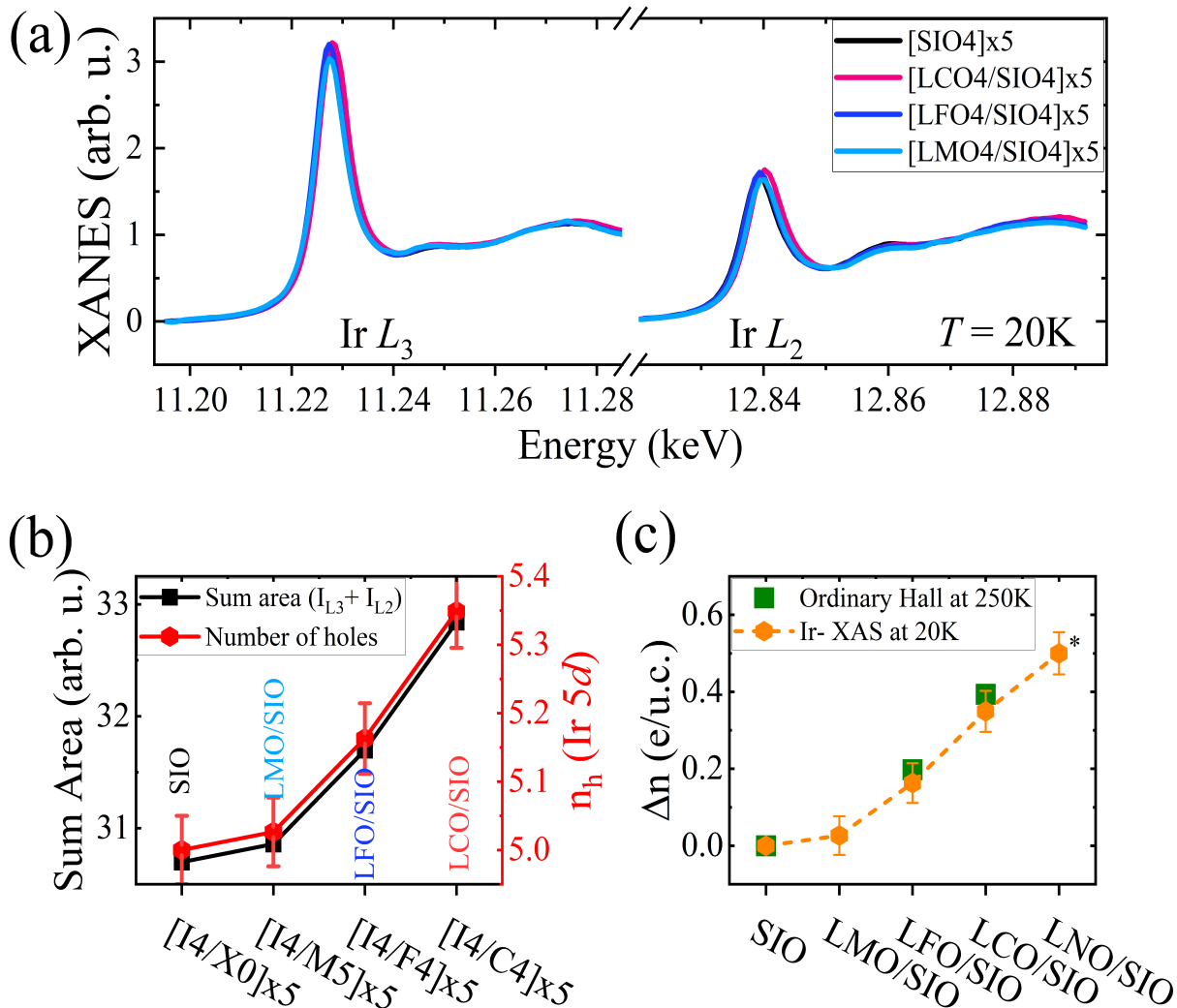


Figure 5.7: Interfacial charge transfer in LaXO₃/SrIrO₃ (X = Mn, Fe, and Co) SLs: (a) normalized Ir L₃ & L₂ XAS for [LMO₄/SIO₄]_{x5}, [LFO₄/SIO₄]_{x5}, [LCO₄/SIO₄]_{x5} SLs. For comparison, we have also included the XAS for SIO(20). (b) Integrated Ir L₃ and L₂ WL sum area and estimated number of 5d holes, (c) the relative amount of electron transfer from SIO to LXO at the interface. The electron transfer estimated from ordinary Hall measurements at 250 K for LCO/SIO and LFO/SIO HSs is included alike. The data for LNO/SIO is taken from Ref. [190].

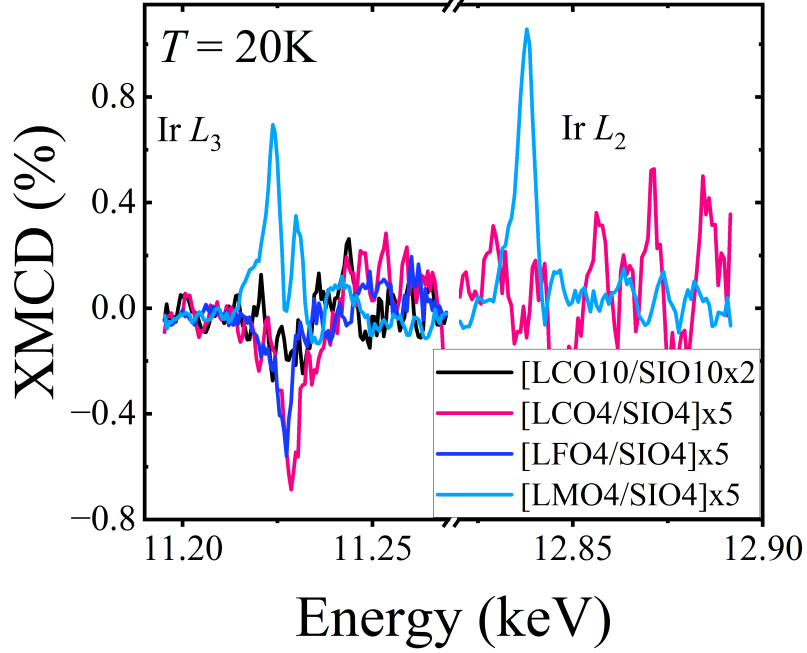


Figure 5.8: Proximity induced interfacial magnetism in $\text{LaXO}_3/\text{SrIrO}_3$ ($X = \text{Mn, Fe, and Co}$) SLs: Ir L_3 & L_2 XMCD for $[\text{LMO}_4/\text{SIO}_4] \times 5$, $[\text{LFO}_4/\text{SIO}_4] \times 5$, $[\text{LCO}_4/\text{SIO}_4] \times 5$ SLs. For comparison, we have also included the XMCD for $[\text{LCO}_{10}/\text{SIO}_{10}] \times 2$ SL.

WL features and is related to the effective SOC operator $\langle \sum l_i \cdot s_i \rangle$ as given by Equ. [3.15]. Despite the different magnitude of ICT at the interfaces, the BR is nearly the same for all SLs, showing that the SOC is not much affected by an ICT or induced magnetism in SIO, see Table [5.2].

To analyse the interfacial magnetism in SIO at $3d/5d$ interfaces, XMCD experiments were performed at Ir L_3 and L_2 edges at 20 K. The single SIO layer does not show any significant XMCD response. For $[\text{LXO}_{10}/\text{SIO}_{10}] \times 2$ SL, we could not observe any meaningful XMCD response. This is very likely due to the small volume fraction of magnetic SIO in the rather thick SIO (10ML). However, as we decrease the SIO thickness and/or increase the number of interfaces, as in $[\text{LXO}_4/\text{SIO}_4] \times 5$ SLs, the Ir L_3 XMCD signal evolves and shows a weak but clear magnetic response. In Fig. [5.8], we show the XMCD spectra for $[\text{LMO}_4/\text{SIO}_4] \times 5$, $[\text{LFO}_4/\text{SIO}_4] \times 5$ and $[\text{LCO}_4/\text{SIO}_4] \times 5$ SLs. For $[\text{LFO}_4/\text{SIO}_4] \times 5$ and $[\text{LCO}_4/\text{SIO}_4] \times 5$ SLs, the Ir L_3 XMCD are negative. However, Ir L_2 XMCD response was below measurement threshold. Note that the L_2 XMCD signals are generally much weaker in iridates compared to that of the L_3 edge. For example, a L_2/L_3 XMCD intensity ratio of about 5% was reported in Sr_2IrO_4 [153]. Negative L_3 XMCD response and absence of L_2 XMCD

Sample	m_t (μ_B/Ir)	m_l (μ_B/Ir)	$m_{s,\text{eff}}$ (μ_B/Ir)	$ m_l/m_{s,\text{eff}} $
[LMO ₄ /SIO ₄] $\times 5$	-0.006 (\downarrow)	-0.008 (\downarrow)	0.002 (\uparrow)	4.61
[LFO ₄ /SIO ₄] $\times 5$	0.021 (\uparrow)	0.008 (\uparrow)	0.013 (\uparrow)	0.67
[LCO ₄ /SIO ₄] $\times 5$	0.015 (\uparrow)	0.006 (\uparrow)	0.009 (\uparrow)	0.67

Table 5.3: Ir magnetic moments, *i.e.*, m_t , m_l , $m_{s,\text{eff}}$ and orbital to spin moment ratio, *i.e.*, $|m_l/m_{s,\text{eff}}|$ estimated using the sum rule for [LXO₄/SIO₄] $\times 5$ (X = Mn, Fe and Co) SLs. The positive and negative moment values represent the moment parallel (\uparrow) or anti-parallel (\downarrow) to the applied magnetic field, respectively.

suggest the parallel alignment of the induced SIO net moments with applied magnetic field in LFO/SIO and LCO/SIO. The XMCD response in [LFO₄/SIO₄] $\times 5$ and [LCO₄/SIO₄] $\times 5$ SLs are very similar and are consistent with the XMCD experiments reported on LNO/SIO SLs [190].

For LMO/SIO, however, a positive Ir L_3 XMCD and an even larger positive Ir L_2 XMCD response are observed. A positive Ir L_3 and L_2 XMCD response have been previously reported for LSMO/SIO SLs [34, 35, 203]. The opposite XMCD response (positive and negative) clearly suggests different interfacial coupling mechanism in LMO/SIO and LXO/SIO (X = Fe, Co) SLs. Despite the different signs, the magnitude of the Ir L_3 XMCD response is comparable in these SLs.

Magneto-optical sum rules were applied to estimate the effective spin, orbital and total magnetic moments separately [137]. However, the rather weak XMCD response and problems associated with the sum rule analysis for 5d-Iridates, a quantitative estimation of the moments are rather challenging. For example, the experimental determination of magnetic dipole term $\langle T_z \rangle$ is challenging which limits the extraction of spin moments as $m_{s,\text{eff}} = m_s + 7\langle T_z \rangle$. Considering $\langle S_z \rangle / \langle T_z \rangle = 0.18$ (theoretically calculated value for Sr₂IrO₄ [153] and BaIrO₃ [204]) will result in $m_s \approx 0.61 \times m_{s,\text{eff}}$. In Table [5.3], we summarize the m_t , m_l , $m_{s,\text{eff}}$ moments and orbital-to-spin moment ratio, *i.e.*, $|m_l/m_{s,\text{eff}}|$ for [LXO₄/SIO₄] $\times 5$ SLs. In LFO/SIO and LCO/SIO SLs, both the m_l and $m_{s,\text{eff}}$ moments are found to be positive in accordance with the parallel alignment of the net moments with the applied magnetic field. The absence of Ir L_2 XMCD in these SLs results in a $|m_l/m_{s,\text{eff}}| = 2/3$, see Equ. [3.18]. However, in LMO/SIO SL, the total moments are dominated by the negative m_l resulting in a large $|m_l/m_{s,\text{eff}}| \approx 4.61$, consistent with the reports on other LSMO/SIO systems [34, 35, 102]. The above observations clearly demonstrate the different interfacial coupling at the LMO/SIO and LXO/SIO (X = Fe, Co) interfaces.

5.4 Discussion

We provided several experimental evidences confirming the ICT scenario at the LXO/SIO interfaces. Electronic (magneto-) transport and magnetization experiments on bilayers clearly show different behavior compared to the parent constituent layers and are related to the interfacial properties.

Theoretically, an ICT is predicted at the TMO interfaces resulting from the O-2p alignment and the differences in the work function. Based on the Fig. [5.1d] [68], an ICT from SIO to LXO ($X = \text{Mn, Fe, Co and Ni}$) is expected where the amount of the ICT will follow the following sequence: $\text{LMO} < \text{LFO} < \text{LCO} < \text{LNO}$.

This is indeed observed experimentally by Hall effect and XAS. For LMO/SIO, charge transfer is nearly negligible. This is consistent with literature [34, 102, 103]. Note that however, with increasing Sr doping at La site, distinct ICT from SIO to LSMO is reported in LSMO/SIO SLs [205] which becomes strongest for SMO/SIO (0.5 electron/ML) [35].

For LFO/SIO, LCO/SIO and LNO/SIO SLs, the charge transfer direction is still the same, *i.e.*, from SIO to LXO but the magnitude gradually increases for $X = \text{Fe}$ to $X = \text{Ni}$. Thus, the ICT direction and also the magnitude follow the same trend as predicted in Ref. [68], *i.e.*, $\text{LMO} < \text{LFO} < \text{LCO} < \text{LNO}$.

Qualitatively, we observe a very similar magnetic behavior of SIO in LFO/SIO and LCO/SIO SLs. The $m_{s,eff}$, m_l and m_t are positive and comparable, with orbital-to-spin moment ratio $m_l/m_{s,eff}$ amounts to $2/3$. The positive m_t shows the parallel alignment of the induced SIO moments with the applied magnetic field and that of the LXO layers. This suggests a very similar interfacial coupling mechanism in the LXO/SIO ($X = \text{Fe and Co}$) SLs. Our results are consistent with the recent observations reported for LNO/SIO SLs [190].

As already discussed in Chapter 4, we recall the recent DFT calculations performed on LCO/SIO SLs [165]. To understand the magnetic ground state in SIO, magnetic states and exchange energies were calculated. Considering only the dominant interactions, *i.e.*, between the nearest neighbors, three different interactions, J_{Co-Co} , J_{Co-Ir} and J_{Ir-Ir} , were calculated for different possible spin orientations. The calculated total energy (ground state) for each spin arrangement is found to be very sensitive to the structural relaxation. This again signifies the strong magneto-structural coupling commonly observed in iridates. Considering the energetically favored spin alignments, J_{Co-Co} shows positive value, *i.e.*, ferromagnetic ordering in LCO layer. The interfacial magnetic exchange, *i.e.*, J_{Co-Ir} , responsible for the magnetic coupling at the interface between Co and Ir, was also found positive, *i.e.*,

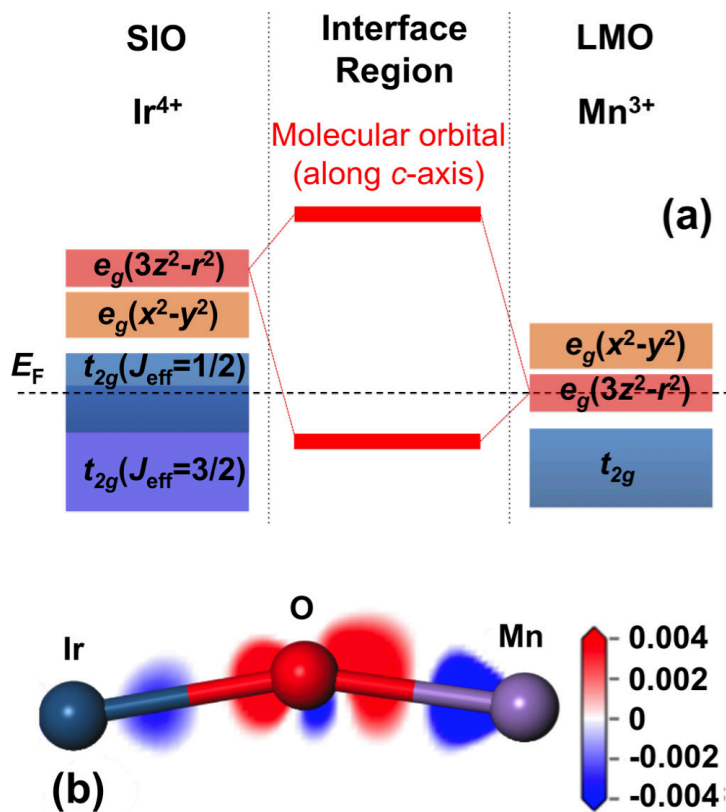


Figure 5.9: Molecular orbital formation and charge redistribution at LMO/SIO interface: (a) band alignment at the LMO/SIO interface along z direction hybridizes the $(3z^2 - r^2)$ orbitals of Ir $5d$ and Mn $3d$ and forms bonding and antibonding molecular orbitals, (b) calculated charge density at the interface showing increased density at the interface (O-atom). A relaxed SIO crystal structure with larger c -axis was considered for the DFT calculations [203].

parallel alignment of the interfacial Co and Ir moments.

In the absence of ICT, an anti-parallel alignment of $m_{s,\text{eff}}$ and m_l is not favored considering $J_{\text{eff}} = 1/2$ ground state in SIO at LMO/SIO interfaces. In perovskite Iridates, $J_{\text{eff}} = 1/2$ state is derived from the $5d_{5/2}$ ($J_{5/2}$, *i.e.*, $J = L + S$) orbitals. However, for $J_{\text{eff}} = 3/2$ derived from $5d_{3/2}$ ($J_{3/2}$, *i.e.*, $J = L - S$), an anti-parallel alignment of $m_{s,\text{eff}}$ and m_l is expected.

Hence, the absence of ICT and anti-parallel alignment of $m_{s,\text{eff}}$ and m_l strongly suggest redistribution of electrons within the $J_{\text{eff}} = 1/2$ and $3/2$ states in LMO/SIO [34, 203]. This is also evident from the BR calculation for SIO/LMO SL. Despite the nearly similar integrated WL sum area (*i.e.*, the hole density), the BR is smaller for LMO/SIO SL compared to SIO, see Table [5.2]. The redistribution is very likely enabled by a Ir-O-Mn molecular orbital (MO) at the LMO/SIO interface [35, 145, 147, 203]. In Fig. [5.9], we show the schematic of a MO formation and the redistribution of electron density calculated by DFT [203]. The $(3z^2 - r^2)$ orbitals of Ir $5d$ and Mn $3d$ hybridize along the surface normal direction z and form

bonding and antibonding MOs at the interface [206], see Fig. [5.9a]. The $(3z^2 - r^2)$ have much stronger hybridization along the z -direction compared to $(x^2 - y^2)$ orbitals. This is consistent with the partial density of states (PDOS) calculations. The calculated charge density difference at the interfacial atoms are shown in Fig. [5.9b]. An increased charge density is visible at the interface region near O-atoms. The bonding MO lies below Fermi energy E_F of constituent SIO and LMO layers, favoring the redistribution of electrons from different orbitals. Interfacial electrons from $J_{\text{eff}} = 1/2$ and $3/2$ transfer to the bonding MO resulting in a changed local electronic structure and BR alike. The redistribution consequently will have strong effect on $m_{s,\text{eff}}$, m_l and their relative alignment, depending on the fraction of $J_{\text{eff}} = 1/2$ and $3/2$ electrons in the bonding MO orbitals [34]. The increased $|m_l/m_{s,\text{eff}}|$ ratio observed in LMO/SIO SL also favors such scenario at the interface, see Table [5.3].

The MO formation scenario due to Ir-X coupling is expected to be stronger at LMO/SIO interfaces compared to other LXO/SIO ($X = \text{Fe}, \text{Co}$ and Ni). In LMO/SIO, the Fermi energy mismatch (ΔE_F) is smallest compared to the other LXO/SIO ($X = \text{Fe}, \text{Co}$ and Ni), see Fig. [5.1c]. In contrast, a weaker hybridization between Ir $5d$ and X $3d$ ($3z^2 - r^2$) orbitals is expected in other LXO/SIO ($X = \text{Fe}, \text{Co}$ and Ni). An increase in ΔE_F obviously favors interfacial electron transfer rather than charge redistribution via MOs, as observed at the LMO/SIO interface. Note that this is only a qualitative description, and electronic structure calculations are needed to confirm the energy range of X^{3+} states in LXO. In our study, no strict correlation between the induced moments in SIO and ICT and the choice of $3d$ -TMO (FM or AFM) is observed.

Lastly, we focus on the strength of the AHE. AHE is strongest in LMO/SIO and LCO/SIO ($\sigma_{xy}^{\text{AHE},s} \sim 8\text{-}10 \Omega^{-1}\text{cm}^{-1}$) but significantly weaker when SIO is coupled to an AFM, *i.e.*, LFO/SIO ($\sigma_{xy}^{\text{AHE},s} \sim 0.5 \Omega^{-1}\text{cm}^{-1}$). Despite the nearly similar induced magnetic moment in SIO, the AHE shows a large variation in LCO/SIO ($\sim 8\text{-}10 \Omega^{-1}\text{cm}^{-1}$) and LFO/SIO ($0.5 \Omega^{-1}\text{cm}^{-1}$), indicating only a minor influence of the induced magnetization in SIO on AHE. It seems more likely that the local effective magnetic field (B_{eff}) at the interface originating from the $3d$ TMO layer plays a crucial role [207]. Naturally, AHE increases with increasing B_{eff} , making it rather insensitive to induced SIO magnetization in the film plane. However, the spin canting due to octahedral distortion may result in some weak residual component (M_z) that could affect AHE (σ_{xy}^{AHE}).

CHAPTER 6

Conclusion & Future Directions

Stay hungry stay foolish.

Steve Jobs, *originally took from the Whole Earth Catalog (1974)*

The presented thesis started with an aim towards realizing a new spin-polarized two-dimensional electron system on the base of correlated quantum materials. The main idea was to add magnetically active layers to an already existing 2DES and to create spin-polarization by magnetic proximity effects. In this direction, we started with heterostructures involving ultrathin (quasi 2D) spin-orbit coupled $5d$ semimetal SIO and $3d$ ferromagnetic insulator LCO. Such artificial $3d/5d$ multilayers also provide a unique playground to explore the exotic physics originating from the competition between strong spin-orbit coupling and electron correlation at the interface of these HSs.

High-quality epitaxial thin films, heterostructures and superlattices were produced by the pulsed laser epitaxy method. The growth was monitored in-situ using reflection high energy electron diffraction, which allowed growth to be controlled on the precision of one atomic layer with atomically sharp interfaces and specific atomic termination. Prior to sample preparation, growth parameters were optimized for each material with respect to the structural quality and composition.

The structural properties of thin films ($t < 15$ nm) are usually influenced by the lattice parameter and crystal symmetry of the substrate material. The structural properties, *e.g.*, crystalline quality, epitaxy, lattice parameters and octahedral distortions, were investigated using high-resolution X-ray diffraction. The growth of 10 ML thick SIO and LCO thin films on STO (001) results in a tetragonal symmetry due to the epitaxial strained growth, in contrast to the orthorhombic (rhombohedral) symmetry of bulk SIO (LCO). The octahedral rotation pattern, which strongly influences the hybridization between B site transition metals and consequently, electronic properties, were investigated by measuring specific orthorhombic distortions. Surprisingly, rotations about in-plane axes (a & b) were found to be suppressed and only an out-of-phase rotation about the c -axis was observed for both SIO and LCO corresponding to a rotation pattern of $(a^0 a^0 c^-)$ in stark contrast to $(a^+ a^+ c^-)$ and $(a^- a^- c^-)$ of bulk SIO and LCO, respectively. The suppression of in-plane rotations in SIO and LCO are very likely related to the bond angle adaptation to the cubic STO ($a^0 a^0 a^0$) substrate due to epitaxy. TEM cross-section analysis reveals atomically sharp interfaces with no distinct interdiffusion of cations across the interface. The stoichiometric composition was confirmed by electron energy loss spectroscopy.

Electronic transport properties were measured on Hall bar structured thin films, HSs and SLs. LCO single-layer films show highly insulating behavior, whereas SIO single-layer and LCO/STO/SIO HS show nearly identical resistivity behavior consistent with the semi-metallic nature of SIO films. In contrast, LCO/SIO bilayer shows increased resistivity com-

pared to SIO and LCO/STO/SIO. Resistivity increases with decreasing temperature ($d\rho/dT < 0$) with a distinct reduction of the slope $\partial\rho/\partial T$ below 100 K.

LCO/SIO bilayer shows anomalous Hall resistivity and a negative contribution to magnetoresistance below 100 K. The AHR and NMR increase with decreasing temperature and become dominant below 30 K. The hysteretic field dependence and coercive field of AMR and NMR are very similar and suggest to share the same origin. For $T \leq 30$ K, anomalous Hall conductivity was found to be independent of longitudinal conductivity, suggesting intrinsic AHE as the dominant contribution. The electron concentration (n_e) is estimated from ordinary Hall measurement at $T = 150$ K and amounts to $n_e = 1.0 \times 10^{21} \text{ cm}^{-3}$ in LCO/SIO bilayer, which is about half the n_e observed in LCO/STO/SIO trilayer HS ($n_e = 1.9 \times 10^{21} \text{ cm}^{-3}$). The angle-dependent MRs were measured by rotating the magnetic field in the film plane. Beside the normal two-fold symmetric anisotropic MR (AMR) component, a four-fold magnetocrystalline anisotropy contribution with (110) easy direction was observed. The observation of AHR, NMR and magnetocrystalline anisotropy AMR strongly advocate for proximity-induced magnetism in SIO. Suppression of these effects with increasing SIO thickness as well as insertion of STO(4) in between LCO/SIO (as in LCO/STO/SIO) also support this scenario. Element-specific X-ray magnetic circular dichroism confirms enhanced induced Ir moments at the interface. Meanwhile, a rather small total moment of $0.02 \mu_B/\text{Ir}$ was estimated using the magneto-optical sum rule. The net SIO moment was found to be aligned parallel to that of LCO.

Electronic transport and magnetization were also probed as a function of electrostatic gating, *i.e.*, charge carrier modulation. A giant tunability of AHR ($\times 7$), NMR ($\times 7$) and two-fold symmetric AMR ($\times 5$) was observed as a function of gate voltage. However, the XMCD response at the Ir site, *i.e.*, magnetism in SIO, did not show any gate voltage (or doping) induced changes. As proposed by DFT calculations, the giant tunability is most likely related to the topological band properties of SIO in LCO/SIO HSs and SLs. Berry curvature manipulation as a function of gate voltage (*i.e.* doping) reasonably explains the giant tunability of AHR in SIO.

To obtain more general insights into the proximity effect, interfacial coupling and exchange in $3d/5d$ HSs, we studied different HSs: LXO(NNO)/SIO ($X = \text{Mn, Fe and Co}$). All four HSs display AHE and NMR; however, the effects are stronger in the case of a FM LXO layer compared to an AFM LXO layer. An ICT from SIO to LXO, as expected for $3d/5d$ HSs, was evidenced by electronic transport and spectroscopy. The observed Ir moments $m_{s,\text{eff}}$, m_l are very similar in LXO/SIO SLs ($X = \text{Mn, Fe and Co}$). However, $m_{s,\text{eff}}$ and m_l alignment

differs for LMO/SIO ($\uparrow\downarrow$) and LFO/SIO ($\uparrow\uparrow$), LCO/SIO ($\uparrow\uparrow$), indicating a non-trivial correlation to the observed ICT or spin-configuration of the neighbored LXO layer. In the absence of an ICT, the anti-parallel alignment of $m_{s,eff}$ and m_l moments and large $|m_l/m_{s,eff}|$ ratio in LMO/SIO indicate significant electron redistribution between Ir $5d_{5/2}$ - $5d_{3/2}$ states. The formation of interfacial MOs might explain the possibility of electron redistribution on the Ir-site, enabling a change of L-S coupling.

The results obtained in this thesis provide important information on the interfacial properties of $3d/5d$ HSs and demonstrate effective coupling between perovskite-related $3d$ -TMO and $5d$ -SIO. The results also demonstrate the **strong interplay of lattice, charge, spin-orbit coupling and electron correlation at the artificial $3d$ - $5d$ transition metal oxide interfaces** and emphasize efficient manipulation of the nontrivial topological band properties of SIO by structural and electronic modifications.

Tuning the energy level of $3d/5d$ states by epitaxial strain or hydrostatic pressure is expected to modify the interfacial coupling. The molecular orbital formation scenario, which strongly depends on the relative energy of the $3d e_g$ and the Ir $J_{eff} = 1/2$ states, will affect the ICT or charge redistribution. Using different lattice-matched substrates (utilizing compressive and tensile strain) or applying hydrostatic pressure on LMO/SIO SLs are promising tools to vary interfacial coupling. Moreover, the enhanced competition between spin-orbit coupling and electron correlation is expected to result in a rich phase diagram with respect to exotic quantum states.

Bibliography

- [1] Albert Fert, Ramamoorthy Ramesh, Vincent Garcia, Fèlix Casanova, and Manuel Bibes. Electrical control of magnetism by electric field and current-induced torques. *Rev. Mod. Phys.*, 96:015005, Mar 2024.
- [2] Gordon E Moore. Cramming more components onto integrated circuits. *Proceedings of the IEEE*, 86(1):82–85, 1998.
- [3] Nicola Jones et al. How to stop data centres from gobbling up the world’s electricity. *Nature*, 561(7722):163–166, 2018.
- [4] Daniel Khomskii. *Transition metal compounds*. Cambridge University Press, 2014.
- [5] Pavlo Zubko, Stefano Gariglio, Marc Gabay, Philippe Ghosez, and Jean-Marc Triscone. Interface physics in complex oxide heterostructures. *Annu. Rev. Condens. Matter Phys.*, 2(1):141–165, 2011.
- [6] Marionna Coll, Josep Fontcuberta, Matthias Althammer, Manuel Bibes, Hans Boschker, Alberto Calleja, Guanglei Cheng, M Cuoco, Regina Dittmann, B Dkhil, et al. Towards oxide electronics: a roadmap. *Applied surface science*, 482:1–93, 2019.
- [7] Harold Y Hwang, Yoh Iwasa, Masashi Kawasaki, Bernhard Keimer, Naoto Nagaosa, and Yoshinori Tokura. Emergent phenomena at oxide interfaces. *Nature materials*, 11(2):103–113, 2012.
- [8] Manuel Bibes, Javier E Villegas, and Agnès Barthélémy. Ultrathin oxide films and interfaces for electronics and spintronics. *Advances in Physics*, 60(1):5–84, 2011.
- [9] Jürg Hulliger, Muhammad Aslam Awan, Bernhard Trusch, and Till A Samtleben. Chemical diversity in view of property generation by a new combinatorial approach. *Zeitschrift für anorganische und allgemeine Chemie*, 631(6-7):1255–1260, 2005.
- [10] Darrell G Schlom. Perspective: Oxide molecular-beam epitaxy rocks! *APL materials*, 3(6), 2015.
- [11] William Nunn, Tristan K Truttmann, and Bharat Jalan. A review of molecular-beam epitaxy of wide bandgap complex oxide semiconductors. *Journal of materials research*, pages 1–19, 2021.

- [12] Hans M Christen and Gyula Eres. Recent advances in pulsed-laser deposition of complex oxides. *Journal of Physics: Condensed Matter*, 20(26):264005, 2008.
- [13] Gertjan Koster, Mark Huijben, and Guus Rijnders. *Epitaxial growth of complex metal oxides*. Elsevier, 2015.
- [14] Matthew Dawber, Nicolas Stucki, Celine Lichtensteiger, Stefano Gariglio, Philippe Ghosez, and J-M Triscone. Tailoring the properties of artificially layered ferroelectric superlattices. *Advanced Materials*, 19(23):4153–4159, 2007.
- [15] A Ohtomo and HY Hwang. A high-mobility electron gas at the LaAlO₃/SrTiO₃ heterointerface. *Nature*, 427(6973):423–426, 2004.
- [16] The interface is still the device - Nature Materials — nature.com. <https://www.nature.com/articles/nmat3244#citeas>.
- [17] Nicolas Reyren, Stefan Thiel, AD Caviglia, L Fitting Kourkoutis, German Hammerl, Christoph Richter, Christof W Schneider, Thilo Kopp, A-S Ruetschi, Didier Jaccard, et al. Superconducting interfaces between insulating oxides. *Science*, 317(5842):1196–1199, 2007.
- [18] AD Caviglia, Stefano Gariglio, Nicolas Reyren, Didier Jaccard, T Schneider, M Gabay, Stefan Thiel, German Hammerl, Jochen Mannhart, and J-M Triscone. Electric field control of the LaAlO₃/SrTiO₃ interface ground state. *Nature*, 456(7222):624–627, 2008.
- [19] AD Caviglia, M Gabay, Stefano Gariglio, Nicolas Reyren, Claudia Cancellieri, and J-M Triscone. Tunable rashba spin-orbit interaction at oxide interfaces. *Physical review letters*, 104(12):126803, 2010.
- [20] Julie A Bert, Beena Kalisky, Christopher Bell, Minu Kim, Yasuyuki Hikita, Harold Y Hwang, and Kathryn A Moler. Direct imaging of the coexistence of ferromagnetism and superconductivity at the LaAlO₃/SrTiO₃ interface. *Nature physics*, 7(10):767–771, 2011.
- [21] Pouya Moetakef, James R Williams, Daniel G Ouellette, Adam P Kajdos, David Goldhaber-Gordon, S James Allen, and Susanne Stemmer. Carrier-controlled ferromagnetism in SrTiO₃. *Physical Review X*, 2(2):021014, 2012.
- [22] Edouard Lesne, Yu Fu, Simón Oyarzún, Juan Carlos Rojas-Sánchez, DC Vaz, H Naganuma, Giuseppe Sicoli, J-P Attané, Matthieu Jamet, E Jacquet, et al. Highly efficient and tunable spin-to-charge conversion through rashba coupling at oxide interfaces. *Nature materials*, 15(12):1261–1266, 2016.
- [23] Paul Noël, Felix Trier, Luis M Vicente Arche, Julien Bréhin, Diogo C Vaz, Vincent Garcia, Stéphane Fusil, Agnès Barthélémy, Laurent Vila, Manuel Bibes, et al. Non-volatile electric control of spin–charge conversion in a SrTiO₃ rashba system. *Nature*, 580(7804):483–486, 2020.

-
- [24] Supriyo Datta and Biswajit Das. Electronic analog of the electro-optic modulator. *Applied Physics Letters*, 56(7):665–667, 1990.
- [25] Sasikanth Manipatruni, Dmitri E Nikonov, Chia-Ching Lin, Tanay A Gosavi, Huichu Liu, Bhagwati Prasad, Yen-Lin Huang, Everton Bonturim, Ramamoorthy Ramesh, and Ian A Young. Scalable energy-efficient magnetoelectric spin–orbit logic. *Nature*, 565(7737):35–42, 2019.
- [26] Wei Niu, Xuefeng Wang, Yongbing Xu, and Rong Zhang. Recent advances on spin-polarized two-dimensional electron gases at oxide interfaces. *ACS Applied Electronic Materials*, 3(1):128–144, 2021.
- [27] D-S Park, AD Rata, IV Maznichenko, S Ostanin, YL Gan, S Agrestini, GJ Rees, M Walker, J Li, J Herrero-Martin, et al. The emergence of magnetic ordering at complex oxide interfaces tuned by defects. *Nature communications*, 11(1):3650, 2020.
- [28] M Salluzzo, Stefano Gariglio, Daniela Stornaiuolo, V Sessi, S Rusponi, C Piamonteze, GM De Luca, M Minola, D Marré, A Gadaleta, et al. Origin of interface magnetism in $\text{BiMnO}_3/\text{SrTiO}_3$ and $\text{LaAlO}_3/\text{SrTiO}_3$ heterostructures. *Physical review letters*, 111(8):087204, 2013.
- [29] Natalya Pavlenko, Thilo Kopp, EY Tsymbal, Jochen Mannhart, and GA Sawatzky. Oxygen vacancies at titanate interfaces: Two-dimensional magnetism and orbital reconstruction. *Physical Review B*, 86(6):064431, 2012.
- [30] Daniela Stornaiuolo, C Cantoni, GM De Luca, Roberto Di Capua, Emiliano Di. Genaro, G Ghiringhelli, Benoit Jouault, D Marrè, Davide Massarotti, F Miletto Granozio, et al. Tunable spin polarization and superconductivity in engineered oxide interfaces. *Nature materials*, 15(3):278–283, 2016.
- [31] HR Zhang, Y Zhang, H Zhang, J Zhang, X Shen, XX Guan, YZ Chen, RC Yu, Nini Pryds, YS Chen, et al. Magnetic two-dimensional electron gas at the manganite-buffered $\text{LaAlO}_3/\text{SrTiO}_3$ interface. *Physical Review B*, 96(19):195167, 2017.
- [32] William Witczak-Krempa, Gang Chen, Yong Baek Kim, and Leon Balents. Correlated quantum phenomena in the strong spin-orbit regime. *Annu. Rev. Condens. Matter Phys.*, 5(1):57–82, 2014.
- [33] Jobu Matsuno, Naoki Ogawa, Kenji Yasuda, Fumitaka Kagawa, Wataru Koshibae, Naoto Nagaosa, Yoshinori Tokura, and Masashi Kawasaki. Interface-driven topological hall effect in $\text{SrRuO}_3 - \text{SrIrO}_3$ bilayer. *Science advances*, 2(7):e1600304, 2016.
- [34] Di Yi, Jian Liu, Shang-Lin Hsu, Lipeng Zhang, Yongseong Choi, Jong-Woo Kim, Zuhuang Chen, James D Clarkson, Claudy R Serrao, Elke Arenholz, et al. Atomic-scale control of magnetic anisotropy via novel spin–orbit coupling effect in $\text{La}_{2/3}\text{Sr}_{1/3}\text{MnO}_3/\text{SrIrO}_3$ superlattices. *Proceedings of the National Academy of Sciences*, 113(23):6397–6402, 2016.

- [35] John Nichols, Xiang Gao, Shinbuhm Lee, Tricia L Meyer, John W Freeland, Valeria Lauter, Di Yi, Jian Liu, Daniel Haskel, Jonathan R Petrie, et al. Emerging magnetism and anomalous hall effect in iridate–manganite heterostructures. *Nature communications*, 7(1):12721, 2016.
- [36] Arun Kumar Jaiswal, Di Wang, Vanessa Wollersen, Rudolf Schneider, Matthieu Le Tacon, and Dirk Fuchs. Direct observation of strong anomalous hall effect and proximity-induced ferromagnetic state in SrIrO₃. *Advanced Materials*, 34(14):2109163, 2022.
- [37] Shingo Kaneta-Takada, Miho Kitamura, Shoma Arai, Takuma Arai, Ryo Okano, Le Duc Anh, Tatsuro Endo, Koji Horiba, Hiroshi Kumigashira, Masaki Kobayashi, et al. Giant spin-to-charge conversion at an all-epitaxial single-crystal-oxide rashba interface with a strongly correlated metal interlayer. *Nature communications*, 13(1):5631, 2022.
- [38] Adarsh S Patri, Kyusung Hwang, Hyun-Woo Lee, and Yong Baek Kim. Theory of large intrinsic spin hall effect in iridate semimetals. *Scientific reports*, 8(1):8052, 2018.
- [39] Tianxiang Nan, TJ Anderson, J Gibbons, K Hwang, N Campbell, H Zhou, YQ Dong, GY Kim, DF Shao, TR Paudel, et al. Anisotropic spin-orbit torque generation in epitaxial SrIrO₃ by symmetry design. *Proceedings of the National Academy of Sciences*, 116(33):16186–16191, 2019.
- [40] Arnoud S Everhardt, DC Mahendra, Xiaoxi Huang, Shehrin Sayed, Tanay A Gosavi, Yunlong Tang, Chia-Ching Lin, Sasikanth Manipatruni, Ian A Young, Supriyo Datta, et al. Tunable charge to spin conversion in strontium iridate thin films. *Physical Review Materials*, 3(5):051201, 2019.
- [41] Hailong Wang, Keng-Yuan Meng, Pengxiang Zhang, Justin T Hou, Joseph Finley, Jiahao Han, Fengyuan Yang, and Luqiao Liu. Large spin-orbit torque observed in epitaxial SrIrO₃ thin films. *Applied Physics Letters*, 114(23), 2019.
- [42] Liang Liu, Qing Qin, Weinan Lin, Changjian Li, Qidong Xie, Shikun He, Xinyu Shu, Chenghang Zhou, Zhishiuh Lim, Jihang Yu, et al. Current-induced magnetization switching in all-oxide heterostructures. *Nature nanotechnology*, 14(10):939–944, 2019.
- [43] S Crossley, AG Swartz, K Nishio, Y Hikita, and HY Hwang. All-oxide ferromagnetic resonance and spin pumping with SrIrO₃. *Physical Review B*, 100(11):115163, 2019.
- [44] Xiaoxi Huang, Shehrin Sayed, Joseph Mittelstaedt, Sandhya Susarla, Saba Karimed-diny, Lucas Caretta, Hongrui Zhang, Vladimir A Stoica, Tanay Gosavi, Farzad Mahfouzi, et al. Novel spin-orbit torque generation at room temperature in an all-oxide epitaxial La_{0.7}Sr_{0.3}MnO₃/SrIrO₃ system. *Advanced Materials*, 33(24):2008269, 2021.

- [45] James M Rondinelli, Steven J May, and John W Freeland. Control of octahedral connectivity in perovskite oxide heterostructures: An emerging route to multifunctional materials discovery. *MRS bulletin*, 37(3):261–270, 2012.
- [46] Victor Moritz Goldschmidt. Die gesetze der krystallochemie. *Naturwissenschaften*, 14(21):477–485, 1926.
- [47] Ghanshyam Pilania, Prasanna Venkataraman Balachandran, James E Gubernatis, and Turab Lookman. Classification of abo₃ perovskite solids: a machine learning study. *Acta Crystallographica Section B: Structural Science, Crystal Engineering and Materials*, 71(5):507–513, 2015.
- [48] Anthony M Glazer. The classification of tilted octahedra in perovskites. *Acta Crystallographica Section B: Structural Crystallography and Crystal Chemistry*, 28(11):3384–3392, 1972.
- [49] AM Glazer. Simple ways of determining perovskite structures. *Acta Crystallographica Section A: Crystal Physics, Diffraction, Theoretical and General Crystallography*, 31(6):756–762, 1975.
- [50] James M Rondinelli and Nicola A Spaldin. Structure and properties of functional oxide thin films: insights from electronic-structure calculations. *Advanced materials*, 23(30):3363–3381, 2011.
- [51] Introduction to Crystal Field Theory — go. <https://chem.libretexts.org/@go/page/6520>.
- [52] John Hubbard. Electron correlations in narrow energy bands. *Proceedings of the Royal Society of London. Series A. Mathematical and Physical Sciences*, 276(1365):238–257, 1963.
- [53] Junjiro Kanamori. Electron correlation and ferromagnetism of transition metals. *Progress of Theoretical Physics*, 30(3):275–289, 1963.
- [54] Martin C Gutzwiller. Effect of correlation on the ferromagnetism of transition metals. *Physical Review Letters*, 10(5):159, 1963.
- [55] Michael Chapman and Carlos SA De Melo. Atoms playing dress-up. *Nature*, 471(7336):41–42, 2011.
- [56] Jeferson A Dias, Marcos AS Andrade Jr, Hugo LS Santos, Márcio R Morelli, and Lucia H Mascaro. Lanthanum-based perovskites for catalytic oxygen evolution reaction. *ChemElectroChem*, 7(15):3173–3192, 2020.
- [57] Rainer Schmidt, J Wu, C Leighton, and I Terry. Dielectric response to the low-temperature magnetic defect structure and spin state transition in polycrystalline LaCoO₃. *Physical Review B*, 79(12):125105, 2009.

- [58] D Fuchs, E Arac, C Pinta, S Schuppler, R Schneider, and H v Löhneysen. Tuning the magnetic properties of LaCoO_3 thin films by epitaxial strain. *Physical Review B*, 77(1):014434, 2008.
- [59] M Merz, P Nagel, C Pinta, A v Samartsev, H v Löhneysen, M Wissinger, S Uebe, A Assmann, D Fuchs, and S Schuppler. X-ray absorption and magnetic circular dichroism of LaCoO_3 , $\text{La}_{0.7}\text{Ce}_{0.3}\text{CoO}_3$, and $\text{La}_{0.7}\text{Sr}_{0.3}\text{CoO}_3$ films: Evidence for cobalt-valence-dependent magnetism. *Physical Review B*, 82(17):174416, 2010.
- [60] Yoshihiko Kobayashi, Toru Mitsunaga, Go Fujinawa, Tadashi Aarii, Miki Suetake, Kichizo Asai, and Jimpei Harada. Structural phase transition from rhombohedral to cubic in LaCoO_3 . *Journal of the Physical Society of Japan*, 69(10):3468–3469, 2000.
- [61] P. G. Radaelli and S.-W. Cheong. Structural phenomena associated with the spin-state transition in LaCoO_3 . *Phys. Rev. B*, 66:094408, Sep 2002.
- [62] D Fuchs, C Pinta, T Schwarz, P Schweiss, P Nagel, S Schuppler, R Schneider, M Merz, G Roth, and H v Löhneysen. Ferromagnetic order in epitaxially strained LaCoO_3 thin films. *Physical Review B*, 75(14):144402, 2007.
- [63] P Raychaudhuri, C Mitra, PDA Mann, and S Wirth. Phase diagram and hall effect of the electron doped manganite $\text{La}_{1-x}\text{Ce}_x\text{MnO}_3$. *Journal of applied physics*, 93(10):8328–8330, 2003.
- [64] LM Zheng, X Renshaw Wang, WM Lü, CJ Li, Tula R Paudel, ZQ Liu, Z Huang, SW Zeng, Kun Han, ZH Chen, et al. Ambipolar ferromagnetism by electrostatic doping of a manganite. *Nature communications*, 9(1):1897, 2018.
- [65] Dirk Fuchs, Thorsten Schwarz, Oswaldo Morán, Peter Schweiss, and Rudolf Schneider. Finite-size shift of the curie temperature of ferromagnetic lanthanum cobaltite thin films. *Physical Review B*, 71(9):092406, 2005.
- [66] D Fuchs, M Merz, P Nagel, R Schneider, S Schuppler, and H Von Löhneysen. Double exchange via t_2g orbitals and the jahn-teller effect in ferromagnetic $\text{La}_{0.7}\text{Sr}_{0.3}\text{CoO}_3$ probed by epitaxial strain. *Physical Review Letters*, 111(25):257203, 2013.
- [67] Shanna Zhu, Dechao Meng, Genhao Liang, Gang Shi, Peng Zhao, Peng Cheng, Yongqing Li, Xiaofang Zhai, Yalin Lu, Lan Chen, et al. Proximity-induced magnetism and an anomalous hall effect in $\text{Bi}_2\text{Se}_3/\text{LaCoO}_3$: A topological insulator/ferromagnetic insulator thin film heterostructure. *Nanoscale*, 10(21):10041–10049, 2018.
- [68] Zhicheng Zhong and Philipp Hansmann. Band alignment and charge transfer in complex oxide interfaces. *Physical Review X*, 7(1):011023, 2017.
- [69] Lin Hao, Di Yi, Meng Wang, Jian Liu, and Pu Yu. Emergent quantum phenomena in atomically engineered iridate heterostructures. *Fundamental Research*, 3(3):313–321, 2023.

- [70] George Jackeli and Giniyat Khaliullin. Mott insulators in the strong spin-orbit coupling limit: from heisenberg to a quantum compass and kitaev models. *Physical review letters*, 102(1):017205, 2009.
- [71] Xiaoran Liu, Yanwei Cao, B Pal, S Middey, M Kareev, Y Choi, P Shafer, D Haskel, E Arenholz, and J Chakhalian. Synthesis and electronic properties of ruddlesden-popper strontium iridate epitaxial thin films stabilized by control of growth kinetics. *Physical review materials*, 1(7):075004, 2017.
- [72] SJ Moon, Hosub Jin, Kyung Wan Kim, WS Choi, YS Lee, Jaejun Yu, G Cao, A Sumi, H Funakubo, Christian Bernhard, et al. Dimensionality-controlled insulator-metal transition and correlated metallic state in 5d transition metal oxides $\text{Sr}_{n+1}\text{Ir}_n\text{O}_{3n+1}$ ($n=1, 2, \text{ and } \infty$). *Physical review letters*, 101(22):226402, 2008.
- [73] M Ahsan Zeb and Hae-Young Kee. Interplay between spin-orbit coupling and hubbard interaction in SrIrO_3 and related pbnm perovskite oxides. *Physical Review B*, 86(8):085149, 2012.
- [74] Lunyong Zhang, Bin Pang, YB Chen, and Yanfeng Chen. Review of spin-orbit coupled semimetal SrIrO_3 in thin film form. *Critical Reviews in Solid State and Materials Sciences*, 43(5):367–391, 2018.
- [75] Abhijit Biswas, Ki-Seok Kim, and Yoon Hee Jeong. Metal insulator transitions in perovskite SrIrO_3 thin films. *Journal of applied physics*, 116(21), 2014.
- [76] Philipp Schütz, Domenico Di Sante, Lenart Dudy, Judith Gabel, Martin Stübinger, Martin Kamp, Y Huang, M Capone, M-A Husanu, VN Strocov, et al. Dimensionality-driven metal-insulator transition in spin-orbit-coupled SrIrO_3 . *Physical review letters*, 119(25):256404, 2017.
- [77] JM Longo, JA Kafalas, and RJ Arnott. Structure and properties of the high and low pressure forms of SrIrO_3 . *Journal of Solid State Chemistry*, 3(2):174–179, 1971.
- [78] TJ Anderson, S Ryu, H Zhou, L Xie, JP Podkaminer, Y Ma, J Irwin, XQ Pan, MS Rzechowski, and CB Eom. Metastable honeycomb $\text{SrTiO}_3/\text{SrIrO}_3$ heterostructures. *Applied Physics Letters*, 108(15), 2016.
- [79] JG Zhao, LX Yang, Y Yu, FY Li, RC Yu, Z Fang, LC Chen, and CQ Jin. High-pressure synthesis of orthorhombic SrIrO_3 perovskite and its positive magnetoresistance. *Journal of applied physics*, 103(10), 2008.
- [80] Peter ER Blanchard, Emily Reynolds, Brendan J Kennedy, Justin A Kimpton, Maxim Avdeev, and Alexei A Belik. Anomalous thermal expansion in orthorhombic perovskite SrIrO_3 : Interplay between spin-orbit coupling and the crystal lattice. *Physical Review B*, 89(21):214106, 2014.
- [81] J Fujioka, T Okawa, A Yamamoto, and Y Tokura. Correlated dirac semimetallic state with unusual positive magnetoresistance in strain-free perovskite SrIrO_3 . *Physical Review B*, 95(12):121102, 2017.

- [82] I Pallecchi, MT Buscaglia, V Buscaglia, E Gilioli, G Lamura, F Telesio, MR Cimberle, and D Marré. Thermoelectric behavior of ruddlesden–popper series iridates. *Journal of Physics: Condensed Matter*, 28(6):065601, 2016.
- [83] Hao Zheng, Jsaminka Terzic, Feng Ye, Xiangang G Wan, D Wang, Jinchen Wang, Xiaoping Wang, Pedro Schlottmann, SJ Yuan, and Gang Cao. Simultaneous metal-insulator and antiferromagnetic transitions in orthorhombic perovskite iridate $\text{Sr}_{0.94}\text{Ir}_{0.78}\text{O}_{2.68}$ single crystals. *Physical Review B*, 93(23):235157, 2016.
- [84] Fei-Xiang Wu, Jian Zhou, LY Zhang, Yan-feng B Chen, Shan-Tao Zhang, Zheng-Bin Gu, Shu-Hua Yao, and Yan-Feng Chen. Metal–insulator transition in SrIrO_3 with strong spin–orbit interaction. *Journal of Physics: Condensed Matter*, 25(12):125604, 2013.
- [85] John H Gruenewald, John Nichols, Jasminka Terzic, Gang Cao, Joseph W Brill, and Sung S Ambrose Seo. Compressive strain-induced metal–insulator transition in orthorhombic SrIrO_3 thin films. *Journal of Materials Research*, 29(21):2491–2496, 2014.
- [86] Jian Liu, J-H Chu, C Rayan Serrao, D Yi, J Koralek, C Nelson, C Frontera, D Kriegner, L Horak, E Arenholz, et al. Tuning the electronic properties of $j_{\text{eff}}=1/2$ correlated semimetal in epitaxial perovskite SrIrO_3 . *arXiv preprint arXiv:1305.1732*, 2013.
- [87] Abhijit Biswas and Yoon Hee Jeong. Effects of substrate temperature on the unusual non-fermi liquid metal to insulator transition in perovskite SrIrO_3 thin films. *Journal of Physics D: Applied Physics*, 48(13):135303, 2015.
- [88] Jin-Seok Chung, Seung Yup Jang, Soon Jae Moon, and Byung Chul Jeon. Pld growth behavior of epitaxially stabilized 5d perovskite SrIrO_3 thin films. *Journal of the Korean Physical Society*, 56(6):1814–1817, 2010.
- [89] DJ Groenendijk, N Manca, G Mattoni, L Kootstra, S Gariglio, Y Huang, E Van Heumen, and AD Caviglia. Epitaxial growth and thermodynamic stability of $\text{SrIrO}_3/\text{SrTiO}_3$ heterostructures. *Applied Physics Letters*, 109(4), 2016.
- [90] KR Kleindienst, K Wolff, J Schubert, R Schneider, and D Fuchs. Structural properties and anisotropic electronic transport in SrIrO_3 . *Physical Review B*, 98(11):115113, 2018.
- [91] AK Jaiswal, R Schneider, R Singh, and D Fuchs. Suppression of twinning and enhanced electronic anisotropy of SrIrO_3 films. *Applied Physics Letters*, 115(3), 2019.
- [92] Jean-Michel Carter, V Vijay Shankar, M Ahsan Zeb, and Hae-Young Kee. Semimetal and topological insulator in perovskite iridates. *Physical Review B*, 85(11):115105, 2012.
- [93] Amit Chauhan and BRK Nanda. Exploration of trivial and nontrivial electronic phases and of collinear and noncollinear magnetic phases in low-spin d^5 perovskites. *Physical Review B*, 105(4):045127, 2022.

-
- [94] Yuefeng F Nie, PDC King, CH Kim, M Uchida, HI Wei, Brendan D Faeth, JP Ruf, JPC Ruff, L Xie, X Pan, et al. Interplay of spin-orbit interactions, dimensionality, and octahedral rotations in semimetallic SrIrO₃. *Physical review letters*, 114(1):016401, 2015.
- [95] Nicola Manca, Dirk J Groenendijk, Ilaria Palleschi, Carmine Autieri, Lucas MK Tang, Francesca Telesio, Giordano Mattoni, Alix McCollam, Silvia Picozzi, and Andrea D Caviglia. Balanced electron-hole transport in spin-orbit semimetal SrIrO₃ heterostructures. *Physical Review B*, 97(8):081105, 2018.
- [96] Kaushik Sen, Dirk Fuchs, Rolf Heid, Kai Kleindienst, Karsten Wolff, Joerg Schmalian, and Matthieu Le Tacon. Strange semimetal dynamics in SrIrO₃. *Nature Communications*, 11(1):4270, 2020.
- [97] Shuo-Ying Yang, Hao Yang, Elena Derunova, Stuart SP Parkin, Binghai Yan, and Mazhar N Ali. Symmetry demanded topological nodal-line materials. *Advances in Physics: X*, 3(1):1414631, 2018.
- [98] DJ Groenendijk, C Autieri, J Girovsky, M Carmen Martinez-Velarte, N Manca, G Mattoni, AMRVL Monteiro, N Gauquelin, J Verbeeck, AF Otte, et al. Spin-orbit semimetal SrIrO₃ in the two-dimensional limit. *Physical review letters*, 119(25):256403, 2017.
- [99] Jobu Matsuno, Kota Ihara, Shugen Yamamura, Hiroki Wadati, Kenji Ishii, V Vijay Shankar, Hae-Young Kee, and Hidenori Takagi. Engineering a spin-orbital magnetic insulator by tailoring superlattices. *Physical review letters*, 114(24):247209, 2015.
- [100] BJ Kim, H Ohsumi, T Komesu, S Sakai, T Morita, H Takagi, and T-h Arima. Phase-sensitive observation of a spin-orbital mott state in Sr₂IrO₄. *Science*, 323(5919):1329–1332, 2009.
- [101] G Cao, J Bolivar, S McCall, JE Crow, and RP Guertin. Weak ferromagnetism, metal-to-nonmetal transition, and negative differential resistivity in single-crystal Sr₂IrO₄. *Physical Review B*, 57(18):R11039, 1998.
- [102] Myoung-Woo Yoo, J Tornos, A Sander, Ling-Fang Lin, Narayan Mohanta, A Peralta, D Sanchez-Manzano, F Gallego, D Haskel, JW Freeland, et al. Large intrinsic anomalous hall effect in SrIrO₃ induced by magnetic proximity effect. *Nature Communications*, 12(1):3283, 2021.
- [103] Elizabeth Skoropata, John Nichols, Jong Mok Ok, Rajesh V Chopdekar, Eun Sang Choi, Ankur Rastogi, Changhee Sohn, Xiang Gao, Sangmoon Yoon, Thomas Farmer, et al. Interfacial tuning of chiral magnetic interactions for large topological hall effects in LaMnO₃/SrIrO₃ heterostructures. *Science advances*, 6(27):eaaz3902, 2020.
- [104] Yuki Ohuchi, Jobu Matsuno, Naoki Ogawa, Yusuke Kozuka, Masaki Uchida, Yoshinori Tokura, and Masashi Kawasaki. Electric-field control of anomalous and topological hall effects in oxide bilayer thin films. *Nature communications*, 9(1):213, 2018.

- [105] Zhong Fang, Naoto Nagaosa, Kei S Takahashi, Atsushi Asamitsu, Roland Mathieu, Takeshi Ogasawara, Hiroyuki Yamada, Masashi Kawasaki, Yoshinori Tokura, and Kiyoyuki Terakura. The anomalous hall effect and magnetic monopoles in momentum space. *Science*, 302(5642):92–95, 2003.
- [106] Keng-Yuan Meng, Adam S Ahmed, Mirko Baćani, Andrada-Oana Mandru, Xue Zhao, Núria Bagués, Bryan D Esser, Jose Flores, David W McComb, Hans J Hug, et al. Observation of nanoscale skyrmions in srruo3 bilayers. *Nano letters*, 19(5):3169–3175, 2019.
- [107] Graham Kimbell, Changyoung Kim, Weida Wu, Mario Cuoco, and Jason WA Robinson. Challenges in identifying chiral spin textures via the topological hall effect. *Communications Materials*, 3(1):19, 2022.
- [108] Graham Kimbell, Paul M. Sass, Bart Woltjes, Eun Kyo Ko, Tae Won Noh, Weida Wu, and Jason W. A. Robinson. Two-channel anomalous hall effect in SrRuO₃. *Phys. Rev. Mater.*, 4:054414, May 2020.
- [109] Graham Kimbell, Changyoung Kim, Weida Wu, Mario Cuoco, and Jason W. A. Robinson. Challenges in identifying chiral spin textures via the topological hall effect. *Communications Materials*, 3(1), April 2022.
- [110] Lingfei Wang, Qiyuan Feng, Han Gyeol Lee, Eun Kyo Ko, Qingyou Lu, and Tae Won Noh. Controllable thickness inhomogeneity and berry curvature engineering of anomalous hall effect in SrRuO₃ ultrathin films. *Nano letters*, 20(4):2468–2477, 2020.
- [111] Joachim Hemberger, Alexander Krimmel, Thomas Kurz, H-A Krug Von Nidda, V Yu Ivanov, AA Mukhin, AM Balbashov, and Alois Loidl. Structural, magnetic, and electrical properties of single-crystalline La_{1-x}Sr_xMnO₃ (0.4 < x < 0.85). *Physical Review B*, 66(9):094410, 2002.
- [112] Sayani Majumdar and Sebastiaan van Dijken. Pulsed laser deposition of La_{1-x}Sr_xMnO₃: thin-film properties and spintronic applications. *Journal of Physics D: Applied Physics*, 47(3):034010, 2013.
- [113] M Kawasaki, A Ohtomo, T Arakane, K Takahashi, M Yoshimoto, and H Koinuma. Atomic control of SrTiO₃ surface for perfect epitaxy of perovskite oxides. *Applied surface science*, 107:102–106, 1996.
- [114] Gertjan Koster, Boike L Kropman, Guus JHM Rijnders, Dave HA Blank, and Horst Rogalla. Quasi-ideal strontium titanate crystal surfaces through formation of strontium hydroxide. *Applied Physics Letters*, 73(20):2920–2922, 1998.
- [115] Gertjan Koster, Guus Rijnders, Dave HA Blank, and Horst Rogalla. Surface morphology determined by (0 0 1) single-crystal SrTiO₃ termination. *Physica C: Superconductivity*, 339(4):215–230, 2000.

-
- [116] Josée E Kleibeuker, Gertjan Koster, Wolter Siemons, David Dubbink, Bouwe Kuiper, Jeroen L Blok, Chan-Ho Yang, Jayakanth Ravichandran, Ramamoorthy Ramesh, Johan E Ten Elshof, et al. Atomically defined rare-earth scandate crystal surfaces. *Advanced functional materials*, 20(20):3490–3496, 2010.
- [117] Marco Malinverni. Optimization of NH_3 -mbe grown p-doped (Al) GaN layers and their implementation in long wavelength laser diodes and tunnel junctions. Technical report, EPFL, 2015.
- [118] Yongqiang Wang and Michael Nastasi. *Handbook of modern ion beam materials analysis*. MRS, Materials Research Soc., 2010.
- [119] Linda E Franken, Kay Grünewald, Egbert J Boekema, and Marc CA Stuart. A technical introduction to transmission electron microscopy for soft-matter: Imaging, possibilities, choices, and technical developments. *Small*, 16(14):1906198, 2020.
- [120] RV Coleman and Acar Isin. Magnetoresistance in iron single crystals. *Journal of Applied Physics*, 37(3):1028–1029, 1966.
- [121] Michael Ziese. Magnetotransport. In *Handbook of Magnetism and Magnetic Materials*, pages 435–475. Springer, 2021.
- [122] Sadamichi Maekawa and Hidetoshi Fukuyama. Magnetoresistance in two-dimensional disordered systems: effects of zeeman splitting and spin-orbit scattering. *Journal of the Physical Society of Japan*, 50(8):2516–2524, 1981.
- [123] E. H. Hall. On a new action of the magnet on electric currents. *American Journal of Mathematics*, 2(3):287–292, 1879.
- [124] E. H. Hall. The hall effect. *Science*, 4(88):351–351, 1884.
- [125] Naoto Nagaosa, Jairo Sinova, Shigeki Onoda, Allan H MacDonald, and Nai Phuan Ong. Anomalous hall effect. *Reviews of modern physics*, 82(2):1539, 2010.
- [126] Yukako Fujishiro, Naoya Kanazawa, Ryosuke Kurihara, Hiroaki Ishizuka, Tomohiro Hori, Fehmi Sami Yasin, Xiuzhen Yu, Atsushi Tsukazaki, Masakazu Ichikawa, Masashi Kawasaki, et al. Giant anomalous hall effect from spin-chirality scattering in a chiral magnet. *Nature communications*, 12(1):317, 2021.
- [127] Stephen R Boona, Hyungyu Jin, and Sarah Watzman. Transverse thermal energy conversion using spin and topological structures. *Journal of Applied Physics*, 130(17), 2021.
- [128] WL Webster. The hall effect in single crystals of iron. In *Mathematical Proceedings of the Cambridge Philosophical Society*, volume 23, pages 800–803. Cambridge University Press, 1927.
- [129] Robert Karplus and JM Luttinger. Hall effect in ferromagnetics. *Physical Review*, 95(5):1154, 1954.

- [130] Michael Victor Berry. Quantal phase factors accompanying adiabatic changes. *Proceedings of the Royal Society of London. A. Mathematical and Physical Sciences*, 392(1802):45–57, 1984.
- [131] T McGuire and RL Potter. Anisotropic magnetoresistance in ferromagnetic 3d alloys. *IEEE Transactions on Magnetics*, 11(4):1018–1038, 1975.
- [132] Hiroyasu Nakayama, Matthias Althammer, Y-T Chen, Ken-ichi Uchida, Yosuke Kajiwara, Daisuke Kikuchi, Takashi Ohtani, Stephan Geprägs, M Opel, S Takahashi, et al. Spin hall magnetoresistance induced by a nonequilibrium proximity effect. *Physical review letters*, 110(20):206601, 2013.
- [133] Vahram L Grigoryan, Wei Guo, Gerrit EW Bauer, Jiang Xiao, et al. Intrinsic magnetoresistance in metal films on ferromagnetic insulators. *Physical Review B*, 90(16):161412, 2014.
- [134] M Buchner, K Höfler, B Henne, V Ney, and A Ney. Tutorial: Basic principles, limits of detection, and pitfalls of highly sensitive squid magnetometry for nanomagnetism and spintronics. *Journal of Applied Physics*, 124(16), 2018.
- [135] Christian M Julien, Atmane Ait-Salah, Alain Mauger, and François Gendron. Magnetic properties of lithium intercalation compounds. *Ionics*, 12:21–32, 2006.
- [136] Gerrit van der Laan and Adriana I Figueroa. X-ray magnetic circular dichroism—a versatile tool to study magnetism. *Coordination Chemistry Reviews*, 277:95–129, 2014.
- [137] Kasper S Pedersen, Jesper Bendix, Alain Tressaud, Etienne Durand, Høgni Weihe, Zaher Salman, Thorbjørn J Morsing, Daniel N Woodruff, Yanhua Lan, Wolfgang Wernsdorfer, et al. Iridates from the molecular side. *Nature communications*, 7(1):12195, 2016.
- [138] W Guo, DX Ji, ZB Gu, J Zhou, YF Nie, and XQ Pan. Engineering of octahedral rotations and electronic structure in ultrathin SrIrO₃ films. *Physical Review B*, 101(8):085101, 2020.
- [139] K Ueno, T Fukumura, H Toyosaki, M Nakano, T Yamasaki, Y Yamada, and M Kawasaki. Anomalous hall effect in anatase Ti_{1-x}Co_xO₂— above room temperature. *Journal of Applied Physics*, 103(7), 2008.
- [140] Duan Feng and Guojun Jin. *Introduction To Condensed Matter Physics, Volume 1*. World Scientific Publishing Company, 2005.
- [141] AK Jaiswal, AG Zaitsev, R Singh, R Schneider, and D Fuchs. Magnetotransport of SrIrO₃ films on (110) DyScO₃. *AIP Advances*, 9(12), 2019.
- [142] Zhi Shiuh Lim, Changjian Li, Xiao Chi, Ganesh Ji Omar, Haijiao Harsan Ma, Zhen Huang, Shengwei Zeng, Ping Yang, Thirumalai Venkatesan, Andriwo Rusydi, et al. Magnetic anisotropy of a quasi two-dimensional canted antiferromagnet. *Nano Letters*, 20(3):1890–1895, 2020.

-
- [143] Meera M Parish and Peter B Littlewood. Classical magnetotransport of inhomogeneous conductors. *Physical Review B*, 72(9):094417, 2005.
- [144] Kei Yosida. Anomalous electrical resistivity and magnetoresistance due to an s-d interaction in Cu – Mn alloys. *Physical Review*, 107(2):396, 1957.
- [145] Satoshi Okamoto, John Nichols, Changhee Sohn, So Yeun Kim, Tae Won Noh, and Ho Nyung Lee. Charge transfer in iridate-manganite superlattices. *Nano Letters*, 17(4):2126–2130, 2017.
- [146] Yosuke Nagaoka. Ferromagnetism in a narrow, almost half-filled s band. *Physical Review*, 147(1):392, 1966.
- [147] Sayantika Bhowal and Sashi Satpathy. Electronic structure and anomalous hall effect in the ferromagnetic 3d- 5d superlattice SrMnO₃/SrIrO₃. *Physical Review B*, 99(24):245145, 2019.
- [148] Nara Lee, Eunjung Ko, Hwan Young Choi, Yun Jeong Hong, Muhammad Nauman, Woun Kang, Hyoung Joon Choi, Young Jai Choi, and Younjung Jo. Antiferromagnet-based spintronic functionality by controlling isospin domains in a layered perovskite iridate. *Advanced Materials*, 30(52):1805564, 2018.
- [149] Kosuke Takiguchi, Le Duc Anh, Takahiro Chiba, Tomohiro Koyama, Daichi Chiba, and Masaaki Tanaka. Giant gate-controlled proximity magnetoresistance in semiconductor-based ferromagnetic–non-magnetic bilayers. *Nature Physics*, 15(11):1134–1139, 2019.
- [150] Feng Ye, Songxue Chi, Bryan C Chakoumakos, Jaime A Fernandez-Baca, Tongfei Qi, and Gang Cao. Magnetic and crystal structures of Sr₂IrO₄: A neutron diffraction study. *Physical Review B*, 87(14):140406, 2013.
- [151] Yuan Zhao, Theresa E Feltes, John R Regalbuto, Randall J Meyer, and Robert F Klie. In situ electron energy loss spectroscopy study of metallic Co and Co oxides. *Journal of Applied Physics*, 108(6), 2010.
- [152] Zhong L Wang, Jin S Yin, Wei Dong Mo, and Z John Zhang. In-situ analysis of valence conversion in transition metal oxides using electron energy-loss spectroscopy. *The Journal of Physical Chemistry B*, 101(35):6793–6798, 1997.
- [153] D Haskel, G Fabbris, Mikhail Zhernenkov, PP Kong, CQ Jin, G Cao, and M Van Veenendaal. Pressure tuning of the spin-orbit coupled ground state in Sr₂IrO₄. *Physical review letters*, 109(2):027204, 2012.
- [154] CH Ahn, A Bhattacharya, M Di Ventura, James N Eckstein, C Daniel Frisbie, ME Gershenson, AM Goldman, IH Inoue, Jochen Mannhart, Andrew J Millis, et al. Electrostatic modification of novel materials. *Reviews of Modern Physics*, 78(4):1185, 2006.

- [155] RC Neville, B Hoeneisen, and CA Mead. Permittivity of strontium titanate. *Journal of Applied Physics*, 43(5):2124–2131, 1972.
- [156] N.W. Ashcroft and N.D. Mermin. *Solid State Physics*. Saunders College Publishing, Fort Worth, 1976.
- [157] Maxim N Chernodub and María AH Vozmediano. Direct measurement of a beta function and an indirect check of the schwinger effect near the boundary in dirac semimetals. *Physical Review Research*, 1(3):032002, 2019.
- [158] Irene Battisti, Vitaliy Fedoseev, Koen M Bastiaans, Alberto De La Torre, Robin S Perry, Félix Baumberger, and Milan P Allan. Poor electronic screening in lightly doped mott insulators observed with scanning tunneling microscopy. *Physical Review B*, 95(23):235141, 2017.
- [159] Jsaminka Terzic, JC Wang, Feng Ye, WH Song, SJ Yuan, Saicharan Aswartham, Lance E DeLong, SV Streltsov, Daniel I Khomskii, and Gang Cao. Coexisting charge and magnetic orders in the dimer-chain iridate $\text{Ba}_5\text{AlIr}_2\text{O}_{11}$. *Physical Review B*, 91(23):235147, 2015.
- [160] Joachim Hemberger, Peter Lunkenheimer, R Viana, R Böhmer, and Alois Loidl. Electric-field-dependent dielectric constant and nonlinear susceptibility in SrTiO_3 . *Physical Review B*, 52(18):13159, 1995.
- [161] Junyi Yang, Lin Hao, Derek Meyers, Tamene Dasa, Liubin Xu, Lukas Horak, Padraic Shafer, Elke Arenholz, Gilberto Fabbris, Yongseong Choi, et al. Strain-modulated slater-mott crossover of pseudospin-half square-lattice in $(\text{SrIrO}_3)_1/(\text{SrTiO}_3)_1$ superlattices. *Physical review letters*, 124(17):177601, 2020.
- [162] Stefano Boseggia, HC Walker, J Vale, R Springell, Z Feng, RS Perry, M Moretti Sala, Henrik M Rønnow, SP Collins, and Desmond Francis McMorro. Locking of iridium magnetic moments to the correlated rotation of oxygen octahedra in Sr_2IrO_4 revealed by x-ray resonant scattering. *Journal of Physics: Condensed Matter*, 25(42):422202, 2013.
- [163] Juan Porras, Joel Bertinshaw, Huimei Liu, Giniyat Khaliullin, NH Sung, J-W Kim, Sonia Francoual, Paul Steffens, Guochu Deng, M Moretti Sala, et al. Pseudospin-lattice coupling in the spin-orbit mott insulator Sr_2IrO_4 . *Physical Review B*, 99(8):085125, 2019.
- [164] Sayantika Bhowal and Sashi Satpathy. Electric field tuning of the anomalous hall effect at oxide interfaces. *npj Computational Materials*, 5(1):61, 2019.
- [165] Samir Rom, Santu Baidya, Subhro Bhattacharjee, and Tanusri Saha-Dasgupta. Magnetism and unconventional topology in $\text{LaCoO}_3/\text{SrIrO}_3$ heterostructure. *Applied Physics Letters*, 122(2), 2023.

- [166] Arun Kumar Jaiswal, Robert Eder, Di Wang, Vanessa Wollersen, Matthieu Le Tacon, and Dirk Fuchs. Giant nonvolatile electric field control of proximity-induced magnetism in the spin-orbit semimetal SrIrO₃. *Advanced Functional Materials*, 34(2):2308346, 2024.
- [167] Hanghui Chen and Andrew Millis. Charge transfer driven emergent phenomena in oxide heterostructures. *Journal of Physics: Condensed Matter*, 29(24):243001, 2017.
- [168] DD Sarma and A Chainani. Electronic structure of perovskite oxides, LaMnO₃ (Ti – Ni), from high-energy electron spectroscopic investigations. *Journal of Solid State Chemistry*, 111(1):208–216, 1994.
- [169] J Töpfer and JB Goodenough. LaMnO₃₊ revisited. *Journal of Solid State Chemistry*, 130(1):117–128, 1997.
- [170] YS Hou, HJ Xiang, and XG Gong. Intrinsic insulating ferromagnetism in manganese oxide thin films. *Physical Review B*, 89(6):064415, 2014.
- [171] X Renshaw Wang, Chiang J Li, WM Lü, TR Paudel, DP Leusink, M Hoek, N Poccia, A Vailionis, T Venkatesan, JMD Coey, et al. Imaging and control of ferromagnetism in LaMnO₃/SrTiO₃ heterostructures. *Science*, 349(6249):716–719, 2015.
- [172] M Eibschütz, S Shtrikman, and David Treves. Mössbauer studies of Fe⁵⁷ in orthoferrites. *Physical review*, 156(2):562, 1967.
- [173] GR Hearne, MP Pasternak, RD Taylor, and P Lacorre. Electronic structure and magnetic properties of LaFeO₃ at high pressure. *Physical Review B*, 51(17):11495, 1995.
- [174] AK Jaiswal, R Schneider, M Le Tacon, and D Fuchs. Magnetotransport of SrIrO₃-based heterostructures. *AIP Advances*, 12(3), 2022.
- [175] A Chainani, M Mathew, and DD Sarma. Electronic structure of La_{1-x}Sr_xFeO₃. *Physical Review B*, 48(20):14818, 1993.
- [176] Somnath Jana, SK Panda, Dibya Phuyal, B Pal, Soham Mukherjee, A Dutta, P Anil Kumar, Daniel Hedlund, Johan Schött, Patrik Thunström, et al. Charge disproportionate antiferromagnetism at the verge of the insulator-metal transition in doped LaFeO₃. *Physical Review B*, 99(7):075106, 2019.
- [177] Dibya Phuyal, Soham Mukherjee, SK Panda, Somnath Jana, Carlo U Segre, Laura Simonelli, Sergei M Butorin, Håkan Rensmo, and Olof Karis. Origin of itinerant carriers in antiferromagnetic LaFe_{1-x}Mo_xO₃ studied by x-ray spectroscopies. *Physical Review Materials*, 4(3):034405, 2020.
- [178] A Scholl, J Stohr, J Luning, Jin Won Seo, J Fompeyrine, H Siegwart, J-P Locquet, F Nolting, S Anders, EE Fullerton, et al. Observation of antiferromagnetic domains in epitaxial thin films. *Science*, 287(5455):1014–1016, 2000.

- [179] J Lüning, F Nolting, A Scholl, H Ohldag, Jin Won Seo, J Fompeyrine, J-P Locquet, and J Stöhr. Determination of the antiferromagnetic spin axis in epitaxial LaFeO_3 films by x-ray magnetic linear dichroism spectroscopy. *Physical Review B*, 67(21):214433, 2003.
- [180] Jin Won Seo, EE Fullerton, F Nolting, A Scholl, J Fompeyrine, and Jean-Pierre Locquet. Antiferromagnetic LaFeO_3 thin films and their effect on exchange bias. *Journal of Physics: Condensed Matter*, 20(26):264014, 2008.
- [181] Flavio Y Bruno, Rainer Schmidt, Maria Varela, Javier Garcia-Barriocanal, Alberto Rivera-Calzada, Fabian A Cuellar, Carlos Leon, Pardeep Thakur, Julio C Cezar, Nicholas B Brookes, et al. Electron doping by charge transfer at $\text{LaFeO}_3/\text{Sm}_2\text{CuO}_4$ epitaxial interfaces. *Advanced Materials*, 25(10):1468–1473, 2013.
- [182] K Sreedhar, JM Honig, M Darwin, M McElfresh, PM Shand, J Xu, BC Crooker, and J Spalek. Electronic properties of the metallic perovskite LaNiO_3 : Correlated behavior of 3d electrons. *Physical Review B*, 46(10):6382, 1992.
- [183] KM Satyalakshmi, RM Mallya, KV Ramanathan, XD Wu, B Brainard, DC Gautier, NY Vasanthacharya, and MS Hegde. Epitaxial metallic LaNiO_3 thin films grown by pulsed laser deposition. *Applied physics letters*, 62(11):1233–1235, 1993.
- [184] M Golalikhani, Q Lei, RU Chandrasena, L Kasaei, H Park, J Bai, P Orgiani, J Ciston, GE Sterbinsky, DA Arena, et al. Nature of the metal-insulator transition in few-unit-cell-thick LaNiO_3 films. *Nature communications*, 9(1):2206, 2018.
- [185] Raoul Scherwitzl, Stefano Gariglio, M Gabay, Pavlo Zubko, M Gibert, and J-M Triscone. Metal-insulator transition in ultrathin LaNiO_3 films. *Physical Review Letters*, 106(24):246403, 2011.
- [186] I Chaitanya Lekshmi, Arup Gayen, DD Sarma, MS Hegde, SP Chockalingam, and N Chandrasekhar. Fabrication of cerium-doped LaNiO_3 thin films on LaAlO_3 (100) substrate by pulsed laser deposition. *Journal of applied physics*, 98(9), 2005.
- [187] Fangdi Wen, Xiaoran Liu, Qinghua Zhang, Mikhail Kareev, Banabir Pal, Yanwei Cao, JW Freeland, AT N'Diaye, P Shafer, E Arenholz, et al. Interface-engineered hole doping in $\text{Sr}_2\text{IrO}_4/\text{LaNiO}_3$ heterostructure. *New journal of physics*, 21(10):103009, 2019.
- [188] F Wrobel, B Geisler, Y Wang, G Christiani, G Logvenov, M Bluschke, E Schierle, PA van Aken, B Keimer, R Pentcheva, et al. Digital modulation of the nickel valence state in a cuprate-nickelate heterostructure. *Physical Review Materials*, 2(3):035001, 2018.
- [189] Yanwei Cao, Xiaoran Liu, M Kareev, D Choudhury, S Middey, D Meyers, J-W Kim, PJ Ryan, JW Freeland, and J Chakhalian. Engineered mott ground state in a $\text{LaTiO}_{3+}/\text{LaNiO}_3$ heterostructure. *Nature Communications*, 7(1):10418, 2016.

- [190] Xiaoran Liu, Michele Kotiuga, Heung-Sik Kim, Alpha T N'Diaye, Yongseong Choi, Qinghua Zhang, Yanwei Cao, Mikhail Kareev, Fangdi Wen, Banabir Pal, et al. Interfacial charge-transfer mott state in iridate–nickelate superlattices. *Proceedings of the National Academy of Sciences*, 116(40):19863–19868, 2019.
- [191] Mengwu Huo, Zengjia Liu, Hualei Sun, Lisi Li, Hui Lui, Chaoxin Huang, Feixiang Liang, Bing Shen, and Meng Wang. Synthesis and properties of $\text{La}_{1-x}\text{Sr}_x\text{NiO}_3$ and $\text{La}_{1-x}\text{Sr}_x\text{NiO}_2$. *Chinese Physics B*, 31(10):107401, 2022.
- [192] JA Alonso, MJ Martinez-Lope, and MA Hidalgo. Hole and electron doping of RNiO_3 $\text{R} = \text{La, Nd}$. *Journal of Solid State Chemistry*, 116(1):146–156, 1995.
- [193] Danfeng Li, Kyuho Lee, Bai Yang Wang, Motoki Osada, Samuel Crossley, Hye Ryoung Lee, Yi Cui, Yasuyuki Hikita, and Harold Y Hwang. Superconductivity in an infinite-layer nickelate. *Nature*, 572(7771):624–627, 2019.
- [194] Ranjan Kumar Patel, Krishnendu Patra, Shashank Kumar Ojha, Siddharth Kumar, Sagar Sarkar, Akash Saha, Nandana Bhattacharya, John W Freeland, Jong-Woo Kim, Philip J Ryan, et al. Hole doping in a negative charge transfer insulator. *Communications Physics*, 5(1):216, 2022.
- [195] Qi Song, Spencer Doyle, Grace A Pan, Ismail El Baggari, Dan Ferenc Segedin, Denisse Córdova Carrizales, Johanna Nordlander, Christian Tzschaschel, James R Ehrets, Zubia Hasan, et al. Antiferromagnetic metal phase in an electron-doped rare-earth nickelate. *Nature Physics*, 19(4):522–528, 2023.
- [196] Marios Hadjimichael, Bernat Mundet, Claribel Domínguez, Adrien Waelchli, Gabriele De Luca, Jonathan Spring, Simon Jöhr, Siobhan McKeown Walker, Cinthia Piamonteze, Duncan TL Alexander, et al. Competition between carrier injection and structural distortions in electron-doped perovskite nickelate thin films. *Advanced Electronic Materials*, 9(5):2201182, 2023.
- [197] Qikai Guo, Saeedeh Farokhipoor, César Magén, Francisco Rivadulla, and Beatriz Noheda. Tunable resistivity exponents in the metallic phase of epitaxial nickelates. *Nature Communications*, 11(1):2949, 2020.
- [198] Jian Liu, M Kareev, B Gray, JW Kim, P Ryan, B Dabrowski, JW Freeland, and J Chakhalian. Strain-mediated metal-insulator transition in epitaxial ultrathin films of NdNiO_3 . *Applied Physics Letters*, 96(23), 2010.
- [199] Le Wang, Sheng Ju, Lu You, Yajun Qi, Yu-wei Guo, Peng Ren, Yang Zhou, and Junling Wang. Competition between strain and dimensionality effects on the electronic phase transitions in NdNiO_3 films. *Scientific reports*, 5(1):18707, 2015.
- [200] TH Kim, Tula R Paudel, RJ Green, K Song, H-S Lee, S-Y Choi, J Irwin, B Noesges, LJ Brillson, MS Rzchowski, et al. Strain-driven disproportionation at a correlated oxide metal-insulator transition. *Physical Review B*, 101(12):121105, 2020.

- [201] Yao Li, Shuhan Zheng, Meifeng Liu, Xiuzhang Wang, Hong Li, Jun-Ming Liu, and Di Wu. Modulated transport and magnetic behavior in antiferromagnetic $\text{NdNiO}_3/\text{SrIrO}_3$ bilayers. *Journal of Applied Physics*, 134(24), 2023.
- [202] Jiayi Zhao, Bingyan Jiang, Jinying Yang, Lujunyu Wang, Hengjie Shi, Guang Tian, Zhilin Li, Enke Liu, and Xiaosong Wu. Magnetotransport induced by anomalous hall effect. *Phys. Rev. B*, 107:L060408, Feb 2023.
- [203] Yujun Zhang, Yong Zheng Luo, Liang Wu, Motohiro Suzuki, Qinghua Zhang, Yasuyuki Hirata, Kohei Yamagami, Kou Takubo, Keisuke Ikeda, Kohei Yamamoto, et al. Interfacial-hybridization-modified Ir ferromagnetism and electronic structure in $\text{LaMnO}_3/\text{SrIrO}_3$ superlattices. *Physical Review Research*, 2(3):033496, 2020.
- [204] Ma Angeles Laguna-Marco, D Haskel, N Souza-Neto, JC Lang, VV Krishnamurthy, S Chikara, G Cao, and Michel van Veenendaal. Orbital magnetism and spin-orbit effects in the electronic structure of BaIrO_3 . *Physical review letters*, 105(21):216407, 2010.
- [205] Di Yi, Charles L Flint, Purnima P Balakrishnan, Krishnamurthy Mahalingam, Brittany Urwin, Arturas Vailionis, Padraic Shafer, Elke Arenholz, Yongseong Choi, Kevin H Stone, et al. Tuning perpendicular magnetic anisotropy by oxygen octahedral rotations in $\text{La}_{1-x}\text{Sr}_x\text{MnO}_3/\text{SrIrO}_3$ superlattices. *Physical review letters*, 119(7):077201, 2017.
- [206] Satoshi Okamoto. Magnetic interaction at an interface between manganite and other transition metal oxides. *Physical Review B*, 82(2):024427, 2010.
- [207] Mizuki Ohno, Takahiro C Fujita, and Masashi Kawasaki. Proximity effect of emergent field from spin ice in an oxide heterostructure. *Science Advances*, 10(11):eadk6308, 2024.

Fitting Parameters:

T	a ($\mu\Omega cm^{-1}$)	ω (T^{-1})	B_c (T)
20	20.1	0.15	2.21
30	17.1	0.19	0.96
50	12.8	0.28	0.14
60	10.1	0.37	0.04
100	2.2	0.15	2.4×10^{-4}

Table 6.1: Fitting parameters extracted from the fitting of ρ_{xy}^{AHE} (see Fig. [4.7]b) with respect to the formula: $\rho_{xy}^{AHE} = a \times \tanh(\omega(B - B_c))$

T	a' (T^{-2})	b' (T^{-2})	ω (T^{-1})	B_c (T)
20	1.15393×10^{-5}	0.01773	0.14128	1
30	1.43539×10^{-5}	0.01265	0.19494	0.5686
50	1.79048×10^{-5}	0.00757	0.32997	0.04201
60	2.00767×10^{-5}	0.00336	0.5	0.02544
100	9.31567×10^{-6}	5.6×10^{-13}	0.15	2.0×10^{-4}

Table 6.2: Fitting parameters extracted from the fitting of MR (see Fig. [4.10]) with respect to the formula: $MR = a'B^2 - b'^2 \tan h^2(\omega(B - B_c))$

T	c_0 (%)	c_2 (%)	ω_2 ($^\circ$)	c_4 (%)	ω_2 ($^\circ$)
5	-0.057	0.017	22.9	0.04	-3.92

Table 6.3: Fitting parameters extracted from the fitting of $AMR(\alpha)$ (see Fig. [4.14]) with respect to the formula: $AMR(\alpha) = c_0 + c_2 \times \cos(2\alpha + \omega_2) + c_4 \times \cos(4\alpha + \omega_4)$

T	c_0 (%)	c_2 (%)	ω_2 (°)	c_4 (%)	ω_4 (°)
+50 V	0.01337	0.03719	186.31	0.02176	2.27
0 V	-0.01844	0.0111	185.48	0.01961	2.33
-50 V	-0.01283	0.00875	190.14	0.01644	-10.14

Table 6.4: Fitting parameters extracted from the fitting of $AMR(\alpha)$ (see Fig. [4.23]) at 20 K with respect to the formula: $AMR(\alpha) = c_0 + c_2 \times \cos(2\alpha + \omega_2) + c_4 \times \cos(4\alpha + \omega_4)$

Additional Figures:

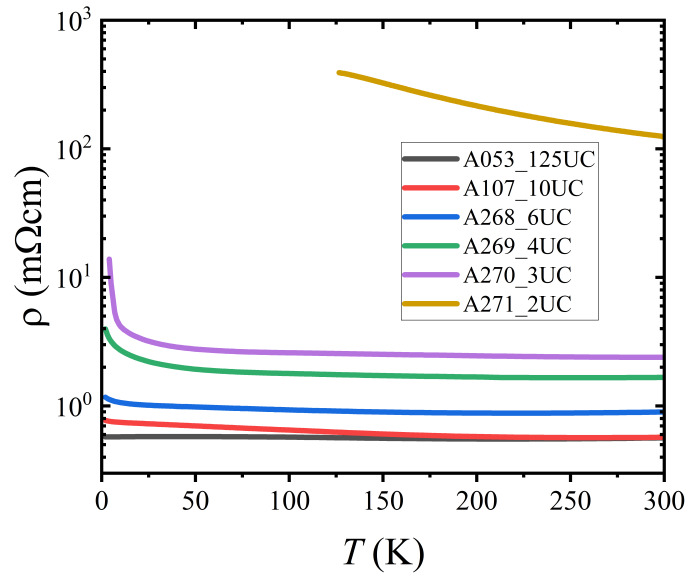


Figure 6.1: Resistivity vs temperature $\rho(T)$ for a set of $SrIrO_3$ thin films as a function of film thickness (t). A MIT is visible for $t \leq 3$ unit cell (UC).

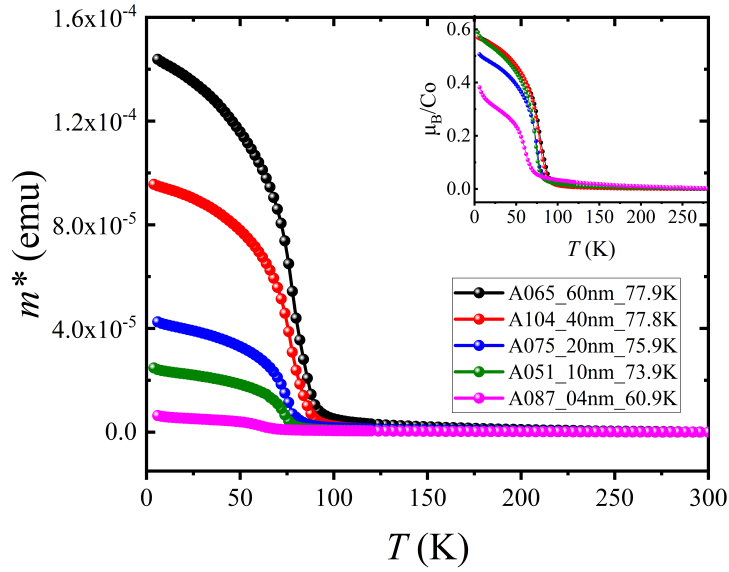


Figure 6.2: Field cooled magnetization vs temperature $m^*(T)$ for LaCoO_3 thin films as a function of film thickness t . In inset, we show the net moment in units of μ_B/Co atom. A change in the transition temperature T_c (defined by the minimum of first derivatives, $\partial M/\partial T$) as a function of t is visible, see the legend.

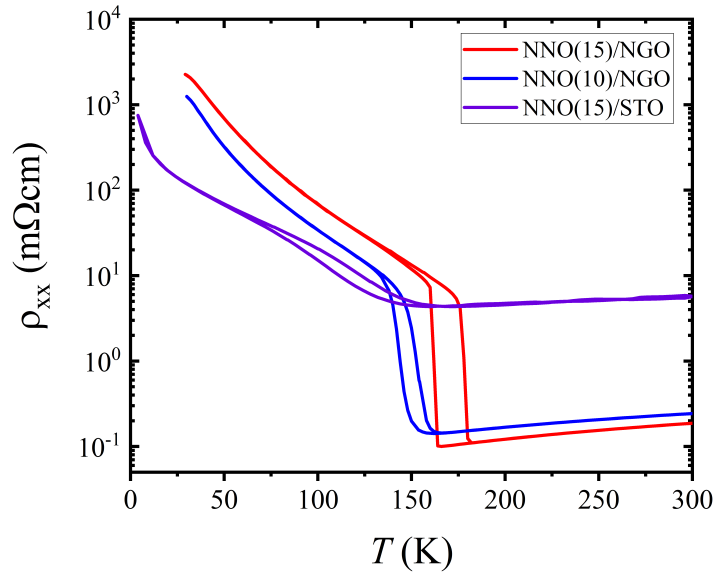


Figure 6.3: Resistivity vs temperature $\rho(T)$ for a set of NdNiO_3 thin films on NdGaO_3 (110) and SrTiO_3 (001) substrate. Film on STO shows increased resistivity compared to the films on NGO.

Abbreviations

Chapter [1]

CMOS:	Complementary Metal-Oxide-Semiconductor
QM:	Quantum Materials
TMO:	Transition Metal Oxide
2DEG or 2DES:	Two Dimensional Electron Gas or System
SP-2DES:	Spin Polarized Two Dimensional Electron System
HS:	Heterostructure
SL:	Superlattices
LAO:	LaAlO ₃
STO:	SrTiO ₃
SIO:	SrIrO ₃
LCO:	LaCoO ₃
SOC or SOI :	Spin Orbit Coupling or Interaction
FM:	Ferromagnet
HM:	Heavy Metal

Chapter [2]

CF:	Crystal Field
U:	Electron-Electron Correlation
RP:	Ruddlesden-Popper
LSAT:	(La _{0.18} Sr _{0.82})(Al _{0.59} Ta _{0.41})O ₃
DSO:	DyScO ₃
GSO:	GdScO ₃
LCO:	LaCoO ₃
ARPES:	Angle Resolved Photoemission Spectroscopy
MIT:	Metal to Insulator Transition
m or m^* :	Magnetic moment
T_c :	Curie Transition
T_N :	Néel Temperature
LSMO:	La _{1-x} Sr _x MnO ₃
XAS:	X-ray Absorption Spectroscopy
AHE or AHR:	Anomalous Hall Effect or resistance
THE:	Topological Hall Effect
DMI:	Dzyaloshinskii-Moriya interaction
SRO:	SrRuO ₃
MFM:	Magnetic Force Microscopy

Chapter [3]

AFM:	Atomic Force Microscopy
PLD:	Pulsed Laser Deposition
RHEED:	Reflection High Energy Electron Diffraction
RBS:	Rutherford Backscattering Spectrometry
UV:	Ultra-violet
T_s	Substrate Temperature
P_{O_2}	Oxygen Partial Pressure
PR	Photo Resist
TiO ₂ -STO:	TiO ₂ terminated SrTiO ₃
SIO:	SrIrO ₃ single layer thin film
LCO:	LaCoO ₃ single layer thin film
LCO/SIO:	LaCoO ₃ /SrIrO ₃ bilayer heterostructure
LCO/STO/SIO:	LaCoO ₃ /SrTiO ₃ /SrIrO ₃ trilayer heterostructure
HR-XRD:	High Resolution X-ray Diffraction
XRR:	X-ray Reflectivity
XRD:	X-ray Diffraction
RSM:	Reciprocal Space Mapping
HIR-XRD:	Half Integer Reflection X-ray Diffraction
d_{ool} :	Out-of-plane lattice parameter
TEM:	Transmission Electron Microscopy
S-TEM:	Scanning Transmission Electron Microscopy
RT:	Resistance (resistivity) versus temperature
HR:	Hall Resistance
AMR:	Angle dependent Anisotropic Magnetoresistance
PPMS:	Physical Property Measurement System
MPMS:	Magnetic Property Measurement System
SQUID:	Superconducting QUantum Interference Device
ZFC:	Zero Field Cooled magnetization
FC:	Field Cooled magnetization
EELS:	Electron Energy Loss Spectroscopy
XAS:	X-ray Absorption Spectroscopy
TEY:	Total Electron Yield
FY:	Fluorescence Yield
XANES:	X-ray Absorption Near Edge Structure
EXAFS:	Extended X-ray Absorption Fine Structure
XMCD:	X-ray Circular Magnetic Dichroism
ESRF:	European Synchrotron Radiation Facility
m_{Total} or m_t :	Total magnetic moment
$m_{Orbital}$ or m_l :	Orbital magnetic moment
m_{Spin} or m_s :	Spin magnetic moment
$m_{Spin,eff}$ or $m_{s,eff}$:	Effective spin magnetic moment

Chapter [4]

ICT:	Interfacial Charge Transfer
OHE:	Ordinary (or Normal) Hall Effect
BC:	Berry Curvature
H_c :	Coercive Field
ρ_{xx} :	Longitudinal Resistivity
ρ_{xy} :	Transverse Resistivity
σ_{xx} :	Longitudinal Conductivity
σ_{xy} :	Transverse Conductivity
θ^{AHE} :	Anomalous Hall Angle
WAL:	Weak-Antilocalization
NMR:	Negative Magnetoresistance
EF:	Electric Field
E_F :	Fermi Level
V_g :	Gate Voltage
DOS:	Density of States
λ_{sc} :	Screening Length
λ_{TF} :	Thomas Fermi Screening Length
ρ_{xy}^s :	Saturation Anomalous Hall Resistivity (at 14T)
ρ_{xy}^r :	Remnant Anomalous Hall Resistivity (at 0T)

Chapter [5]

LXO:	LaXO ₃ (X = Mn, Fe, Co and Ni)
MO:	Molecular Orbital
B-MO:	Bonding Molecular Orbital
A-MO:	Antibonding Molecular Orbital
PDOS:	Partial Density of States
Nb-STO:	Nb doped SrTiO ₃
LFO:	LaFeO ₃
LNO:	LaNiO ₃
NNO:	NdNiO ₃

List of publications

Thesis related publications

- **Giant Nonvolatile Electric Field Control of Proximity-Induced Magnetism in the Spin-Orbit Semimetal SrIrO₃**
AK Jaiswal, R Eder, D Wang, V Wollersen, M Le Tacon, D Fuchs
Advanced Functional Materials 34 (2), 2308346, 2024
- **Direct Observation of Strong Anomalous Hall Effect and Proximity-Induced Ferromagnetic State in SrIrO₃**
AK Jaiswal, D Wang, V Wollersen, R Schneider, M Le Tacon, D Fuchs
Advanced Materials 34 (14), 2109163, 2023
- **Magnetotransport of SrIrO₃-based heterostructures**
AK Jaiswal, R Schneider, M Le Tacon, D Fuchs
AIP Advances 12 (3), 035120, 2022

Other publications

- **Robust spin-orbit coupling in semi-metallic SrIrO₃ under hydrostatic pressure**
D Fuchs, AK Jaiswal, F. Wilhelm, D. Wang, A. Rogalev, M Le Tacon
*Submitted
- **Flexible strained membranes of multiferroic TbMnO₃**
H. Shi, F. Ringe, D. Wang, O. Moran, K. Nayak, AK Jaiswal, M Le Tacon, D Fuchs
Appl. Phys. Lett. 125 (1), 011901, 2024
- **Strained single crystal high entropy oxide manganite thin films**
Z Zhao, Moaz Waqar, AK Jaiswal, A R Raghavan, D Fuchs, J Lin, T. n Brezesinski, SS Bhattacharya, H Hahn, X Pan, R Kruk, A Sarkar
Appl. Phys. Lett. 125 (1), 011902, 2024
- **Strain-Driven Bidirectional Spin Orientation Control in Epitaxial High Entropy Oxide Films**
Z Zhao, AK Jaiswal, D Wang, V Wollersen, Z Xiao, G Pradhan, F Celegato, P Tiberto, M Szymczak, J Dabrowa, M Waqar, D Fuchs, X Pan, H Hahn, R Kruk, A Sarkar
Advanced Science 10 (27), 2304038, 2023

Conference Contributions

- **MSCA QUSTEC EUCOR Summer School 2021**
September 2021, Engelberg, Switzerland (Poster, in-person)
- **International Workshop on Oxide Electronics (iWOE)**
October 2021, Genova, Italy (Poster, online)
- **Moonlight Seminar**
October 2021, KIT, Germany (Oral)
- **Magnetism & Magnetic Materials (MMM) and Intermag**
January 2022, Florida, USA (Poster, Online)
- **Karlsruhe Graduate School on Quantum Matter Retreat Meeting**
September 2022, Germany (Oral, in-person)
- **MSCA QUSTEC EUCOR Summer School 2022**
September 2022, Freiburg im Breisgau, Germany (Poster, in-person)
- **QUOROM 6, 7, 8 on-line conference on Oxide electronics**
March 2022, Sep 22, Feb 23, Germany (Participation, online)
- **APS march Meeting 2023**
March 2023, Las Vegas, USA (Poster, in-person)
- **European MRS Spring Meeting**
May 2023, Strasbourg, France (Oral, in-person)
- **Karlsruhe Graduate School on Quantum Matter Retreat Meeting**
June 2023, Germany (Poster, in-person)
- **KSQM QUSTEC European Summer School in Quantum Science and Technology**
September 2023, Durbach, Germany (Poster, in-person) **Best poster award*

Acknowledgements

This journey started in September 2018 when I joined Thin Films and Interfaces group, IQMT (then IFP) for my master's thesis. After a fruitful year, I continued my research as a PhD candidate. During my time as a PhD scholar, many people have enriched me with their valuable guidance, support and assistance. At this point, I would like to express my acknowledgment to all those who have contributed to this thesis directly or indirectly.

Firstly, I express my sincere gratitude to Prof. Matthieu Le Tacon for accepting me as a PhD candidate and giving me the opportunity to carry out my dissertation work at IQMT. My research and especially this thesis benefited enormously from the invaluable discussions that we had. His constant support has been overwhelming in this journey.

Furthermore, I am deeply grateful to my advisor, Dr. Dirk Fuchs. I immensely benefited from his expertise and insights in the field. He welcomed me with a warm heart and patiently answered all my questions, even the stupid ones. He introduced the finer details of the experiments, which helped me to develop the ability to design and perform experiments independently. Without his guidance, encouragement, and belief in me, it would not have been possible to perform this research work and write this thesis in its present form. His support, and, most importantly, day-to-day guidance have been invaluable throughout my doctorate journey.

I also sincerely thank Prof. Wulf Wulfhekel for acting as a co-referee for my thesis and providing valuable feedback.

Additionally, I would like to thank Prof. Andrea Caviglia from the University of Geneva for hosting me in his group. It was a nice experience with the amazing group in Geneva.

I express my gratitude to Dr. Robert Eder, Prof. Tanusri Saha-DasGupta, and Samir Rom for theoretical support, which helped me understand the experimental findings.

I acknowledge other Thin Films and Interfaces group members: Dr. Rudolf Schneider, Dr. Alexander Zaitsav, and Andre Beck, for their immense support. I also thank the mechanical and electronic workshops for their help in designing and fixing the experiments. In particular, Mr. Otto Walz was always available to help with IT, electronics and administration problems. My profound gratitude goes to our institute secretaries, Carmen Dörflinger and Dorothea Trauttmann, for all their help with administrative work.

Sincere thanks to MSCA-QUSTEC (EUCOR) (agreement number 847471) for funding the PhD work. I express my regards to QUSTEC coordinators Nataliia Voievoda, Vedran

Lopandic, and Johanne Martinez for their assistance in QUSTEC engagement, paperwork, and training.

I sincerely thank Dr. Karston Wolff and Fariba Ghorbani for introducing me PPMS and PLD systems, respectively and Dr. Kaushik Sen for the scientific discussions we had in the initial phase of my PhD.

I thank Dr. Di Wang and Vanessa Wollersen for the TEM measurements. I also wish to thank Dr. Richard Thelen and KNMF for granting us access to the AFM facility at IMT.

I thank Dr. J. Schubert, Forschungszentrum Jülich, Peter Grünberg Institute Jülich, Germany for RBS measurements.

Special thanks to Dr. Andrei Regalov and Dr. Fabrice Wilhelm from ID12, ESRF for their valuable support during our beamtime at ESRF. Also, thanks to ESRF for providing beamtime (HC-5007, HC-5409).

Over the years, IQMT has been a second home to me. I gratefully acknowledge everyone with whom I have come across. My officemates: Dr. Kaushik Sen, Dr. Karsten Wolff, Dr. Yi Yao, Dr. Saumya Mukherjee, Dr. Mehdi Frachet, Dr. Huanhuan Shi, and Paolo Battistoni. It was my pleasure to share office (324) with you all and discuss various topics ranging from science to sports, politics, language, and different cuisines. Colleagues: Dr. Christoph Meingast, Dr. Rolf Heid, Dr. Amir Haghighirad, Dr. Frederic Hardy, Dr. Michael Merz, Dr. Kristin Willa, Dr. Robert Eder, Dr. Kai Grube, Dr. Frank Weber, Dr. Stefan Schuppler, Dr. Peter Nagel, Dr. Roland Schäfer, Dr. Roland Hott, Dr. Michaela Sofia Souliou, Dr. Igor Vinograd, Dr. Santanu Pakhira, Dr. Philippa McGuinness, Dr. Liran Wang, Dr. Daniel Arnold, Amir Ghiami, Tom Lacmann, Anmol Shukla, Paolo Battistoni, Fabian Henßler, Mark, Arthur.

A big thanks to all my teachers and academic mentors who introduced and motivated me to pursue a career in science and especially physics. Thank you so much for all the blessings and support. I am forever obliged for their guidance and influence.

I am thankful to my friends: Abhinav, Akhilesh, Aman, Chaitanya, Neha, Shalu, Snigdha, Swati, Vaibhav and Dr. Nanhe Gupta. Thanks to everyone who made my stay in Karlsruhe memorable. Special thanks goes to my friends: Veerraju Mohana, Vanitha, Vinay, Poorwa, Anmol, Ananyo, Ashutosh, Prince. Thank you so much for the time we spent together.

Last but not least, I am forever indebted to my grandparents, parents and family members for always motivating and supporting me over the years. Their belief in me and constant encouragement have been instrumental throughout this journey.

This thesis is a testament to the collective effort of teamwork, and it is likely that I have forgotten a few names. I also thank them for their presence and influence.

Thank you.

